Elementary Morphing Shells

Department of Engineering
University of Cambridge

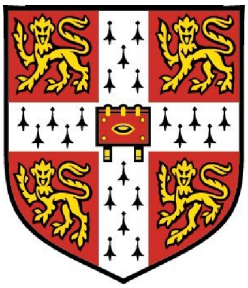

Evripides G. Loukaides

A dissertation submitted for the degree of
Doctor of Philosophy

Girton College

September 10th, 2013

The work described in this dissertation was carried out in the Department of Engineering at the University of Cambridge between October 2009 and August 2013. The author declares that, except for commonly understood and accepted ideas, or where specific reference is made to the work of other authors, the contents of this dissertation are the result of his own work and include nothing which is the outcome of work done in collaboration. This dissertation has not been previously submitted, in part or in whole, to any other academic institutions for any degree, diploma or other qualifications. This dissertation is 167 pages long, and contains approximately 39000 words and 80 figures.

.....

Evripides G. Loukaides
September 10^{th}, 2013

Acknowledgements

My deepest gratitude goes to my supervisor, Dr Keith Seffen, for his ceaseless support and mentorship. He shared his time and his ideas enthusiastically and suffered tremendous pestering from my part without protest—most importantly, a genuine pursuit of wonder and discovery was present in all our research and conversations. It is not an exaggeration to state that I always left his office with a renewed sense of excitement about my work. At the same time, I feel obliged to my advisor, Dr Simon Guest, for his precious advice on various occasions and his interest in my work.

I am grateful to all my colleagues in the Advanced Structures Group for providing a spectrum of expertise to draw from. I am particularly indebted to my deskmate and friend Ioannis Mitsos for countless constructive discussions, on topics ranging from the technical to the philosophical. The Structures Group at CUED provided an ideal environment for the pursuit of knowledge. The diversity and depth of experience was a constant resource and numerous individuals were helpful along the way. I must thank Alistair Ross for continuous assistance in the departmental workshops, as well as Dr Muhammad Shahid and Peter Knott for giving me a practical introduction to laminates.

I would be remiss if I did not thank Dr Corrado Maurini for a thoroughly educational month in Paris during my second year. The bulk of the work in Chapter 5 is a result of my time working with him. His group members at Institut Jean Le Rond d'Alembert were pleasant hosts and eager collaborators. Dr Stoyan Smoukov, of the Department of Material Science and Metallurgy at the University of Cambridge, allowed me to use his group's lab space and his insight for the actuation experiment in Chapter 7. The Micromechanics group at CUED gracefully lent me their equipment for the needs of the same work. Tobias Uth expertly assisted in the operation of the high-speed camera; he also proved a most agreeable and patient housemate over the past four years.

Beyond the spirited co-workers I was surrounded by, I was lucky to have the benefit of understanding friends, both in Cambridge and elsewhere. Among those, I am especially beholden to Sozos, Vanessa, Padma and Kyriacos for their kindness and their zest for life. Time is an expensive commodity and I appreciate you being so generous with yours. I also had the fortune of receiving endless support from my family. After a decade abroad it is invaluable to know that a loving home is always there when you need it.

Finally, I would like to aknowledge and express graditude for financial support from the Cyprus State Scholarship Foundation and the Alexander S. Onassis Public Benefit Foundation.

Elementary Morphing Shells

Evripides G. Loukaides

Abstract

Multistable shells are not yet completely understood. Even under the widespread Uniform Curvature (UC) assumption, the limits of this behaviour have not been established and the influence of individual material and geometric parameters has not been described conclusively; this research explores these open questions. In addition, this project was motivated by the need for practical design guidelines and the pursuit of alternative construction and actuation methods for multistable shells. Our analysis is based on an expression for the strain energy of a shell under a set of simplifying assumptions—primarily the aforementioned UC assumption. We extend this concept beyond the work of previous authors by admitting a more diverse range of anisotropic materials. Furthermore, we take advantage of some aspects of the mathematical field of Catastrophe Theory (CT) to maximise the generality of available results. When appropriate, we examine aspects of our predictions by constructing relevant shell structures, with particular focus on material considerations. A commercial Finite Element Analysis package provides additional means of analysis and comparison. On the theoretical front, the influence of certain control parameters on the availability of multistability is described in closed-form while a unique graphical overview of the limits of this behaviour is provided. In the lab, a novel tristable shell is constructed from a laminate and the use of specialized materials is scrutinised. In a subsequent project, a bistable spherical cap made from a customized material is actuated by a magnetic field—the ensuing snap-through event is recorded with a high-speed camera, leading to valuable insights on the transition geometry. Furthermore, we confirm the possibility of bistability for developable, non-prestressed shells, composed of a single material, using grid shells and thin honeycomb shells.

Contents

CONTENTS

Nomenclature

Abbreviations

CT	Catastrophe Theory
CUED	Cambridge University Engineering Department
DOF	Degree(s) of Freedom
FE or FEA	Finite Element method or Finite Element Analysis
FVK	the Föppl-Von Kármán model
GC	Gaussian Curvature
LVC	Linear Variation of Curvatures
MEP	Minimum Energy Path
MFC	Macro-Fibre Composite
PDE	Partial Differential Equation
PDMS	Polydimethylsiloxane; an elastomer
PP	Polypropylene; a thermoplastic
TPU	Thermoplastic Polyurythane
UC	Uniform Curvature

Greek Symbols

$\chi_x, \chi_y, \chi_{xy}$	changes in curvatures and twisting curvature ($= \kappa - \kappa_0 - \kappa_F$)
Δg	dimensionless change in Gaussian curvature
$\delta\chi$	volume magnetic susceptibility difference between the particle and the surrounding medium
$\epsilon_x, \epsilon_y, \gamma_{xy}$	direct strains and shear strain
$\kappa_x, \kappa_y, \kappa_{xy}$	absolute curvatures. The subscript "0" denotes initial value. In Chapter 2 an overbar signifies dimensionless curvatures.

$\kappa_{xF}, \kappa_{yF}, \kappa_{xyF}$	residual curvatures freely induced by prestress. When this is combine with initial curvature, the subscripted symbol h is used instead
λ	eigenvalues
μ_0	magnetic susceptibility of free space
$\nu, \beta, \psi, \eta, \alpha$	relative anisotropic stiffness terms
ϕ	geometrical and material shape factor for shell
ρ	radius of curvature—sometimes subscripted to indicate direction
$\sigma_x, \sigma_y, \tau_{xy}$	direct stresses and shear stress

Mathematical Symbols

$\|\ \|$	determinant of the enclosed matrix
$\mathcal{H}$	the Hessian operator

Roman Symbols

a, b, h, d	local and global dimensions of shell
B	magnetic flux density in Tesla (T)
E, G, K	Young's, shear and bulk modulus in the x-direction. Other subscripts signify the corresponding direction.
g	Gaussian Curvature
$h_{()}$	see entry for $\kappa_{xF}, \kappa_{yF}, \kappa_{xyF}$
L	volume fraction in composite
M_x, M_y, M_{xy}	bending moments and twisting moment per unit length of shell
N_x, N_y, N_{xy}	normal forces and shearing force per unit length of shell
R	characteristic radius of curvature of shell
t	shell thickness
U, U_B, U_S	total strain energy and strain energy densities of bending and stretching respectively
V	magnetizable volume
w	out-of-plane displacements
x, y, z	orthogonal coordinates within plate; z is normal to the middle surface of the plate. In some instances the "1, 2, 3" convention is used instead, or the "1, 2, 6" convention in the case of laminates

ABD constitutive matrix for shell, taken from the literature for fibre-reinforced composites

Subscripts

$()_0$ term corresponding to initial state

$()_d$ diagonal direction

$()_F$ term corresponding to prestressing

$()_m, ()_f$ subscripts indicate matrix and fibre properties respectively

Chapter 1

Introduction

1.1 Inspiration and Motivation

Traditional engineering requires stiff, static structures. Excessive deformation and shape-shifting are considered undesirable. But, we need only look at the ubiquitous keyboard to recognise the plethora of structures that incorporate motion. They need to do so repeatedly and they need to do so reliably. When the constraints of immobility have to be removed, we usually see elaborate machines in place with a variety of actuating mechanisms and links. This in turn presents a number of difficulties in terms of the design process and imposes severe complexities with respect to construction and maintenance. A category of structures known as *multistable* or *morphing shells* circumvents many of these issues.

Multistable shells are defined to be thin structures capable of maintaining stiffness in different geometries. Contrary to most currently available mechanisms, it is most striking to consider their simplicity. They can be composed of a single, conventional material and have a continuous initial shape. This offers dramatic improvements with respect to mechanical methods of shape change. Furthermore additional benefits arise in terms of weight and cost. With this in mind, a deeper understanding of the shape-changing capabilities of shells is sought.

As is noted by Calladine (1989), progress in the study of shells has followed technological demand, and the study of multistable shells does not escape this trend. The emergence of composite laminates and the accidental discovery of bistability in those structures made this a current topic of interest (Hyer, 1981b). However, the aim of this work is not only to provide practical knowledge for the technologist, but understanding for the scientist and engineer. This duality is a recurring theme in this dissertation.

Although not fully understood, morphing shells are not absent from everyday life. Their use is commonly widespread in the form of the "flick" bracelet that bicyclists and children often use (see Fig. 1.1 for an example). At the same time, the same category

Figure 1.1: The common "flick" bracelet, sometimes used as a toy or as trouser cuffs by cyclists. They can be easily manufactured out of curved metal strips: for bistability, prestressing is needed, and can be introduced by passing the strip through a roller.

of structures includes the bistable spherical cap that certain button mechanisms employ. Potential future uses include morphing aeroplane wings, shape-shifting car bodies and deployable structures for space applications. In turn the respective motivation for these is better aerodynamic control, reduced air resistance and more efficient packing techniques.

Nature provides inspiration in this field, in the snapping of *Dionaea muscipula* or Venus flytrap, as it is commonly known. A simple mechanical model equivalent can be manufactured with a simple "flick" bracelet at its core, as shown in Fig. 1.3. A complicated natural mechanism is reproduced by relatively simple means and almost no cost.

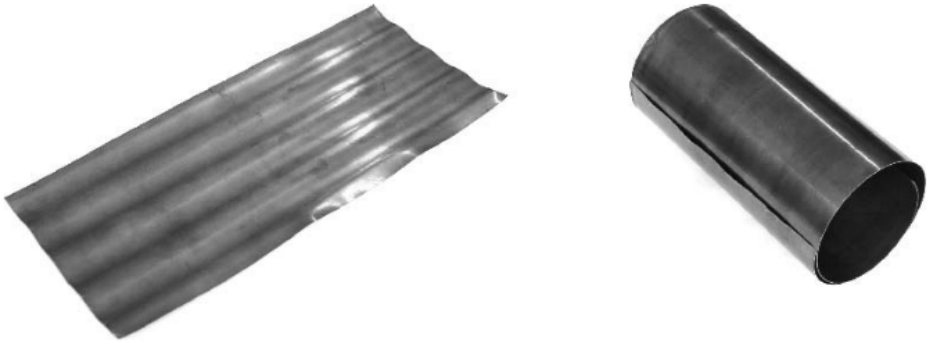

Figure 1.2: A bistable corrugated shell shown in both its globally flat and cylindrical states from Norman *et al.* (2008a). The corrugations run along a single direction and flatten out when the shell is in the cylindrical configuration.

The function of this category of structures is scale independent. In a lot of cases, their constructibility is similarly achievable in multiple scales. Hence, the various applications range from the micro-scale to the architectural scale as noted above. In the context of structural engineering, the behaviour of multistable shells includes both linear-elasticity and non-linear behaviour around snap-through events. It is important to note this distinction with other attempts at morphing structures using "smart materials," including

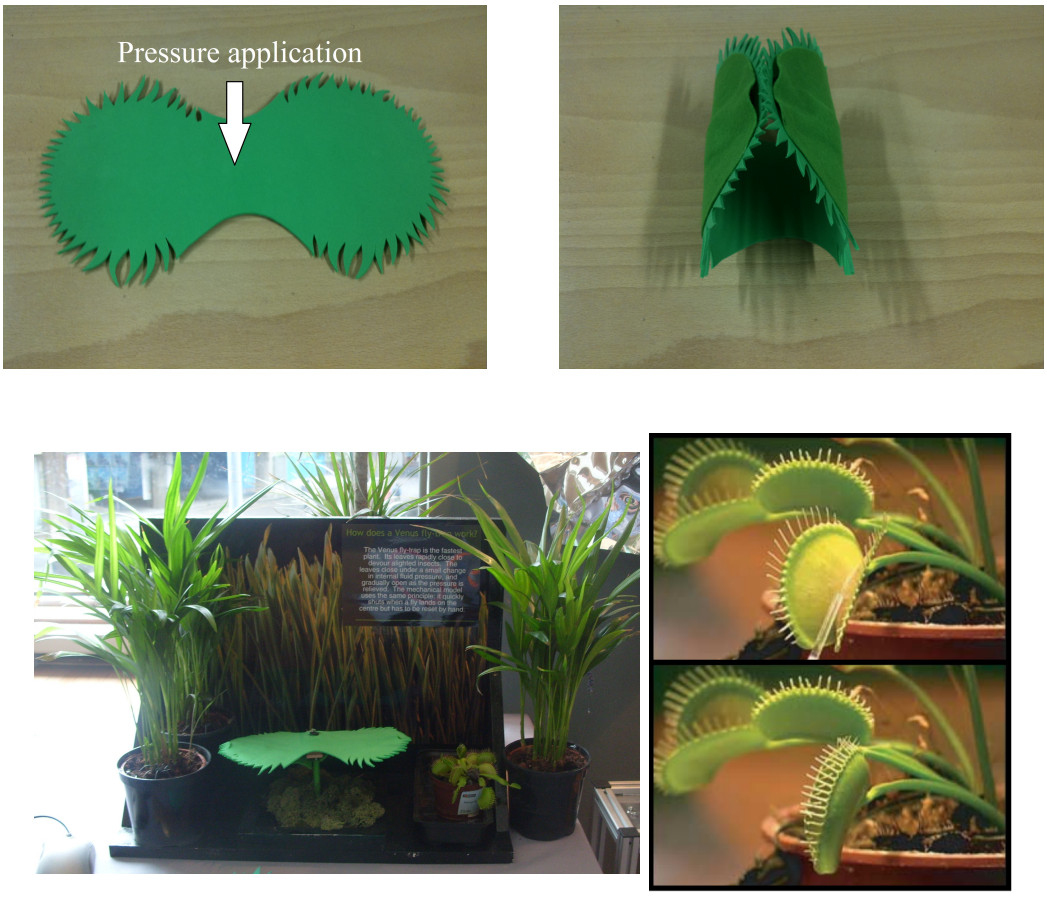

Figure 1.3: A display with a mechanical model of the Venus Flytrap plant and an actual plant in the bottom right for comparison—from Forterre *et al.* (2005). Application of minimal pressure by the "user" made the structure jump to a closed configuration. A closer view of the mechanical model is shown below is open (top left) and closed (top right) configurations. The underlying mechanism is a bistable "flick" bracelet. This display (bottom left) was constructed by the author for the Royal Society's 350$^{\text{th}}$ Anniversary Summer Science Exhibition.

shape memory alloys.

The actuation of multistable shells is an application-specific topic, and is difficult to generalise. However, actuation is a necessary component of any practical application, and part of this work addresses theoretical and practical aspects of that process. The domestic kettle switch is usually a bimetallic morphing shell that undergoes large deformations, actuated by heat. In such applications, the actuator is provided; for new applications, custom solutions need to be devised. The power requirements of the transition from one shape to the next can prove critical, especially considering the large range of scale available to these structures.

For precise development of related technologies, a deep understanding of possible behaviour is required. Our main motivation is this pursuit and the role of material properties, geometry and all other contributing parameters are of interest. However, this dissertation is not about new materials, it is about achieving new technologies with traditional materials. Hence, we first try to understand the influence of material parameters, so that we can then emulate them by heterogeneous structures made from common materials.

At the same time we are interested in feasible and optimised construction methods. Widespread adoption of these technologies depends on the related ease of manufacturing and their associated costs. This research focuses on multistable shells of spatially uniform initial curvature—we refer to these as *elementary morphing shells*. Corrugated and dimpled shells are closely related structures but are beyond the scope of this work.

1.2 Dissertation overview

This work can be described as a collection of **distinct investigations** that focus on particular aspects of the behaviour and technology of multistable shells. A diverse collection of tools is used, which adds to the breadth of the research, but to some extend hinders the continuity of the narrative. An attempt to maintain an overarching framework is made, but we alert the reader to various techniques that are specific to certain Chapters or Sections. This section gives an overview of the dissertation and places each project within the greater context of morphing shells—a literature review of relevant work is presented in Chapter 2 and assists in providing context.

Chapter 3 is primarily concerned with consolidating our treatment of materials. It offers examples of materials currently in use for the construction of multistable shells, and formalises their constitutive behaviour. In addition, it introduces alternative material concepts for such constructions, and again, gives a mathematical basis for the calculation of material properties. A brief sense of dimensionality for material parameters is also given, but we reserve more detailed calculations for actual design cases later in the dissertation.

In Chapter 4 material considerations are combined with a compatibility condition to formulate a strain energy expression under the Uniform Curvature (UC) assumption. This is an extension of much recent work by other authors and proves an incredibly powerful, yet simple tool in producing closed-from descriptions or numerical investigations of possible morphing behaviour. Even though we present a dimensionless formulation, the examination in this Chapter is limited in scope, since it uses the traditional approach to find equilibria for specific cases. The work in Chapter 5 overcomes these limitations by drawing inspiration from Catastrophe Theory (CT), a mathematical tool that is also introduced in that Chapter. In this—more abstract—approach, more general conclusions are drawn about the possible behaviour of multistable shells. Specifically, closed-form descriptions are given for the boundaries between possible stability regimes as they relate to various material, geometry and control parameters.

Chapter 6 uses the knowledge from earlier Chapters for the design and construction of a composite, tristable shell. This experimental work is no longer in the abstract domain, and some dimensional considerations are taken to ensure a successful design. The practical complications of such an endeavour are noted to assist future efforts. Experimental work continues in Chapter 7, which showcases a novel approach to actuation: a bistable, spherical shell is constructed with a magnetically sensitive material, and is then remotely actuated by a magnetic field. The transition of the shell between the two stable configurations is recorded by a high-speed camera to highlight the shape change during actuation. In the same Chapter, the actuation of multistable shells is given a brief theoretical treatment, using the formulation from Chapter 4.

The presentation of research concludes with Chapter 8, which introduces grid shells and honeycomb shells as candidate structures for multistability. Based on homogenised properties of such materials from Chapter 3, various designs are predicted to be bistable by the model in Chapter 4. Some structures are then tested through Finite Element Analysis, where parametric studies help establish the influence of certain local and global dimensions, while a physical demonstrator is subsequently constructed. Finally, in Chapter 9 the conclusions of this research and potential future directions are listed.

Chapter 2

Literature Review

2.1 Introduction

In this Chapter, we present a historical overview of previous work in the field of morphing shells. In mathematical terms, the problem of shell multistability relates to the larger problem of buckling; a topic too vast to be adequately presented here. In turn, the theoretical understanding of shells and plates is also essential to the treatment of multistable shells, but equally broad. Instead, this review focuses on various themes within multistable shells that form parallel and sometimes-intersecting streams of research. First, efforts to model the problem of multistable shells have been consistent over the past 50 years. For much of that time, theoretical formulations have described extremely specific cases of the problem. On the experimental front, the construction and analysis of fibre reinforced bistable shells has been an almost continuous activity over the past 40 years. A more recent trend in the literature is to draw inspiration from and provide comparison with multistable shells and growth phenomena in nature.

This thesis touches upon an array of these themes, and it is challenging to tie them together in this literature review without the additional knowledge that subsequent chapters provide. But we also highlight novel shells that are multistable, but not considered in the literature; this is another aim—that of synthesizing new forms using traditional materials. For example, the concept of multistable grid shells is not, to the knowledge of the author, encountered anywhere in the literature. Consequently, a brief review of grid shells is attempted in this Chapter and in Chapter 3, but does not tie into multistability before Chapter 8. Similarly, for additional topics like Classical Laminate Theory, some review is done in Chapter 3 and not here.

Before presenting technical information on these topics, the definitions of relevant terms are essential. *Morphing* and *shape-changing* structures are blanket terms for structures that have the ability to change their form or shape in a significant manner, involving large deformations. They include foldable devices such as origami shells and inflatable

structures. A great number of shape-changing structures are rooted in mechanical design and might use various hinges and linkages to achieve large deformations. A lot of academic work focuses on a subset of morphing structures called *deployable* structures; again, a rather generic term. The term usually refers to structures that can be packed in a confined configuration but be deployed to a structure of greater dimensions when necessary. This transition might often incorporate motors or hydraulic actuators.

Within the field of morphing thin structures, we focus on multistable shells. A shell usually refers to a single, continuous body with one dimension much smaller than the other two. A *multistable* shell is capable of maintaining stiffness in more than one distinct geometries. From a strain energy perspective, the shell reaches a local minimum at each of those configurations. When transitioning from one stable geometry to another, the shell needs to overcome an energy hump between the two, and for part of the transition, it normally experiences a negative stiffness. We refer to this event as a *snap-through* phenomenon.

Guiding or *actuating* the shell through this non-linear event is often a multi-parameter optimization problem, since questions of power consumption, geometry, and material limits come into play. In fact, in formulating the problem of actuation, the nature of the guiding forces adds another layer of complexity. In the case of embedded piezoelectric actuators, for example, modelling the actuating forces as an additional in-plane stress might be appropriate. However, if we are using a single contact point hydraulic actuator, an out-of-plane concentrated force needs to be incorporated in the formulation.

2.2 Shell theory and mathematical tools

The small-displacement theory of plates and shells was initially developed by Love based on assumptions by Kirchhoff (Love, 1888). This work treats shells as zero through-thickness surfaces that carry certain elastic properties such as bending and stretching stiffnesses, and makes additional requirements for small strains, small rotations and a constant shell thickness during deformation. Later work by Von Kármán expanded this formulation, to allow for greater deformations but we reserve further details for Chapter 4.

Perhaps the earliest appearance of the problem of large-deformation shell morphing involves the buckling of the measuring tape: An extended measuring tape of sufficient length will suffer a snap-through; its stiffness will be dramatically reduced and then increase again, allowing the bent structure to reach equilibrium under its own weight (Fig. 2.1). Initially it was a question of interest because it was noticed that the curvature of the bent structure matched the local curvature. We have an account of this problem being presented to—but not solved by—A. E. H. Love. Description of the episode, along with an elegant solution can be found in the Love Centenary Lecture by Calladine (1988).

The study of tape springs returned to prominence again after the potential for use in space applications was conceived. They can act as both stiffeners (once deployed) and actuators (after elastic folding) for membranes and other lightweight structures. Seffen & Pellegrino (1999) present equations to model the fold in initially straight tape springs, where the deformation of the buckled geometry is predicted and associated dynamic effects are examined. This analysis was extended by Seffen *et al.* (2000) to show that initial curvature in the longitudinal direction does not significantly alter the large deformation bending behaviour.

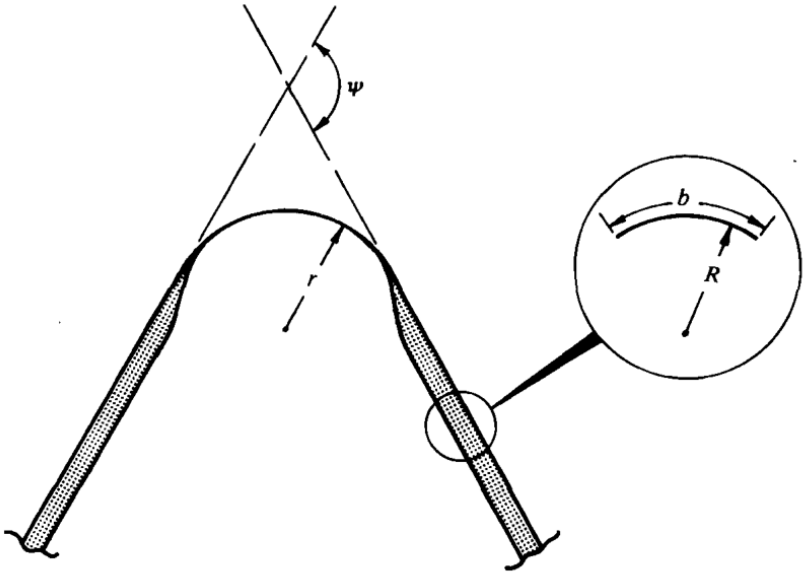

Figure 2.1: Calladine (1988) presents an elegant explanation for the post-snapping behaviour of the tape measure. A diagram from that work shows the bent measuring tape as well as the cross-section of the tape when straight. Both the initial and final configurations display spatially uniform curvature. Although not a case of multistability, the problem involves large displacements and non-linear geometry changes. The total strain energy of the bent state is at a minimum when $r = R$.

The study of the bimetallic disk independently by Panov (1947) and Wittrick *et al.* (1953) is probably the first formal examination of morphing bistable shells, but they had been in use by engineers for significantly longer. They both set up differential equations for the deformation of a spherical disk. Wittrick *et al.* (1953) shows some immediately useful results, such as the temperature hysteresis when actuating between the two states, and the geometry needed for the second stable equilibrium to appear; "`. . . initial central rise of the disk must be greater than approximately twice the total thickness.`"

By their very definition, morphing shells involve large deformations. Such behaviour is described analytically by the Föppl-von Kármán equations, which however can only be solved in closed-form for a very limited number of loading and boundary conditions including, for example, the deformations of a circular disk under axisymmetric loading

and boundary conditions (Mansfield, 2005).

Buckling of shells became popular with advances in lightweight girder construction in the mid-twentieth century, and again progress can be attributed to von Kármán (Berger & Fife, 1966). Calladine (1989) explains that the partial differential equations that result from classical buckling analysis are not analytically soluble in general cases. It is worth stressing that in the mathematical sense, multistability of shells describes a process of buckling. In this particular case however, a stable state follows the non-linear event. This differentiation between a catastrophic and a desirable event is what sets this behaviour apart.

The buckling of a spherical cap can be seen as both (an unlikely) structural failure in architectural domes and as a necessary transition leading to a useful second geometry. The greatest part of the relevant literature deals with the much wider catastrophic event, but very early the special significance of multistability was recognised. A case study by Chien & Hu (1956) offers a theoretical solution for the axisymmetric case of moment loading at the boundary. For large uniform pressure loads however, Huang (1964) observes a discrepancy between numerical results and experimental data. An asymmetric displacement field removes this discrepancy but the study did not conclusively explain its causes.

At the same time, one cannot ignore the rise of computational tools in the past decades. The combination of abundant computational power with the Finite Element (FE) method has become an indispensable tool for engineers and it serves to corroborate both experimental and theoretical endeavours. For example we can see an early use of a numerical method in extracting patterns of behaviour for the snapping of isotropic spherical caps in a study by Brodland & Cohen (1987). The effects of the slenderness of the shell and the ratio of height to planform width are examined in a displacement-controlled virtual experiment. Specific numerical techniques such as the Riks Method and quasi-static application of dynamic, so-called "explicit" methods in modern commercial software packages allow for faster handling of the snap-through behaviour.

A powerful mathematical tool that directly addresses the problem of bifurcation analysis is Catastrophe Theory. This theoretical approach was originally described by Thom (1972) in the classic text *Stabilité structurelle et morphogenèse*. It provides an analytical framework for phenomena where a sudden dramatic change in state is experienced after a gradual change in a parameter. The many applications of this theory in the sciences and later in engineering were presented by example by various researchers (Gilmore, 1993; Thompson, 1982; Zeeman, 1977), and these include topics in biology, astrophysics and psychology. One example relating to animal behaviour is illustrated in Fig. 2.2. Examples in structural engineering are given by Thompson & Hunt (1984), where the transition of shells from regions of monostability to regions of multistability is such an event. This

allowed for an analytical overview of multistable shells that is presented in Chapter 5.

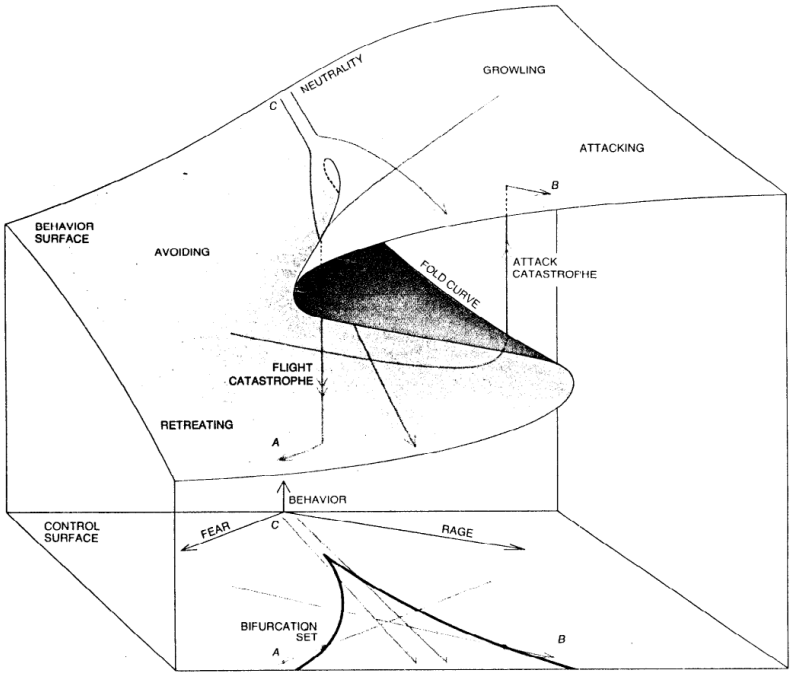

Figure 2.2: Initially, Catastrophe Theory (CT) influenced a variety of fields with parameters that were difficult to quantify. In this diagram taken from Zeeman (1977), an attempt is made to explain how sudden, dramatic changes in a "dog's" behaviour are possible even through small, smooth changes in the controlling parameters. The mathematical aspects of CT are explained further in Chapter 5.

2.3 Composite shells

In retrospect, some 30 years later, slender laminates became a popular material for morphing applications after a seminal study by Hyer (1981b). This work showed that built-in stresses during the curing of asymmetric fibre reinforced composites could produce bistability. Specifically, the difference in thermal expansion of the material in the fibre direction and the direction perpendicular to the fibres, causes these stresses. In subsequent work (Hyer, 1981a, 1982), this behaviour was explained analytically with a case-specific prediction of associated strains and curvatures.

Since laminates combine control of form with control over material properties, an extensive research field was inaugurated. For a great part, this focused on thermal effects induced during curing (Dano & Hyer, 2002, 1998; Mattioni *et al.*, 2008; Pirrera *et al.*, 2011). Some recent work introduces similar stresses to laminates through the prestressing of fibres (Daynes *et al.*, 2008, 2010). This technique in particular, but also laminates in general, require specialised equipment and carry significant costs.

The ability of prestressing to induce multistability is valid in isotropic materials as well. Some initial inspiration was found in the tape spring, and is discussed by Ke-

badze *et al.* (2004). The distribution of residual stresses via an elasto-plastic forming process is presented and modelled. Mathematical modelling is achieved through various assumptions, most notably that the shell is uniformly curved. In terms of construction at least, this is the simplest method for introducing shell multistability, since it only involves passing the shell through rollers in various orientations, or otherwise plastically deforming it. This locks in stresses that facilitate multistability.

Non-prestressed—either through thermal curing stresses or otherwise—bistable composites were only studied very recently. Slit tubes have a similar geometry to the tape springs mentioned in Section 2.2. They can exhibit bistability in the shape of a rolled and unrolled configuration. Iqbal *et al.* (1998) and Iqbal & Pellegrino (2000) use an energy approach to establish particular laminate layups that support bistability. Twisting can be ignored from this model since both stable configurations have one curvature in a principal direction equal to zero, *i.e.* they have zero Gaussian curvature and are *developable*. This simplification of the formulation is very powerful in algebraic terms and results in a very manageable model. The work on slit tubes was the result of a practical needs to explain an existing invention in the form of the RolaTube deployable mast shown in Fig. 2.3.

In the papers by Guest & Pellegrino (2006), again initially unstressed, cylindrical, bistable shells are considered. The model can predict stability modes based on the layup of the composite and the orientation of initial curvature. Similar work can be seen in Galletly & Guest (2004b): differential equations with respect to geometrical parameters are set up assuming a beam model. Bistability is specifically shown for antisymmetric layups confirming work by Iqbal *et al.* (1998) and Iqbal & Pellegrino (2000). A new twisted equilibrium is also examined for symmetric layups, but it is shown that it is not always stable. Galletly & Guest (2004a) assume a shell model instead of a beam model, and noting that the initial geometry is cylindrical. The resulting fourth-order differential equation for the out-of-plane displacement results in a cross-sectional profile of the secondary geometry, when that is stable. This model also detects an expected boundary layer near the edges, whose width varies with the layup configuration.

Over time, particular applications for multistable laminates were also examined. The idea of a morphing airfoil composed of two bistable shells is discussed by Schultz (2008). Most recently, Daynes *et al.* (2011) presented a bistable composite air inlet. In addition, the bistable shell concept can be extended in combination with various joints, thus producing more elaborate structures. One such design is presented in Dai *et al.* (2012). In another modification of the core structure, Mattioni *et al.* (2009) use varying layups through the planform to produce non-uniform bistable behaviour; parts of the shell are kept monostable, while the remaining, cantilevered section is bistable. Arrieta *et al.* (2010) create an energy harvester based on a bistable plate with attached piezoelectric patches. The two distinct energy wells allow for large energy extraction over a wide frequency,

Figure 2.3: RolaTube produces a deployable mast using a fibre-reinforced composite material. It is neutrally stable since it can stand freely at any intermediate geometry between two cylindrical extremes. The resulting mast has an adjustable height and can be easily transported in its rolled-up configuration.

achieving broadband non-linear energy harvesting. This is, for certain applications, a benefit over linear vibration energy harvesters. There is a clear connection here with the converse process of dynamically actuating a shell, but the objective is usually to limit deformations and not encourage significant shape-change as in our study. The literature on this is quite vast—especially as it relates to piezoelectric actuators, but since this work does not examine dynamic effects, we do not include it here.

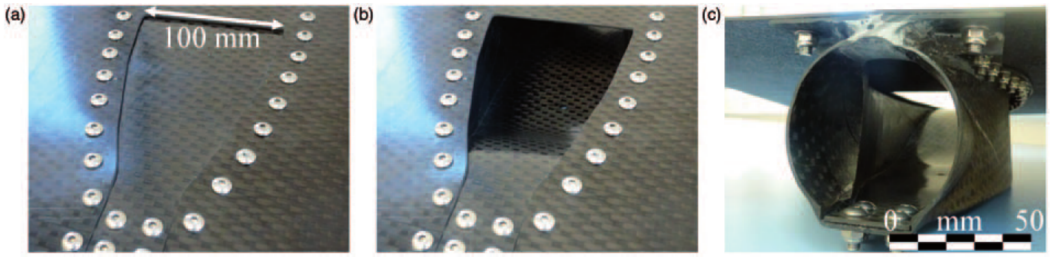

Figure 2.4: Photographs of a bistable air inlet demonstrator taken from Daynes *et al.* (2011). The composite structure is shown in top views of its closed and open states and a bottom view of the closed state (from left to right).

2.4 The effect of local geometrical features

In addition to composite shells, some work has looked at corrugations as means of introducing or stabilizing different shell geometries. Corrugations stiffen the shell in one direction thus introducing orthotropy, while at the same time they allow elastic cross-sectional deformation. These factors combine to promote multistability (Norman *et al.*, 2008b). A 'twisting' curvature bistability was observed in this work, and allowed for a tristate shell to be constructed—a third cylindrical state is also stable.

Norman *et al.* (2008a) show that shells with a fixed pattern can present global bistability. The texture is sinusoidal in two orthogonal direction, while the flat corrugated shell is rolled plastically about the two orthogonal flexible axis. If the rolling along the two axis happens in the same sense, this results in anticlastic bistable behaviour. Conversely, if the rolling happens in the opposite sense, the resulting structures displays synclastic bistable behaviour. In one study (Golabchi & Guest, 2009), dimpled patterns are modelled by considering the superposition of two orthogonal directions of corrugations. Both experimental and computational techniques are used in the same study to investigate the combination of texture with prestress, which again introduces the potential for multistability.

A subsequent investigation of curved corrugated shells was made in Norman *et al.* (2009). We should note that no multistability is observed here, instead the focus was on the morphing capabilities of these shells. These structures belong to the category of compliant shells since the local geometry changes to accommodate large deflections

in the global sense. Hence, they need to be treated at different scales and a kinematic hierarchy can be established, as described by Seffen (2012), in an extensive analysis of various compliant shells with traditional and new techniques.

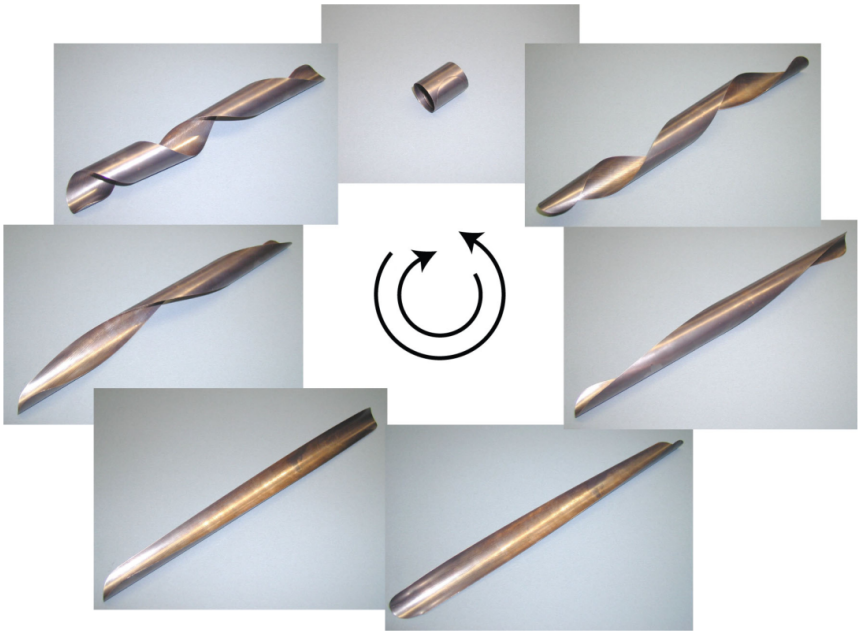

Figure 2.5: The zero stiffness shell described and constructed in Guest *et al.* (2010) is shown here. An infinite array of free-standing configurations is available by twisting the structure.

A truly multistable shell is presented by Seffen (2006). Sinusoidal dimples are mechanically introduced to a copper-beryllium shell, and are made bistable through heat treatment. By pushing these individual, bistable dimples toward either side of the shell, the global shape is immediately affected. The potential global shapes then are only limited by the number of local dimples. A similarly diverse structure can be found in a paper by Guest *et al.* (2010), which described a zero-stiffness shell structure that has no change in energy over a path of twisted configurations, hence allowing an infinite number of shapes (shown in Fig. 2.5).

The effect of local geometry on global behaviour was partly the inspiration for the work in Chapter 8. This approach of removing material to induce multistability is—as far as we know—a new one. Hence, while there are significant studies on the buckling of grid shells, honeycombs and perforated shells, none deals with multistable behaviour. The initial investigation of the corresponding material properties was heavily reliant on experimental and theoretical work on perforated shells by Slot & O'Donnell (1971). For elementary modeling of grid and honeycomb shells, we drew information from a rich review of lattice models by Ostoja-Starzewski (2002).

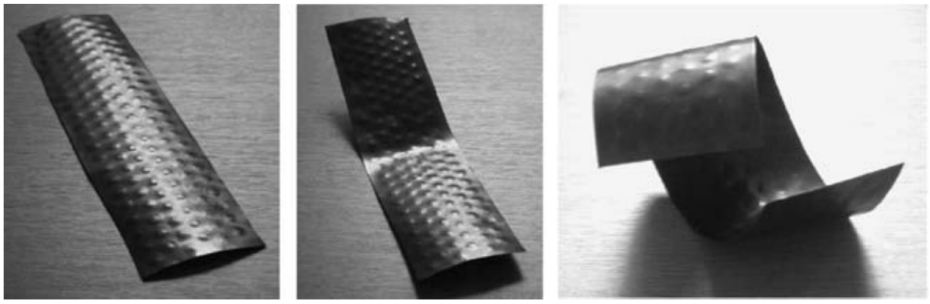

Figure 2.6: Seffen (2006) presented a novel concept for a dimpled multistable shell. By "popping" individual bistable dimples on the surface of a metallic sheet, a large number of possible global geometrical states becomes possible.

2.5 Contemporary work

The area of multistable shells has been particularly active in the past decade. This expresses the great potential of this area for engineering applications. It also reveals a link to other particularly active fields. For example, the relevance of shell multistability to biological structures is immediately accessible in a paper by Forterre *et al.* (2005). The snapping of the Venus flytrap is examined, and it is shown that the actuating capacity of the plant is not sufficient to explain the fast closing action. Instead, material and geometrical parameters help bring the structure to the brink of an elastic instability. Specifically the combination of double curvature with a material that couples stretching and bending to an appropriate extend, seems to afford the plant a quick transition between two geometries.

A model by Seffen (2007) is a direct influence on this work. It uses an energy approach for orthotropic, elliptical plates under the Uniform Curvature assumption. The same assumption was made earlier by Mansfield (1962) for the modelling of a thin heated plate. It accounts for both membrane and bending forces and considers the effect of double initial curvature. In consequence, the deformed curvatures are allowed to be independent. Using this formulation, it is shown that bistability depends on the change in Gaussian curvature. For example, in the absence of initial twist, isotropy precludes bistability for negative initial Gaussian curvature. Conversely, material properties—shear modulus in particular—can be manipulated to introduce bistability independently of the sign of the initial Gaussian curvature.

A subsequent work by Seffen & Guest (2011) makes use of this formulation to examine the influence of prestress on the bistable capability of thin shells. The known description of opposite-sense prestressing is confirmed, and a novel, neutrally-stable shell is presented as the consequence of same-sense prestressing. Closed-form expressions for both cases are at hand and are further examined. A requirement for bistability is established; a shear modulus above the isotropic value is required for bistability of orthotropic shells, whereas

the neutrally stable case is accessible only for isotropic materials.

The model by Seffen (2007) was expanded by Vidoli & Maurini (2008). The authors reveal the theoretical possibility of an initially uniform-curvature shell, based on an isotropic material, capable of three stable states. An extensible numerical model is initially used to display this property. In an analytical section, an inextensible model is used for stability analysis, showing the influence of different material parameters. This paper in fact, along with the work in Chapter 5, motivated the design and construction of a novel tristable shell described in Chapter 6.

More recently, Fernandes *et al.* (2010) continue with the Uniform Curvature model to establish the possibility of quasi-static actuation for bistable shells. The caveats of this approach are that the shell needs to have built-in stresses and actuation needs to occur in multiple directions. Still, this provides an excellent method of tackling the challenges of the dynamic movement complications associated with snap-through behaviour. They corroborate their results with a FE model of a laminate that develops built-in stresses during curing. This virtual testing is based on the use of orthotropic actuation.

The theoretical possibility of tristability for a related category of structures was presented by Giomi & Mahadevan (2012). These authors lift the Uniform Curvature requirement, but allow the planform geometry to assume infinite size in one direction, thus simplifying the boundary conditions. They examine various anisotropic material configurations for these "strip" planforms. Different spatial distributions for the curvature are also examined. Specifically, they find that strips with positive spontaneous (preferred) curvature are always bistable, but for strips with negative spontaneous curvature, bistability depends on the presence of spontaneous twist and suitable material stiffness. Their investigation of the tristable strips agrees with the analysis by Vidoli & Maurini (2008) for the Uniform Curvature case, but shows the feasibility of non-uniform curvature strips. This work also complements the analysis of a tristable corrugated shell by Norman *et al.* (2008b).

The theoretical prediction of an initially doubly-curved, orthotropic, tristable shell motivated a pursuit for the construction of a physical demonstrator. We present the design and construction process for such a shell in Chapter 6, based on the theoretical framework of Chapter 4. A similar structure was presented by Coburn *et al.* (2012), based on work by Vidoli & Maurini (2008). We note that the two results were publicly presented simultaneously for the first time at the 8th European Solid Mechanics Conference in Graz, Austria, in July 2012.

The connection of multistability of shells to growth mechanics and morphogenesis is evident in an article by Seffen & Maurini (2012). The authors use a similar formulation as in Seffen (2007) and Vidoli & Maurini (2008) for a flat disk, to treat both growth and actuation scenarios. In the case of growth, extensional strains are assumed while in the

case of actuation, bending strains are assumed. The formulation allows for some closed form results that are compared to past Finite Element Analysis (FEA) data. The possible shape response is presented: "`Bending growth buckles into an almost developable mode of constant Gaussian curvature whereas extensional growth increases the Gaussian curvature only after buckling.`" The effect of combining the two modes is also briefly examined.

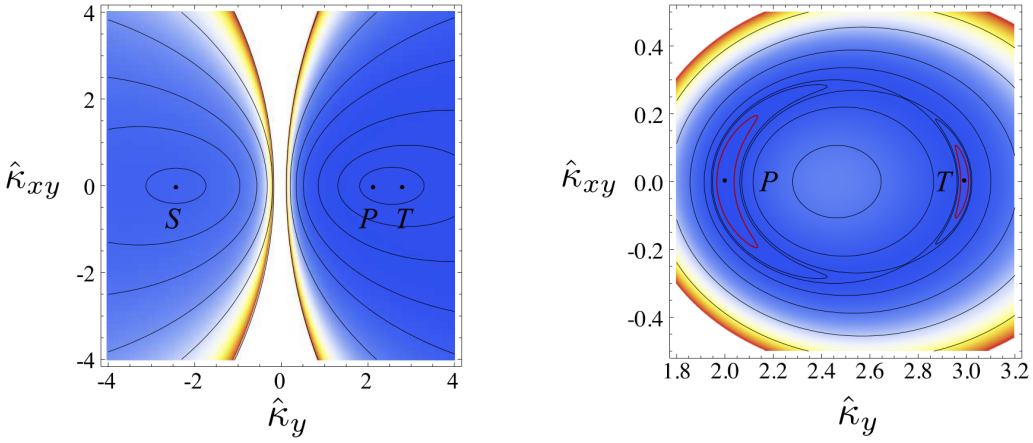

Figure 2.7: Giomi & Mahadevan (2012) analysed the morphing capabilities of thin strips. In this plot from their work the possibility of a tristable thin strip is shown by plotting the corresponding strain energy (left). The primary, secondary and tertiary states are noted by their initials. On the right, a detail in the region of the primary and tertiary states is presented.

2.5.1 Actuation

The limits of the Uniform Curvature (UC) assumption are met in this dissertation, especially as they relate to actuation and intermediate shapes. A few authors have attempted higher order models in recent years. Pirrera *et al.* (2010) use high-order Ritz approximations to model bistable plates, which allow for the parameter space to be explored via path-following techniques. They capture some intricacies of the snap-through behaviour—as it relates to laminates—that were previously observed experimentally. The computational nature of this approach, precludes generalizations. Most recently, Vidoli (2013) deduced the Föppl-Von Kármán energy functional, allowing for linear and quadratic variations of curvature. By the use of relevant examples, it is shown that these higher-order functionals can describe smooth transitions between shapes of positive and negative Gaussian curvature—a region inaccessible by the UC energy landscape, presented in Chapter 4.

At the same time, experimental studies on actuation of multistable shells are fairly common, but again mostly restricted to laminates. Portela *et al.* (2008) use a Macro-Fibre Composite (MFC) actuator to evaluate its feasibility as a switch between stable states for asymmetrical laminates. This analysis is matched with corresponding Finite

Element Analysis, with moisture effects included. The authors note that the low force capability of MFCs limit the potential size of bistable shells, while the MFC significantly impacts the shells stiffness. Similar proof-of-concept studies were subsequently performed by other authors (Giddings *et al.*, 2011; Gude *et al.*, 2011), again with the use of MFCs as actuators.

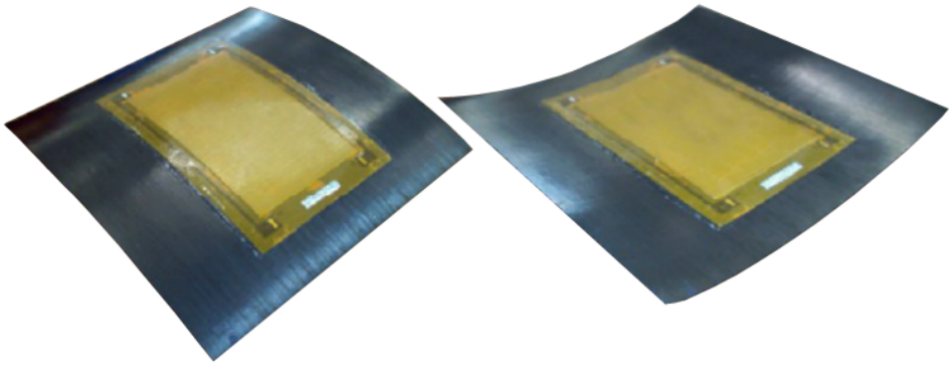

Figure 2.8: Macro-Fibre Composite actuators have been the focus of many studies on actuation of multistable shells. In this image from Portela *et al.* (2008) the two states are shown with the characteristic MFC patch epoxied on the top of a composite shell.

2.6 Concluding remarks

In this Chapter a literature review of historical and contemporary topics relating to multistable shells was presented. A brief background was sufficient to show the theoretical challenges with obtaining exact solutions. At the same time we noted the useful results that have been obtained by simplified theoretical models and advances in computational modelling. Although there are known issues with the UC assumption that this dissertation also employs, there are quite a few problems to be exhausted. For example, we revealed a number of challenges with respect to design and actuation of physical multistable shells. In the Chapter that follows we briefly look at the potential for material properties' control through the choice of the material itself and through related adjustments.

Chapter 3

Material considerations

3.1 Introduction

In Chapter 2 we described briefly some of the challenges that relate to multistable shells, and some of the questions that this dissertation answers in the following Chapters. Before developing theoretical tools however, we provide some practical information on available materials that are either commonly used for constructing multistable shells, or are considered in this work. The characteristics of the materials presented here prescribe to some extend the form of both our theoretical and experimental investigations. The following sections explain the spectrum of mechanical characteristics for some composite materials—in particular laminates—and for some types of perforated, or otherwise patterned shells.

3.2 General constitutive law

A step towards simplification for thin structures is achieved when the out-of-plane stresses are ignored and thus only a two-dimensional state of stress is considered. When this is a realistic assumption we can describe the material properties with a single, 3×3 matrix:

$$\mathbf{E} = \frac{E}{1-\nu^2/\beta}\begin{bmatrix} 1 & \nu & \psi \\ \nu & \beta & \eta \\ \psi & \eta & \alpha \end{bmatrix}. \tag{3.1}$$

The vector of strains is $\boldsymbol{\epsilon} = [\epsilon_x\ \epsilon_y\ \gamma_{xy}]^T$ and the vector of stresses is $\boldsymbol{\sigma} = [\sigma_x\ \sigma_y\ \tau_{xy}]^T$. By only admitting small strains, and can assume linear-elastic behaviour, thus we have $\boldsymbol{\sigma} = \mathbf{E}\boldsymbol{\epsilon}$. E is the Young's modulus in the x-direction: ν, ψ, β, η and α are independent constants that express the ratio of stiffnesses in other directions; ψ and η are bending-stretching coupling terms, and α defines the material shear stiffness. More analytically,

they can be defined through the following expressions:

$$E = E_x, \quad E_y = \beta E_x, \tag{3.2}$$

$$\nu_{yx} = \nu, \quad \nu_{xy} = \frac{\nu}{\beta}. \tag{3.3}$$

Also, we have

$$G = G_{xy} = \alpha \frac{E}{1 - \nu^2/\beta}, \tag{3.4}$$

which defines the parameter α. In the isotropic case:

$$G_{\text{iso}} = \frac{E}{2(1+\nu)} \qquad \Rightarrow \qquad \alpha_{\text{iso}} = \frac{1-\nu}{2}. \tag{3.5}$$

These are used extensively throughout this work.

3.3 Composite materials

The diversity and specificity of multistability requirements demand a material whose constitutive properties can be tailored to them. Laminate composites are an ideal candidate for such a construction. They are commonly available and based on the selection of constituent matrix and fibre materials, a vast range of stiffnesses can be manufactured. Furthermore, their shape can be specified with relevant ease. A short review of composite materials adds context: They are commonly found in nature in the form of wood, bone, teeth and many other materials; and their industrial production in recent decades is in the order of millions of tonnes per year (Hull & Clyne, 1996). Long-fibre reinforced composites are made of a strong, stiff and elongated material, surrounded by a softer, binding matrix. Because of the orientation of embedded fibres, or because of properties of the constituent materials themselves, composites are frequently anisotropic, which is relevant to our design.

For this category of composites, the reinforcement is usually in the form of fibres, but whiskers and particles occasionally serve that purpose. Various materials, including carbon, glass and aramid fibres, and ceramics are sometimes used as reinforcement. Some of these can be combined with multiple matrix materials, while others are designed to match a specific matrix material (Hull & Clyne, 1996). For matrices, on the other hand, commonly used materials are thermosetting resins (epoxy resins & polyesters), thermoplastics (polypropylene), metals (Al, Mg, Ti) and ceramics.

The fibres can be placed in a variety of arrangements within the matrix, depending on the properties we are trying to achieve. A common geometry is produced by placing fibres in a thin layer or lamina in a single direction. A unidirectional lamina is also

called a ply. These layers can be stacked in various configurations, thus allowing us remarkable flexibility in material design. A short description of these can be written as $[\theta_1/\theta_2/\ldots/\theta_n]$, where θ is the angle of fibre directionality for each ply, relevant to a fixed axis and n is the number of plies. Hence a $[0/90]$ is a laminate with two plies at 90° to each other. A subscript "s" in this notation signifies a symmetric layup, e.g. $[-45/+45]_s = [-45/+45/+45/-45]$. Treating each ply as a homogeneous material is the key to predicting the properties of the entire structure, the resulting composite is called a *laminate*.

3.3.1 Classical Laminate Theory (CLT)

Focusing on laminates allows us to show some of the limitations and advantages of composites; we further limit our overview on long-fibre composites. Let us consider elastic deformation of a single, unidirectional ply and assume perfect bonding between the fibres and the matrix. A Cartesian coordinate system is employed to describe the constitutive properties, where the three orthogonal directions are labelled "1", "2" and "3" according to well-known convention: "1" is the direction of the fibres along the ply; directions "2" and "3" define the plane perpendicular to the direction of the fibres. Defining these directions allows us to list all the relevant material parameters: the Young's modulus along the fibres, E_1, and the transverse stiffnesses, E_2 and E_3; there are three shear stiffnesses: G_{12}, G_{13} and G_{23}. Finally, depending on the arrangement of the fibres, we can have as many as three different Poisson's ratios—one for each direction—to consider. They are given by

$$\nu_{ij} = -\frac{\epsilon_j}{\epsilon_i} \qquad i,j = 1,2,3, \tag{3.6}$$

and where ϵ_i stand for strain along the i-direction. The total number of constants is nine. However, if we consider the orthotropy of the material, we can reduce this number significantly. Specifically, the 2-3 plane can be regarded as a plane of isotropy, since all stiffnesses in the plane are the same (Jones, 1999)—thus $E_2 = E_3$, $G_{13} = G_{12}$ and $\nu_{13} = \nu_{12}$. In addition, from Hull & Clyne (1996):

$$\frac{\nu_{12}}{E_1} = \frac{\nu_{21}}{E_2}, \tag{3.7}$$

which is a consequence of the reciprocal theorem, and

$$G_{23} = \frac{E_2}{2(1+\nu_{23})}, \tag{3.8}$$

again as a consequence of the isotropy of the 2-3 plane. The Young's moduli in the case of long-fibre reinforced composites are calculated via the following expressions for the axial

and transverse directions respectively (Hull & Clyne, 1996):

$$E_1 = L_m E_m + L_f E_f, \tag{3.9}$$

$$E_2 = \frac{E_m E_f}{L_m E_f + L_f E_m}, \tag{3.10}$$

where the subscripts m and f indicate the matrix and fibre material respectively while L is the volume fraction in the composite.

Similarly for the shear stiffnesses, we have

$$G_{12} = \frac{G_m G_f}{L_m G_f + L_f G_m}. \tag{3.11}$$

Finally for the Poisson's ratios,

$$\nu_{12} = L_m \nu_m + L_f \nu_f. \tag{3.12}$$

Immediately ν_{21} can be calculated by the reciprocal relationship in Eq. (3.7) In the other direction, ν_{23} can be obtained by considering the overall volume change of the material. More analytically, if we apply a hydrostatic stress on the material we have

$$\Delta = \epsilon_1 + \epsilon_2 + \epsilon_3 = \frac{\sigma_H}{K}, \tag{3.13}$$

where σ_H is the hydrostatic stress and K is the bulk modulus. Applying stress in only one direction, σ_2, we have

$$\sigma_H \left(= \frac{\sigma_1 + \sigma_2 + \sigma_3}{3} \right) = \frac{\sigma_2}{3}. \tag{3.14}$$

Thus

$$\epsilon_3 = \frac{\sigma_2}{3K} - \epsilon_1 - \epsilon_2. \tag{3.15}$$

By definition,

$$\nu_{23} = -\frac{\epsilon_3}{\epsilon_2} = \frac{\sigma_2}{3K\epsilon_2} + \frac{\epsilon_1}{\epsilon_2} + 1, \qquad \text{or} \tag{3.16}$$

$$\nu_{23} = 1 - \nu_{21} - \frac{E_2}{3K}. \tag{3.17}$$

ν_{23} requires the value of the bulk modulus. This is found to be

$$K = \left[\frac{L_f}{K_f} + \frac{1 - L_f}{K_m} \right]^{-1}. \tag{3.18}$$

All the above are theoretically derived through idealised models. However, the estimates

obtained from these formulae should suffice for our purposes.

The constitutive matrix for laminates is commonly called the **ABD** matrix for convenience; since each ply in a laminate is in fact a shell, we use the same convention here:

$$\begin{bmatrix} N_x \\ N_y \\ N_{xy} \\ M_x \\ M_y \\ M_{xy} \end{bmatrix} = \begin{bmatrix} A_{11} & A_{12} & A_{16} & B_{11} & B_{12} & B_{16} \\ A_{12} & A_{22} & A_{26} & B_{12} & B_{22} & B_{26} \\ A_{16} & A_{26} & A_{66} & B_{16} & B_{26} & B_{66} \\ B_{11} & B_{12} & B_{16} & D_{11} & D_{12} & D_{16} \\ B_{12} & B_{22} & B_{26} & D_{12} & D_{22} & D_{26} \\ B_{16} & B_{26} & B_{66} & D_{16} & D_{26} & D_{66} \end{bmatrix} \begin{bmatrix} \epsilon_x \\ \epsilon_y \\ \gamma_{xy} \\ \kappa_x \\ \kappa_y \\ \kappa_{xy} \end{bmatrix}, \tag{3.19}$$

where A_{ij} are extensional stiffnesses, B_{ij} are bending-extension coupling stiffnesses and D_{ij} are bending stiffnesses. Note that subscripts "1", "2", "6" refer to the x-direction, the y-direction and shearing effects in the x-y plane, respectively—as defined by Hull & Clyne (1996). We further define:

$$\mathbf{N} = [N_x \; N_y \; N_{xy}]^T, \quad \mathbf{M} = [M_x \; M_y \; M_{xy}]^T \tag{3.20}$$

for later use.

In CLT, we make the same assumptions as in Kirchhoff plate theory. The main difference is the in-plane anisotropy of each ply. In the case of unidirectional long-fibre laminates, each ply has orthotropic properties. In addition, in CLT we assume perfect bonding between each layer. Combining these assumptions, we can produce an **ABD** matrix for each laminate by integrating material properties through the thickness of the shell. The material properties change discontinuously between laminae, so an appropriate sum suffices for this calculation. Depending on the angle of each ply, a rotational transformation of the constitutive matrix needs to be calculated before the summation:

$$\mathbf{C}' = T^{-1}\mathbf{C}RTR^{-1}, \tag{3.21}$$

where

$$T = \begin{bmatrix} \cos^2\theta & \sin^2\theta & 2\sin\theta\cos\theta \\ \sin^2\theta & \cos^2\theta & -2\sin\theta\cos\theta \\ -\sin\theta\cos\theta & \sin\theta\cos\theta & \cos^2\theta - \sin^2\theta \end{bmatrix}, \qquad R = \begin{bmatrix} 1 & 0 & 0 \\ 0 & 1 & 0 \\ 0 & 0 & 2 \end{bmatrix}. \tag{3.22}$$

The **ABD** matrix then can be calculated by summing over the individual constitutive

Table 3.1: Young's moduli and Poisson's ratios for some common matrix materials. Data taken from Hull & Clyne (1996).

Matrix	Young's Modulus (GPa)	Poisson's Ratio
Epoxy resins	3-6	0.38-0.4
Polyesters	2-4.5	0.37-0.39
Polypropylene	1-1.4	0.3
Al	70	0.33
SiC	400	0.2

matrices for the rotated plies:

$$A_{ij} = \sum_{k=1}^{N} (C_{ij})_k (z_k - z_{k-1}) = \sum_{k=1}^{N} (C_{ij})_k t_k, \tag{3.23a}$$

$$B_{ij} = \frac{1}{2} \sum_{k=1}^{N} (C_{ij})_k (z_k^2 - z_{k-1}^2) = \sum_{k=1}^{N} (C_{ij})_k t_k \bar{z}_k, \tag{3.23b}$$

$$D_{ij} = \frac{1}{3} \sum_{k=1}^{N} (C_{ij})_k (z_k^3 - z_{k-1}^3) = \sum_{k=1}^{N} (C_{ij})_k \left(t_k \bar{z}_k^2 + \frac{t_k^3}{12} \right), \tag{3.23c}$$

where the subscript "k" denotes the kth ply and $\bar{z}$ is the distance from a ply's centroid to the mid-plane of the layup. The C terms describe a constitutive matrix for each ply and the units in SI are $\mathrm{Pa\,m}$, $\mathrm{Pa\,m^2}$ and $\mathrm{Pa\,m^3}$ for the A, B and D terms respectively.

With help from some data tables we can now produce some numeric ranges. Tables 3.1 and 3.2 give the properties of some common materials used for the matrix and the fibre reinforcement respectively. Since these are isotropic materials we can calculate the shear modulus and the bulk modulus immediately from the Young's modulus and Poisson's ratio. We can then calculate the practical ranges for our engineering constants based on these materials. We have already described the process through the equations above. In Table 3.3 we show values of β and α for three distinct values of the reinforcement volume fraction. Some of the combinations of matrix and fibres is not realistic but since we are only establishing rough ranges, we do not examine that further. The average value of the Young's modulus was used for the materials that are shown to have a range of stiffnesses.

From Table 3.3, we can draw some rough conclusions about the ranges of β, α and ν as they relate to common composites, in the context of single, unidirectional plies. A sensible range for β is 0.01–1, for α, 0.01–0.4 and for ν, 0.01–0.3. As noted earlier, by combining plies at different angles, the possibilities for these ranges are greatly expanded, and can be calculated through CLT.

Table 3.2: Young's moduli and Poisson's ratios for some common fibre materials. Data taken from Hull & Clyne (1996).

Fibre	Young's Modulus (GPa)	Poisson's Ratio
Boron	400	0.2
E-glass	76	0.22
Nicalon^{TM}	190	0.2
Saffil^{TM}	300	0.26

Table 3.3: Estimated values of (β, α, ν) for different combinations of matrix and fibres. We investigate the values 0.2, 0.5 and 0.8 for the fibre volume fraction.

f = 0.2		Fibres			
	β, α, ν	Boron	E-glass	Nicalon^{TM}	Saffil^{TM}
Matrix	Epoxy	0.08, 0.03, 0.03	0.34, 0.12, 0.04	0.16, 0.06, 0.06	0.10, 0.04, 0.04
	Polyesters	0.06, 0.02, 0.02	0.26, 0.09, 0.03	0.12, 0.04, 0.04	0.08, 0.03, 0.03
	PP	0.02, 0.01, 0.01	0.11, 0.04, 0.01	0.05, 0.02, 0.01	0.03, 0.01, 0.01
	Al	0.68, 0.24, 0.21	1.00, 0.35, 0.24	0.90, 0.31, 0.27	0.77, 0.27, 0.24
	SiC	1.00, 0.40, 0.20	0.91, 0.36, 0.21	0.97, 0.39, 0.19	0.99, 0.39, 0.21
f = 0.5					
Matrix	Epoxy	0.06, 0.02, 0.02	0.29, 0.10, 0.03	0.13, 0.05, 0.04	0.09, 0.03, 0.03
	Polyesters	0.05, 0.02, 0.01	0.22, 0.08, 0.02	0.10, 0.03, 0.03	0.06, 0.02, 0.02
	PP	0.02, 0.01, 0.00	0.09, 0.03, 0.01	0.04, 0.01, 0.01	0.02, 0.01, 0.01
	Al	0.62, 0.23, 0.16	1.00, 0.36, 0.21	0.86, 0.32, 0.23	0.72, 0.26, 0.21
	SiC	1.00, 0.40, 0.20	0.83, 0.33, 0.23	0.95, 0.38, 0.19	0.99, 0.38, 0.23
f = 0.8					
Matrix	Epoxy	0.11, 0.04, 0.03	0.43, 0.16, 0.04	0.22, 0.08, 0.05	0.15, 0.05, 0.04
	Polyesters	0.09, 0.03, 0.02	0.35, 0.13, 0.03	0.17, 0.06, 0.04	0.11, 0.04, 0.03
	PP	0.03, 0.01, 0.01	0.16, 0.06, 0.01	0.07, 0.03, 0.01	0.04, 0.02, 0.01
	Al	0.75, 0.29, 0.17	1.00, 0.38, 0.22	0.92, 0.35, 0.21	0.82, 0.30, 0.22
	SiC	1.00, 0.40, 0.20	0.84, 0.33, 0.25	0.96, 0.38, 0.19	0.99, 0.37, 0.25

An example from the literature

Consider a composite bistable shell from Iqbal & Pellegrino (2000) with the elastic constants in Table 3.4. The laminate is composed of five plies in orientations given by [+45/-45/0/+45/-45], and these properties describe an **ABD** matrix equal to:

$$\begin{bmatrix} 13.9 & 6.0 & 0 & 0 & 0 & -0.55 \\ 6.0 & 8.8 & 0 & 0 & 0 & -0.55 \\ 0 & 0 & 6.19 & -0.55 & -0.55 & 0 \\ 0 & 0 & -0.55 & 0.97 & 0.67 & 0 \\ 0 & 0 & -0.55 & 0.67 & 0.95 & 0 \\ -0.55 & -0.55 & 0 & 0 & 0 & 0.69 \end{bmatrix}, \tag{3.24}$$

where the units are GPa mm for **A**, GPa mm^2 for **B** and GPa mm^3 for **D**.

Bending and twisting are decoupled since both D_{16} and D_{26} are zero, but stretching and bending are coupled, since the submatrix $\mathbf{B} \neq \mathbf{0}$. In effect, the directions of the two axes ("1" and "2") are principal directions of curvature. With these parameters in hand, Iqbal & Pellegrino (2000) were also able to calculate the strain energy for the shell and describe the main features of the bistable behaviour of these shells.

E_1	26.6 GPa
E_2	2.97 GPa
G_{12}	1.39 GPa
ν_{12}	0.4
ν_{21}	0.04

Table 3.4: Unidirectional elastic constants for a composite bistable shell taken from Iqbal & Pellegrino (2000). The matrix is polypropylene with embedded glass fibres. Five plies were used in a [+45/-45/0/+45/-45] configuration. The direction of the central fibre lamina is indicated by "1", while the direction perpendicular to that with "2".

Coupling parameters

The parameters η and ψ, mentioned earlier, describe the coupling between bending and twisting. They can be defined in terms of the **A** matrix as:

$$\psi = \frac{A_{16}}{A_{11}}, \qquad \eta = \frac{A_{26}}{A_{11}}, \tag{3.25}$$

or by a similar definition that corresponds to the **D** matrix. The two sets of calculations do not agree for all materials, but they are identical for a large spectrum of cases, and specifically for symmetric layups of laminates.

Here we try to obtain these coupling parameter values for an example case. Continuing from previous work, we take some indicative values from Guest & Pellegrino (2006), which detail four **ABD** matrix examples: an isotropic shell, one antisymmetric 45° layup, one symmetric 45° layup and one symmetric 40° layup. The last two present bending–twisting coupling, and are each made of five 0.21mm thick layers of laminae. These in turn are composed of unidirectional glass fibres in a polypropylene matrix.

The symmetric 45° layup has a [+45, -45, 0, -45, +45] configuration. The **D** matrix is our main focus here:

$$\begin{bmatrix} 0.868 & 0.665 & 0.345 \\ 0.665 & 0.848 & 0.345 \\ 0.345 & 0.345 & 0.681 \end{bmatrix}. \tag{3.26}$$

The units are in $\mathrm{GPa\,mm^3}$. In building our equations though we divided by D_{11}. Hence

$$\begin{bmatrix} 1.0000 & 0.7661 & 0.3975 \\ 0.7661 & 0.9770 & 0.3975 \\ 0.3975 & 0.3975 & 0.7846 \end{bmatrix}. \tag{3.27}$$

So we have the values $\psi = \eta = 0.3975$. Similarly for the symmetric 40° layup we get $\psi = 0.364$ and $\eta = 0.257$.

3.4 Patterned materials

In Section 2.4 we gave examples of material properties manipulation through the addition of dimple patterns on metallic sheets. Another method we mentioned is the removal/addition of material from/to a homogeneous layer. If we consider the fibre-reinforced laminates from the previous section, it is helpful to note that most of the stiffness usually is due to the fibre material, and the matrix merely holds the structure together. It is thus relevant to study a corresponding material with the matrix removed, but with the fibres bound together, with the resulting structure resembling a 2D truss.

The resulting pattern describes either a grid shell, a honeycomb or a perforated plate. These structures are closely related. In fact, there are no clear boundaries between the definitions of the three. For the purposes of this Chapter—and again in Chapter 8, we use all three terms to distinguish between different dimensional ratios in the local geometries of our materials. Exact assumptions and specifications are now defined accordingly.

3.4.1 Grid shells and honeycombs

Grid shells—also known as lattice shells and reticulated shells—are defined in the same way as conventional shell structures, but are composed of grids rather than continuous

materials. These grids are usually composed of beam-like elements rigidly connected to each other. There are numerous construction and cost benefits associated with grid shells, but here we noted the following: they allow light through—at least much more so than a continuous structure; they allow the exchange of gasses and fluids between the spaces that they define, which can be a critical characteristic in engineering applications; they are generally lighter than their continuous counterparts; and finally, in architectural terms, the particular discrete topology can be aesthetically desirable (Malek, 2012).

Since we defined the grid shell in a global sense, we proceed to define a local geometry, and namely the geometry for the constituent beam-elements. We assume a rectangular cross-section for the members or ligaments and that all members are identical in dimensions. The exact dimensions of the cross-section and the length of the beam-elements are a subject of analysis. A visualisation of both the global pattern and the local geometry is displayed in Fig. 3.1: On the left a regular orthotropic grid is shown, while on the right the local geometry of the beam-elements is labelled in detail. Specifically the length, height and width of the beam are identified with the symbols d, h and b respectively.

By considering different orientations for the grid shell, a dramatic variation of the in-plane mechanical properties can be achieved. For example, there must be a reduction in stiffness if we compare the Young's modulus in the "1" direction vs the stiffness in the x-direction. In the former, deformation originates in the stretching of the beam-elements while in the latter, their bending contributes the most. These effects are explained further in the next section.

In Chapter 8 we refer to a related category of structures, called honeycombs. Beyond a certain height to width ratio for the cross-section, h:b, it is no longer acceptable to treat the global structure as a grid shell. In analytical terms, for grid shells it is reasonable to assume members to be beams, but for honeycombs, members are treated as shells. The in-plane properties of grid-shells and honeycombs for a given pattern should be the same, but we expect the out-of-plane properties to vary significantly with the height of the elements, h.

Mechanical properties

A square grid shell can easily allow adjustment of the modular ratio for an orthotropic shell by adjusting the cross-sectional areas of beam-elements in the two directions. At the same time, we can expect the Poisson ratio to increase dramatically after the removal of material in such a pattern. An exaggerated effect can be visualised in the form of a square truss, with the nodes of the grid in our design corresponding to hinges in the truss and the strips of material corresponding to rod elements. Stresses in the diagonal direction clearly affect the geometry in the principal direction more intensely than on a solid plate. With this setup in mind, we can visualise the square pattern turning into a diamond-shaped

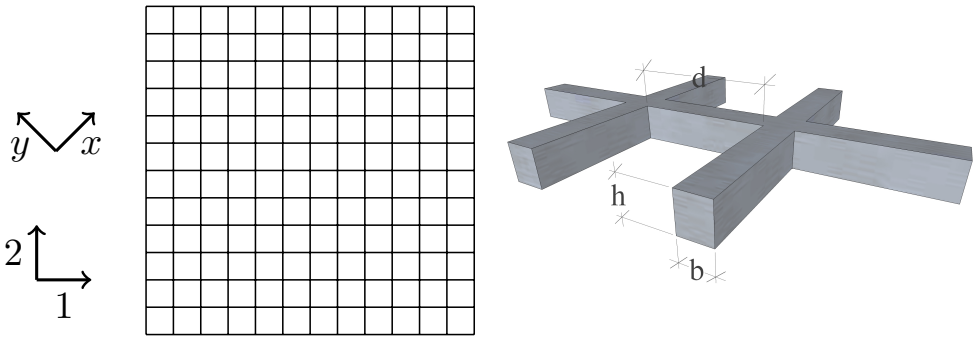

Figure 3.1: Detail of the square grid shell and the local geometry with the relevant dimensions. This is a perfectly orthotropic material. Multistability is promoted by high Poisson ratio and high shear stiffness in the directions of the principal curvatures of the shell. Hence we align the diagonal of the grid with these directions (x-y).

pattern to accommodate the applied loading. The effect of loading along the principal direction though would be carried by the structure along that same direction, with the perpendicular rods remaining unstressed, and hence with no geometrical change in that direction, *i.e.* the Poisson ratio vanishes.

In reality though, there is some stiffness due to the nodes, and a truss equivalent is not ideal. It is more appropriate to consider each beam-element as having fixed supports at both ends, since symmetry dictates no rotation at the nodes. Consequently, the resulting displacements for a unit cell rotated by 45° and in tension are primarily due to the bending of the beam-elements. A diagram of expected deformation for a unit cell is shown in Fig. 3.2, overlaid on the original, unstressed square geometry.

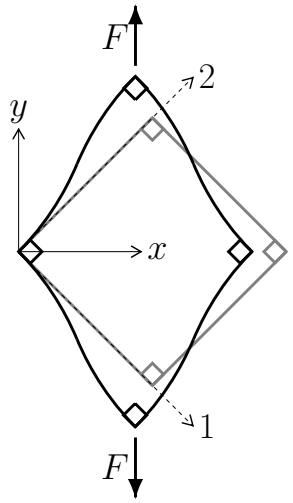

Figure 3.2: A diagram of a square unit cell on a grid shell, before and after the application of an external force. Assuming rigid nodes, and accounting for symmetry, each beam-element is treated as an Euler-Bernoulli beam, fixed at both ends. The local (1-2) and global (x-y) coordinate systems, are both displayed.

But we need not limit our design considerations to qualitative analysis. For an elementary quantitative analysis, we turn to a model by Lebée & Sab (2013), which assumes

the grid elements to be identical beams. While that work proceeds to describe a more elaborate, and more accurate formulation, we admit the simpler formulation for the purposes of this study. If we consider a square grid, as pictured in Fig. 3.1, then we have matrices **A** and **D** with respect to the local coordinate system (1-2-3), where 3 is the out-of-plane direction, given by:

$$\mathbf{A} = \begin{pmatrix} \dfrac{ES_1}{d} & 0 & 0 \\ 0 & \dfrac{ES_1}{d} & 0 \\ 0 & 0 & \left(\dfrac{d}{GS_2} + \dfrac{d^3}{12EI_3}\right)^{-1} \end{pmatrix}, \tag{3.28}$$

$$\mathbf{D} = \begin{pmatrix} \dfrac{EI_2}{d} & 0 & 0 \\ 0 & \dfrac{EI_2}{d} & 0 \\ 0 & 0 & \dfrac{GJ}{d} \end{pmatrix}, \tag{3.29}$$

where S_1 is the cross-sectional area of a beam ($= bh$) and S_2 is its shear area ($= hd$); I_2 and I_3 are moments of inertia; E and G are moduli of the homogeneous material; and J is the torsion constant. An approximation for the latter for a rectangular section is found in Young & Budynas (2002), to be equal to:

$$J = hb^3 \left[\frac{1}{3} - 0.21\frac{b}{h}\left(1 - \frac{b^4}{12h^4}\right)\right], \tag{3.30}$$

when $h > b$. The formulation for **D** again assumes beam-like behaviour for each element, with a neutral mid-surface of zero in-plane strains.

Treating these matrices as properties of a homogenised plate requires that the unit cell is sufficiently smaller than the global size of the structure. We will return to this topic with specific dimensions later in this dissertation, but note that we are dealing with elastic phenomena locally, a fact that enhances our homogenisation claim.

The **A** and **D** matrices noted above can be used to obtain the corresponding matrices in different orientations with Eq. (3.21) as is done for CLT. For example, if we want to obtain equivalent in-plane, homogenised moduli for a sheet in a direction 45° to the direction of the beam-elements, we first apply a rotational transformation to **A**, producing:

$$\mathbf{A}_d = \begin{pmatrix} \frac{Ehb\left[d^3+2db^2+2b^3(1+\nu)\right]}{2d\left[d^3+2b^3(1+\nu)\right]} & \frac{Ehb\left[d^3-2db^2+2b^3(1+\nu)\right]}{2d\left[d^3+2b^3(1+\nu)\right]} & 0 \\ \frac{Ehb\left[d^3-2db^2+2b^3(1+\nu)\right]}{2d\left[d^3+2b^3(1+\nu)\right]} & \frac{Ehb\left[d^3+2db^2+2b^3(1+\nu)\right]}{2d\left[d^3+2b^3(1+\nu)\right]} & 0 \\ 0 & 0 & \frac{Ehb}{2d} \end{pmatrix}, \quad (3.31)$$

where the d subscript refers to the diagonal (45°) orientation with respect to the unit cell's local geometry. From this, we can extract corresponding homogenised parameters quite easily:

$$\nu_{\mathrm{A}} = \frac{A_{d21}}{A_{d11}} = \frac{d^3-2db^2+2b^3(1+\nu)}{d^3+2db^2+2b^3(1+\nu)} \quad (3.32)$$

and

$$\alpha_{\mathrm{A}} = \frac{A_{d33}}{A_{d11}} = \frac{d^3+2b^3(1+\nu)}{d^3+2db^2+2b^3(1+\nu)}. \quad (3.33)$$

The same procedure can produce corresponding parameters for bending by operating on the **D** matrix. These are:

$$\nu_{\mathrm{D}} = \frac{A_{d21}}{D_{d11}} = \frac{-400h^5b^2+252h^4b^3-21b^7+100h^7(1+\nu_s)}{400h^5b^2-252h^4b^3+21b^7+100h^7(1+\nu_s)}, \quad (3.34)$$

and

$$\alpha_{\mathrm{D}} = \frac{D_{d33}}{D_{d11}} = \frac{100h^7(1+\nu_s)}{400h^5b^2-252h^4b^3+21b^7+100h^7(1+\nu_s)}. \quad (3.35)$$

We plot values of these parameters for different local dimensions in Fig. 3.3. The values for the Poisson ratio and the shear stiffness parameter, α, that correspond to the matrix **A** are almost unchanged by the variation of the geometry. There values are very close to unity for the entire range of geometry that we are examining. The same values, when estimated from the corresponding **D** matrix vary significantly—in the range of 0–1 for ν and 0.5–1 for α. Recall that for our model to be valid $h > b$, hence we only plot the estimates for $h/b > 1$.

3.4.2 Perforated shells

Perforated shells are topologically similar to grid shells, since they both appear as discontinuous, thin structures. Here we reserve the term for plates with circular sections of material removed in a regular pattern from a thin layer. The resulting structure is significantly harder to model than a grid shell. There are stress concentrations at particular points along connecting ligaments and other complications. Most work that attempts a homogenisation of these structures does so either empirically, or through the use of com-

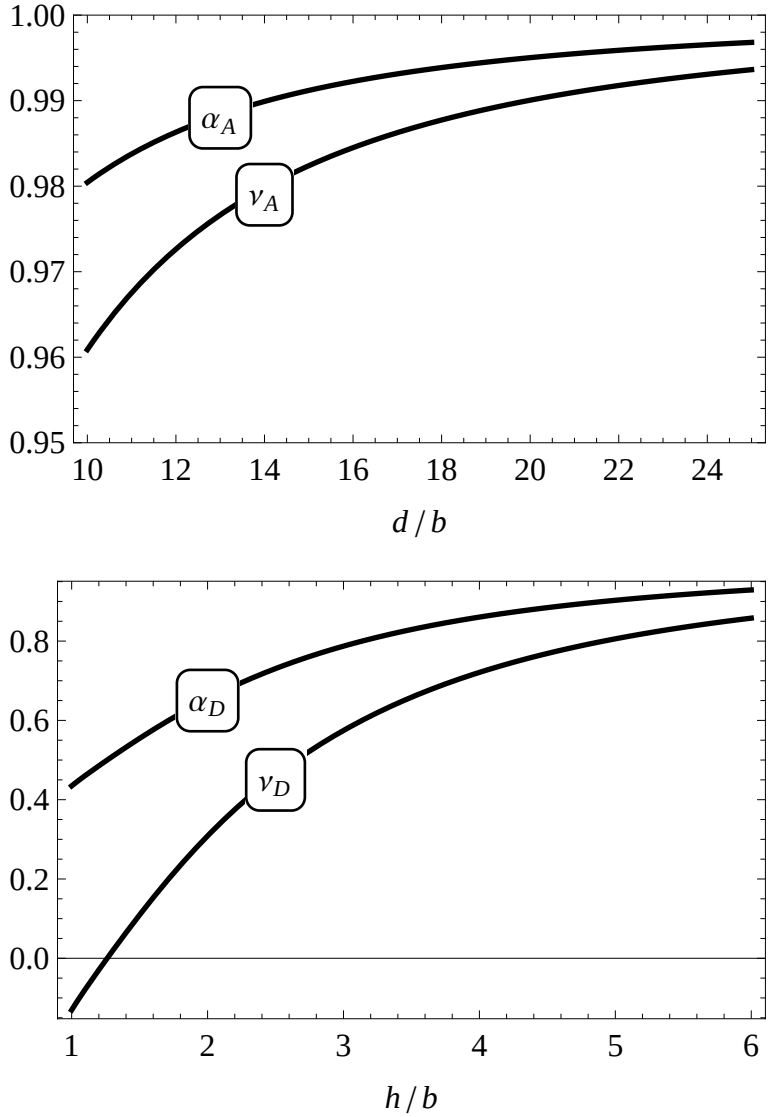

Figure 3.3: Plots of the variation of the Poisson ratio and the shear stiffness-related parameter for grid shell structures with respect to the local geometry. These estimates are made in correspondence to **A** and **D** matrices, which in turn were the product of the simple beam model presented in this section. Their analytical form is shown in Eqs. (3.32) to (3.35).

putational tools. We will not attempt an in depth examination here; we merely wish to show the potential for stiffness manipulation through this patterning of materials.

Our primary sources are works by Slot & O'Donnell (1971) and O'Donnell (1973), which give partly empirical and partly closed-form equivalent properties for thick and thin perforated plates. The former refers to in-plane properties while the latter presents properties in bending. Again the configuration of interest is a square pattern, shown in Fig. 3.4. In the works mentioned, the authors link the global properties of the plate with local dimensions such as ligament width, perforation size and plate thickness. It is helpful to define ligament efficiency; the ratio of the distance between adjacent perforations' peripheries and the distance between adjacent perforations' centres.

What is of interest here is the range of the estimated homogenised material properties. The works referenced are able to claim a wide range, for all parameters, depending on local dimensions and the properties of the constituent material. For example, from Slot & O'Donnell (1971) and for in-plane behaviour, the Poisson ratio of a perforated plate (with constituent material having $\nu = 0.3$), in a direction 45° to the direction the pattern can be more than 0.8 for a ligament efficiency of 0.1. Similarly, the elastic moduli E and G can vary tremendously with ligament efficiency and orientation adjustments.

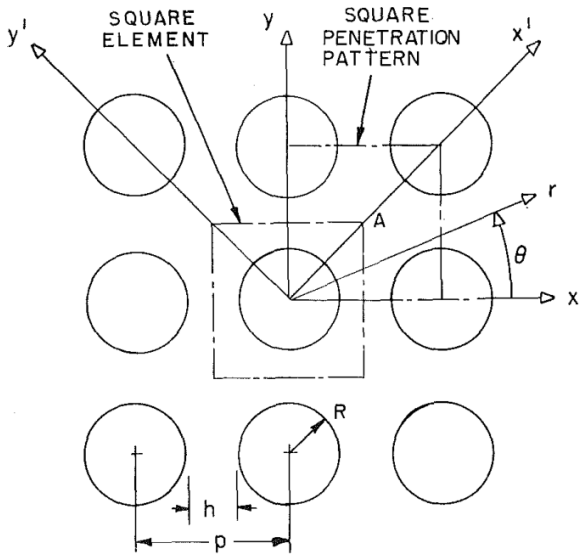

Figure 3.4: Diagram of one of the perforation patterns studied by Slot & O'Donnell (1971) and copied from the same work. It shows some of the local dimensions that affect the global homogenised parameters.

In a later work, O'Donnell (1973) states that "`For thinner plates, the relative torsional and bending stiffnesses of the ligaments vary markedly with plate thickness. Thus, the effective elastic constants for the bending of thin plates are strongly depended on the thickness.`" In effect, we have to treat the in-plane and out-of-plane properties separately and deducing the bending behaviour from in-plane behaviour is not possible. Nevertheless, the same paper presents closed-form

expressions for effective out-of-plane properties and provides the tools to investigate the limits of feasible parameter values.

3.5 Influence of prestressing

The prestressing of materials is often used to alter the load-behaviour of structures—most commonly in concrete construction—but is also sometimes encountered as an artefact of various manufacturing methods; the curing of laminates, for example, is often responsible for residual stresses in the structure, which relate to bistable behaviour, first noted by Hyer (1981b). The plastic deformation of isotropic materials can generate similar residual stresses and support multistability as shown by Kebadze *et al.* (2004). Finally, environmental effects, such as a through-thickness thermal gradient, can be used to impose curvature-inducing strains. It becomes apparent that a thorough investigation of shell multistability needs to include consideration for prestressing in its various forms. Given the current prominence of embedded piezoelectric actuators for shells, mentioned in Section 2.5.1, and the development of bistable laminate with prestressed fibres by Daynes *et al.* (2010), it is essential to understand how a shell responds to these conditions.

We present a constitutive relationship between prestress and curvature, an amended version of a formulation from Mansfield (2005) referring to thermal stresses. First, note our symbols for the mid-plane, or membrane strains, ϵ_0, and the *prestressing curvatures*, κ_F. The mid-surface strains can be calculated by averaging the through-thickness strain field, ϵ_F, over the thickness of the shell:

$$\epsilon_0 = \frac{1}{t}\int_{-\frac{t}{2}}^{\frac{t}{2}} \epsilon_F dz, \tag{3.36}$$

while the prestressing curvatures are:

$$\kappa_F = \frac{12}{t^3}\int_{-\frac{t}{2}}^{\frac{t}{2}} z\epsilon_F dz, \tag{3.37}$$

complying with the *Kirchhoff* hypothesis which states: ‘‘`normals to the centre surface of a plate remain normal during deformation.`’’ The free curvature of the shell can then be expressed as:

$$\kappa = \kappa_F + \mathbf{D}^{-1}\mathbf{M}, \tag{3.38}$$

where $\mathbf{M}$ is the tensor of moments in the shell, $\mathbf{D}$ corresponds to the $\mathbf{ABD}$ matrix from Eq. (3.19), and any bending-stretching coupling is ignored, *i.e.* $\mathbf{B}$ is assumed equal to zero.

3.6 Concluding remarks

This Chapter gave some characteristics of materials that are relevant to the construction of shells, and multistable shells in particular. The brief list presented is not exhaustive, but it helps establish a practical context for the theoretical investigations that follow. Furthermore, the idealisations we made in this Chapter, and the ensuing estimation tools will be useful for design purposes later on. In the next Chapter we develop a mathematical formulation for the strain energy of an elliptical multistable shell based on the Uniform Curvature (UC) assumption.

Chapter 4

Analytical model

4.1 Introduction

In this Chapter we define a theoretical framework for studying the structural mechanics of morphing shells with actuation capabilities. We begin with a brief historical review of the theoretical context to this work. In Section 4.3 we give some relevant definitions of geometrical quantities and constitutive parameters and produce governing equations for anisotropic multistable shells based on the Uniform Curvature (UC) assumption. In Section 4.4.1 this model is used to produce some closed-form solutions for some simple cases. For some additional cases, where closed-form solutions are not possible, we present numerical solutions.

4.2 Theoretical background

In Chapter 2 a generic review of progress in the study of shells was presented. Here we focus further on the theoretical tradition that relates to the model we will be constructing and using for our analysis. Many of our techniques and assumptions originally stem from Mansfield (2005) and the mechanics of shells in general; he considers the small-deflection theory of plates, initially by Lagrange (1811). The basic assumptions are reproduced here.

- Points which lie on a normal to the mid-plane of the undeformed plate lie on a normal to the mid-plane of the deflected plate.
- The stresses normal to the mid-plane of the plate, arising from the applied loading, are negligible in comparison with the stresses in the plane of the plate.
- The slope of the deflected plate in any direction is small so that its square may be neglected in comparison with unity.

- The mid-plane of the plate is a 'neutral plane,' that is, any mid-plane stresses arising from the deflection of the plate into a non-developable surface may be ignored.

These allow for in-plane properties to be used in extrapolating out-of-plane deformation. For a more accurate formulation of the large-deflections scenario, middle-surface stresses also need to be accounted for, *i.e.* the last assumption needs to be amended. Middle-surface stresses arise in the bending of non-developable shells, and when the boundary conditions restrict movement in the plane of a plate. In this endeavour, the Föppl-Von Kármán model, is generally considered the most successful and was used extensively by various authors. We quote from Vidoli (2013): `‘‘ [the FVK model] considers, indeed, the minimal geometrical nonlinearity able to catch the dependence of the shell membranal strain on the transverse displacement field.’’` A wealth of applications takes advantage of this formulation, including, but not limited to; aero-elastic buckling of panels, wrinkling of soft tissues and morphing structures (corresponding references can be found in the same publication). However, the resulting partial differential equation (PDE) from the FVK equilibrium condition can often be difficult to solve exactly, especially when the additional constrain of initial curvature is added.

Mansfield (1962) overcame the limitations of the FVK model by pioneering the use of the Uniform Curvature assumption (UC) to approach large deflection problems and specifically to reduce the problem of a heated plate to three degrees of freedom. He is responsible for the following compatibility equation:

$$\nabla^4 \Psi = -\frac{1}{2} E t \Diamond^4(w, w), \tag{4.1}$$

from geometrical compatibility and where Ψ is the middle-surface force function. The two operators are defined by

$$\nabla^2 f = \frac{\partial^2 f}{\partial x^2} + \frac{\partial^2 f}{\partial y^2}, \tag{4.2}$$

due to Laplace, and

$$\Diamond^4(f, g) = \frac{\partial^2 f}{\partial x^2}\frac{\partial^2 g}{\partial y^2} - 2\frac{\partial^2 f}{\partial x \partial y}\frac{\partial^2 g}{\partial x \partial y} + \frac{\partial^2 f}{\partial y^2}\frac{\partial^2 g}{\partial x^2}, \tag{4.3}$$

due to Mansfield. By considering "lenticular" sections, where the moment diminish at the periphery, he produced exact solutions of the FVK equations. The same author later justified the obvious weakness of the model to describe a known variation of the curvature at the boundary layer when constant thickness shells are considered. In Mansfield (2005), the approximate width of the boundary layer is calculated for an initially flat strip, thickness t, bent to a curvature κ along its length by end moments applied to its ends. The

resulting width of $0.77\sqrt{t/\kappa}$ is very small for thin shells in large-deflection scenarios.

Hyer (1981a) produced an even simpler model, using the same UC assumption, and discretising the FVK equations with the Rayleigh-Ritz method. The simplicity of this model proved powerful in many instances and was used in various studies, especially relating to composite plates under thermal loads (Dano & Hyer, 1998; Salamon & Masters, 1995). At the same time, deficiencies of the UC assumption were noted. Gigliotti *et al.* (2004) note that the importance of planform aspect ratio is missed by both models. The failure of the UC assumption to exactly capture the boundary condition was mentioned above and led to various efforts to construct models with many more degrees of freedom (Aimmanee & Hyer, 2004; Pirrera *et al.*, 2011).

At the same time, a set of workers persisted in extending the Mansfield model, especially in association with multistable shells, producing various practical results along the way (Fernandes *et al.*, 2010; Guest & Pellegrino, 2006; Seffen, 2007). The work that follows—an extension of the work in Seffen (2007)—clearly falls within this tradition, and the corresponding symbols are employed where appropriate. Here, the FVK model is not followed and a compatibility expression linking bending and stretching leads to a strain energy expression.

4.3 Governing equations

We consider a homogeneous shell with elliptical planform whose major and minor semi-axes' lengths are a and b respectively. We define an extrinsic coordinate system, $Oxyz$, with origin O at the centre of the ellipse. The shell periphery can be thus shown to be $(x/a)^2+(y/b)^2 = 1$ when viewed from the z-direction and this is assumed, even for shallow out-of-plane displacements, which are given in terms of the curvatures $(\kappa_x, \kappa_y, \kappa_{xy})$:

$$w = -\frac{1}{2}\kappa_x x^2 - \kappa_{xy} xy - \frac{1}{2}\kappa_y y^2. \tag{4.4}$$

By assuming shallow displacements, the curvatures can be defined by $\kappa_x = -\partial^2 w/\partial x^2$ in the x-direction, $\kappa_y = -\partial^2 w/\partial y^2$ in the y-direction, and $\kappa_{xy} = -\partial^2 w/\partial x \partial y$ is the twisting curvature. When the subscript "0" is added to any quantity, it denotes initial value. The shell is assumed to be *uniformly* curved, *i.e.* there is no spatial variation with x or y coordinates. The implications of a non-uniform boundary layer were addressed in the previous section.

Additionally, no external loads are present in our model, thus referring to a free-standing structure in practical terms. The characteristic radius of curvature, R, is defined as the largest radius of curvature in a given direction. It allows for a comparison between

different out-of-plane shapes of shells and helps to make curvatures dimensionless as described later. Residual stresses are introduced to the shell following prestressing, which—per our assumptions—only causes uniform bending stresses. These stresses are distinct from the self-stresses the structure develops to reach equilibrium.

For plane stress behaviour, the constitutive elasticity matrix, $\mathbf{E}$, is repeated here from Chapter 3 and written as

$$\mathbf{E} = \frac{E}{1-\nu^2/\beta}\begin{bmatrix} 1 & \nu & \psi \\ \nu & \beta & \eta \\ \psi & \eta & \alpha \end{bmatrix}. \tag{4.5}$$

Realistic value ranges for these parameters were discussed in the previous chapter. The generalised structural response for a shell element of unit surface area is given by:

$$\begin{bmatrix} \mathbf{N} \\ \mathbf{M} \end{bmatrix} = \begin{bmatrix} \mathbf{A} & \mathbf{B} \\ \mathbf{B} & \mathbf{D} \end{bmatrix} \begin{bmatrix} \mathbf{e} \\ \mathbf{k} \end{bmatrix}. \tag{4.6}$$

which is a condensed form of Eq. (3.19) and where $\mathbf{N}$ represents the middle-surface forces, $\mathbf{M}$ the bending moments; $\mathbf{e}$ represents the middle-surface strains and $\mathbf{k}$ represents the curvatures. The sub-matrices are defined by

$$\mathbf{A} = \int_{\text{thickness}} \mathbf{E}\,\mathrm{d}z, \quad \mathbf{B} = \int_{\text{thickness}} \mathbf{E}z\,\mathrm{d}z, \quad \mathbf{D} = \int_{\text{thickness}} \mathbf{E}z^2\,\mathrm{d}z. \tag{4.7}$$

For a homogeneous material of uniform thickness, that gives:

$$\mathbf{A} = \mathbf{E}t, \quad \mathbf{B} = \mathbf{0}, \quad \mathbf{D} = \mathbf{E}t^3/12, \tag{4.8}$$

where t is the thickness of the layer, and

$$\mathbf{N} = \mathbf{A}\mathbf{e}, \quad \mathbf{M} = \mathbf{D}\mathbf{k}. \tag{4.9}$$

From Eq. (4.7) it is obvious that $\mathbf{B}$ indeed diminishes for any shell that is symmetric with respect to the middle-surface. This makes our formulation applicable not only to through-thickness homogeneous shells, but to various composites. For example, fibre-reinforced laminates with symmetric layups can be included. At the same time, this assumption fails to capture certain materials, including various cases of unsymmetrical layups for laminates when $\mathbf{B}$ is not equal to zero.

Let us further define

$$\mathbf{e} = [\epsilon_{x0}\ \epsilon_{y0}\ \gamma_{xy0}]^T, \quad \mathbf{k} = [\chi_x\ \chi_y\ 2\chi_{xy}]^T, \tag{4.10}$$

within which

$$\chi_x = \kappa_x - \kappa_{x0} - \kappa_{xF}, \quad \chi_y = \kappa_y - \kappa_{y0} - \kappa_{yF}, \quad \chi_{xy} = \kappa_{xy} - \kappa_{xy0} - \kappa_{xyF}. \tag{4.11}$$

Here, the subscript "0" denotes the initial in-plane strains; the χ terms are the elastic changes in curvature ($\kappa - \kappa_0$), and include the aggregated bending effect due to the residual stresses through the thickness. These "F" subscripted terms are the set of curvatures that would be adopted by the unconstrained middle surface of the shell when the bending moments are zero, *i.e.* when $\mathbf{k} = \mathbf{0}$ and $\kappa - \kappa_0 = \kappa_F$. The calculation of resulting mid-surface curvature from a strain field along the thickness of the shell is presented in Section 3.5.

We now consider the elastic deformation of the shell, in order to calculate the stretching and bending densities, U_S and U_B,

$$U_B = \frac{1}{2}\mathbf{M}^T\mathbf{k}, \quad U_S = \frac{1}{2}\mathbf{N}^T\mathbf{e}. \tag{4.12}$$

Substituting for $\mathbf{M}$ from Eq. (4.9) and for $\mathbf{k}$ from Eq. (4.10), multiplying, and tidying up, we get

$$U_B = \frac{Et^3}{24(1-\nu^2/\beta)}\left(\chi_x^2 + 2\nu\chi_x\chi_y + \beta\chi_y^2 + 4\psi\chi_x\chi_{xy} + 4\eta\chi_y\chi_{xy} + 4\alpha\chi_{xy}^2\right). \tag{4.13}$$

For U_S, we adopt the following approach: via geometrical compatibility for the middle surface of a shell, we know from Calladine (1989),

$$-\Delta g = \frac{\partial^2\epsilon_{x0}}{\partial y^2} + \frac{\partial^2\epsilon_{y0}}{\partial x^2} + \frac{\partial^2\gamma_{xy0}}{\partial x\partial y}, \tag{4.14}$$

where Δg is the change in Gaussian Curvature and is equal to

$$\Delta g = \kappa_x\kappa_y - \kappa_{xy}^2 - \kappa_{x0}\kappa_{y0} + \kappa_{xy0}^2. \tag{4.15}$$

This expression can also be produced from Eq. (4.1) after replacing force function with stresses from the constitutive matrix. The middle-surface stresses can be expressed by an Airy function Φ as per Mansfield (2005):

$$\frac{N_x}{t} = \frac{\partial^2\Phi}{\partial y^2}, \quad \frac{N_y}{t} = \frac{\partial^2\Phi}{\partial x^2}, \quad \frac{N_{xy}}{t} = -\frac{\partial^2\Phi}{\partial x\partial y}. \tag{4.16}$$

By inverting the first of Eq. (4.9) and substituting into Eq. (4.14), the uniform change in Gaussian curvature is expressed in terms of Φ using Eq. (4.16). The full expression is:

$$-\frac{E\Delta g}{1-\nu^2/\beta}\delta = (\beta\alpha-\eta^2)\frac{\partial^4\Phi}{\partial y^4} - (2\nu\eta-2\psi\beta)\frac{\partial^4\Phi}{\partial y^3\partial x} + (2\psi\eta-2\nu\alpha+\beta-\nu^2)\frac{\partial^4\Phi}{\partial y^2\partial x^2} - (2\psi\nu-2\eta)\frac{\partial^4\Phi}{\partial y\partial x^3} + (\alpha-\psi^2)\frac{\partial^4\Phi}{\partial x^4}, \quad (4.17)$$

where

$$\delta = (\beta-\nu^2)\alpha - \eta^2 + 2\nu\eta\psi - \beta\psi^2, \quad (4.18)$$

which is proportional to the general determinant of $\mathbf{E}$ from Eq. (4.5).

Substituting Φ with a fourth degree polynomial provides one solution, since the left-hand side above is constant. But we provide additional equilibrium conditions for a precise solution: there are no direct normal and shearing forces on the periphery of the shell; there are no net direct or shearing forces across both x- and y-axes. This is satisfied by

$$\underbrace{\int_{y=-b}^{y=+b}(N_x, N_{xy})\,\mathrm{d}y = 0,}_{\text{on } x=0} \qquad \underbrace{\int_{x=-a}^{x=+a}(N_y, N_{xy})\,\mathrm{d}x = 0\,.}_{\text{on } y=0} \quad (4.19)$$

From Eq. (4.16), the middle-surface forces are second-order polynomials, which can be shown to be

$$\frac{N_x}{t} = S\big[x^2 + \frac{3a^2}{b^2}y^2 - a^2\big], \qquad \frac{N_y}{t} = S\big[\frac{3b^2}{a^2}x^2 + y^2 - b^2\big], \qquad \frac{N_{xy}}{t} = -2Sxy. \quad (4.20)$$

Which comply with our boundary conditions. From compatibility, Eq. (4.16), we obtain

$$S = -\frac{Ea^2b^2\Delta g}{\xi} \quad (4.21)$$

where the constant ξ, is given by

$$\xi = (1-\nu^2/\beta)[6a^4(\beta\alpha-\eta^2) + 6b^4(\alpha-\psi^2) + 2a^2b^2(\beta-\nu^2-2\nu\alpha+2\psi\eta)]/\delta. \quad (4.22)$$

Reversing the first expression in Eq. (4.9) and inputting the result for $\mathbf{e}$ in the second expression in Eq. (4.12) produces an expression for the stretching strain energy density given by

$$U_S = \frac{1-\nu^2/\beta}{2Et\delta}[(\beta\alpha-\eta^2)N_x^2 + 2(\psi\eta-\nu\alpha)N_xN_y + (\alpha-\psi^2)N_y^2 + 2(\nu\eta-\psi\beta)N_xN_y + 2(\psi\nu-\eta)N_yN_{xy} + (\beta-\nu^2)N_{xy}^2]. \quad (4.23)$$

By integrating the two energy densities over the area of the elliptical surface we produce

the total potential energy, U. We only present the final result here, in its dimensionless form

$$\bar{U} = U\frac{12(1-\nu^2/\beta)R^2}{E\pi\alpha bt^3}, \quad \bar{\kappa} = \kappa R, \quad \rho = \frac{b}{a}, \tag{4.24}$$

where, recall, R is the characteristic radius. In addition, we define

$$u = 3(\beta\alpha - \eta^2) + \rho^2(2\psi\eta - 2\nu\alpha + \beta - \nu^2) + 3\rho^4(\alpha - \psi^2), \tag{4.25}$$

$$v = \frac{4\rho}{\pi}[(\nu\eta - \psi\beta) + \rho^2(\psi\nu - \eta)] \tag{4.26}$$

and

$$\phi = \frac{b^4}{t^2R^2}\cdot\frac{\delta}{2u^2}(u - v). \tag{4.27}$$

So, the final expression for the dimensionless energy is:

$$\begin{aligned}\bar{U} = \frac{\phi}{2}[\bar{\kappa}_x\bar{\kappa}_y - \bar{\kappa}_{xy}^2 - \bar{\kappa}_{x0}\bar{\kappa}_{y0} + \bar{\kappa}_{xy0}^2]^2 + \frac{1}{2}[(\bar{\kappa}_x - \bar{\kappa}_{x0} - \bar{\kappa}_{xF})^2 \\ + 2\nu(\bar{\kappa}_x - \bar{\kappa}_{x0} - \bar{\kappa}_{xF})(\bar{\kappa}_y - \bar{\kappa}_{y0} - \bar{\kappa}_{yF}) \\ + \beta(\bar{\kappa}_y - \bar{\kappa}_{y0} - \bar{\kappa}_{yF})^2 + 4\psi(\bar{\kappa}_x - \bar{\kappa}_{x0} - \bar{\kappa}_{xF})(\bar{\kappa}_{xy} - \bar{\kappa}_{xy0} - \bar{\kappa}_{xyF}) \\ 4\eta(\bar{\kappa}_y - \bar{\kappa}_{y0} - \bar{\kappa}_{yF})(\bar{\kappa}_{xy} - \bar{\kappa}_{xy0} - \bar{\kappa}_{xyF}) + 4\alpha(\bar{\kappa}_{xy} - \bar{\kappa}_{xy0} - \bar{\kappa}_{xyF})^2].\end{aligned} \tag{4.28}$$

Statical equilibrium configurations are found when we set the derivatives of $\bar{U}$ with respect to the three curvatures equal to zero. *i.e.*

$$\frac{\partial\bar{U}}{\partial\bar{\kappa}_x} = 0, \qquad \frac{\partial\bar{U}}{\partial\bar{\kappa}_y} = 0, \qquad \frac{\partial\bar{U}}{\partial\bar{\kappa}_{xy}} = 0. \tag{4.29}$$

After rearranging, we find, respectively for $\partial\bar{U}/\partial\bar{\kappa}_x$, $\partial\bar{U}/\partial\bar{\kappa}_y$ and $\partial\bar{U}/\partial\bar{\kappa}_{xy} = 0$,

$$\begin{aligned}\bar{\kappa}_x + \mu\bar{\kappa}_y + 2\psi\bar{\kappa}_{xy} &= \bar{\kappa}_{x0} + \nu\bar{\kappa}_{y0} + \\ &\quad 2\psi\bar{\kappa}_{xy0} + \bar{\kappa}_{xF} + \nu\bar{\kappa}_{yF} + 2\psi\bar{\kappa}_{xyF},\end{aligned} \tag{4.30}$$

$$\begin{aligned}\mu\bar{\kappa}_x + \beta\bar{\kappa}_y + 2\eta\bar{\kappa}_{xy} &= \nu\bar{\kappa}_{x0} + \beta\bar{\kappa}_{y0} + \\ &\quad 2\eta\bar{\kappa}_{xy0} + \nu\bar{\kappa}_{xF} + \beta\bar{\kappa}_{yF} + 2\eta\bar{\kappa}_{xyF},\end{aligned} \tag{4.31}$$

$$\begin{aligned}2\psi\bar{\kappa}_x + 2\eta\bar{\kappa}_y + 2(2\alpha + \nu - \mu)\bar{\kappa}_{xy} &= 2\psi\bar{\kappa}_{x0} + 2\eta\bar{\kappa}_{y0} + \\ &\quad 4\alpha\bar{\kappa}_{xy0} + 2\psi\bar{\kappa}_{xF} + 2\eta\bar{\kappa}_{yF} + 4\alpha\bar{\kappa}_{xyF},\end{aligned} \tag{4.32}$$

where μ is given by:

$$\mu = \nu + \phi\Delta g = \nu + \phi(\bar{\kappa}_x\bar{\kappa}_y - \bar{\kappa}_{xy}^2 - \bar{\kappa}_{x0}\bar{\kappa}_{y0} + \bar{\kappa}_{xy0}^2). \tag{4.33}$$

These are for an unloaded, elastic shell of elliptical planform and constant thickness. They account for both bending and stretching, while at the same time, offering a great simplification compared with classical shell theory. With the traditional route—as represented by the FVK equations mentioned in Section 4.2—we would have arrived at a set of complicated PDEs, making our pursuit of a solution landscape remarkably more complicated and computationally intensive. The leap is made by assuming no variation in the curvature of the shell and diminishing boundary loads. The latter assumption was made exactly valid with respect to edge forces by choosing appropriate functions for the mid-surface forces in the shell. On the other hand, boundary moments may not be zero but their effect dissipates along the boundary layer discussed earlier, and explained to be relatively narrow for thin shells.

4.3.1 Stability

The stability of each state can be examined through the generalised stiffness matrix. This is produced from the Taylor expansion of the generalised energy expression, where a form is given by Guest & Pellegrino (2006), and then extended by Seffen (2007):

$$H = \begin{bmatrix} \partial^2\bar{U}/\partial\bar{\kappa}_x^2 & \partial^2\bar{U}/\partial\bar{\kappa}_x\partial\bar{\kappa}_y & \partial^2\bar{U}/\partial\bar{\kappa}_x\partial\bar{\kappa}_{xy} \\ \partial^2\bar{U}/\partial\bar{\kappa}_y\partial\bar{\kappa}_x & \partial^2\bar{U}/\partial\bar{\kappa}_y^2 & \partial^2\bar{U}/\partial\bar{\kappa}_y\partial\bar{\kappa}_{xy} \\ \partial^2\bar{U}/\partial\bar{\kappa}_{xy}\partial\bar{\kappa}_x & \partial^2\bar{U}/\partial\bar{\kappa}_{xy}\partial\bar{\kappa}_y & \partial^2\bar{U}/\partial\bar{\kappa}_{xy}^2 \end{bmatrix}. \tag{4.34}$$

After substituting Eq. (4.28), and differentiating appropriately, H becomes

$$\begin{bmatrix} 1+\phi\kappa_y^2 & \mu+\phi\kappa_x\kappa_y & -2\phi\kappa_y\kappa_{xy}+2\psi \\ \mu+\phi\kappa_x\kappa_y & \beta+\phi\kappa_x^2 & -2\phi\kappa_x\kappa_{xy}+2\eta \\ -2\phi\kappa_{xy}\kappa_y+2\psi & -2\phi\kappa_{xy}\kappa_x+2\eta & 4\alpha-2\phi\Delta g+4\phi\kappa_{xy}^2 \end{bmatrix}. \tag{4.35a}$$

An equilibrium solution is stable when H is positive definite. In practice we examine that by checking whether the eigenvalues of H, the generalised stiffness matrix, are positive. When the minimum eigenvalue is zero the solution is considered neutrally stable. When numerical calculation is involved, we allow for a window around zero ($\pm w$) to account for computational precision errors in solutions that follow, *i.e.* some leeway is provided for the inability of algorithms to produce an exact zero in many cases. Such issues can also be dealt with appropriate functions in modern software—for example, `Chop[]` in Mathematica (Wolfram Research Inc., 2008)—but can be otherwise tedious. More

formally the criterion is:

$$\min\big(\text{eig}(H)\big) > w \quad \longrightarrow \quad \text{stable solution} \tag{4.36a}$$

$$-w \leq \min\big(\text{eig}(H)\big) \leq w \quad \longrightarrow \quad \text{neutrally stable solution} \tag{4.36b}$$

In Chapter 5 some aspects of Catastrophe Theory, a mathematical construct, are invoked to formalise matters.

4.4 Initial investigation

When available, a closed-form solution for the curvatures is the preferred result since it provides a mathematically exact picture, which we can manipulate for further analysis. This is only possible for some specialised cases. Some of these results were presented by Seffen (2007), but are used here to contrast with similarly simple cases that present no closed-form solutions. In addition, the phrase "characteristic equation" is defined in this chapter: this equation is the product of solving the governing equations—Eqs. (4.30) to (4.32)—explicitly in terms of μ, and substituting in the constraint Eq. (4.33). It was used extensively by Seffen (2007) to produce closed-form solutions and is solved numerically for higher polynomial degrees.

4.4.1 Closed-form solutions

The initial part of our methodology consists of attempts to find closed-form solutions for the governing equations. For specialised cases with some of the parameters set to zero or unity, this is both feasible and useful. We now present a sample of these attempts. Some of the closed-form results were obtained by Seffen & Guest (2011); we expand on those and complement with cases that need to be solved numerically.

Here, the material coupling constants, η and ψ, are assumed to be zero. Removing the coupling parameters removes the κ_{xy} term from Eqs. (4.30) and (4.31) and the terms κ_x and κ_y from Eq. (4.32), decoupling the latter equation from the preceding two. The modular ratio, β, is assumed to be unity. Initial twist (κ_{xy0}) is also assumed to be zero while we assume no resultant twist (κ_{xy}) is present, *i.e.* only untwisted solutions are considered. These greatly simplify the system of equations:

$$\kappa_x + \mu\kappa_y = \kappa_{x0} + \nu\kappa_{y0} + \kappa_{xF} + \nu\kappa_{yF}, \tag{4.37}$$

$$\mu\kappa_x + \kappa_y = \nu\kappa_{x0} + \kappa_{y0} + \nu\kappa_{xF} + \kappa_{yF}, \tag{4.38}$$

$$(2\alpha + \nu - \mu)\kappa_{xy} = 0, \tag{4.39}$$

$$\mu = \nu + \phi(\kappa_x\kappa_y - \kappa_{xy}^2 - \kappa_{x0}\kappa_{y0} + \kappa_{xy0}^2). \tag{4.40}$$

Within the given assumptions, Eq. (4.39) provides great insight; either $\kappa_{xy} = 0$ or $\mu = 2\alpha + \nu$. In the latter case, with a constant μ, inextensible behaviour is described, since the change in Gaussian Curvature, Δg, is equal to a constant. In the former case, which describes untwisted solutions, Eq. (4.39) is decoupled from the other three equations and the system can be reduced to an equation with respect to μ that is presented later in this section.

Various cases for the initial shape were considered, which are defined by the corresponding values for κ_{x0} and κ_{y0}. For example, the developable flat and cylindrical initial shapes are compared with the non-developable spherical and saddle plates. The prestressing cases are chosen primarily for the symmetry (or anti-symmetry) that they introduce to the equations and facilitates a closed-form solution. In practice the prestressing could be established by choosing appropriate material or environmental factors.

Initially flat shell with opposite-sense prestressing

In some cases this investigation leads to rather simple closed-form solutions. For example, taking the initially flat case, $\kappa_{x0} = \kappa_{y0} = 0$, with opposite-sense prestressing, $\kappa_{xF} = -\kappa_{yF} = k_1$, Eq. (4.37) and Eq. (4.38) become:

$$\kappa_x + \mu\kappa_y = k_1(1 - \nu), \tag{4.41}$$

$$\mu\kappa_x + \kappa_y = -k_1(1 - \nu), \tag{4.42}$$

with k_1 denoting the prestressing value. Equation (4.39) is not relevant as we discount twist. A symmetrical solution has $\kappa_x = -\kappa_y = \kappa$, and using Eq. (4.40), $\mu = \nu - \phi\kappa^2$. We substitute κ_x, κ_y and μ in Eq. (4.41), and obtain a third order polynomial expression in terms of κ:

$$\kappa + \frac{\phi}{(1 - \nu)}\kappa^3 = k_1, \tag{4.43}$$

i.e. initially no bistable behaviour is observed. Another solution is produced by setting $\mu = -1$, which makes Eqs. (4.41) and (4.42) combine to give

$$\kappa_x - \kappa_y = (1-\nu)k_1, \tag{4.44}$$

while Eq. (4.40) gives

$$\kappa_x \kappa_y = -\frac{1-\nu}{\phi}. \tag{4.45}$$

From these two results, we can obtain a second order polynomial equation in terms of κ_x by eliminating κ_y:

$$\kappa_x\big[\kappa_x - (1-\nu)k_1\big] = -\frac{1-\nu}{\phi}, \tag{4.46}$$

or

$$\kappa_x^2 - (1-\nu)k_1\kappa_x + \frac{1-\nu}{\phi} = 0. \tag{4.47}$$

The solution to this returns the one principal curvature as:

$$\kappa_x = \frac{k_1(1-\nu)}{2}\left(1 \pm \left[1 - \frac{4(1+\nu)}{\phi k_1^2(1-\nu)^2}\right]^{\frac{1}{2}}\right) \tag{4.48}$$

while the other can be found by substituting Eq. (4.48) into Eq. (4.44):

$$\kappa_y = -\frac{k_1(1-\nu)}{2}\left(1 \mp \left[1 - \frac{4(1+\nu)}{\phi k_1^2(1-\nu)^2}\right]^{\frac{1}{2}}\right). \tag{4.49}$$

Examining the stability of these solutions—according to Section 4.3.1—we conclude that the curvature is defined by the first—monotonically increasing—solution until a value of prestress k_1^*. Thereafter this equilibrium path is unstable and we move on the secondary equilibrium path described by Eqs. (4.48) and (4.49). We can calculate the value of k_1^* by setting the discriminant of Eq. (4.47) equal to zero:

$$1 - \frac{4(1+\nu)}{\phi k_1^2(1-\nu)^2} = 0. \tag{4.50}$$

Solving this for k_1, we get

$$k_1^* = \sqrt{\frac{4(1+\nu)}{\phi(1-\nu)^2}}. \tag{4.51}$$

Figure 4.1a shows the solution in graphical form. In this plot and others in this Chapter stable paths are shown with continuous curves, while dashed lines signify unstable paths and dotted paths mark neutrally stable paths. In cases where κ_x and κ_y diverge, κ_x is shown in black while κ_y in grey. Following the plot for increasing k_1, initially the flat shell morphs into a saddle shape, but at k_1^* the shell buckles and moves towards a cylindrical

shape. After buckling, the symmetry between κ_x and κ_y introduces bistability since either orientation for the cylindrical shape is feasible.

Initially saddle-shaped shell with opposite-sense prestressing

In this case, $\kappa_{x0} = -\kappa_{y0} = \kappa_0$ and $\kappa_{xF} = -\kappa_{yF} = k_1$, while the governing equations become

$$\kappa_x + \mu\kappa_y = \kappa_0 - \nu\kappa_0 + k_1 - \nu k_1 = (1-\nu)(\kappa_0 + k_1), \tag{4.52}$$

$$\mu\kappa_x + \kappa_y = \nu\kappa_0 - \kappa_0 + \nu k_1 - k_1 = -(1-\nu)(\kappa_0 + k_1), \tag{4.53}$$

$$\mu = \nu + \phi(\kappa_x\kappa_y + \kappa_0^2). \tag{4.54}$$

Again by symmetry, one solution is $\kappa_x = -\kappa_y$. We can obtain a third order equation in terms of any of the three unknowns $(\kappa_x, \kappa_y, \mu)$. Another solution is given by $\mu = -1$. Substituting this value we get

$$\kappa_y^2 + (1-\nu)(\kappa_0 + k_1)\kappa_y + \left(\kappa_0^2 + \frac{\nu+1}{\phi}\right) = 0 \quad \Rightarrow \tag{4.55}$$

$$\kappa_y = \frac{1}{2}\left(-(1-\nu)(\kappa_0 + k_1) + \sqrt{(1-\nu)^2(\kappa_0 + k_1)^2 - 4\left(\kappa_0^2 + \frac{\nu+1}{\phi}\right)}\right). \tag{4.56}$$

We can find the point of bifurcation, relating to the buckling of the shell, by setting the square root equal to zero:

$$(1-\nu)^2(\kappa_0 + k_1)^2 - 4\left(\kappa_0^2 + \frac{\nu+1}{\phi}\right) = 0. \tag{4.57}$$

This gives

$$k_1^* = \frac{2\sqrt{(\nu-1)^2\phi\,(\kappa_0^2\phi + \nu + 1)} - \kappa_0(\nu-1)^2\phi}{(\nu-1)^2\phi}, \tag{4.58}$$

and κ_x easily follows from Eq. (4.52), after substituting $\mu = -1$:

$$\kappa_x = \kappa_y + (1-\nu)(\kappa_0 + k_1). \tag{4.59}$$

Setting $\kappa_0 = 0$ lets the solutions agree with the previous case, as expected. The same can be verified by looking at a plot of the solution in Fig. 4.1b, which is obviously "contained" in the plot Fig. 4.1a. The geometry starts as a saddle-shaped shell, and past buckling tends

towards a cylindrical shape—more so with increasing k_1. Once more, two orthogonally symmetrical shapes are available to us, and with one of the two curvatures diminishing, the shell approaches a developable geometry.

Initially spherical shell with same-sense prestressing

In this case, $\kappa_{x0} = \kappa_{y0} = \kappa_0$, and $\kappa_{xF} = \kappa_{yF} = k_1$. Similarly to the previous section, we take advantage of symmetry and notice that combining Eqs. (4.37) and (4.38) produces two sets of solutions; $\kappa_x = \kappa_y$ and $\mu = 1$. For the former, the following third order equation is produced:

$$\kappa_x\Big[1 + \nu + \phi\big(\kappa_x^2 - \kappa_0^2\big)\Big] = (\kappa_0 + \kappa_1)(1 + \nu). \tag{4.60}$$

For $\mu = 1$, we can substitute into Eq. (4.37) to get

$$\kappa_x = (\kappa_0 + \kappa_1)\,(1 + \nu) - \kappa_y. \tag{4.61}$$

In turn, we can substitute this in toEq. (4.40), to obtain a second order equation with respect to κ_y:

$$\nu + \phi\Big(\kappa_y\big[(\kappa_0 + \kappa_1)(1 + \nu) - \kappa_y\big] - \kappa_0^2\Big) = 0. \tag{4.62}$$

The subsequent solution for κ_y is

$$\kappa_y = \frac{1}{2}\left[(\kappa_0 + \kappa_1)(1 + \nu) \pm \sqrt{(\kappa_0 + \kappa_1)(1 + \nu) - 4\left(\kappa_0^2 + \frac{1 - \nu}{\phi}\right)}\right], \tag{4.63}$$

Again we can find the point of bifurcation from the discriminant:

$$k_1^* = -\kappa_0 + 2\sqrt{\frac{1 - \nu + \kappa_0^2\phi}{(1 + \nu)^2\,\phi}}. \tag{4.64}$$

The initially flat subcase can be easily obtained by setting $\kappa_0 = 0$ in these expressions.

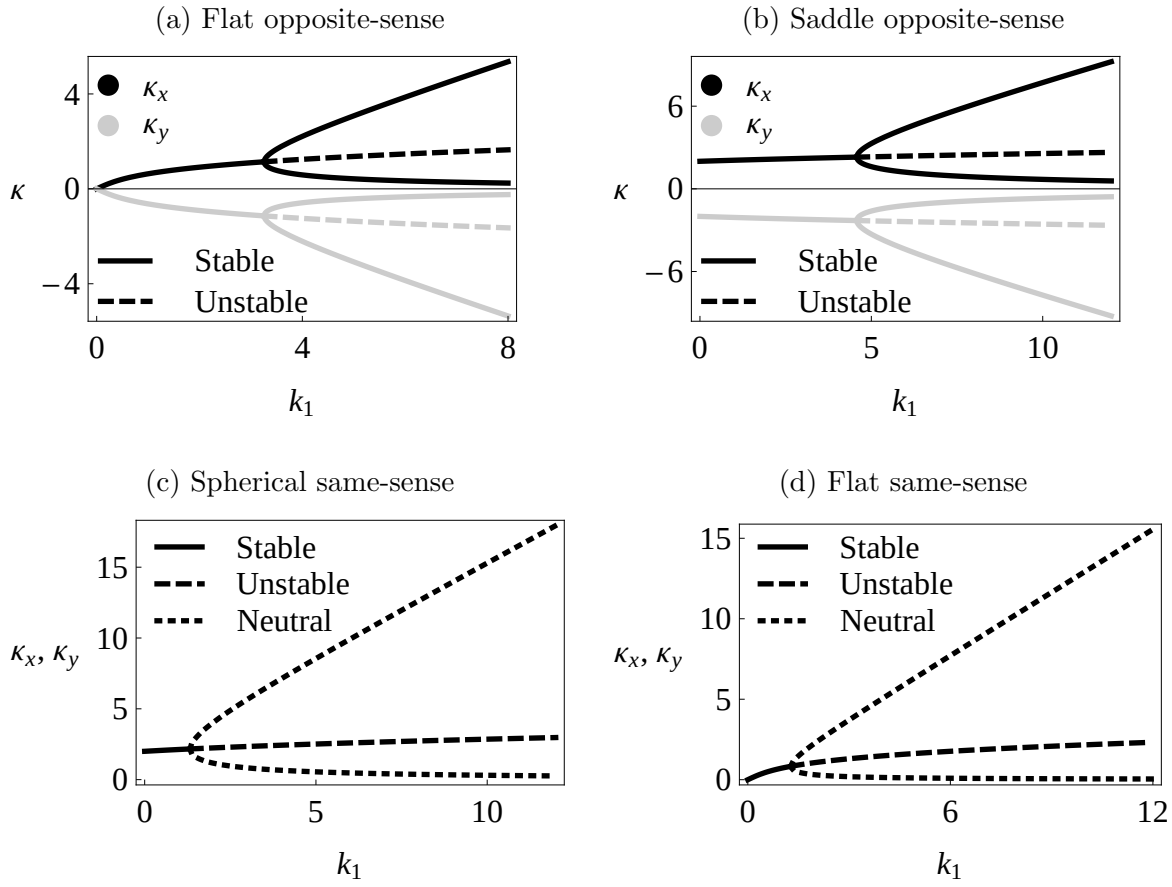

Figure 4.1: Curvature variation with prestressing for cases with a closed-form solution. The prestressing is either in the same-sense or in the opposite-sense along the two principal directions—and is symbolised by k_1. Continuous lines signify stability, while dashed lines signify instability and dotted lines signify neutral stability. For low values of prestressing the plots at the bottom describe monostability—and a spherical shape—until a point of bifurcation of the curvatures. Beyond that point the initial equilibrium path becomes unstable and a new, neutrally stable equilibrium path emerges. It describes an increasingly developable geometry, that approaches the shape of a cylinder. Neutral stability suggests that the cylindrical shape has no preference with respect to orientation. A similar scenario arises for the cases at the bottom where the monostable shape has the geometry of a saddle. The post-buckling behaviour is restricted to bistability, since the resulting cylinder prefers principal curvatures along the x and y axes.

Initially cylindrical shell with same-sense prestressing

This case can be defined by $\kappa_{x0} = \kappa_0$, $\kappa_{y0} = 0$ and $\kappa_{xF} = \kappa_{yF} = k_1$. The equations become:

$$\kappa_x + \mu\kappa_y = \kappa_0 + (1+\nu)k_1, \tag{4.65}$$

$$\mu\kappa_x + \kappa_y = \nu\kappa_0 + (1+\nu)k_1, \tag{4.66}$$

$$\mu = \nu + \phi(\kappa_x\kappa_y). \tag{4.67}$$

In this case, there are no obvious symmetries or algebraic simplifications we can try. Despite the lack of a closed-form solution, we present this to show the complexity that easily arises from these equations, even for relatively simple cases. If we do proceed with the algebra, we can express κ_x and κ_y in terms of μ,

$$\kappa_x = \frac{\kappa_0(1-\mu\nu) + k_1(1+\nu)(1-\mu)}{(1-\mu^2)}, \tag{4.68}$$

$$\kappa_y = \nu\kappa_0 + (1+\nu)k_1 - \mu\left[\frac{\kappa_0(1-\mu\nu) + k_1(1+\nu)(1-\mu)}{(1-\mu^2)}\right], \tag{4.69}$$

and substitute in Eq. (4.67),

$$\begin{aligned}(\mu-\nu)(1-\mu^2)^2 = \phi\big[(1-\nu\mu)\kappa_0 + k_1(1-\mu)(1+\nu)\big] \\ \left(\big[\nu\kappa_0 + (1+\nu)k_1\big](1-\mu^2) - \mu\big[(1-\nu\mu)\kappa_0 + k_1(1-\mu)(1+\nu)\big]\right),\end{aligned} \tag{4.70}$$

which is a fifth order characteristic equation and has to be solved numerically for μ. The resulting values of μ are substituted in Eq. (4.69) to obtain the corresponding geometry and the stability is assessed via Eq. (4.35a). This case, along with the remaining three without a closed-form solution, is plotted in Fig. 4.2. In the range of prestressing we have examined, a single stable solution is valid. Despite prestressing the cylindrical shell in both direction the geometry moves towards a tighter cylinder for high values of k_1.

Summary and interpretation

For the sake of brevity, not all the results from the cases in Section 4.4.1 are presented here except in their graphical form. Figure 4.1 presents the four cases that did have closed-form solutions, found through algebraic manipulation. Going through them, we observe a single stable geometry until a point of bifurcation, for some critical value of $k_1 = k_1^*$. At that point the equilibrium path diverges into a response with disparate curvatures; two branches representing the κ_x and κ_y curvatures. For all four cases the

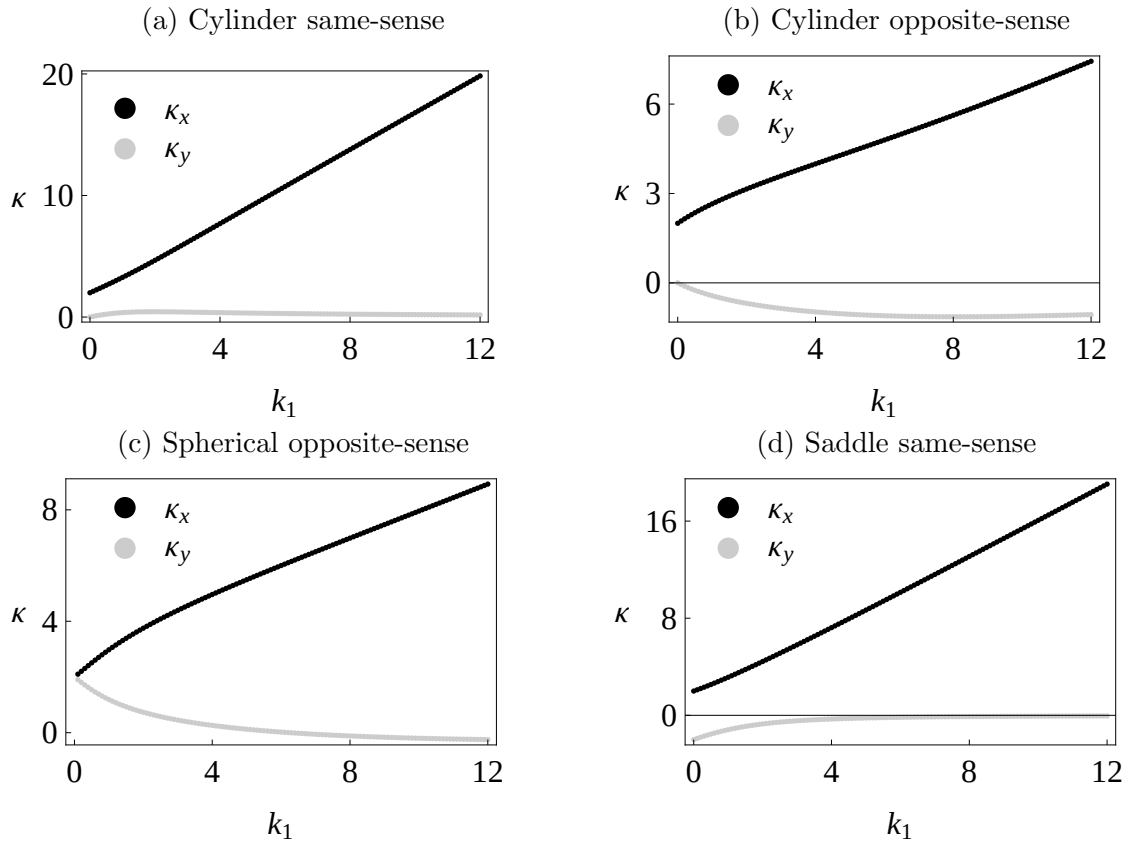

Figure 4.2: Curvature variation with prestressing for cases with no closed-form solution—a counterpart to Fig. 4.1. These were solved numerically in Mathematica and show only one stable geometry. For large values of prestress the initial shape becomes qualitatively irrelevant as the shells approach a cylindrical geometry—but maintains a quantitative effect on the magnitude of the behaviour.

nature of the stable geometry changes. If we take Fig. 4.1d for example (initially flat, same-sense prestressing), we note that initially the plate develops a spherical cap geometry since $\kappa_x = \kappa_y$, but after critical prestressing the magnitudes of κ_x and κ_y diverge. κ_y is asymptotically approaching zero while κ_x is asymptotically approaching $k_1(1+\nu)$, *i.e.* a cylindrical shape. In other words, *we have a switch from a non-developable geometry to an almost-developable geometry*—which approaches fully developable at the limit. The original path of the solution becomes unstable after the bifurcation point.

A similar process can be observed for the initially spherical shell with opposite-sense prestressing, whose solution is shown in Fig. 4.1b. Here we begin with a saddle-shaped shell and apply prestress in the opposite sense. Initially this conserves the shape and magnifies the curvatures. After a critical prestress however, we observe bifurcation and the shape approaches a cylinder as the magnitude of k_1 increases. Due to the built-in symmetry in this case, the cylinder can be oriented in either one of the x- and y-directions. Once again, the initial geometry becomes unstable after the bifurcation point.

The spherical same-sense prestressing is, in fact, a translated version of the flat same-

Closed-form Solution	Numerical Solution
Flat Same-sense	Cylindrical Same-sense
Flat Opposite-sense	Cylindrical Opposite-sense
Spherical Same-sense	Spherical Opposite-sense
Saddle Opposite-sense	Saddle Same-sense

Table 4.1: Categories of cases with and without closed-form solutions.

sense so it behaves identically. Similarly, the flat opposite-sense prestressing case is a translated version of the saddle opposite-sense, along the k_1-axis. This makes physical sense since once prestress is raised above zero, the two initially flat-plate geometries immediately move towards either a spherical or a saddle-shape depending on the direction of the prestressing.

The remaining four cases were solved numerically and are shown in Fig. 4.2. They all present a single stable geometry but we observe the magnitude of κ_y approaching zero while the curvature in the x-direction approaches linear behaviour. In other words, for high values of k_1, prestressing dominates and the initial shape becomes irrelevant. This also means all solutions approach a cylindrical shape.

Table 4.1 matches each case with the outcome of the investigation. As mentioned earlier, some of these results were obtained by Seffen & Guest (2011), however direct algebraic manipulation of the governing equations served as a great introduction to the topic and the associated challenges. In particular the need for computational assistance became apparent as we allowed more parameters to vary.

4.5 Twisting prestress

Our next goal is to study the effects of imposed twist, κ_{xyF}. This has not been studied at any length before and provides ground for novel observations. In practise, such an imposed twist can be produced through the use of the commercially available MFCs, also mentioned in Chapter 2. These composites offer in-plane longitudinal actuation of embedded fibres through the application of appropriate voltage. If two such patches are placed on the top and bottom of a shell in a $\pm 45°$ configuration, with one patch in tension and the other in compression, twist would be generated in the structure.

Going back to Eqs. (4.30) and (4.31), if we again assume the coupling parameters diminish and the prestress in the principal directions is zero, then the right hand sides diminish. The system now becomes:

$$\kappa_x + \mu\kappa_y = 0, \tag{4.71}$$

$$\mu\kappa_x + \beta\kappa_y = 0, \tag{4.72}$$

$$2(2\alpha + \nu - \mu)\kappa_{xy} = 4\alpha\kappa_{xyF}, \tag{4.73}$$

$$\mu = \nu + \phi(\kappa_x\kappa_y - \kappa_{xy}^2), \tag{4.74}$$

We attempt a closed-form solution. From Eq. (4.71) and Eq. (4.72) we can deduce that $\mu = \pm\sqrt{\beta}$, also $\kappa_x = \mp\sqrt{\beta}\kappa_y$. From Eq. (4.73) we know:

$$\kappa_{xy} = \frac{4\alpha\kappa_{xyF}}{2(2\alpha + \nu \mp \sqrt{\beta})}. \tag{4.75}$$

We can now use Eq. (4.74) to produce a closed-form solution in terms of κ_y. This turns out to be:

$$\kappa_y = \sqrt{\frac{1}{\phi\mu}\left[\nu - \mu - \frac{\phi(4\alpha\kappa_{xyF})^2}{4(2\alpha + \nu - \mu)^2}\right]}, \tag{4.76}$$

with μ as stated above.

The twisting curvature,κ_{xy}, increases linearly with twisting prestress, κ_{xyF}, as we would expect from Eq. (4.73), since the two are proportional. The other two curvatures, κ_x and κ_y remain at zero until a critical value of $\kappa_{xyF} = \kappa^*_{xyF}$, as shown in Fig. 4.3. This can be calculated by solving Eq. (4.76) for $\kappa_y = 0$, which gives

$$\kappa^*_{xy} = \sqrt{\frac{\nu - \mu}{\phi}}. \tag{4.77}$$

Substituting this into Eq. (4.73) we get

$$\kappa^*_{xyF} = \sqrt{\frac{\nu - \mu}{\phi}}\frac{(2\alpha + \nu - \mu)}{\alpha}. \tag{4.78}$$

We go a step further however and notice the effects of varying β and α. We observe the magnitudes of the curvatures are increased by a reduction of α and an increase of β. We can see how β in particular, directly dictates which curvature dominates. For values of β smaller than unity, the curvature in the y-direction dominates while roles are reversed for β greater than unity. The x- and y-direction curvatures are equal when $\beta = 1$. This was expected since physically β dictates the ratio of the stiffnesses in the two directions. The overall behaviour of the curve is not significantly altered in any other way through variation of α and β.

The stability of the solutions in this section was verified numerically, but we note the analytical work done by Fernandes *et al.* (2010). It is also noteworthy that in the same

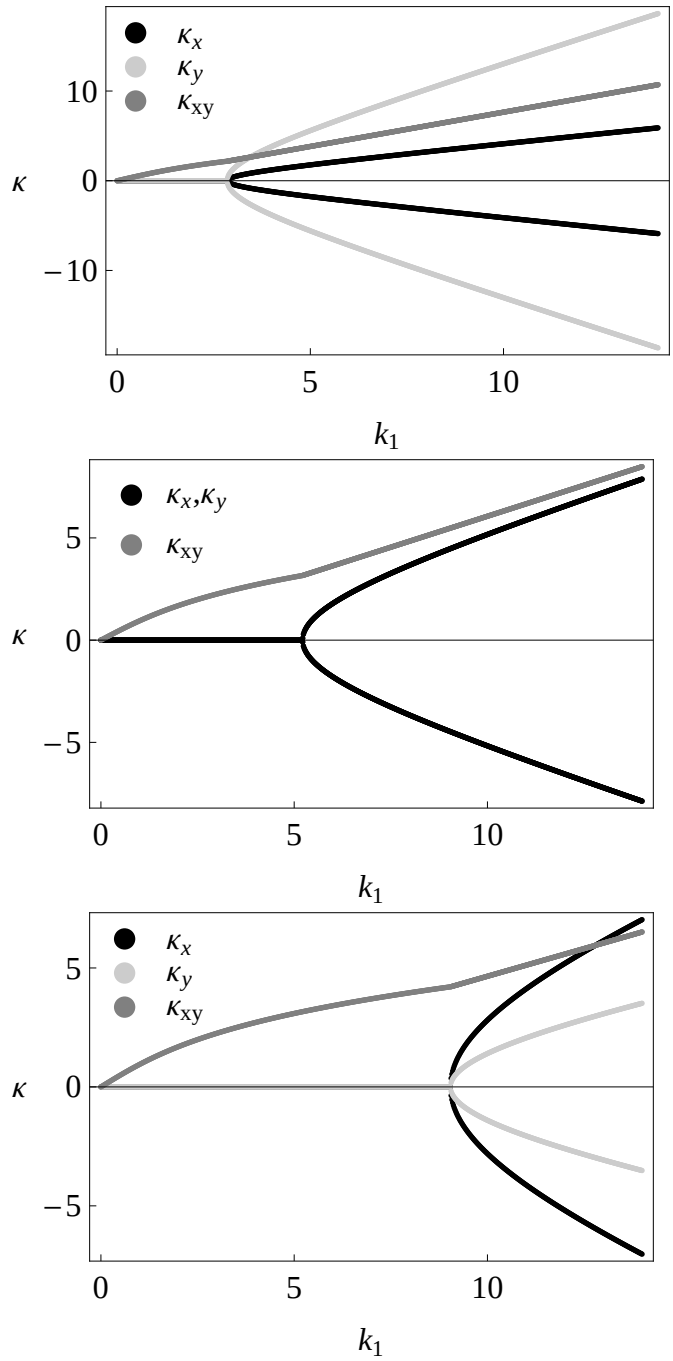

Figure 4.3: Curvatures versus twisting prestress while $\alpha = 1$ and β varies: $\beta = 0.1$ (top); $\beta = 1$ (centre); $\beta = 4$ (bottom). Only stable solutions are shown for clarity. This shows bistability can be achieved with only twisting prestressing. All cases start flat and only a twisting prestress is applied. The increasing twisting prestress does not influence the non-twisting curvatures up to a critical point, after which the shell develops a double curvature, in addition to the pre-existing twisting curvature. Variations in β change the relative magnitudes of the κ_x and κ_y curvatures in the post-buckling phase. k^*_{xy} is the critical twisting prestress where the shell jumps from one geometry to the other.

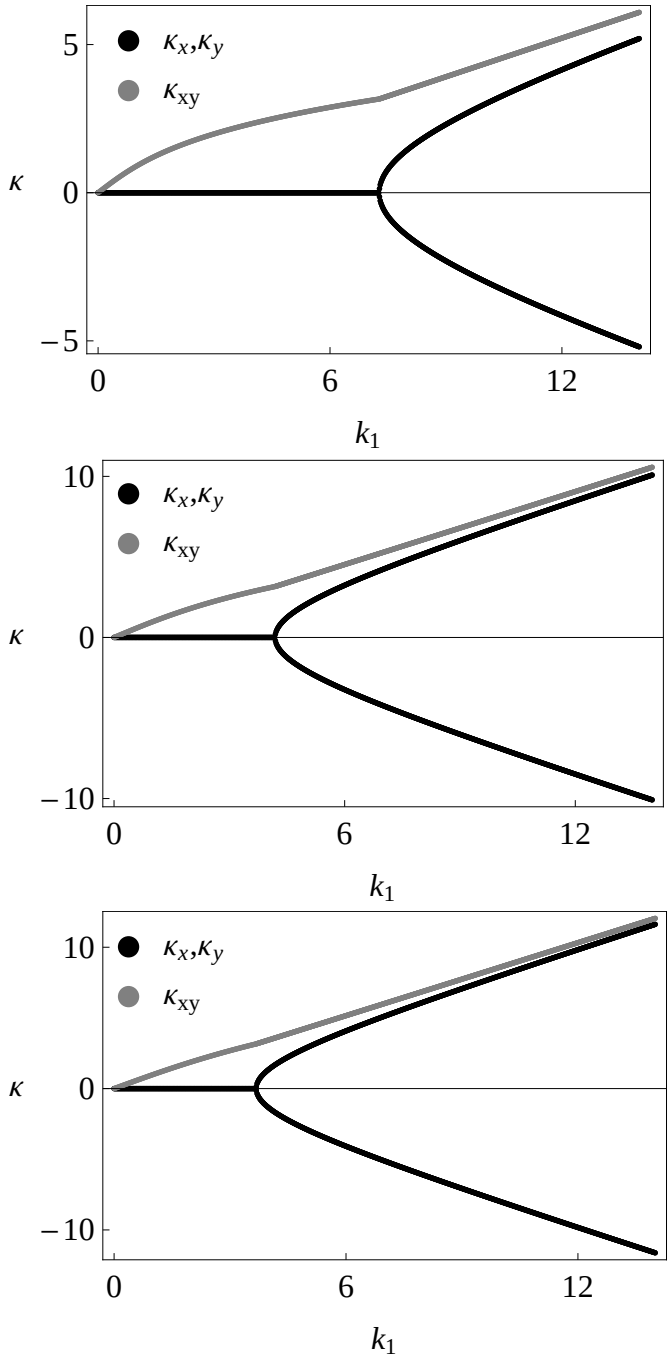

Figure 4.4: Curvatures vs prestressing twist while $\beta = 1$ and α varies: $\alpha = 0.5$ (top); $\alpha = 2$ (centre); $\alpha = 4$ (bottom). Notice the symmetry between κ_x and κ_y after the bifurcation. The qualitative response of the shell doesn't change with α, but the value of the critical point is reduced for higher values of the parameter.

work, we find paths for twisted solutions when actuated in the principal directions that are remarkably similar to the solutions here, produced with twisting prestress. Finally, we also note the study of the eigenvalues of the stability matrix by Seffen (2007), but we do not expand further here since a new, more generic approach is presented in Chapter 5.

4.6 Colourmaps

Another tool is a particular visualization method that allows us to "step back" and have a more general view of the parameter ranges for multistability without presenting explicit solutions for the new shapes: instead, we simply indicate the degree, or number, of stable states under variation of chosen parameters. With this method, we are able to go further than the limited cases that can be easily manipulated algebraically. This was inspired by a similar method found in papers by Seffen (2007) and Seffen & Guest (2011), in which the effect of disparate prestressing is considered for $\beta = 1$; we include a variation of β in our results, which is applicable to a huge array of orthotropic materials that have unequal moduli in two orthogonal directions.

For easier manipulation of the prestressing we define the parameters:

$$c_1 = \kappa_{x0} + \nu\kappa_{y0} + 2\psi\kappa_{xy0} + \kappa_{xF} + \nu\kappa_{yF} + 2\psi\kappa_{xyF}, \tag{4.79}$$

$$c_2 = \nu\kappa_{x0} + \beta\kappa_{y0} + 2\eta\kappa_{xy0} + \nu\kappa_{xF} + \beta\kappa_{yF} + 2\eta\kappa_{xyF}, \tag{4.80}$$

$$c_3 = 2\psi\kappa_{x0} + 2\eta\kappa_{y0} + 4\alpha\kappa_{xy0} + 2\psi\kappa_{xF} + 2\eta\kappa_{yF} + 4\alpha\kappa_{xyF}, \tag{4.81}$$

which are, in a sense, the forcing terms in Eqs. (4.30) to (4.32), and were also used by Seffen & Guest (2011).

We are only considering cases with $\eta, \psi = 0$ here, which considerably simplifies the investigation. In the absence of twisting prestress, the governing equations can be written as:

$$\kappa_x + \mu\kappa_y = c_1, \tag{4.82}$$

$$\mu\kappa_x + \beta\kappa_y = c_2, \tag{4.83}$$

$$(2\alpha + \nu - \mu)\kappa_{xy} = c_3(= 0). \tag{4.84}$$

The characteristic equation for μ here is taken from Seffen & Guest (2011):

$$(\mu - \nu)(\beta - \mu^2)^2 - \phi(c_2 - \mu c_1)(c_1\beta - \mu c_2) = 0. \tag{4.85}$$

which can be obtained by solving for κ_x and κ_y in the above and substituting in Eq. (4.40).

At the same time, we only consider untwisted solutions, *i.e.* κ_{xy} is taken to be zero and

The value for β is chosen and then for each real root of μ in Eq. (4.85) we examine the stability of the solution as explained in Section 4.3.1. This procedure is repeated for a range of values of c_1 and c_2. Thus, the landscape of stable states is established, without solving for specific material parameters. Initially some plots for $\beta = 1$ were attempted in comparison with similar plots by Seffen & Guest (2011). These are shown in Fig. 4.5, where we immediately see a dramatic change in behaviour between the case with isotropic value for α $\big((1-\nu)/2\big)$ and a higher-than-isotropic value of α $\big(2(1-\nu)\big)$. For the isotropic case we only have bistable areas in the region of $c_1 = -c_2$, and beyond a pair of critical values. At the higher value of α these regions remain, but additional areas along $c_1 = c_2$, also produce bistability. In our choice of the ranges for c_1 and c_2 we simply need to go beyond the critical values we mentioned above. The landscape of the solutions continues indefinitely beyond those points, so capturing the ranges close to the critical values is sufficient.

4.6.1 Investigation for $\beta \neq 1$

Finally, we used colourmaps to investigate the effect of β variation on multistability. A sample of results is shown in Fig. 4.6. There is little we can establish through these graphs alone, but we clearly see that an increase in β results in the shrinking of the bistable area. We see this when we compare Fig. 4.6b and Fig. 4.6d, where α remains unchanged but β is increased. The remaining two plots in that figure show that α has a similar influence: If we compare Fig. 4.6c and Fig. 4.6d—where β remains unchanged and α increases—we observe an expansion in the bistable region. In addition, an anti-symmetry between the effect of the two prestressing parameters, c_1 and c_2, is detected.

4.7 Concluding remarks

In this Chapter, an analytical model for multistable shells was developed. An expression for the strain energy was introduced in terms of the shell curvatures, which were assumed to be spatially uniform. Additionally, an initial investigation of possible behaviour was performed using this model, leading to some closed-form solutions for particular cases. When our algebraic tools fail, we attempt a numerical approach. Traditional techniques used in this Chapter cannot be directly generalised and are limited to the particular cases they refer to. The focus on particular parameter ranges and specific cases can be useful in a design context—in our investigation of β and α variation for example—but to understand possible behaviour, limiting the number of relevant parameters is helpful. The next Chapter presents an alternative method that succeeds in establishing the essential

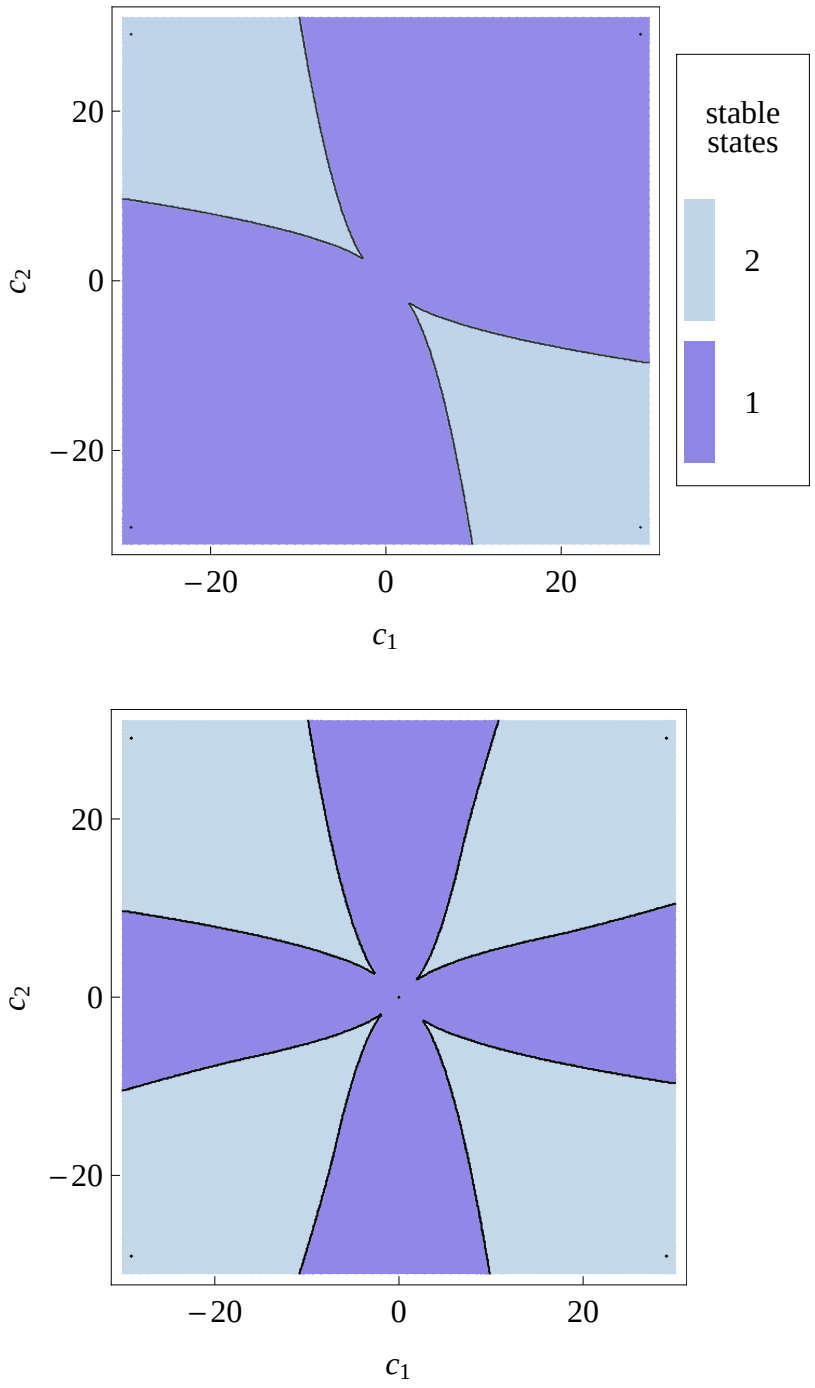

Figure 4.5: Number of stable states for a range of c_1 and c_2—defined in Eqs. (4.79) and (4.80)—while $\beta = 1$ and $\alpha = (1-\nu)/2$ (top), $\alpha = 4(1-\nu)/2$ (bottom): light blue offers bistable configurations; dark blue blue is monostable.

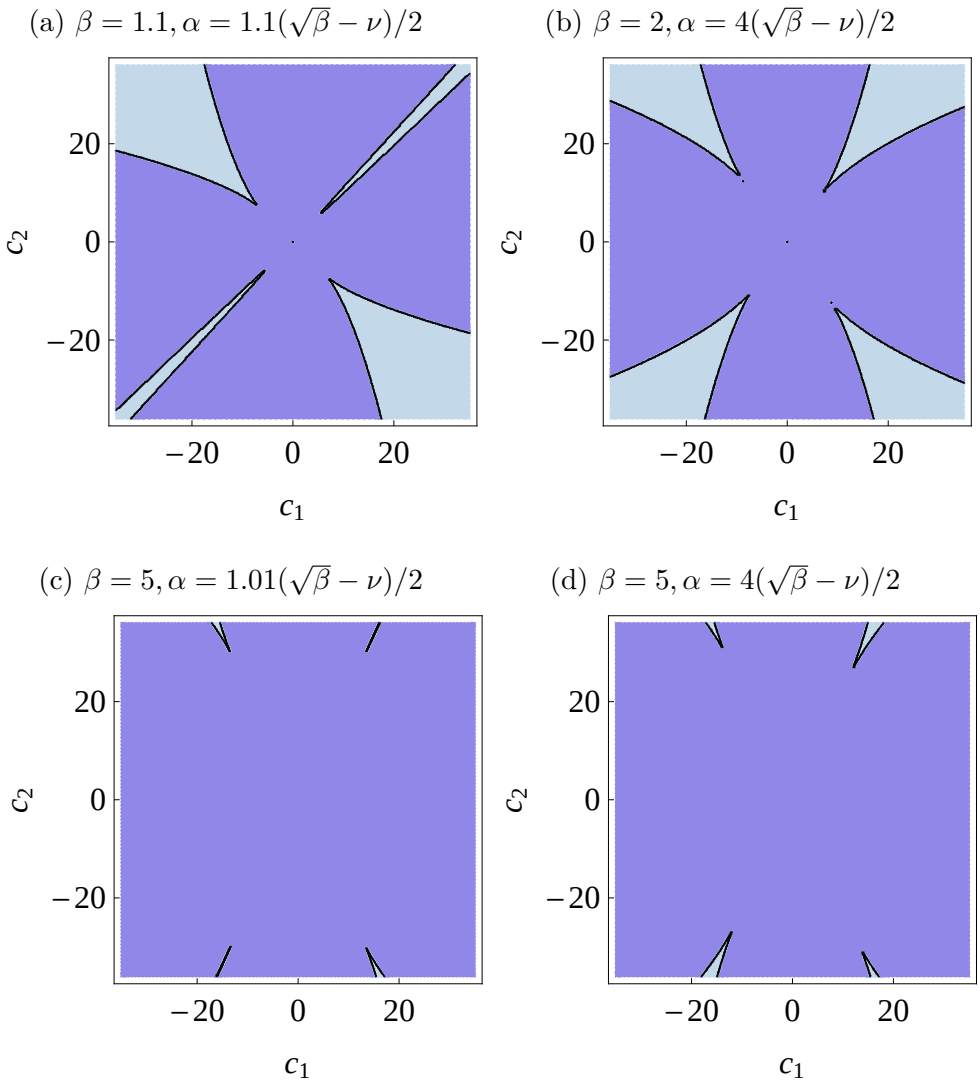

Figure 4.6: Number of stable states for a range of c_1 and c_2 while $\beta \neq 1$ and α varies: light blue offers bistable configurations; dark blue is monostable.

parameters for calculating the limits of multistable behaviour and provides a conclusive overview of possible behaviour.

Chapter 5

Behaviour Boundaries

5.1 Introduction

In Chapter 4, a theoretical framework for multistable shells was established and closed-form solutions for a limited set of bistable behaviour were obtained. Central to this approach is the strain energy potential, which is algebraic in nature owing to the widespread assumption of uniform curvatures (UC). In this Chapter, we operate upon this polynomial expression by employing tools from Catastrophe Theory (CT), to describe conclusively regions of stability—their extent and their boundaries—in terms of controlling parameters of initial shape, material properties and prestress. Importantly, we do not have to solve explicitly for all possible equilibria, rather only for those that lie at the interface between differently stable regimes. With this strategy we gain an advantage from a synthesis viewpoint as well; we find regions of interest quickly, and then can obtain the requisite material and geometrical parameters.

In the context of this thesis, this Chapter serves two goals: it introduces CT as an alternative theoretical tool for multistable shells; through this new tool, an overview of the behaviour becomes possible. The outline of this Chapter is as follows: Section 5.2 introduces same basic concepts about CT. In Section 5.3, the strain energy potential for multistable shells, from Chapter 4 is simplified, mainly by eliminating redundant parameters. Section 5.4 uses CT to characterise and distinguish regions of consistent multistable behaviour in terms of geometric, material and prestress parameters: we also choose to study the stability of one special critical point of interest, the meeting point of all three stability regions. In Section 5.5 we conclude with a summary.

5.2 Catastrophe Theory

In general, CT allows us to examine how systems respond to small changes in their controlling parameters. To state this more clearly: if we consider a potential $V(x_i, c_a)$,

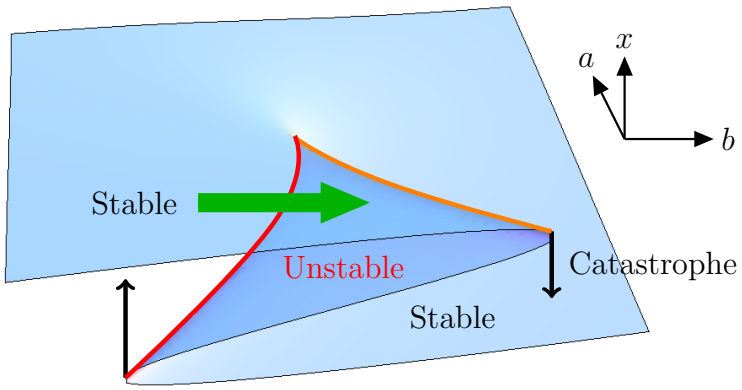

Figure 5.1: For an overarching view, we are inspired by Catastrophe Theory, a mathematical field that examines precisely those points were transitions between regimes happen. In this diagram of the famed cusp catastrophe, the surface plotted describes all stationary points—which satisfy $\partial V/\partial x = 0$, with $V = x^4 + ax^2 + bx$, and a, b as control parameters. However, depending on the region they can either be stable or unstable. Within the cusp region (red and orange boundaries) we have two stable and one unstable solutions, and outside it, only one stable solution. Mathematically those boundaries can easily be identified since at those parameter-locations, the Hessian diminishes.

with n state variables x_i and l control parameters c_a ($1 \leq i \leq n$, $1 \leq a \leq l$), the equilibria, $x_i(c_a)$, can be found by solving:

$$\frac{\partial V(x_i, c_a)}{\partial x_i} = 0 \qquad (i = 1, 2, \ldots, n) \tag{5.1}$$

CT then reveals how the equilibria, or "critical points", $x_i(c_a)$ of $V(x_i; c_a)$, perform as the control parameters, c_a, change. Their stability is assessed using the Hessian matrix of V and, according to Thom's splitting lemma, the interesting behaviour occurs when the Hessian becomes singular (Gilmore, 1993). For the Hessian to be singular it is sufficient for the determinant of the Hessian to be zero, *i.e.*

$$\Big|\mathcal{H}\big(V(x_i, c_a)\big)\Big| = \mathbf{0}, \tag{5.2}$$

where $\mathcal{H}$ is the Hessian operator.

This scenario is called a catastrophe, and original work by Thom (1972) classifies all the possible forms for energy potentials with up to six control variables (Stewart, 1983)—the original list stopped at four—and less than three state parameters. As the name implies, these events can sometimes lead to sudden failures in practice, and CT can help us detect and prevent the generating circumstances. In many other cases, we study the catastrophe event, in order to understand and control a useful transition between stability regimes—as in the multistable shells here, and this might be realised, for example, by embedding

actuators in the structure (Fernandes *et al.*, 2010).

5.2.1 An example from the literature

Before relating the tools of CT with multistable shells, an example from the literature that examines a simpler structure—the bistable Euler arch—is shown. Stewart (1983) presents a straightforward analysis of this, which is repeated here. The structure under consideration is an idealised arch, composed of two equal rigid rods, connected by a springy hinge and constrained to two dimensions. There are two work-producing forces acting on the arch; a vertical force, F_a, at the joint and a compressive force F_b at the base of the arch. θ is the angle of inclination of the rods to the horizontal. The length of the rods is l and the stiffness of the hinge is k, where $k > 0$. The arch is nominally horizontal when no forces act, *i.e.* $F_a = F_b = 0$. The energy of the system is:

$$U_{ab}(x) = 2k\theta^2 + F_a \sin\theta - 2F_b(1 - \cos\theta) \tag{5.3}$$

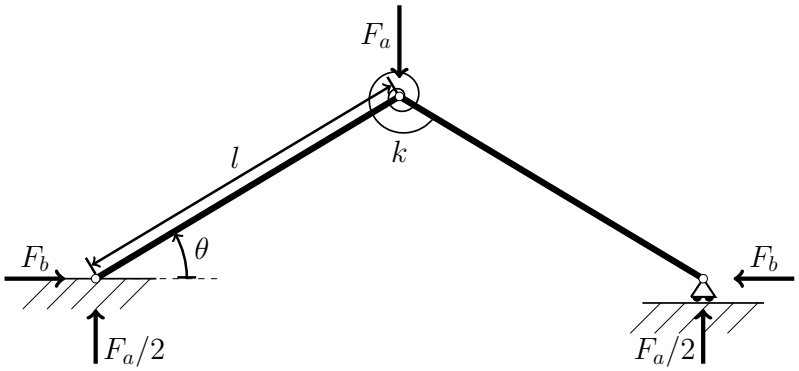

Figure 5.2: A diagram of the idealised Euler arch. Consider two identical, pinned rods, each inclined to the horizontal, connected with a springy joint. A vertical force is applied on the connection and compressive horizontal forces are applied at both ends. Depending on the magnitudes of these forces the structure either has one or three equilibria (in the latter case one equilibrium is unstable). This example is used to introduce the analysis later performed for multistable shells.

The corresponding equilibria for θ can be found by setting the derivative with respect to θ equal to zero:

$$0 = \frac{\partial U_{ab}}{\partial \theta} = 4k\theta + F_a \cos\theta - 2F_b \sin\theta \tag{5.4}$$

This equation is not straightforward to solve, but we can obtain some interesting analytical results by considering the case $F_a = 0$, which returns

$$\sin\theta = \frac{2k}{F_b}\theta. \tag{5.5}$$

This represents the points of intersection of a straight line with the sine curve, for $-\frac{\pi}{2} < \theta < \frac{\pi}{2}$. Hence, either one or three equilibria are available. The change in behaviour occurs at $F_b = 2k$, a point of pitchfork bifurcation when θ is considered with respect to F_b—an explanatory plot is shown in Fig. 5.3. With reference to Eq. (5.5) when $F_b = 2k$, the line θ is tangential to $\sin\theta$.

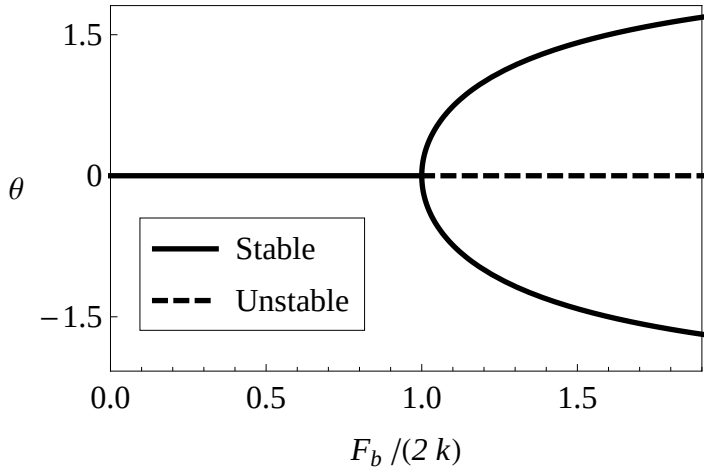

Figure 5.3: The characteristic shape of the pitchfork bifurcation, plotted here as the solutions of Eq. (5.5) for θ with respect to $F_b/(2k)$.

For additional analytical results we can use the Taylor expansion of Eq. (5.3), near the bifurcation point. To simplify calculation the additional parameter $S_b = F_b - 2k$ is defined. Now we can write

$$U_{ab}(\theta) = 2k\theta^2 + F_a\left(\theta - \frac{\theta^3}{6}\right) + 2(2k + S_b)\left(-\frac{\theta^2}{2} + \frac{\theta^4}{24}\right) + O(5), \tag{5.6}$$

where $O(5)$ represents terms of order five and higher with respect to θ. With some simplification we obtain

$$U_{ab}(\theta) = F_a\theta - S_b\theta^2 + \frac{F_a}{6}\theta^3 + \frac{2k + S_b}{12}\theta^4 + O(5), \tag{5.7}$$

and the cubic term can be eliminated by substituting

$$y = \theta - \theta^3/6, \tag{5.8}$$

with the resulting expression:

$$\bar{U}_{ab}(y) = U_{ab}(\theta) = F_a y - S_b y^2 + \left(\frac{k}{6} + \frac{S_b}{4}\right) y^4 + O(5). \tag{5.9}$$

The terms equal and above fifth-order are neglected. The term $y^4 S_b/4$ is also removed, since considering S_b similar to y, this is also a fifth-order term. The final expression is

$$\bar{U}_{ab}(y) = \frac{k}{6} y^4 - S_b y^2 + F_a y. \tag{5.10}$$

Ignoring some scaling in the parameters, Eq. (5.10) is identical to the cusp catastrophe—one of the seven elementary catastrophes identified by Thom (1972)—shown in Fig. 5.1. When such a reduction to a standard form is possible, established knowledge of the corresponding elementary catastrophe provides direct and definite conclusions. Here, we continue to follow Stewart (1983) to establish some practical conclusions from first principles. Eq. (5.10) can be brought to the canonical form of the cusp catastrophe by setting $k = \frac{3}{2}$ and replacing $-S_b$ with $S_b^*/2$. The magnitude of these variables does not change the qualitative behaviour near the catastrophe, instead it shows how the polynomial is in the same form as the standard expression:

$$\frac{y^4}{4} + S_b^* \frac{y^2}{2} + F_a y. \tag{5.11}$$

Applying the conditions from Eqs. (5.1) and (5.2) and eliminating y, the critical boundary—at which the determinant of the Hessian becomes zero—is given by

$$\left(\frac{S_b^*}{3}\right)^3 + \left(\frac{F_a}{2}\right)^2 = 0. \tag{5.12}$$

This is plotted in Fig. 5.4a and shows a characteristic "cusp" shape. In Fig. 5.4b we plot a colourmap based on numerical evaluation of stable equilibria in the same domain. The two procedures provide us with similar information about the limits of bistable behaviour. They differ in that in the first case we have a closed-form description of the limits—potentially useful in other ways—and in that the second method requires significantly more computation. Both differences favour the use of the CT approach.

5.3 Removal of redundant parameters

CT allows us to examine the strain energy potential in view of its global stability characteristics. Beforehand, we simplify Eq. (4.28) by isolating those parameters directly responsible for controlling multistability: any other parameters that do not are given a nominal value, as described in this section. This is not practical from a design perspective when exact parameters are needed, but it is extremely powerful in examining the limits

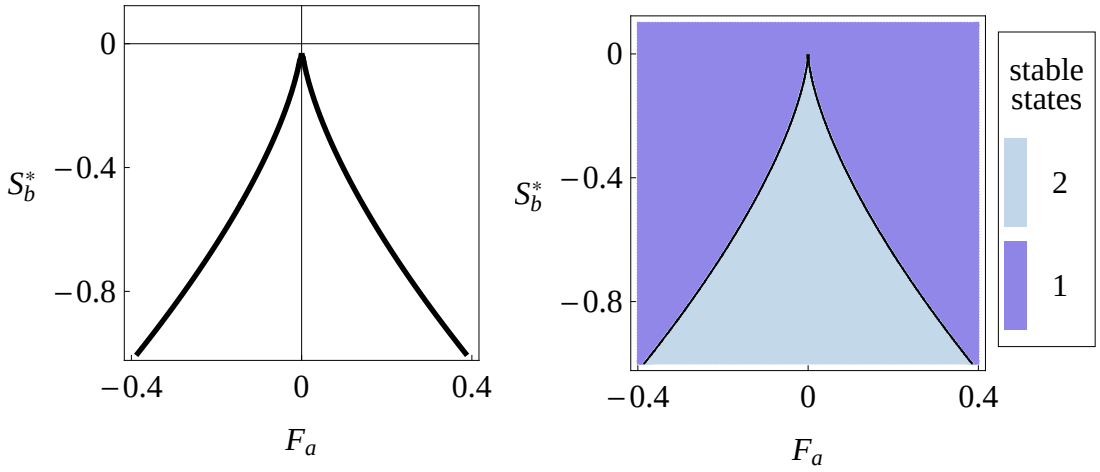

(a) Closed-form critical boundaries

(b) Numerical solution

Figure 5.4: The plot on the left represents Eq. (5.12), which in turn is the product of simple algebraic manipulation of a polynomial energy expression. It shows the critical boundaries where stable equilibria are added or removed from the system's response. The colourmap on the right was drawn by numerically checking the included domain according to Eqs. (5.1) and (5.2). The first method can relate the essential behavioural characteristics without the computational requirements of the second method. In fact, when the potential relates to a canonical catastrophe, the stability characteristics can be found in the literature. For cases beyond these, and when empirical information is not available, computationally checking a single point in each region is sufficient to provide the behaviour of each region.

of the behaviour and understanding the influence of each variable.

First, we prove β to be a scaling parameter with respect to the overall energy. We transform the dimensionless curvatures by setting $\bar{\kappa}_x = \hat{\kappa}_x\sqrt{\beta}$, with similar transformations for the terms with "F" and "0" subscripts: none is needed for y-direction terms. For the terms associated with twisting, we substitute $\bar{\kappa}_{xy} = \hat{\kappa}_{xy}\sqrt[4]{\beta}$, to help establish β as a scaling parameter of the expression:

$$\begin{aligned}\tilde{U} = \frac{\phi}{2}\sqrt{\beta}\big(\hat{\kappa}_x\hat{\kappa}_y - \hat{\kappa}_{xy}^2 - \hat{\kappa}_{x0}\hat{\kappa}_{y0} + \hat{\kappa}_{xy0}^2\big)^2 + \frac{1}{2}\big[\beta(\hat{\kappa}_x - \hat{\kappa}_{x0} - \hat{\kappa}_{xF})^2 \\ + 2\nu\sqrt{\beta}(\hat{\kappa}_x - \hat{\kappa}_{x0} - \hat{\kappa}_{xF})(\hat{\kappa}_y - \hat{\kappa}_{y0} - \hat{\kappa}_{yF}) + \beta(\hat{\kappa}_y - \hat{\kappa}_{y0} - \hat{\kappa}_{yF})^2 + \\ + 4\alpha\sqrt{\beta}(\hat{\kappa}_{xy} - \hat{\kappa}_{xy0} - \hat{\kappa}_{xyF})^2\big], \quad (5.13)\end{aligned}$$

giving a scaled expression of the energy, $\hat{U} = \tilde{U}/\beta$,

$$\hat{U} = \frac{\phi}{2\sqrt{\beta}}\big(\hat{\kappa}_x\hat{\kappa}_y - \hat{\kappa}_{xy}^2 - \hat{\kappa}_{x0}\hat{\kappa}_{y0} + \hat{\kappa}_{xy0}^2\big)^2 + \frac{1}{2}\big[(\hat{\kappa}_x - \hat{\kappa}_{x0} - \hat{\kappa}_{xF})^2 + \frac{2\nu}{\sqrt{\beta}}(\hat{\kappa}_x - \hat{\kappa}_{x0} - \hat{\kappa}_{xF})(\hat{\kappa}_y - \hat{\kappa}_{y0} - \hat{\kappa}_{yF}) + (\hat{\kappa}_y - \hat{\kappa}_{y0} - \hat{\kappa}_{yF})^2 + \frac{4\alpha}{\sqrt{\beta}}(\hat{\kappa}_{xy} - \hat{\kappa}_{xy0} - \hat{\kappa}_{xyF})^2\big]. \quad (5.14)$$

β can be removed by introducing new variables, equivalent to the pre-factors on each of the above terms, namely: $\bar{\alpha} = 4\alpha\sqrt{\beta}, \bar{\nu} = \nu\sqrt{\beta}, \bar{\phi} = \phi\sqrt{\beta}$:

$$\hat{U} = \frac{\bar{\phi}}{2}\big(\hat{\kappa}_x\hat{\kappa}_y - \hat{\kappa}_{xy}^2 - \hat{\kappa}_{x0}\hat{\kappa}_{y0} + \hat{\kappa}_{xy0}^2\big)^2 + \frac{1}{2}\big[(\hat{\kappa}_x - \hat{\kappa}_{x0} - \hat{\kappa}_{xF})^2 + 2\bar{\nu}(\hat{\kappa}_x - \hat{\kappa}_{x0} - \hat{\kappa}_{xF})(\hat{\kappa}_y - \hat{\kappa}_{y0} - \hat{\kappa}_{yF}) + (\hat{\kappa}_y - \hat{\kappa}_{y0} - \hat{\kappa}_{yF})^2 + \bar{\alpha}(\hat{\kappa}_{xy} - \hat{\kappa}_{xy0} - \hat{\kappa}_{xyF})^2\big], \quad (5.15)$$

and β is simply a linear scaling factor for the strain energy, which can be set to unity without changing the stability properties of the shell. Similarly for $\bar{\phi}$, we apply an isotropic transformation such that $\hat{\kappa} = \tilde{\kappa}/\sqrt{\bar{\phi}}$ (applied to the κ_x, κ_y and κ_{xy} terms), and we re-cast the strain energy by defining:

$$\tilde{U} = \bar{\phi}\hat{U}. \quad (5.16)$$

As a result, $\bar{\phi}$ emerges as another linear scaling factor, which is also set equal to unity, for convenience. In addition, we can combine the initial curvatures and prestress into three new control parameters by setting:

$$h_x = \hat{\kappa}_{x0} + \hat{\kappa}_{xF}, \qquad h_y = \hat{\kappa}_{y0} + \hat{\kappa}_{yF}, \qquad g_0 = \hat{\kappa}_{x0}\hat{\kappa}_{y0}. \quad (5.17)$$

Control parameters related to twist are set equal to zero for simplicity, although we note their relevance to multistability as shown in Section 4.5. The twisting curvature must be retained as a state variable for propriety in assessing stability. Substituting the new variables, we obtain the required form of strain energy potential as:

$$\tilde{U} = \frac{1}{2}\big(\tilde{\kappa}_x\tilde{\kappa}_y - \tilde{\kappa}_{xy}^2 - g_0\big)^2 + \frac{1}{2}\big[(\tilde{\kappa}_x - h_x)^2 + 2\bar{\nu}(\tilde{\kappa}_x - h_x)(\tilde{\kappa}_y - h_y) + (\tilde{\kappa}_y - h_y)^2 + \bar{\alpha}\tilde{\kappa}_{xy}^2\big]. \quad (5.18)$$

We now have an equivalent system whose control parameters are g_0, h_x, h_y, $\bar{\alpha}$ and $\bar{\nu}$.

5.4 Analysis of different parameter regions

In this section we apply the tools from Section 5.2 to extract information from the simplified expression in Section 5.3. The focus is on obtaining closed-form solutions and, to that end, additional simplifications are made and presented below. Algebraically, our task is made easier if we express the curvatures in a new coordinate system (κ_m, κ_d, κ_{md}), such that $\tilde{\kappa}_x = \kappa_m + \kappa_d$, $\tilde{\kappa}_y = \kappa_m - \kappa_d$ and $\tilde{\kappa}_{xy} = \kappa_{md}$: similarly, we set $h_x = h_m + h_d$, $h_y = h_m - h_d$. Thus the system becomes symmetric about our reference axes, rather than antisymmetric, and we have a new expression for the dimensionless energy after updating Eq. (5.18):

$$U_{md} = \frac{1}{2}\Big[(\kappa_m + \kappa_d - h_m - h_d)^2 + (\kappa_m - \kappa_d - h_m + h_d)^2 \\ + 2\bar{\nu}(\kappa_m + \kappa_d - h_m - h_d)(\kappa_m - \kappa_d - h_m + h_d) + \left(g_0 + \kappa_d^2 - \kappa_m^2 + \kappa_{md}^2\right)^2 + \bar{\alpha}\kappa_{md}^2\Big]. \tag{5.19}$$

The equilibria equations corresponding to these updated state variables can be verified as:

$$-2\left[\kappa_m\left(-1 + g_0 + \kappa_d^2 - \kappa_m^2 - \bar{\nu}\right) + h_m(1 + \bar{\nu})\right] = 0, \tag{5.20a}$$

$$2\left[\kappa_d\left(1 + g_0 + \kappa_d^2 - \kappa_m^2 - \bar{\nu}\right) + h_d(-1 + \bar{\nu})\right] = 0, \tag{5.20b}$$

$$\kappa_{md}\left(\bar{\alpha} + 2g_0 + 2\kappa_d^2 - 2\kappa_m^2 + 2\kappa_{md}^2\right) = 0. \tag{5.20c}$$

Considerable simplification is achieved by considering only untwisted solutions, *i.e.* setting $\kappa_{md} = 0$ in Eq. (5.20c). This narrows the scope of this work considerably but allows for much more powerful results within the context of untwisted equilibria. Some numerical work on the nature of twisted solutions can be found in Section 4.5, and it involves twisting prestress. Fernandes *et al.* (2010) presented an algebraic analysis of the stability of twisted equilibria and we refer the reader to that work for closed-form expressions. After eliminating κ_{md}, the remaining three equations—Eqs. (5.2), (5.20a) and (5.20b)—contain six unknowns in κ_m, κ_d, h_m, h_d, g_0 and $\bar{\nu}$.

We choose to specify $\bar{\nu}$, the Poisson's ratio term, and g_0, the initial dimensionless Gaussian curvature, because we are interested specifically in the effects of prestress: this reduces the number of unknowns to three, thereby enabling unique solutions for the remaining parameters, when we also consider Eq. (5.2). Their final expressions are obtained using the symbolic solver in Mathematica (Wolfram Research Inc., 2008). We give compact expressions for h_d and h_m below with κ_d still incorporated—κ_m is also found in terms

of κ_d. In total, there are four solutions, depending on the choice of sign within "±", and they define the relationships between parameters on the critical boundaries:

$$h_m = \pm \frac{\sqrt{-3f + 9\kappa_d^2 + 6g_0 - 6\bar{\nu} + 3}\,(f + g_0 - \bar{\nu} - 4)}{9(\bar{\nu} + 1)}, \tag{5.21a}$$

$$h_d = -\frac{\kappa_d\,(f + g_0 - \bar{\nu} + 2)}{3(\bar{\nu} - 1)}, \tag{5.21b}$$

$$\kappa_m = \mp \frac{\sqrt{1 + 2g_0 + 3\kappa_d^2 - 2\bar{\nu} - f}}{\sqrt{3}}, \tag{5.21c}$$

and

$$h_m = \pm \frac{\sqrt{f + 3\kappa_d^2 + 2g_0 - 2\bar{\nu} + 1}\,(f - g_0 + \bar{\nu} + 4)}{3\sqrt{3}(\bar{\nu} + 1)}, \tag{5.22a}$$

$$h_d = \frac{\kappa_d\,(f - g_0 + \bar{\nu} - 2)}{3(\bar{\nu} - 1)}, \tag{5.22b}$$

$$\kappa_m = \pm \frac{\sqrt{1 + 2g_0 + 3\kappa_d^2 - 2\bar{\nu} + f}}{\sqrt{3}}, \tag{5.22c}$$

where

$$f = \sqrt{12\kappa_d^2 + (g_0 - \bar{\nu} + 2)^2}, \tag{5.23}$$

in all of the above equations.

After substituting a numerical range for κ_d, we can plot these expressions on the (h_x, h_y) plane for specified values of $\bar{\nu}$ and g_0, which returns the critical boundaries as certain curves. By repeating this process for a range of g_0 values, for the same value of $\bar{\nu}$, successive (h_x, h_y) planes can be assembled in the direction of g_0, to render the critical boundaries as *surfaces* in Cartesian space of axes (h_m, h_d). One set of surfaces is given in Fig. 5.5 and the volumetric space between surfaces corresponds to the values of prestress and initial shape needed to yield equilibria of the same stability properties.

The influence of the Poisson ratio is shown in Fig. 5.6, where we repeat the same surfaces, but for $\bar{\nu} = 0.6$ and $\bar{\nu} = 0.9$. In general, higher values of the Poisson ratio seem to facilitate multistability, since the volume of the bistable and tristable regions in the plot, clearly increases.

We confirm the degree of stability by plotting some of the original horizontal slices in Fig. 5.7. They clearly show the boundary curves and the junction, or "critical", points at which they intersect, and how they evolve with g_0. By considering the topological features of the boundary curves in the vicinity of the critical points, we can pronounce directly upon the degree of stability around them using Thom's classification (Thom, 1972). In

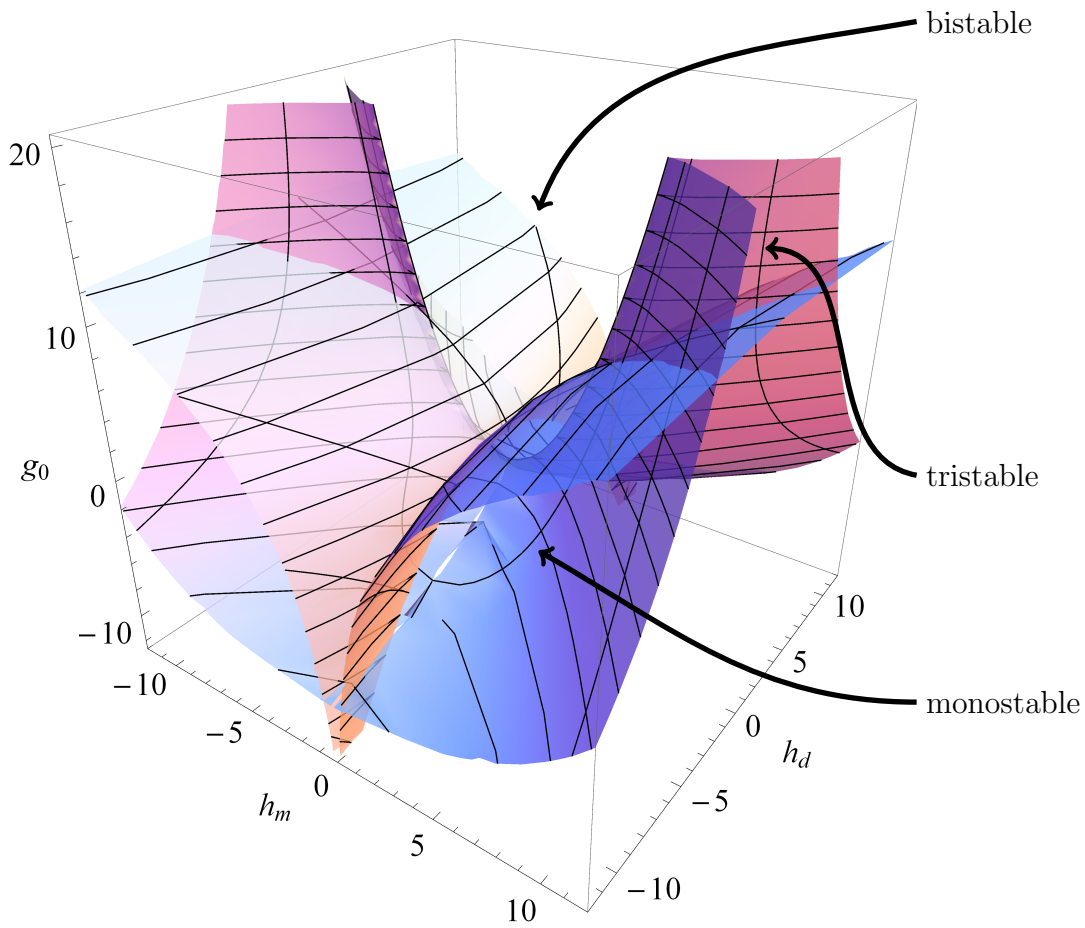

Figure 5.5: Surfaces of the critical boundaries after solving the system of Eq. (5.1) and 5.2 with the specified range $-10 < \kappa_d < 10$ and $\bar{\nu} = 0.3$—in this scenario, $\bar{\nu}$ is equal to the Poisson ratio since $\beta = 1$. Each surface divides the parameter space into multistable and monostable regions. The volume above the top set of surfaces and below the bottom set of surfaces is bistable: the volume where the two bistable regions overlap, describes a tristable region, and this feature is prominent at the four sides of the diagram. The remaining space between the surfaces shows monostable regions. The h_m- and h_d-axes represent ranges in prestressing while the vertical axis relates to the initial Gaussian curvature.

particular, the pitchfork bifurcation, which manifests as a fold catastrophe, marks the transition from monostable to bistable regions along the $h_m = 0$ and $h_d = 0$ lines. In Fig. 5.7 we see, for different values of the initial Gaussian curvature, the outline of all curves indicating loss of equilibria or stability on the (h_m,h_d) plane.

As Fig. 5.5 reveals, there are only four critical points that allow passage from monostable to tristable regions and their location is of interest. Based on previous knowledge (Seffen & Guest, 2011) and on the symmetry in the energy expression above, we know that moving along $h_y = \pm h_x$, or equivalently, by setting $h_d = 0$ and $h_m = 0$, we can locate those points. We solve Eq. (5.1) and 5.2 again but including these constraints, and the resulting solutions for κ_d are found to be, first, for $h_m = 0$ and $h_d < 0$:

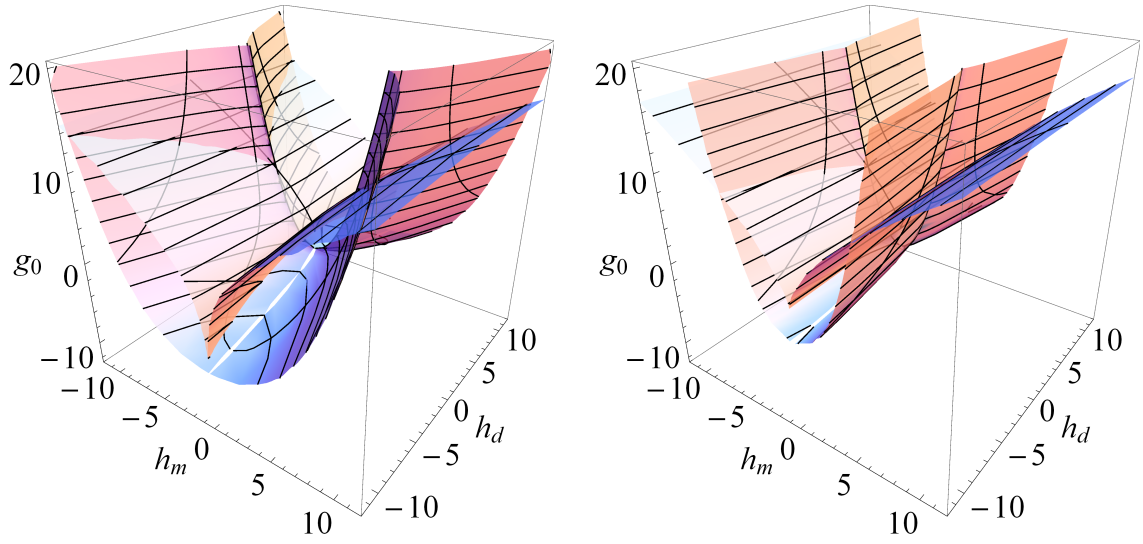

(a) $\bar{\nu} = 0.6$ (b) $\bar{\nu} = 0.9$

Figure 5.6: The influence of the Poisson ratio, through the $\bar{\nu}$ parameter, becomes obvious in these two figures. They are identical to Fig. 5.5, except for the variation of $\bar{\nu}$. We can see the monostable region diminishing with increasing values of the Poisson ratio.

$$\kappa_d = \frac{\sqrt{\bar{\nu} - 1 - g_0}}{\sqrt{3}}, \quad \text{or} \quad \kappa_d = -\sqrt{\bar{\nu} + 1 - g_0}, \quad \text{and} \quad \kappa_m = 0, \tag{5.24}$$

and for $h_d < 0$;

$$\kappa_d = -\frac{\sqrt{\bar{\nu} - 1 - g_0}}{\sqrt{3}}, \quad \text{or} \quad \kappa_d = \sqrt{\bar{\nu} + 1 - g_0}, \quad \text{and} \quad \kappa_m = 0. \tag{5.25}$$

For $h_d = 0$, we have for $h_m < 0$:

$$\kappa_m = \frac{2\sqrt{g_0 + 1 - \bar{\nu}}}{\sqrt{\bar{\nu} + 1}}, \quad \text{or} \quad \kappa_m = \sqrt{\bar{\nu} + 1 - g_0}, \quad \text{and} \quad \kappa_d = 0, \tag{5.26}$$

and for $h_m > 0$;

$$\kappa_m = -\frac{2\sqrt{g_0 + 1 - \bar{\nu}}}{\sqrt{\bar{\nu} + 1}}, \quad \text{or} \quad \kappa_m = -\sqrt{\bar{\nu} + 1 - g_0}, \quad \text{and} \quad \kappa_d = 0. \tag{5.27}$$

These describe the shapes of equilibria when $h_x = \pm h_y$, and the conditions for g_0 and $\bar{\nu}$ can be obtained from substituting the above back into Eq. (5.21) and Eq. (5.22) to reveal:

$$g_0 = \bar{\nu} + 7, \qquad g_0 = \bar{\nu} - 2, \tag{5.28}$$

when $h_d = 0$. The solution $\bar{\nu} - 2$ can be dismissed since it produces imaginary curvatures. When $h_m = 0$, we obtain

$$g_0 = \bar{\nu} - 7. \tag{5.29}$$

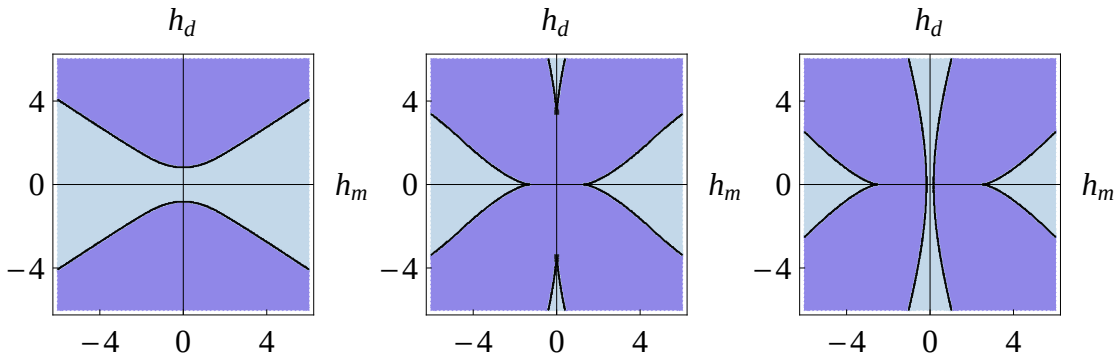

(a) $g_0 < \bar{\nu} - 1$ (b) $\bar{\nu} - 1 < g_0 < \bar{\nu} + 1$ (c) $g_0 > \bar{\nu} + 1$

Figure 5.7: Colourmaps showing the number of stable states across the (h_m,h_d) plane by taking slices through the previous figure. Darker blue shows monostable regions while lighter shows bistable regions, and the boundaries between them represent catastrophes, since the determinant of the Hessian diminishes at those locations. Again, $\bar{\nu} = 0.3$ to match the parameters in Fig. 5.5. The initial Gaussian curvature has a significant effect on the stability of feasible solutions. For low, negative values of g_0, bistability is mostly observed near $h_d = 0$. As we increase g_0, bistable behaviour diminishes along that line and increases along $h_m = 0$.

Correspondingly, each of the four cusp critical points are identified in terms of $\bar{\nu}$, by substituting in Eqs. (5.21) and (5.22), as

$$(h_m, h_d, g_0) = \left(\pm\frac{4\sqrt{2}}{\bar{\nu}+1}, 0, (\bar{\nu}+7) \right), \left(0, \pm\frac{4\sqrt{2}}{\bar{\nu}-1}, (\bar{\nu}-7) \right). \tag{5.30}$$

These points are significant in various ways, but most prominently because they show parameter values where all three possible stability regions meet. They also indicate bounding values of the parameters that allow tristability. We mark one such point in Fig. 5.8.

5.4.1 Stability near the cusp catastrophe

Although used here as inspiration for a specialised engineering enquiry, CT usually deals with investigating the stability characteristics of potential functions when the derivatives of the expression diminish for arbitrary degrees of differentiation. In the context of this work, such an investigation, albeit specialised, can be useful in understanding actuation between shells of different stability properties. In practical terms, if we want to have a morphing shell that can act as both a monostable, and a multistable structure, we would need to manipulate our parameters and pass through a critical point in the parameter space. The behaviour at that specific point can be of interest.

To pursue this question, we return to the strain energy expression, Eq. (5.18), with which we can study the stability of the shell at the vicinity of the cusp catastrophe. We previously explained how Eq. (4.35a) is used to establish stability of equilibria. This is

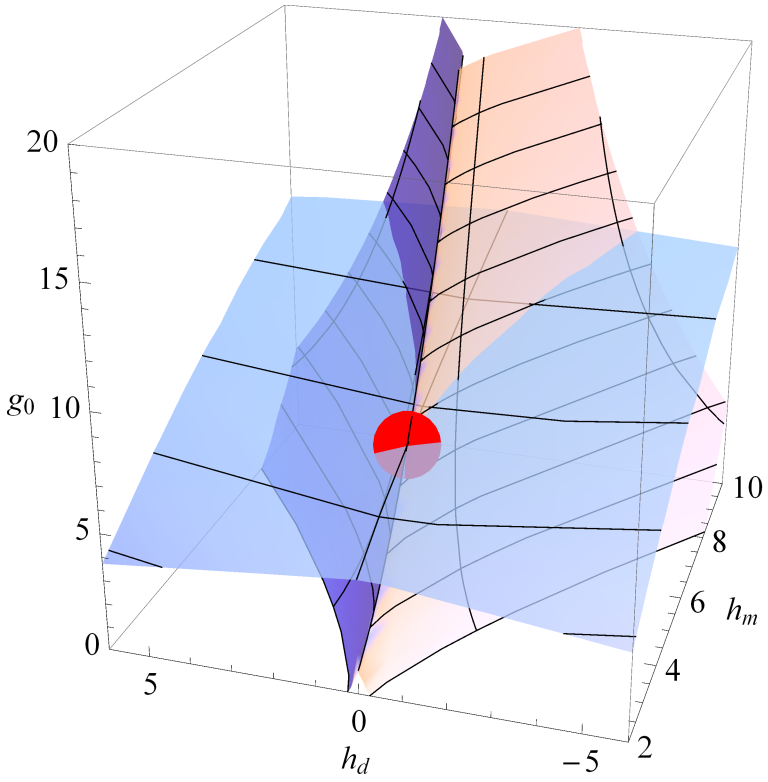

Figure 5.8: There are four distinct parameter-space points that allow a transition from the monostable to the tristable region—normally the bistable region is a necessary intermediate. The locations of these points can found algebraically and here we focus on one (red dot) by zooming into Fig. 5.5. These points represent limits in parameters that admit tristability but are also useful in considering shells of controlled multistability, *i.e.* structures that can exist in multiple stability regions.

straightforward for non-critical points. However, at critical points, where the determinant of the stability matrix is zero by definition, further calculation is needed. We offer an example by studying the stability of a solution at one of the cusp catastrophe points we have calculated above.

Solving for the curvatures, we get $(\kappa_m^*, \kappa_d^*) = (2\sqrt{2}, 0), (-\sqrt{2}, 0)$, and these identify those values of state variables around which we expand the strain energy expression. This is achieved by specifying sliding coordinates δ_m and δ_d, with $\kappa_m = \kappa_m^* + \delta_m\epsilon$ and $\kappa_d = \kappa_d^* + \delta_d\epsilon$, *i.e.* the coordinate system origin is translated to the location of the catastrophe. The final form of energy is given by:

$$U_s = \text{constant} + \Big[2h_d\delta_d(\bar{\nu}-1) + 2\delta_m\big(-\bar{\nu}h_m - h_m + 4\sqrt{2}\big)\Big]\epsilon + 18\delta_m^2\epsilon^2 + 4\sqrt{2}\delta_m\big(\delta_m^2 - \delta_d^2\big)\epsilon^3 + \frac{1}{2}\big(\delta_d^2 - \delta_m^2\big)^2\epsilon^4 + O(7). \quad (5.31)$$

The constant and first order terms can be ignored since they do not affect stability. The coefficient of the second order of the expansion is $18\delta_m^2$, which shows that we have stability in the m-direction, but the stability in the d-direction is undetermined, as shown

graphically in Fig. 5.9a. Thus, to investigate this further the coefficient of the third-order are needed. They are equal to $4\sqrt{2}\delta_m\left(\delta_m^2-\delta_d^2\right)^2$ and are plotted in Fig. 5.9b, which shows a saddle geometry and signifies instability. Loss of stability at cusp critical points is typical as noted by Thompson & Hunt (1984). Thus in practical terms, this brief examination shows, the structure would not be stable at this critical point.

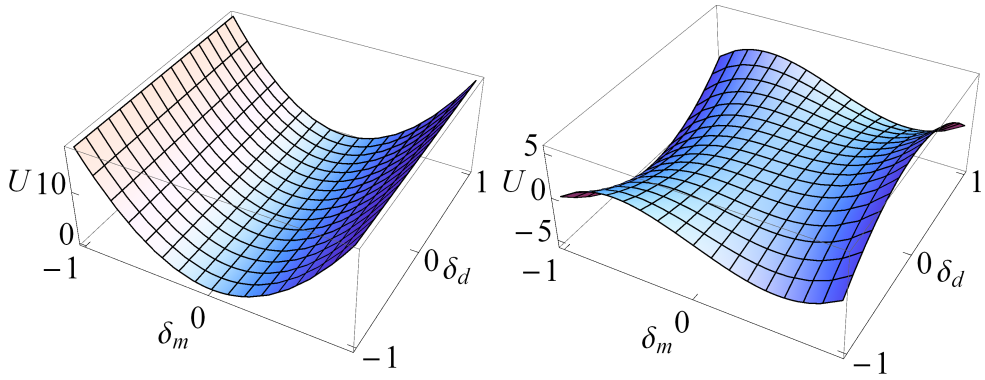

(a) Second order coefficient (b) Third order coefficient

Figure 5.9: We find the Taylor expansion of the energy expression near the critical point that separates the monostable and tristable regions along $h_d = 0$. The coefficients of the second and third orders of the expansion are in terms of δ_d and δ_m and are plotted here.

5.5 Concluding remarks

This Chapter has presented the landscape of possible stable geometries for uniformly curved shells. We have shown conclusively that where twist is ignored, the maximum number of stable states is three, and we have determined the conditions responsible for the transition between regions of multistability in terms of material parameters, prestress and initial shape. Specifically, we note that double initial curvature is always a prerequisite for tristability and that a minimum threshold exists for the Poisson ratio—given the remain parameters, below which tristability cannot be observed.

The existence of a tristable shell was predicted by Vidoli & Maurini (2008) briefly before the commencement of this work. This Chapter provided additional theoretical support for this and established tristability as the limit of multistable behaviour for initially uniformly curved shells. However, such a shell has not been observed in nature or in an experiment. The construction of such a shell is the topic of the next Chapter.

Chapter 6

A Novel Tristable Shell

6.1 Introduction

The establishment of an upper bound for multistability of elementary morphing shells in Chapter 5 as well as the explicit prediction of a tristable shell by Vidoli & Maurini (2008) motivate the construction of such a structure. Despite its apparent simplicity, an initially uniformly-curved, tristable shell has never been constructed or observed in Nature to the extent of our knowledge. This Chapter presents both the design originating from our model and the construction method for such a shell. Initial attempts are made with a layup of unidirectional fibre reinforced material—which allow some control over material constitutive behaviour—and a single ply of a woven composite. The former does not offer a robust result but is included because it contributed greatly to our understanding of design requirements. The woven composite shell is a reliable design.

6.2 Optimal geometry

In Chapter 5 we draw some global conclusions for elementary multistable shells: most notably, we show that there is a limit to multistable behaviour, and that the limits to this behaviour, observable as phase boundaries in the stability landscape, are controlled through a subset of relevant parameters. For a specific example, the modular ratio β, was shown to be a mere scaling parameter with respect to these phase diagrams. However, in quantitative design, these parameters are immediately relevant, along with the practical complexity that they carry.

One of the most practical conclusions from Chapter 5 was that we cannot have tristability without the shell having initial Gaussian curvature. This precludes the use of initially flat sheets, even if we are capable of imposing free curvatures via prestressing of fibres or any other means—those referred to by the subscript "F" in Chapters 3 and 4. At the same time, this simplifies our design strategy in the following sense: it precludes the

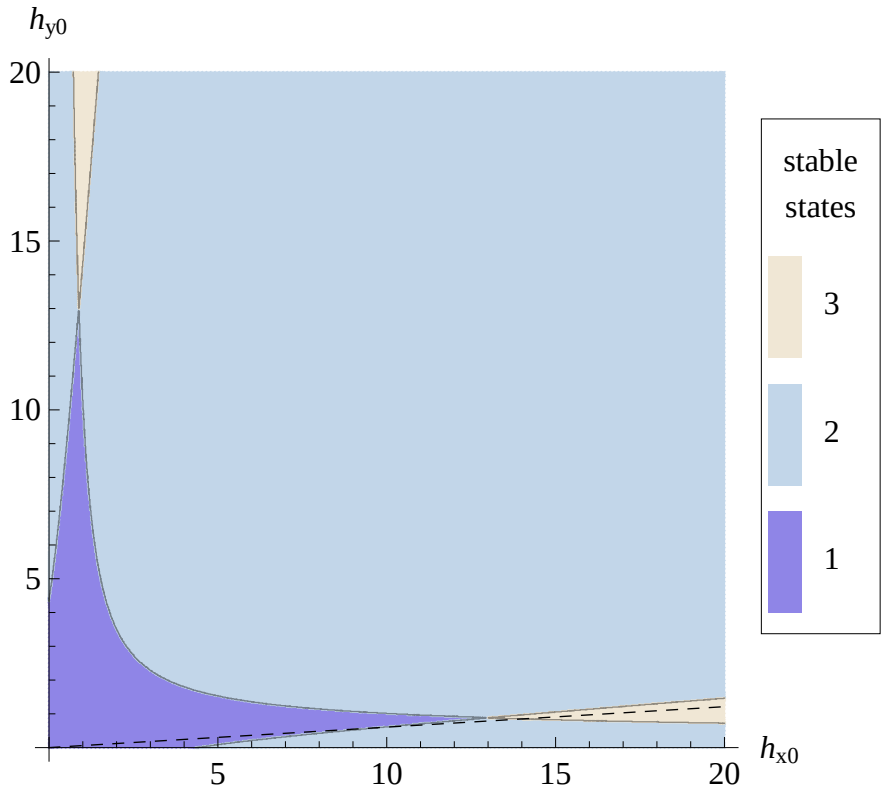

Figure 6.1: A colourmap of stability regimes with respect to the initial principal curvatures, h_{x0} and h_{y0}, for circular, orthotropic shells. The strain energy expression used here was rendered dimensionless after multiplying with an appropriate dimensional parameter, given in Chapter 4. A variation of this plot was originally presented by Vidoli & Maurini (2008) as the first evidence of tristability, but it is based on the model by Seffen (2007), also used here to produce a viable design. For this plot the Poisson ratio is fixed at 0.7 while the shear stiffness is four times the isotropic value. The modular ratio is fixed at unit value. Toward the origin of the plot, the behaviour is mostly monostable, while bistability dominates the remaining geometry space for these material parameters. A narrow band of tristable behaviour appears for a very specific ratio between the two curvatures. Approximate line fitting between the origin and the tristability boundary—which appears as a dashed line—gives a ratio of 1:16.5 between the two dimensionless curvatures.

use of free curvatures in our design, and leaves only the initial real curvatures to optimise.

Specifically, for tristability to happen, we need to target a very narrow region in material and geometrical property-space. Vidoli & Maurini (2008) displayed this in dimensionless phase diagrams. Even under the many simplifying assumptions made there, these regions are very constricting. Hence, in addition to whatever other practical considerations, the selection for a target point in parameter space must also be optimised. With respect to the initial dimensionless curvatures for an untwisted shell, the relevant plot is shown in Fig. 6.1, and is created in a similar manner to the figures in Section 4.6: points from the displayed domain are individually substituted in the strain energy expression and the corresponding equilibria solved for numerically, while the resulting solutions are substituted in the Hessian to assess stability.

The two tristability regions shown for positive initial curvatures—at the top left and bottom right corners of Fig. 6.1—are symmetric with respect to the principal directions, hence, there is no loss of generality in focusing on one of them. To optimise our design, we try to target the geometrical centre of the bottom right region. Since the area conveniently resembles a triangle, we find the line bisecting the acute angle. This roughly gives a ratio of 1:16.5 between the two initial curvatures. This slope characterises the line connecting the vertex and the origin. The triangular, tristable region seems to continue with a wider base for higher values of initial curvature. Hence, designs with higher curvatures are desirable. However, if we assign dimensions to our planform, such high curvatures quickly become irrelevant to the shallow shell assumption or even impossible on doubly-curved shells; the radius of curvature in each direction has a trivial lower bound equal to the elliptical planform's major-axis length in that direction—at those values the shell begins wrapping around itself. Even ignoring the shallow shell assumption, for the geometry to be consistent the surface would resemble a closed shell. Such structures are significantly different than the open shells we are examining.

A related challenge is to mathematically describe a mould that does not violate the Uniform Curvature (UC) assumption—or at least minimises the discrepancy. Our formulation uses the elliptic paraboloid description for the out-of-plane, initial shape of the shell. This description is convenient for algebraic manipulation and complies with the UC assumption for shallow shells. For deeper shells however, the difference between the local Gaussian Curvature (GC) and the assumed UC can become significant. In Fig. 6.2 we overlay a paraboloid surface on a sphere to show that, even though, for shallow shells the discrepancy is minimal, it can quickly become critical as the shell diameter increases. Hence, we consider alternative geometries as the basis of our tristable shell design. We use the intrinsic expression for the GC as our metric. This is defined in $\mathbb{R}^n$ as the ratio of the second, (II), and the first, (I), fundamental forms—mathematical objects that help describe surface properties, given in Pressley (2010):

$$\mathrm{GC} = \frac{\det(II)}{\det(I)}. \tag{6.1}$$

For a surface in $\mathbb{R}^3$, given by $z = f(x, y)$ in Cartesian (x, y, z) space, this reduces to:

$$\mathrm{GC} = \frac{\dfrac{\partial^2 f}{\partial x^2}\dfrac{\partial^2 f}{\partial y^2} - \left(\dfrac{\partial f}{\partial x \partial y}\right)^2}{1 + \left(\dfrac{\partial f}{\partial x}\right)^2 + \left(\dfrac{\partial f}{\partial y}\right)^2}. \tag{6.2}$$

Notice that the numerator above is equal to $\kappa_x \kappa_y - \kappa_{xy}^2$, while the denominator accounts for the area change over which the solid angle is calculated.

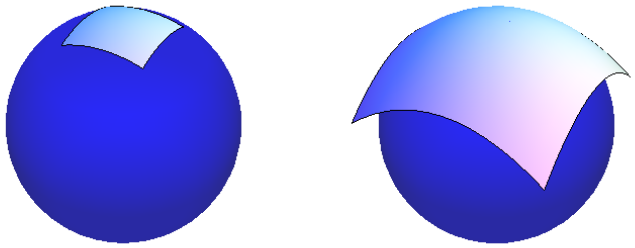

Figure 6.2: Our formulation assumes a paraboloid geometry for multistable shells, an algebraically convenient description that does not deviate from the UC assumption for shallow shells. However, for deeper shells—*i.e.* with a higher ratio of radius of curvature, ρ, to planform radius, a—the edges of the shell are significantly distant from ideal geometry. This is shown here by contrasting the paraboloid geometry to a sphere of the same radius of curvature. The two paraboloid surfaces only differ in the size of the planform radius, while the radius of curvature is the same for both surfaces and the sphere. This observation led us to seek alternative geometries for our mould designs.

The doubly curved surfaces that we compare the paraboloid to are the swept arc—common in CAD software—and the torus: the essential difference is that one is generated from a line and the other is a portion of a closed surface, and they are both shown in Fig. 6.3.

The Cartesian description for the paraboloid was defined in Section 4.3:

$$f_{\text{paraboloid}} = -\left(\frac{x^2}{2\rho_x} + \frac{y^2}{2\rho_y}\right). \tag{6.3}$$

For the swept arc, we being by considering a circular arc in the x-z plane, with radius ρ_x. If the apex of this arc is tangent to the x-y plane, the Cartesian expression for the arc is:

$$-\left(\rho_x - \sqrt{\rho_x^2 - x^2}\right). \tag{6.4}$$

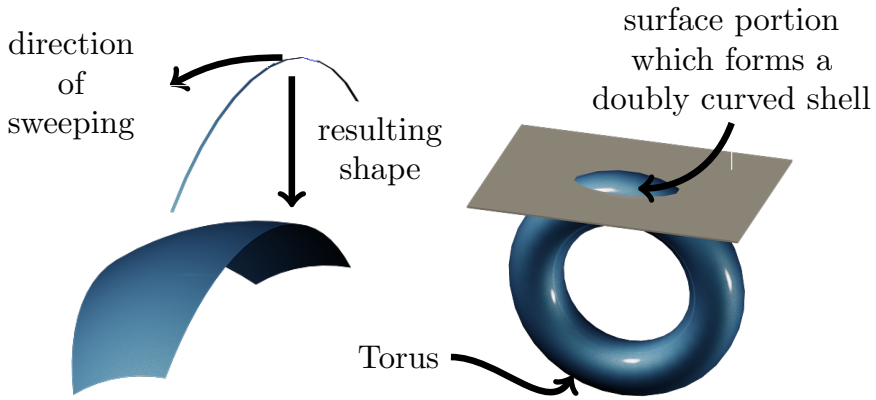

Figure 6.3: The paraboloid geometry can differ significantly from the UC assumption for deep shells. We consider the alternative geometries defined by a swept arc (left) and the surface of a torus (right). The former is plotted by rotating an arc about a central point, while the latter by rotating the centre of a circle about a central point. These diagrams help portray the subtle differences. The swept arc ensures a UC in one direction (of the original arc), while the torus surface curvatures vary in both directions. The corresponding Cartesian equations are given in Eqs. (6.3), (6.6) and (6.12).

If we then rotate this arc about a point at a distance ρ_y under the origin, and about the x-axis, each point in the original arc traces a new arc in the y-z plane. Each of those arcs is described by

$$-(\rho_y - \sqrt{\rho_y^2 - y^2} - z_0), \tag{6.5}$$

where z_0 is the z-coordinate of the corresponding point in the original arc. If we substitute z_0 from Eq. (6.4), we get the expression for the swept surface:

$$f_{\text{swept}} = -(\rho_x + \rho_y - \sqrt{\rho_x^2 - x^2} - \sqrt{\rho_y^2 - y^2}). \tag{6.6}$$

In order to derive the corresponding Cartesian expression for the torus, we consider a circle of radius r_1 on the y-z plane with its centre at point $(0, r_2)$. The Cartesian equation for this circle is:

$$(z + r_2)^2 + y^2 = r_1^2. \tag{6.7}$$

The coordinate z can be expressed in terms of y as

$$z_c = \sqrt{r_1^2 - y^2} - r_2. \tag{6.8}$$

We can obtain a torus by rotating this circle about the y-axis. The equation for the bigger circle is

$$z^2 + x^2 = z_c^2. \tag{6.9}$$

Then, z, can be found to be:

$$z = \sqrt{(\sqrt{r_1 - y^2} - r_2)^2 - x^2}. \tag{6.10}$$

The torus is translated along z, such that the top of the external surface is tangent to the x-y plane for consistency with the other geometries, which gives:

$$z = \sqrt{(\sqrt{r_1 - y^2} - r_2)^2 - x^2} - (r_1 + r_2). \tag{6.11}$$

The internal radius of the torus, r_1, is equal to the curvature of the surface in the y-direction, ρ_y. The second principal radius of curvature is approximately taken to be equal to the difference between r_2 and r_1 at the outer rim of the torus. Substituting r_1 and r_2 in terms of ρ_x and ρ_y finally gives:

$$f_{\text{torus}} = \sqrt{\left(\sqrt{\rho_y^2 - y^2} + \rho_x - \rho_y\right)^2 - x^2} - \rho_x. \tag{6.12}$$

The expression for the GC, and all three geometrical descriptions assume that there is no surface twist. The percentage deviation from UC can be defined as

$$\frac{|\text{GC} - (\rho_x \rho_y)^{-1}|}{(\rho_x \rho_y)^{-1}} 100\%. \tag{6.13}$$

and is plotted across the planform of a candidate design. Figure 6.4 compares this deviation for a square planform of side dimension 120, corresponding to the radius of a mould presented later in this Chapter. Even though at the centre of the planform, all the geometries trivially conform to the UC assumption, toward the edges, the deviation grows. For the specific example, it is clear that the torus minimises the discrepancy. At the centre of the side of maximum x-axis values, the percentage deviations are 19.9%, 6.1% and 0.0% for the paraboloid, the swept arc and the torus respectively. It is thus *preferable to use the torus geometry* where possible.

6.3 Dimensional considerations

In Chapters 4 and 5 we pursue a dimensionless formulation to allow generalisation of our results. Equation (5.18) shows the lowest number of dimensionless control variables that can be achieved by our assumptions. Some of the relevant conclusions are reiterated below and are a product of manipulation of this expression. However, for design purposes, we need to revert to an original dimensional expression to expand the range of candidate ma-

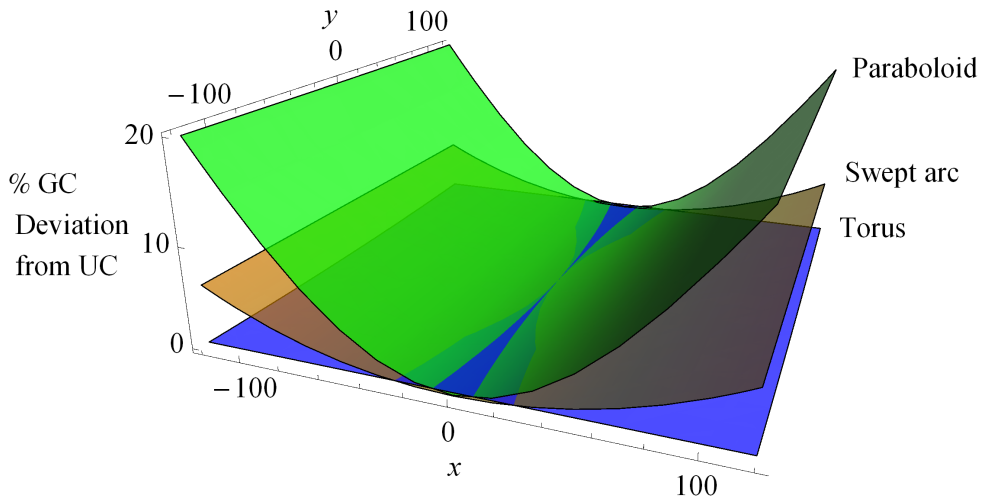

Figure 6.4: Three different geometries are compared for consistency with the UC assumption. To produce an appropriate metric the intrinsic Gaussian Curvature is calculated across a rectangular planform. The percentage deviation from the assumed uniform value, $(\rho_x\rho_y)^{-1}$, is shown. The dimensions used for this comparison are from the larger mould design, *i.e.* $\rho_x = 182\,\text{mm}, \rho_y = 5775\,\text{mm}, a = b = 120\,\text{mm}$. It is shown for this set of parameters that the torus is clearly a better option than the swept arc, which in turn is more consistent than the paraboloid.

terials. We use the expression for the strain energy from Chapter 4 that includes coupling terms in the constitutive matrix—the parameters defining the prestress are omitted for reasons explained in Section 6.2. It is presented in full here since it is only presented in its dimensionless form in Chapter 4:

$$U = \frac{\pi b^2 t \mathrm{E}}{48\rho(1-\nu^2/\beta)}\Bigg(\frac{b^4\delta(u-v)}{u^2}\big(\kappa_{xy}^2 - \kappa_x\kappa_y + \kappa_{x0}\kappa_{y0} - \kappa_{xy0}^2\big)^2 + 2t^2\big[(\kappa_x-\kappa_{x0})^2 + \beta(\kappa_{y0}-\kappa_y)^2 + 2\nu(\kappa_x-\kappa_{x0})(\kappa_y-\kappa_{y0}) + 4\psi(\kappa_x-\kappa_{x0})(\kappa_{xy}-\kappa_{xy0}) + 4\eta(\kappa_y-\kappa_{y0})(\kappa_{xy}-\kappa_{xy0}) + 4\alpha(\kappa_{xy}-\kappa_{xy0})^2\big]\Bigg), \quad (6.14)$$

where

$$u = 3(\beta\alpha - \eta^2) + \rho^2(2\psi\eta - 2\nu\alpha + \beta - \nu^2) + 3\rho^4(\alpha - \psi^2), \quad (6.15a)$$

$$v = \frac{4\rho}{\pi}\big((\nu\eta - \psi\beta) + \rho^2(\psi\nu - \eta)\big), \quad (6.15b)$$

$$\delta = (\beta - \nu^2)\alpha - \eta^2 + 2\nu\eta\psi - \beta\psi^2. \quad (6.15c)$$

This is the basis for the numerical and graphical solutions in the following sections.

6.3.1 Geometry

Once we return to our dimensional formulation, the ratio between the radius of the planform and the thickness of the shell becomes a critical parameter. As can be deduced from the complexity of Eq. (6.14), a relationship between planform parameters a, b and the thickness t that ensures tristability is not amenable in closed form. This requirement however, is easily studied numerically with the standard technique described in Chapter 4. Specifically, we use Eq. (6.14) to solve for equilibria with respect to the curvatures, and check their stability by ensuring the eigenvalues of the Hessian matrix are all positive. Thus, the only difference with previous "colourmaps" is the inclusion of dimensional quantities.

We begin this examination by re-plotting Fig. 6.1 with dimensional quantities in Fig. 6.5a where the axes represent the radii of curvature in mm. The region of interest, *i.e.* the tristable region, is now restricted along the axis in a narrow triangle. The apex of the triangle marks a possible optimal dimension for potential designs—a value that does change with variation of other properties.

The graph shown in Fig. 6.5b plots the change in stability regimes with respect to the radius of a circular shell and its thickness. An inspection of the figure shows that the thickness needs to be more than two orders of magnitude smaller than the planform radius of a circular shell. A direct consequence of this observation is that for multi-layered materials, such as laminated composites, a design that reduces the number of layers is desirable; however, the radius of curvatures will be relatively large, necessitating a correspondingly large planform.

Finally, we show a "colourmap" of stability regions with respect to planform radius and one of the radii of curvature, fixing the second radius in a constant ratio with the first (Fig. 6.6). The tristability region is quite prominent here, and we use this same plot later in this Chapter in relation with our practical designs.

6.3.2 Material

The stability performance according to dimensionless material properties is the focus of Chapter 5. It is useful to consider the effect of stiffness and the Poisson ratio within the context of absolute geometries, so that a more complete view of the exact design requirements becomes available. Specifically, the effect of the shear stiffness and the Poisson ratio with respect to stability regimes is shown in Fig. 6.7, where the shell has a circular planform and takes one of two shell thicknesses. From this figure it is evident that:

- there is a lower bound but no obvious upper bound for shear stiffness with respect to tristability;

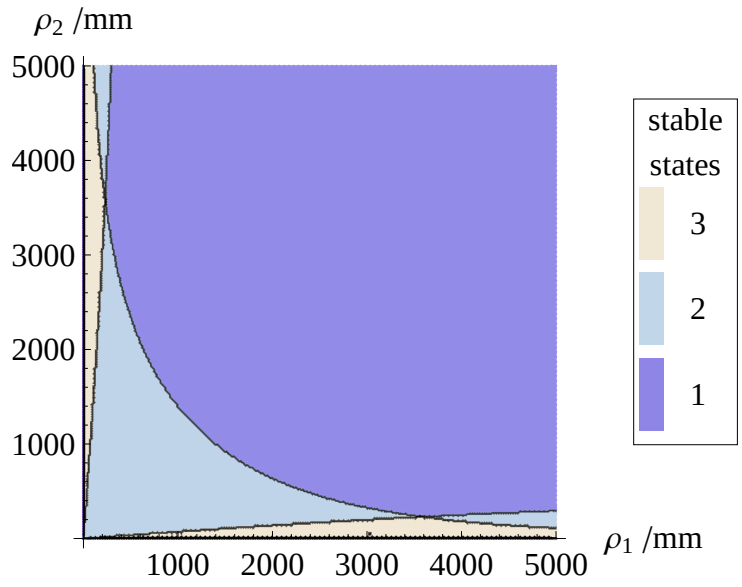

(a)

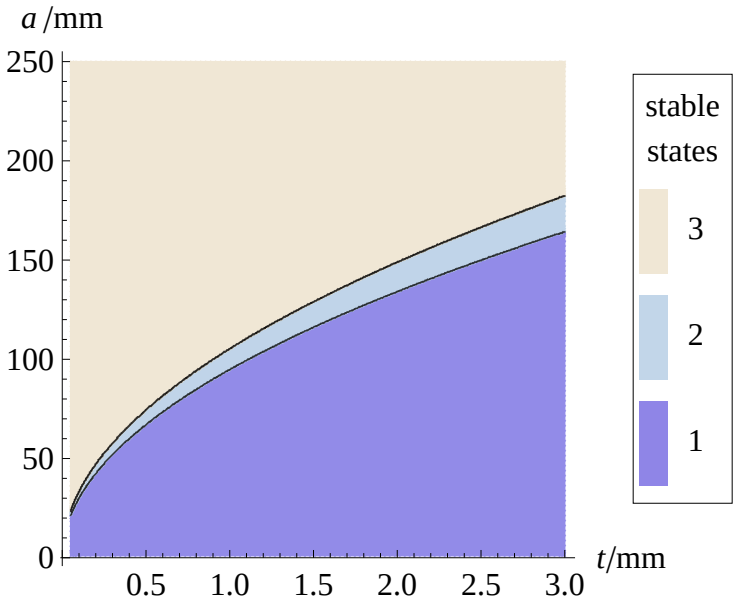

(b)

Figure 6.5: (a) Plot of the different stability regimes with respect to initial radii of curvature. This is a dimensional version of the plot shown in Fig. 6.1. The material assumptions here match the properties of the unidirectional e-glass/nylon $[\pm 45]_S$ layup, with a planform of 120 mm. The radii have a strict lower bound depending on the planform radius—in this case 120 mm. There is clearly an optimal region for tristability close to the apex of an almost triangular region. In this graph, the optimal region lies approximately between 3000 mm and 4000 mm. (b) The three stability regimes are shown with respect to the radius of a circular shell and its thickness. The remaining parameters are fixed to match our first mould geometry and nylon-glass material parameters. The thickness needs to be less than the planform radius by two orders of magnitude for tristability to be possible.

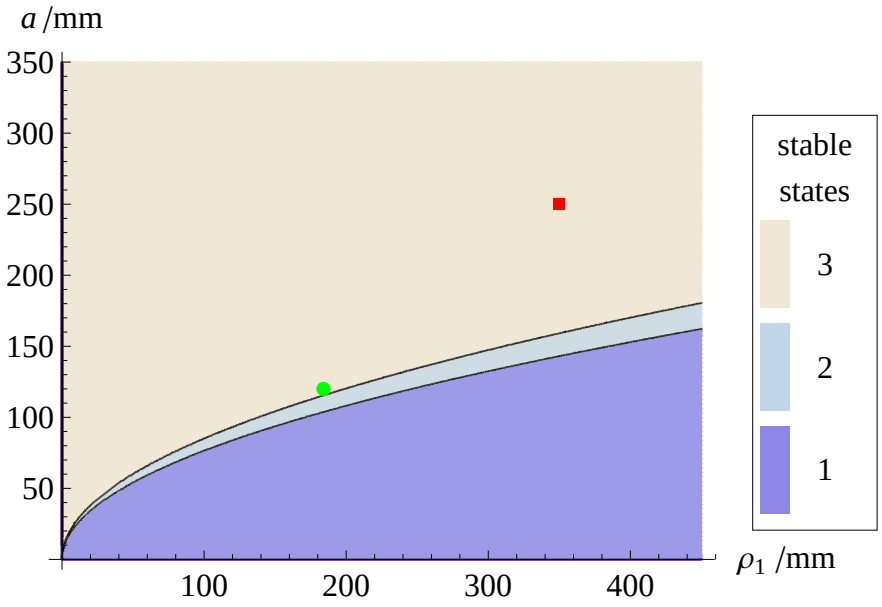

Figure 6.6: The influence of geometry as expressed by absolute values of the planform radius and the principle radius of curvature. The second radius of curvature is fixed at 16.5 times the value of the first one. The shell takes a circular shape and the material properties are those of the unidirectional nylon-glass laminate presented in Table 6.2. The two dots represent the two mould geometries that are tested. Choosing the optimal geometry is the primary objective in Sections 6.2 and 6.3.1. The benefit of a larger planform (red square) is shown here. A smaller planform (green dot) is closer to the bistable region and is susceptible to material imperfections and manufacturing errors.

- there is both a lower bound and an upper bound—decreasing with thickness—for the Poisson ratio with respect to tristability.

The latter conclusion in particular is of interest, since Vidoli & Maurini (2008) concluded that approaching β (in this case equal to unity) with the square of the Poisson ratio is beneficial for increasing the tristable region. This rule of thumb is helpful in design, but we note that Poisson ratio values close to unity do not always produce tristable shells. Hence, case-specific considerations need to be taken, and will be detailed.

6.4 Unidirectional laminate design

A design based on unidirectional plies is first tackled using CLT. One challenge here lies in the assumption in Chapter 4 of a homogeneous material throughout the thickness of the shell, which makes many designs impossible to model accurately. We show below however, that this model weakness is not universal. With some adjustments, a vast array of laminates can be modelled with our strain energy expression from Eq. (6.14).

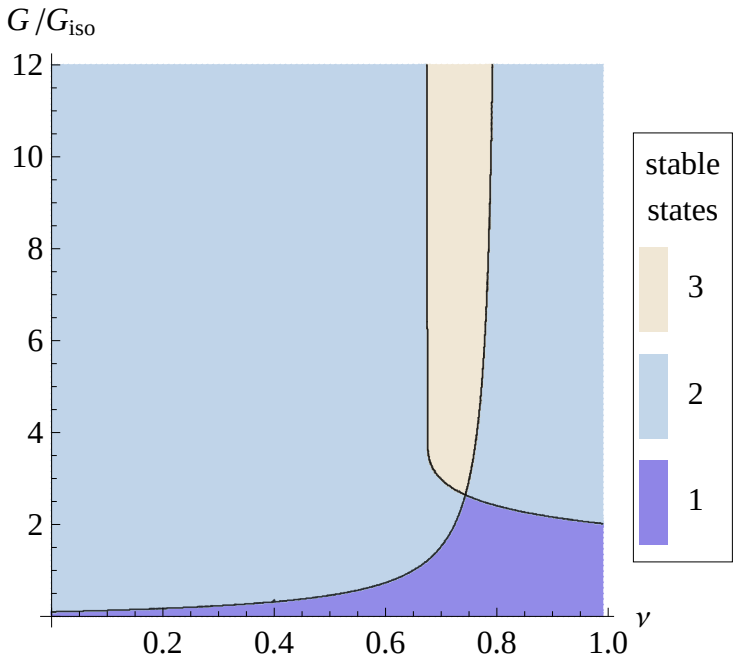

(a) $t = 1.08\,\text{mm}$

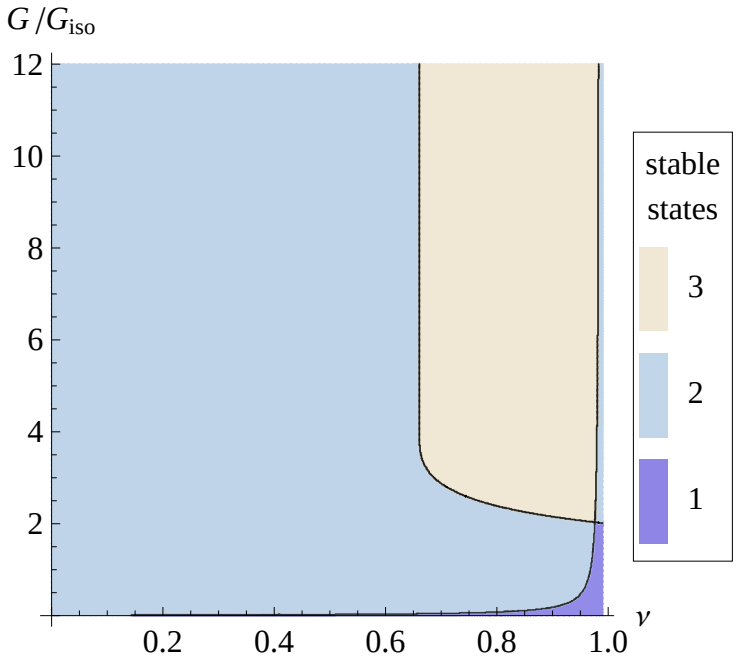

(b) $t = 0.325\,\text{mm}$

Figure 6.7: The influence of the shear stiffness and the Poisson ratio on the feasibility of different stability regimes. Here, a specific geometry is considered—the parameters agree with the smaller mould design. On the top plot, the thickness of the $[\pm 45]_S$ e-glass/nylon layup from Section 6.4 is assumed ($t = 1.08\,\text{mm}$). On the bottom plot, the thinner ($t = 0.325\,\text{mm}$) single ply of the woven glass-TPU from Section 6.7.2 is assumed. Both the shear stiffness and the Poisson present a lower bound for tristability, but only the Poisson ratio offers an upper bound in the thicker shell. The shear stiffness is given in proportion to the isotropic value, G_{iso}, corresponding to the value of the principal Young's modulus.

Our model does not account for stretching-bending coupling. One way to get around this restriction is to focus on symmetric layups that always produce $\mathbf{B} = \mathbf{0}$, as can be deduced from Eq. (3.23c) and following the standard **ABD** notation for composites. Recall that we also need to choose an orthotropic layup with a high Poisson ratio and high shear modulus associated with the principal directions, and these are obtained by symmetric layers at 45° to the principal directions. We also need a lower thickness, so we choose a $[\pm 45°]_S$ laminate, shown in an exploded view in Fig. 6.8.

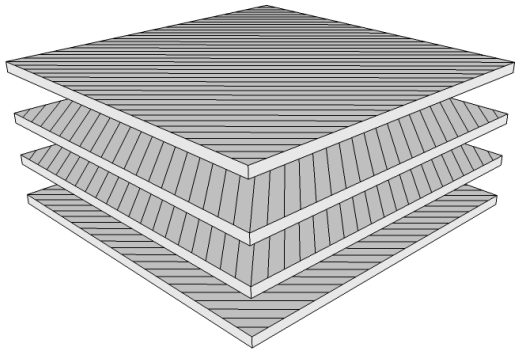

Figure 6.8: An exploded view of the $[\pm 45]_S$ layup design for a unidirectional laminate. This design uses the minimum possible number of plies, four, for a symmetric laminate while promoting a high Poisson ratio in the principal directions.

Material	E (GPa)	ν	G (GPa)	Density ($\mathrm{Mg/m^3}$)
e-glass	80	0.22	32	2.6
nylon 11	1	0.4	0.35	1

Table 6.1: Approximate mechanical properties for the constitutive materials in the long-fibre, unidirectional laminate used (Biron, 2012; Wallenberger & Bingham, 2010). Note that the density is quoted in their choice of units and not in SI.

Our material is an e-glass/nylon composite tape, having a fibre proportion corresponding to 62% of the total mass, and equivalent to a volume fraction of 39%. E-glass refers to an industry standard for borosilicate electrical grade glass (Lu & Wong, 2009). Wallenberger & Bingham (2010) and Biron (2012) provide approximate values for the mechanical properties of the constitutive materials in Table 6.1, which, when combined with the CLT from Chapter 3 produce the following **ABD** matrix for the final laminate:

$$\begin{bmatrix} 11.83 & 10.37 & 0 & 0 & 0 & 0 \\ 10.37 & 11.83 & 0 & 0 & 0 & 0 \\ 0 & 0 & 10.41 & 0 & 0 & 0 \\ 0 & 0 & 0 & 1.62 & 1.42 & 1.0 \\ 0 & 0 & 0 & 1.42 & 1.62 & 1.0 \\ 0 & 0 & 0 & 1.0 & 1.0 & 1.42 \end{bmatrix}. \tag{6.16}$$

Recall from Eq. (3.24) that the units are GPa mm for $\mathbf{A}$, GPa mm^2 for $\mathbf{B}$ and GPa mm^3 for $\mathbf{D}$. Note that the $\mathbf{B}$ matrix is zero, as expected for a symmetric layup, however, there is a discrepancy in the coupling terms in the $\mathbf{A}$ and $\mathbf{D}$ matrices. Unlike the formulation in Chapter 4, the two matrices here are not proportional to each other. Even though this slightly complicates our formulation, this change can be accounted for, and we present the appropriate modification to our model in the next Section.

If we consider only matrix $\mathbf{A}$ and combine this result with our assumptions in Chapter 3, we can obtain homogenised, orthotropic values through simple algebraic calculations. In this case, the corresponding values are:

$$E_1 = E_2 = 2.14\,\text{GPa}, \qquad \nu_{12} = \nu_{21} = 0.88, \qquad G_{12} = 10.4\,\text{GPa}. \tag{6.17}$$

Recall that is the absolute values of the Poisson ratio and the shear modulus compared to the isotropic value that are of interest, specifically that need to be maximised. For the Poisson ratio, the high value is apparent, and for the shear modulus, the comparison with the isotropic value reveals:

$$\frac{G_{12}}{G_{\text{iso}}} = \frac{2(1+\nu_{12})}{E_1} G_{12} = 18.4, \tag{6.18}$$

which is a value more than an order of magnitude above our requirements.

This **ABD** matrix is subject to a number of influencing parameters. As already mentioned, the mechanical properties we use for the constitutive materials are averages over a range, rather than exact values; the properties of the final product are subject to significant variation with the age of the tape we are using; environmental parameters such as humidity/temperature during storage and precise curing conditions all affect the final properties. Hence, we must validate these stiffness values through experiments.

6.4.1 Coupling terms

Our model assumes a uniform material throughout the thickness, and the two sub-matrices can be expressed as $\mathbf{A} = \mathbf{E}t$ and $\mathbf{D} = \mathbf{E}t^3/12 = \mathbf{A}t^2/12$. This proportionality relationship between $\mathbf{A}$ and $\mathbf{D}$ holds for all terms of the constitutive relationship for this design, except

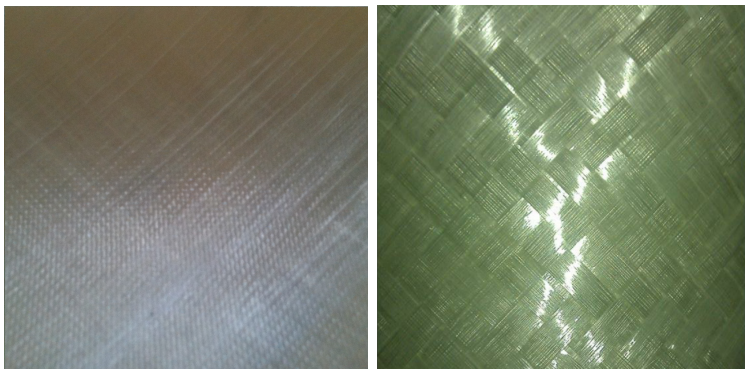

Figure 6.9: The two materials used for attempted designs. On the left, a cured sample of unidirectional e-glass/nylon. On the right, an sample of woven glass-TPU before curing.

the coupling terms at positions (1,3) and (2,3)—and their symmetric (3,1), (3,2)—in the matrices. In particular, the alternating orientations of the laminae produce alternating signs for these terms, and sum up to zero for the **A** matrix, but not for the **D** matrix. In practical terms, the in-plane shear-extension coupling is zero, while the out-of-plane bending-twisting coupling is not zero.

This inconsistency can be remedied by looking at the basis of our formulation. The **A** matrix only affects the stretching energy. From Eq. (6.14), the only change occurs in the coefficient of the expression representing the change in Gaussian curvature—this is to be expected, since this coefficient relates to stretching. In particular, only the terms u, v and δ are affected, and are reduced to:

$$\bar{u} = 3\beta\alpha + \rho^2(-2\nu\alpha + \beta - \nu^2) + 3\rho^4\alpha, \tag{6.19a}$$

$$\bar{v} = 0, \tag{6.19b}$$

$$\bar{\delta} = (\beta - \nu^2)\alpha. \tag{6.19c}$$

.

The remaining coupling terms, corresponding to the terms D_{16} and D_{26} can be substituted into Eq. (6.14). The corresponding terms can be obtained after some manipulation of the terms from the **ABD** matrix, following standard CLT calculations. Specifically the D_{16} and D_{26} can be related to ψ and η with:

$$\psi_D = D_{16}\frac{12(1-\nu^2/\beta)}{Et^3}, \qquad \eta_D = D_{26}\frac{12(1-\nu^2/\beta)}{Et^3}. \tag{6.20}$$

With this small amendment, laminates and other non-homogeneous materials can be included in the model and easily tested before construction, as long as **B** remains zero. An example of the effect these parameters have on multistability can be seen in Fig. 6.10, where we use colourmaps to show different regimes with respect to ψ_D and η_D. The pattern

that emerges is quite intricate, therefore special consideration needs to be given to these parameters. At the same time however, according to our model, the existence of coupling does not preclude multistability. The point in the same plot marks the corresponding estimated coupling parameters for a unidirectional laminate design that is presented later in this Chapter.

Material Testing

Samples are created for material testing in order to establish constitutive values, with flat sheets of unidirectional e-glass/nylon being placed placed in the $[\pm 45]_S$ configuration. These are then attached to a flat steel plate and held in place with adhesive tape. A breather fabric and then a vacuum sheet are placed over the layup and secured with sealant tape, with a vacuum seal crossing the barrier. Non-stick layers of material are placed between the composite and the adjacent materials. A pump is used to lower pressure inside the vacuum bag and force the laminae together. The apparatus is placed in a commercial oven and held at 200°C for one hour.

Strain rosettes are attached to three rectangular strips of the cured composite. The approximate dimensions of the strips are 30 mm by 80 mm. An Instron machine tensions the samples until yielding along the direction of the fibres. The apparatus is set up to measure strains along the fibres in both directions and along the diagonal direction, providing a complete description of in-plane behaviour. The initial, elastic part of the behaviour is used to obtain the moduli and Poisson ratio from appropriate stress-strain data plots.

Material	$E_1 = E_2$ (GPa)	$\nu_{12} = \nu_{21}$	G_{12} (GPa)	t (mm)
Unidirectional Nylon-Glass	4.29	0.69	16.3	1.08
Twill woven TPU	0.96	0.95	3.07	0.325

Table 6.2: Experimental material properties for both composites used. The values for the woven TPU material are from Pirroni (2012).

This testing produces the values shown in Table 6.2. The discrepancies in the absolute values between the CLT prediction and the tested values can be explained by the many influencing parameters mentioned before. More importantly though, the relative values of the parameters are consistent with our design. Specifically, the Poisson ratio and the ratio of the shear stiffness to the Young's modulus are sufficiently large. We can offer additional detail in the form of an equivalent **ABD** matrix retrieved from the experimental moduli. Inserting the values for the moduli into Eq. (3.1), we can obtain the **E** matrix and, in turn, using Eq. (4.8) produce the final expression:

$$\begin{bmatrix} 8.84 & 6.10 & ? & 0 & 0 & 0 \\ 6.10 & 8.84 & ? & 0 & 0 & 0 \\ ? & ? & 17.60 & 0 & 0 & 0 \\ 0 & 0 & 0 & 0.86 & 0.59 & ? \\ 0 & 0 & 0 & 0.59 & 0.86 & ? \\ 0 & 0 & 0 & ? & ? & 1.71 \end{bmatrix}. \tag{6.21}$$

Once again, the units are GPa mm for **A**, GPa mm^2 for **B** and GPa mm^3 for **D**. As the matrix indicates, there are no experimental values for the coupling parameters at hand. However, the CLT prediction made earlier can offer an appropriate approximation. Based on our CLT prediction, we can state that the missing A_{16} and A_{26} terms are equal to zero, while we need to infer a value for D_{16} and D_{26}. Assuming consistent proportional values between the two predictions, one convenient metric is the ratio of D_{16} and D_{26} to D_{11}. From Eq. (6.16), that ratio is 1:1.62 in both cases. Taking the experimental value for D_{11} from Eq. (6.21), values for ψ and η are calculated. Starting from Eq. (6.20),

$$\eta_D = \psi_D = D_{16}\frac{1-\frac{\nu^2}{\beta}}{E} = \frac{D_{11}}{1.62}\frac{1-0.69^2}{4.29} = 0.62. \tag{6.22}$$

.

This also implies a value of 0.53 for both D_{16} and D_{26}.

6.5 Woven composite design

Another way to incorporate long fibres in composites is through woven, braided and knitted patterns inside the matrix. The theoretical analysis of such materials is significantly more challenging than the CLT we presented earlier. A historical review of relevant studies can be found in Miravete (1999). Most commonly, a combination of CLT with computational methods is used for predictions of homogenised properties. This is a very active field of research, but beyond the scope of the present work.

We are mainly interested in the in-plane stiffness and Poisson ratio of orthogonal woven-fibre composites, and we find relevant information from Tong *et al.* (2002). In general, we expect the same range of homogenised properties as for an orthogonal laminate layup, *i.e.* in the direction of the fibres, compared with any other direction, we expect: A higher Young's Modulus, a low Poisson ratio and a low shear stiffness. Conversely, in the direction diagonal to the fibres, all three trends are reversed.

Here, a twill woven composite is used, composed of Thermoplastic Polyurythane (TPU) with glass fibres. The material is initially selected because it provides orthotropic properties within a *single thin ply*. The fibres are at 45° to the principal curvatures of

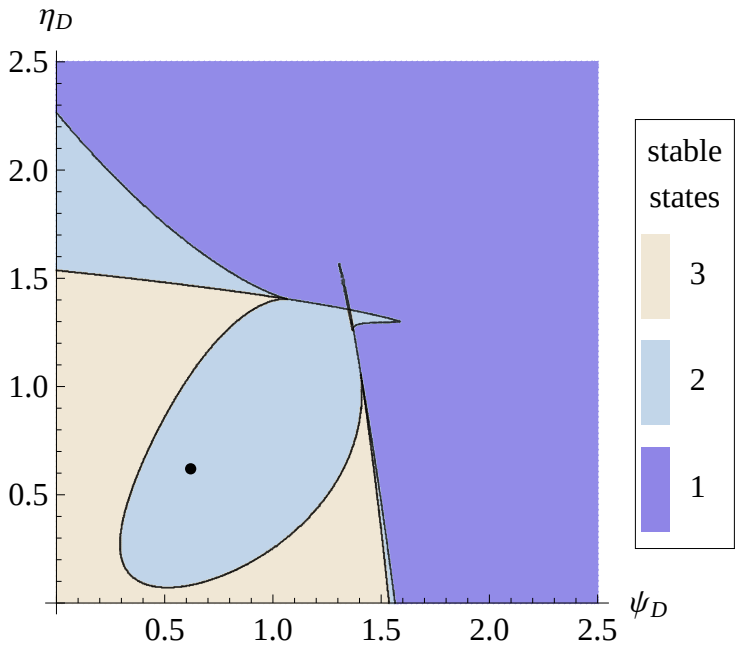

Figure 6.10: Multistability regimes for the unidirectional layup design, $[\pm 45]_S$, with respect to the bending-twisting parameters. This first design does not comply with early predictions. This discrepancy can be attributed to a number of factors but here we focus on the bending-twisting parameters which—unlike the stretching-shearing—parameters, do not diminish in this layup. All parameters correspond to the e-glass/nylon material and the larger mould design; the influence of the coupling parameters is shown. A black dot notes the estimated values for the coupling parameters in this design.

the design—similar to the unidirectional design. The benefit from a lower total thickness is noted, since the ply thickness for the TPU is measured at 0.325 mm—almost a quarter of the unidirectional laminate layup.

With no access to any theoretical predictive tools, we use experimental results from Pirroni (2012), shown in Table 6.2, to obtain the properties of the material at hand. This testing occurred simultaneously and in the same facilities with the testing described in Section 6.4.1. Since the same batch of material and similar curing procedures are used for both studies, we can assume no deviation from the known material behaviour.

6.6 Predicted geometries and material parameters

For convenience and consistency, the design specifications and the predictions of the theoretical formulation are presented in charts produced by a Mathematica script (Figs. 6.11 to 6.13). The script accepts the following inputs given at the top of the screen shot: the radius for an assumed circular planform; the overall shell thickness; the radii of curvature in the two principal directions; the Young's modulus; the Poisson ratio; the shear stiffness; the two coupling parameters relating to bending. Using a dimensional form of the energy expression given in Eq. (4.28), it solves for equilibria based on Eq. (4.29) and selects the stable solutions for display and plotting. The equivalent moduli and $\mathbf{A}$, $\mathbf{D}$ matrices are also presented for completeness. The plots are based on a parametric equation for the torus surface and they are drawn to scale.

Tristability is predicted for both designs. The predicted secondary and tertiary geometries follow this pattern in either case: an almost cylindrical state, in the same sense as the initial geometry; an almost spherical state, in the opposite sense as the original geometry. The second state is of similar curvature as the original geometry while the third state is noticeably shallower.

6.7 Construction of Shells

6.7.1 Unidirectional laminate

As noted in Section 6.4, an initial candidate design for a unidirectional laminate is found in a $[\pm 45^\circ]_S$ layup. A material immediately available to us is composed of a Nylon-11 matrix with embedded e-glass fibres. This material is fairly common and preliminary material properties are widely known. They are used in conjunction with CLT and the specific dimensions of our sample to predict whether it could indeed fall within the tristable region. Material properties are also tested for a cured sample in the design layup and produces values shown in Table 6.2. The coupling parameters are not tested for and, at

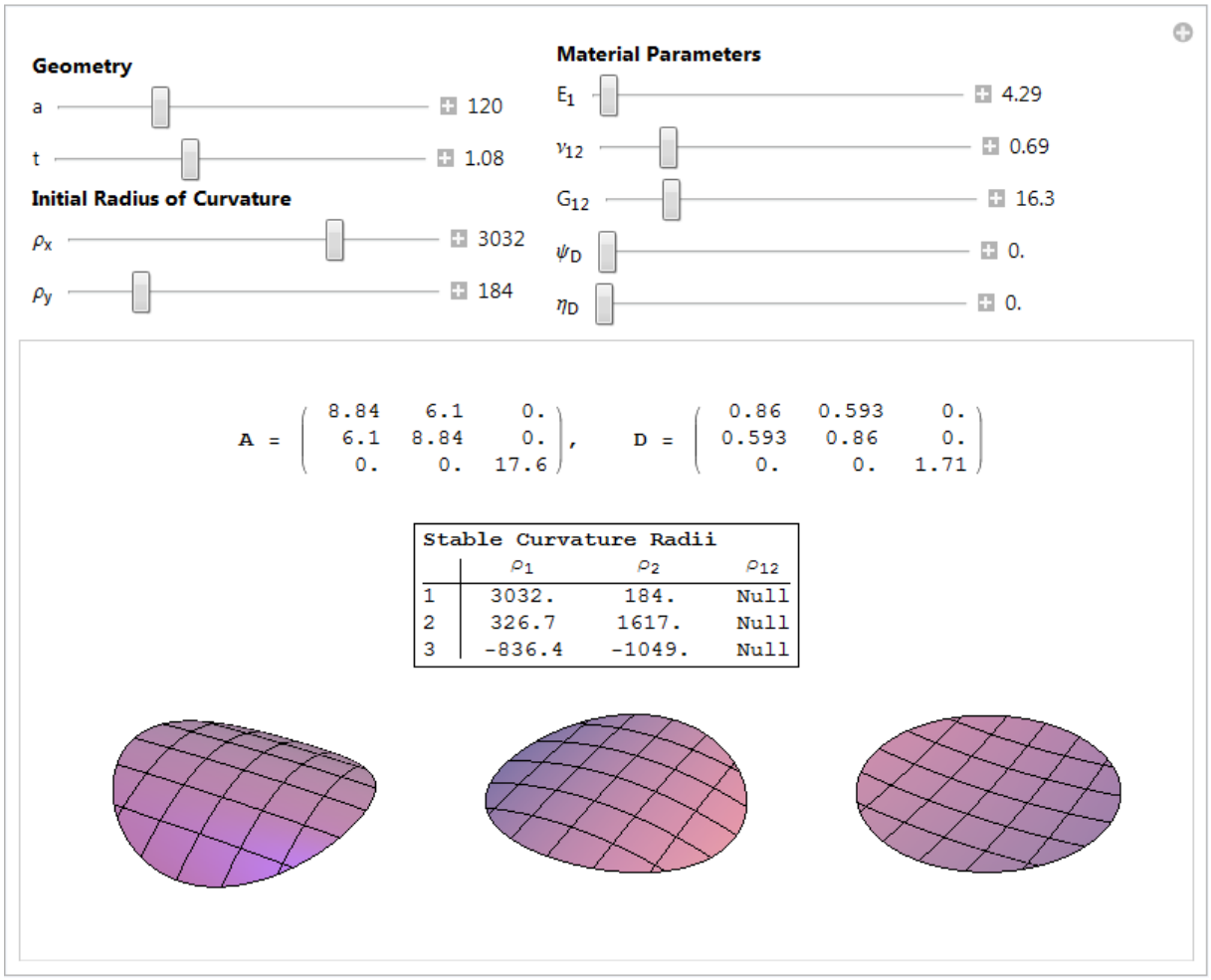

Figure 6.11: A summary of the design parameters and predicted behaviour for the unidirectional laminate-based design. All dimensions are in millimetres while the moduli are given in GPa. In this preliminary scenario the coupling parameters are not considered in the design. Beyond the initial geometry, our model predicts a second stable state, almost symmetrical and in the same sense as the first (centre), and a third, almost-spherical state in the opposite sense (right).

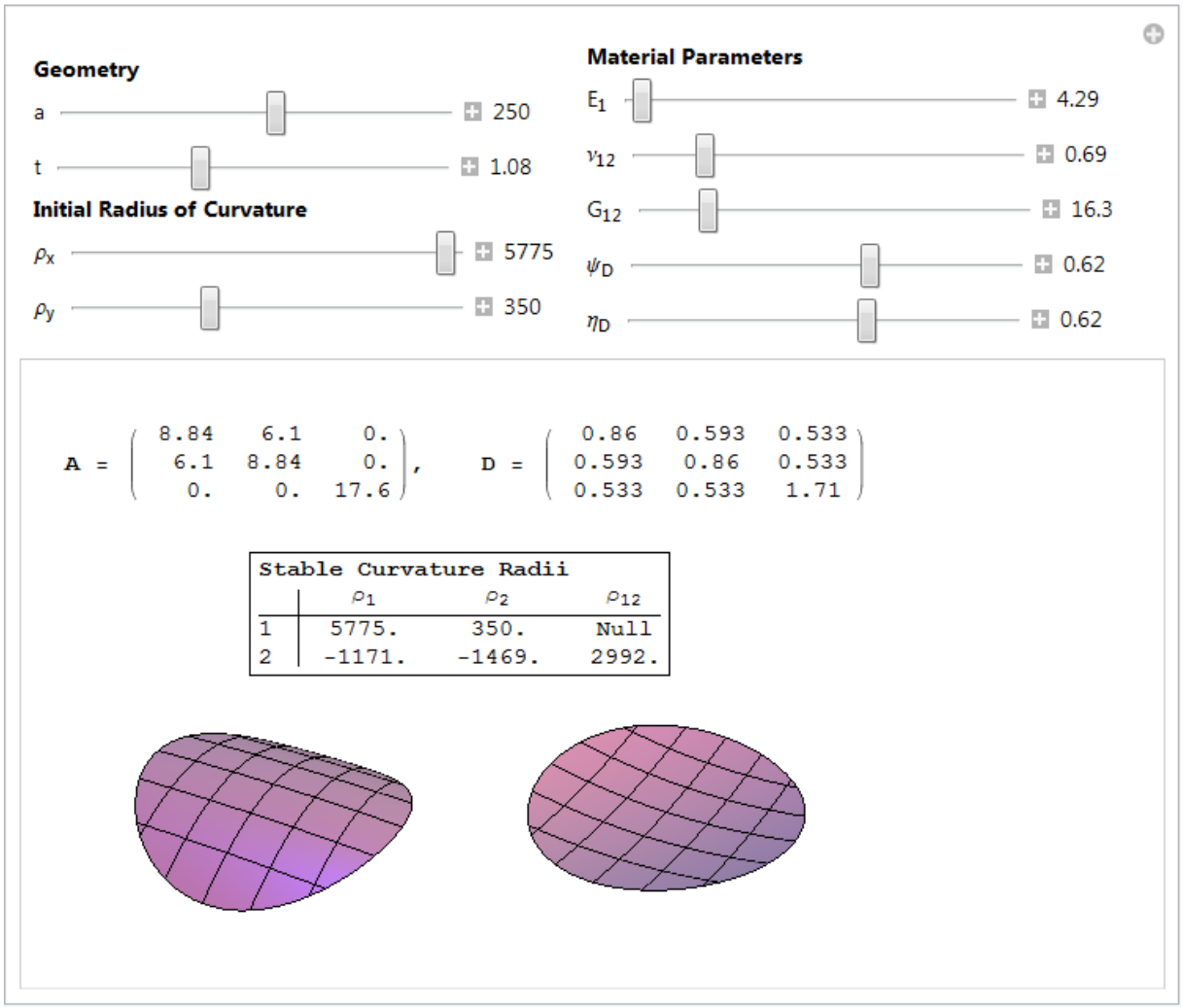

Figure 6.12: A summary of the design parameters and predicted behaviour for the unidirectional laminate-based design. All dimensions are in millimetres while the moduli are given in GPa. For this case, we note the non-diminishing value of the **coupling parameters** ψ_D and η_D for bending, that is treated in Section 6.4.1. We also increase the radius of the planform which generally increases the likelihood of tristability. However, the coupling parameters do not fall within the tristable region as seen in Fig. 6.10, and only allow bistability. This helps explain the inconsistency of our preliminary efforts. An additional result that can be glimpsed at here, is the non-zero twist for secondary equilibria. This behaviour does not appear for materials with diminishing coupling parameters and no initial twisting curvature.

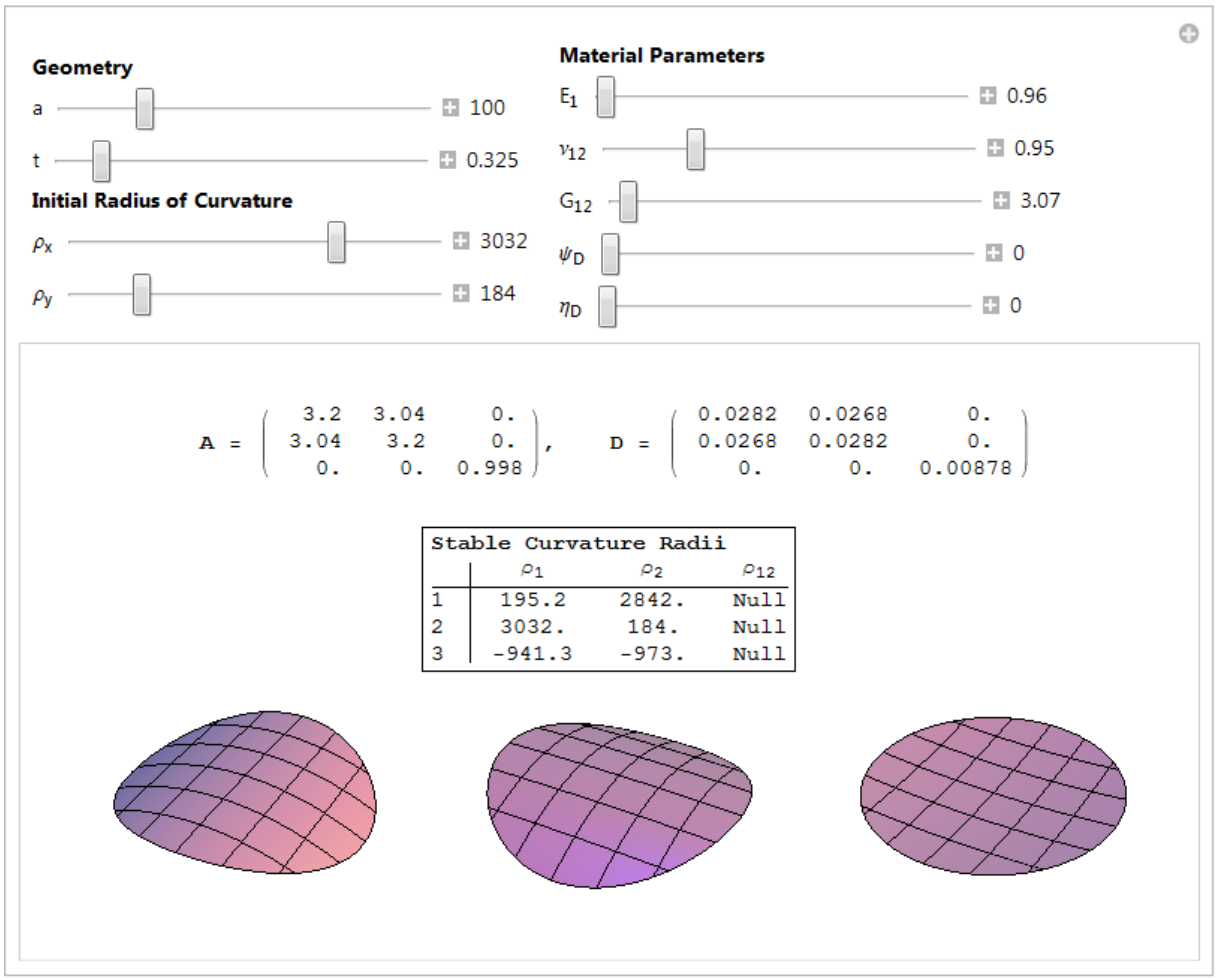

Figure 6.13: A summary of the design parameters and predicted behaviour for the woven fibre-based design. All dimensions are in millimetres while the moduli are given in GPa. The predicted behaviour is similar to the unidirectional design while the significantly thinner profile expands the range of tristable behaviour as noted in Section 6.3. The initial, almost-cylindrical, geometry is shown in the centre. A second state, almost a 90° rotation of the first is shown to the left. A third, almost-spherical state, in the opposite sense as the other two, is shown to the right.

first, ignored in this design.

The initial aim is to construct a hand-held tristable shell to function as a demonstrator and appropriate dimensions are chosen. The four plies in our design result in a thickness of 1.08 mm, while a planform radius is chosen at 120 mm, in accordance with the design in Fig. 6.11. The initial curvatures are chosen to follow the optimised ratio mentioned in Section 6.2 (1:16.5). Considering the physical dimensions of the shell, a natural limit to the curvatures is also imposed, with the principal radii of curvature chosen to be $\rho_1 = 3032$ mm and $\rho_2 = 184$ mm. The mould is drawn as part of a torus on CAD software and constructed by a CNC machine from a block of aluminium in CUED's workshops.

The layup for the laminate is constructed on the mould itself with an anti-stick layer between the two. A breather material is placed below a final plastic layer, which is secured with sealant tape to the mould. An appropriately placed valve allows the introduction of a vacuum and with the imposed external pressure, the top plastic layer presses the laminate to the geometry of the mould. The apparatus is then placed in a commercial oven for curing at 200° C for approximately one hour. This period does not include the time allowed for the mould to reach the desirable temperature.

Figure 6.14: Samples are cured in a commercial oven. The composite is laid-up and vacuum-pressed against an aluminium mould to match the desirable geometry. A thermocouple is attached to the mould to allow for precise monitoring of the temperature.

The resulting samples are bistable, leading to additional experimental and theoretical probing. One can observe from Fig. 6.5b that while this particular setup is within the tristable region, it lies close to the boundary with bistable behaviour hence the slightest imperfection in the construction process, or in the material, renders the sensitive third state unstable—it pushes the design point closer to, even into, the bistable regime—and this happens several times. Once this proximity to the boundary is taken into account, a

larger planform is chosen as a more suitable candidate.

The larger mould is constructed with a planform radius of 250 mm and radii of curvature equal to $\rho_1 = 5775$ mm and $\rho_2 = 350$ mm. The improvement in the reliability of the sample can be seen in Fig. 6.6. This plot shows the three stability regimes with respect to one principal radius of curvature and the planform radius. The second radius of curvature is fixed at 16.5 times the value of the first one. The planform is taken to be circular while the material properties are the ones given previously for the e-glass/nylon laminate.

This performs slightly better; it is stable under its own weight in the three predicted geometries, but only for a few minutes *immediately after curing*. This temporary tristable behaviour can be seen in Fig. 6.15. We can hypothesise on various reasons for this.

- Due to the age of our laminate, the fibres detach from the matrix after external forces are applied a few times.
- Construction errors such as misalignment of the fibres and wrinkling during vacuum-forming can create local imperfections. These in turn can greatly influence the stability of the secondary and tertiary states.
- Most likely, the influence of the coupling terms in the **D** matrix is the critical parameter. The failure of this design motivates the work in Section 6.4.1 and helps explain sources of error in our prediction. This result is not conclusive though because the values for ψ_D and η_D are estimates and are not verified experimentally.
- Conversely the temporary availability of three stable states immediately after curing can be attributed to softness of the material before complete cooling, *i.e.* the material properties—including coupling parameters—do not reach their final values.
- Finally, such plastics can experience creep and general relaxation, particularly after the repetitive loading applied when actuating bistable shells.

Figure 6.15: The initial design involves a unidirectional e-glass/nylon design in a $[\pm 45°]_S$ layup. This sample only exhibits temporary tristability immediately after curing, most likely due to the influence of the bending-twisting coupling parameters on the stability of the available equilibria.

6.7.2 Woven composite

With the woven TPU, favourable parameters are observed on all accounts, except one; the reduction of the direct stiffness in absolute value is not optimal, meaning that a very flexible shell is produced. This motivates a reduction of the planform area to compensate for self-weight bending effects and the smaller mould design (with dimensions $\rho_1 = 3032\,\text{mm}$, $\rho_2 = 184\,\text{mm}$, $a = b = 120\,\text{mm}$) becomes preferable.

The resulting tristable shell is shown in Fig. 6.16 and it qualitatively matches our theoretical prediction. In practical terms, the low bending stiffness of the single ply makes the relative effect of self-weight significant, *i.e.* the structure is capable of holding three distinct geometries without the application of external loads, but the precise stress-free geometries are difficult to establish; deformation due to gravity is too large to be ignored. In consequence, a quantitative comparison of predicted and actual geometries is not presented here. Nevertheless, this prototype serves as a proof-of-concept and strongly supports both the predictive and design capabilities of the model in Chapter 4.

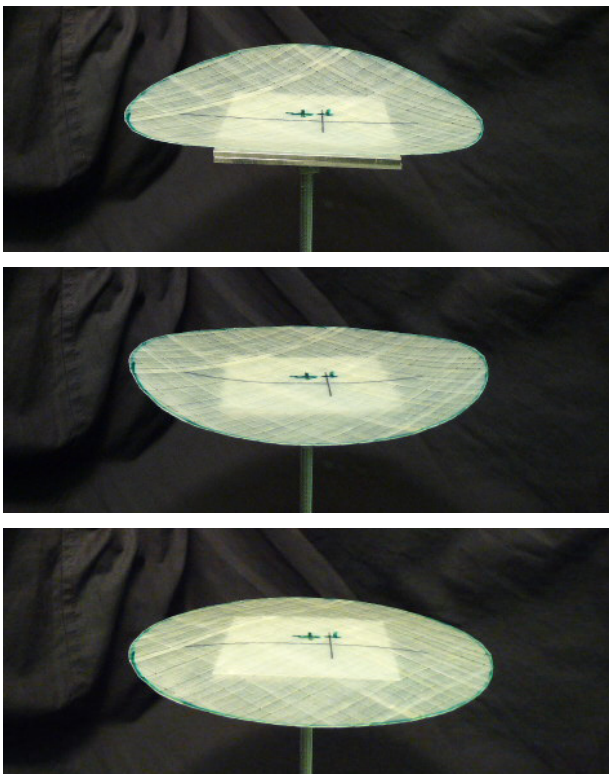

Figure 6.16: A tristable shell made from twill-woven, glass-reinforced TPU. We observe two same-sense, almost cylindrical states at similar energy levels, and a third, opposite-sense, almost-spherical state. The design had the following specifications: a double initial curvature; a high Poisson ratio; a high shear modulus.

6.8 Concluding remarks

Manufacturing of a novel tristable shell was attempted, with two distinct composite materials. A UC model was used to both predict and design this shell, showing its effective applicability despite its simplicity. The same model was used to account for the coupling parameters so common to composite structures. This small addition to the theoretical model can have a significant impact on reducing manufacturing restrictions at a later stage. One design based on a symmetric layup of a unidirectional fibre reinforced laminate did not prove robust. A subsequent design based on a woven fibre composite proved consistently reliable.

The next Chapter deals with actuation of multistable shells. The capabilities of the UC model towards this objective are examined. In the same Chapter, we present some experimental work involving remote magnetic actuation of a bistable spherical cap.

Chapter 7

Actuation

7.1 Introduction

The practical applications of multistable shells must also consider the movement and energy requirements between the different equilibrium states. In this Chapter we propose a novel method for remotely actuating shape-change through magnetic fields. Using high-speed photography and FE simulations, we investigate transition geometries. In addition, we present theoretical tools for discovering efficient actuation paths based on our Uniform Curvature (UC) model, and discuss its limitations.

7.2 A single-DOF system

An example from the literature is presented here to provide context for some of the concepts that follow. We define a structure similar to the Euler arch from Section 5.2.1, but with some slightly modified parameters, constituting a single degree of freedom (DOF) system. The structure shown in Fig. 7.1, is composed of two rods of equal length and stiffness E, pin-jointed to each other at B and to rigid supports, A and C, creating a simple arch ABC. Both rods are inclined at an angle θ to the horizontal, with θ_0 signifying the initial angle, when no forces are applied. The total horizontal length of the arch is $2L$.

We "actuate" this structure by applying a vertical force to the pin at point B and we are interested in the vertical movement of the same point, δ. The external force is applied slowly so that static equilibrium can be assumed at each stage. In practice, we could use a hydraulic actuator or other similar technology to apply this external force. A derivation of the equilibrium relationships follows for this actuation path, but can also be found in numerous texts—we only note Leckie & Dal Bello (2009) from which we borrow our nomenclature.

After a force has been applied, point B moves downwards and the rods shorten. The

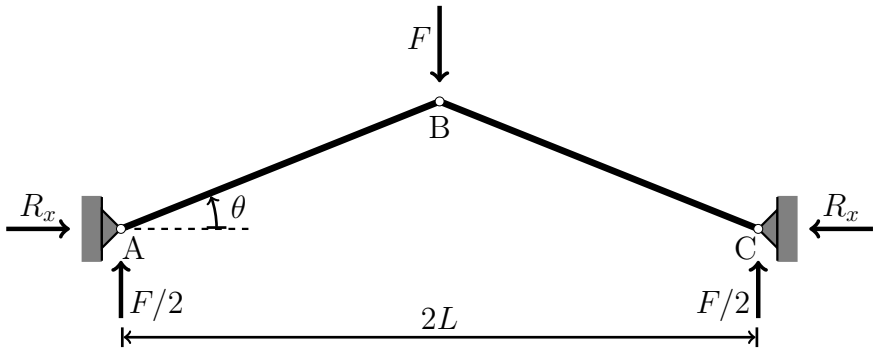

Figure 7.1: A simple bistable arch structure used to demonstrate the concepts of snap-through and actuation.

change of length for each, Δ, is:

$$\Delta = L\left(\frac{1}{\cos\theta} - \frac{1}{\cos\theta_0}\right). \tag{7.1}$$

The axial force through each rod, P, can be calculated given its stiffness E and area A, as in:

$$P = \frac{AE\Delta}{L} = AE\left(\frac{1}{\cos\theta} - \frac{1}{\cos\theta_0}\right). \tag{7.2}$$

Equilibrium of pin B as a free body demands:

$$F - 2P\sin\theta = 0, \tag{7.3}$$

resulting in the applied force, having the following relationship:

$$F = 2AE\left(\frac{1}{\cos\theta} - \frac{1}{\cos\theta_0}\right)\sin\theta. \tag{7.4}$$

From the geometry of the arch we can also calculate the vertical displacement of the pin B in terms of θ:

$$\delta(\theta) = L(\tan\theta_0 - \tan\theta). \tag{7.5}$$

A force-displacement diagram for the pin B during actuation can be obtained by parametrically plotting Eqs. (7.4) and (7.5), since both expressions are in terms of θ. Noting the slope of the plot in Fig. 7.2, the system begins with a positive stiffness, resisting the external force, F, until a local maximum (shown as a triangle on the plot) where the stiffness switches sign. This reversal of stiffness is commonly referred to as a *snap-through* event, even in the absence of secondary stable equilibria. When it reaches this point, under force-controlled movement, the structure follows the dashed path, to another state of positive stiffness. The continuous path can be achieved through displacement-controlled actuation. In this example, there is a second equilibrium point (noted with a diamond)

that corresponds to $\theta = 0$, but is unstable since the system maintains a negative stiffness. The plot crosses the δ axis again a third time (shown by a black dot) after the slope reverts to a positive value at a local minimum. This is the second stable geometry, symmetric to the initial configuration about the line connecting points A and B in Fig. 7.1.

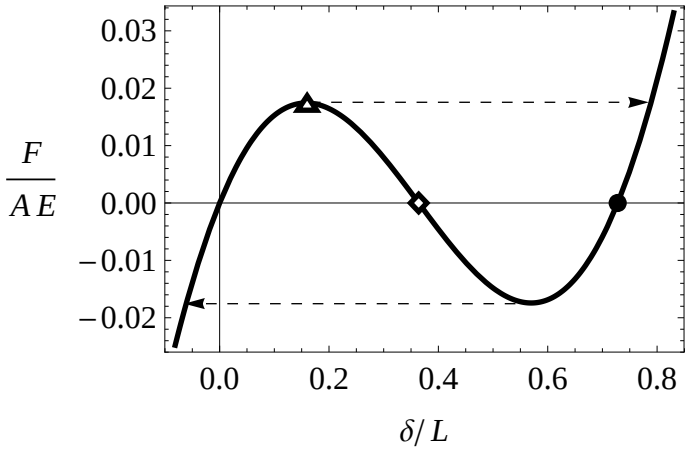

Figure 7.2: Dimensionless force-displacement diagram for the arch in Fig. 7.1, with θ_0 equal to $\pi/9$. The structure experiences a snap-through when the external force F grows sufficiently, *i.e.* past the local maximum noted with a triangle, and the dashed path is followed. The second stable configuration with indicated with a black dot, where the curve crosses the δ/L-axis for the third time and the stiffness of the system is positive. By controlling displacement, rather than force, a quasi-static transition can be achieved along the continuous path on the plot.

The concept of embedded actuation is encountered frequently in this dissertation so it is also portrayed here with an amendment to the structure above. Consider the same structure, but with embedded actuators, f, in each rod, as shown in Fig. 7.3. The controlled straining of the rods changes the change of length for each such that:

$$\bar{\Delta} = L\left(\epsilon_f + \frac{1}{\cos\theta} - \frac{1}{\cos\theta_0}\right). \tag{7.6}$$

The strain energy of the arch is then available, if we consider the deformation and stiffness of the two rods:

$$U_{\text{arch}} = \frac{EA}{L}\bar{\Delta}^2 = EAL\left(\epsilon_f + \frac{1}{\cos\theta} - \frac{1}{\cos\theta_0}\right)^2. \tag{7.7}$$

Plotting the energy expression with respect the angle θ shows the bistability of the structure. In Fig. 7.4 we set $\theta_0 = \pi/9$ and show the energy for a range of θ ($-3\pi/2 < \theta < 3\pi/2$). The darkest plot corresponds to the case with no internal actuation, *i.e.* with ϵ_f equal to zero. The two minima at $\pm\theta_0$ represent the two stable geometries of the arch, while we also note the local maximum at $\theta = 0$ which is a third, unstable equilibrium.

In the same Figure, we examine the influence of the actuating strain on the energy

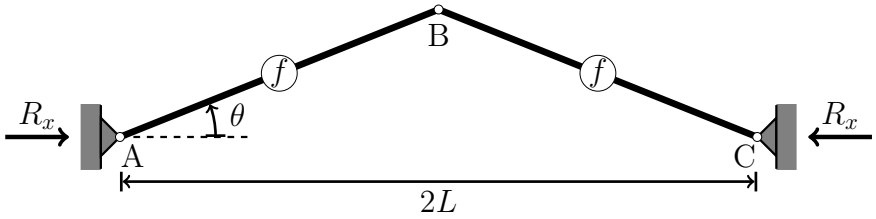

Figure 7.3: The same structure as in Fig. 7.3, but with an embedded actuators, f, in each rod. Applying strain through such a system, actively actuates the structure, but also alters the energy landscape, as shown in Fig. 7.4.

landscape. For increasing ϵ_f the plots appear lighter, and show the minima moving towards θ equal zero. Once they meet at that point, the structure appears to be monostable, since a single minimum exists for that value of actuating strain. In practical terms, this corresponds to both rods being horizontal. Reducing the actuating strain from this configuration forces the arch into one of two stable geometries (with B either above or below the AC line), but a slight perturbation is needed to choose the one over the other. This example shows how persistent internal actuation can "shift" a structure from a bistable to a monostable regime.

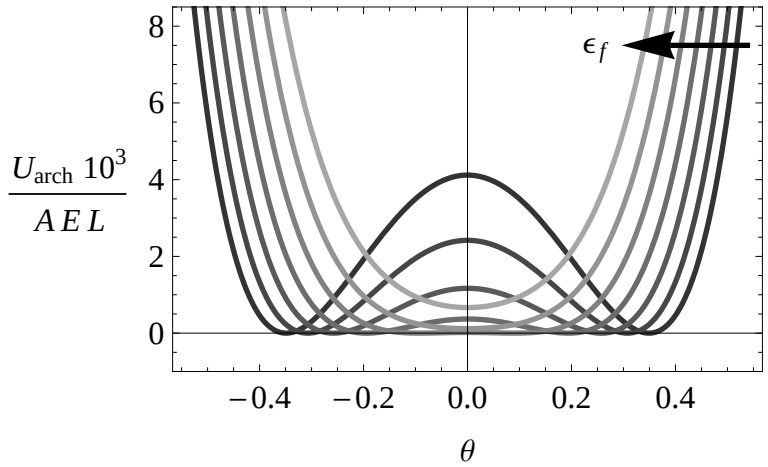

Figure 7.4: Strain energy of the bistable arch in Fig. 7.3. The darkest plot shows the energy landscape with not internal actuation. We clearly distinguish the two symmetric minima that signify two stable geometries for the system. A third inflection point at $\theta = 0$ is a local maximum with respect to the energy and hence an unstable equilibrium. For increasing actuating strain, ϵ_f, the minima move closer together with respect to θ, until they meet at a single minimum for θ equal to zero.

This section provided closed-form calculations and interpretation of graphical results for a single DOF actuated structure. In this context, we defined the concept of a snap-through event and described the relevant characteristics of the strain energy and force-displacement plots. The behaviour of the same system when embedded actuation is used was also examined, shown the change in the energy landscape. None of these ideas change significantly for higher DOF, but they become increasingly harder to explain in closed-

form or graphically.

7.3 Actuating multistable shells

Actuation of generic, monostable shells encompasses an extensive and challenging field. There is a growing number of "smart materials" that can be used for such a purpose, and choosing the right one depends on the specific requirements of the application. A review by Huber *et al.* (1997) provides a comprehensive guide, taking into account various performance metrics. In most cases, beyond choosing an actuator, additional decisions have to be made with regards to the location and number of devices.

Since many engineering shells are constructed with composite laminates, one heavily-studied category of actuators is based on piezoelectric materials. This preference is justified since thin layers of piezoelectric materials can be embedded in a laminate and in combination with a voltage provide means of actuation. In addition, many such studies focus on dynamic effects that require a quick response time by the actuator. In this regard, piezoelectric actuators are highly advantageous. On the other hand, the ceramics usually used for the construction of such actuators have a limited capacity for strain, and consequently can be disadvantaged by the large strains that multistable shells might undergo.

The motivation for the actuation of multistable shells is fairly different, since our objective is to overcome the "potential well" that separates two stable states, rather than provide real time actuation to a continuum of geometries. In addition, from work by Fernandes *et al.* (2010) we know that the ability to provide orthotropic actuation—*i.e.* have separate free strains in the two in-plane directions—will also be a desirable feature; uncoupled multi-parameter actuation expands available actuation paths. This creates very specific requirements in terms of achievable strains by our structure and by extension defines the desirable strains for our actuation mechanism.

Our theoretical model is based on a calculation of the strain energy, and thus provides a direct resource for studying energy-favourable actuation paths, as well as the related energy expenditure. Some of these capabilities were shown by Fernandes *et al.* (2010). They describe a method of actuating multistable shells such that dynamic effects are avoided. However, this involves a specific practical example and does not optimise energy requirements. A more detailed description of the concept is given in Section 7.5. First, a practical concept for the actuation of multistable shells is shown in the following section, to add a realistic view of the geometric transition.

7.4 An alternative actuation concept

The following section describes an alternative method of actuation between the two stable geometries of a spherical cap. Using a commonplace polymer, cured together with iron particles, we create a magnetic rubber composite. With this material we construct a magnetically sensitive bistable shell. This structure is manipulated to a second state by the body force exerted by an array of Neodymium, N42 grade magnets.

To observe this transition, a high-speed camera recorded the event. The resulting footage allows us to make a number of observations including the favourable transitional geometry, the duration of the snap-through movement and the required forces and distances between the two bodies. A Finite Element simulation is constructed and compared to the physical results. This virtual model is initially set up in a perfectly symmetrical configuration, and later on a slight tilt is introduced to investigate the effect of geometrical imperfections on our experiment.

7.4.1 Shell design and manufacturing

The bistability of the spherical cap has been investigated previously in depth (Brodland & Cohen, 1987; Chien & Hu, 1956; Wittrick *et al.*, 1953). The overlap of this phenomenon with thermal loads on thin shells has also been the topic of some studies (Aggarwala & Saibel, 1970). The parameters of interest for such a design can be limited to the dimensions of the shell; its thickness and the ratio of its height to its curvature. In addition, we want to ensure the material can withstand the resulting strains.

The shell is constructed with the material described above and according to the following geometrical specifications: the radius of curvature of the shell is 22 mm for a cap of base radius equal to 18 mm. Various thicknesses are created and tested, in the range of 1–3 mm. Appropriate male and female moulds are constructed through 3D printing technology—specifically, the commercially available MakerBot Replicator^{TM} is used (MakerBot Industries, LLC, 2012). The moulds are sanded and treated with an anti-stick spray, which helps the removal of the samples after curing.

The material chosen for the shells has an array of advantages. Polydimethylsiloxane (PDMS) is commercially available and relatively cheap. From an engineering perspective it is desirable in this case for its high capacity for strain, its formability, its easy curing, and its ability to allow various inclusions—here, iron trimmings are used. The commercial name of the PDMS we use is the Sylgard®184 Silicone Elastomer, to which the iron is added at a proportion of 50% by weight. After pouring the mixture in a mould, the samples are cured for 45 minutes at 100°. We give the relevant mechanical properties in Table 7.1.

E (kPa)	G (kPa)	ν
750	250	0.5

Table 7.1: Approximate mechanical properties for PDMS; E and G are taken from Lötters *et al.* (1997), ν is given the commonly accepted value for rubbers.

7.4.2 Experimental setup and observations

In order to film the snap-through behaviour, the spherical cap is secured to a thin cylindrical rod by a pin through its centre. The magnets are placed on a movable base with the centres of the two objects aligned to the axis of the supporting rod. The movement of the magnets is finely adjusted through a threaded rod directly connected to them. The magnets are then manually moved at a slow pace ($< 1\,\mathrm{mm/s}$) until the snap-through is observed. Considering the relative speed of the magnets to the speed of the snap-through, we can assume the setup to have been stationary for the duration of the shell transition.

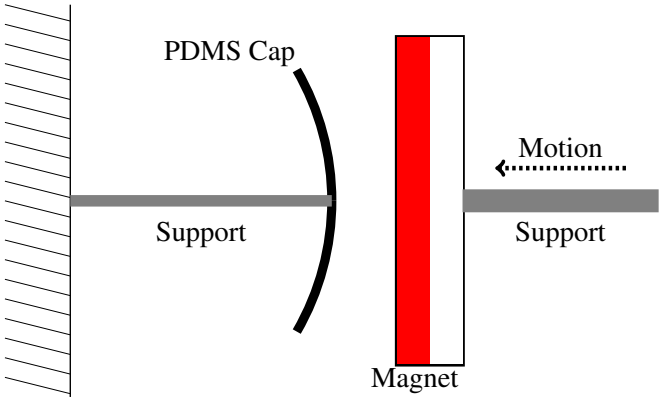

Figure 7.5: Diagram of the experimental setup for remotely actuating a PDMS spherical cap with a permanent magnet. The cap is stationary while the magnet is moved via a support towards the cap until a snap-through is observed.

The high-speed camera is a Phantom v12.0 (Vision Research Inc., 2013), which is capable of capturing 3000 frames per second: so, for a few tenths of a second for a full transition, we are afforded a few hundred frames at this rate. At such high shutter speeds, high luminescence is required and is provided by suitable floodlights. The brightness of the images is then slightly manipulated to enhance the contrast between the shell and the background—the software provided with the camera includes this feature.

The transitions in every tested case are asymmetric, since one side of the shell initiated the movement towards the magnet. The opposite edge of the shell is pushed backwards and a temporary S-shape is observed. As parts of the shell approach the magnets the external magnetic force overcomes the intermediate internal stresses and the shell is pulled to a full reversed geometry. Since the external body force is not immediately removed, the edges continue deforming towards the magnets. The resulting shape until the removal

of the external force approaches a cylindrical geometry, since two opposing sides of the shell's periphery approach the magnet. When the magnet is pulled away, the shell remains at an approximately spherical geometry, with a narrow band of opposite-sense curvature at the boundary.

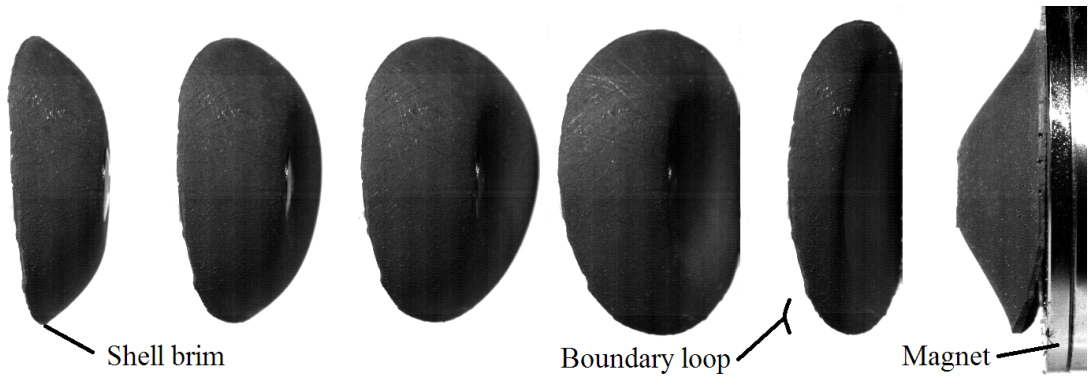

Figure 7.6: A high-speed camera captured the transition of the shell—an event that approximately lasts a tenth of a second. One noteworthy aspect of the transition is the non-axisymmetrical geometry that develops during the snap-through. This is a consequence of the high circumferential stiffness at the brim of the shell. The "boundary loop" is opposing stretching, and bending action is favoured in the shell's global response.

7.4.3 Finite element model

Despite the impressive capabilities of modern high-speed photography, the data we obtain is only visual, hence an FE model is constructed for comparison and some quantitative results. Abaqus/CAE (Abaqus, Inc., 2007) is used to design a part matching the physical shell described above. A deformable 3D part was created and given the swept shell configuration available in the Abaqus graphical user interface. The dimensions were prescribed according to the physical shell, with the meshing on Abaqus resulting in a total of 1571 elements. We fixed a circular area in the centre of the part to simulate the pin constraint, while the magnetic pull was modelled as a body force. The force had a spatially varying amplitude, explained further in the following section. A Dynamic Implicit step was used for the loading. The force was applied instantaneously on the structure while the duration of the step was 0.1 s with a maximum step increment of 0.0004.

Magnetic field and force

The magnetic field of a permanent magnet is not always a straightforward calculation. It depends on the exact geometry of the magnet itself, as well as on the magnetic material and surrounding medium. The calculation involves multiple integrals over a complex expression (McCraig & Clegg, 1987). In addition, material imperfections and geometrical

irregularities can alter an idealised formula. In this case however, we are mostly interested in the qualitative interaction of the structure with the magnetic body force, so a rough description of the field will suffice. Here we use a numerical estimation from Blinder (2011) for a cylindrical permanent magnet, which involves a triple integral that is solved numerically in cylindrical coordinates. The `FindFit` function in Mathematica is used to obtain an analytical expression usable in Abaqus: suitable polynomial expressions are chosen for both the radial and axial components of the field and the corresponding coefficients are found through a least-square fit. A comparison between the polynomial, best-fit expression and the original, analytical expression is plotted in Fig. 7.7 and shows a close match.

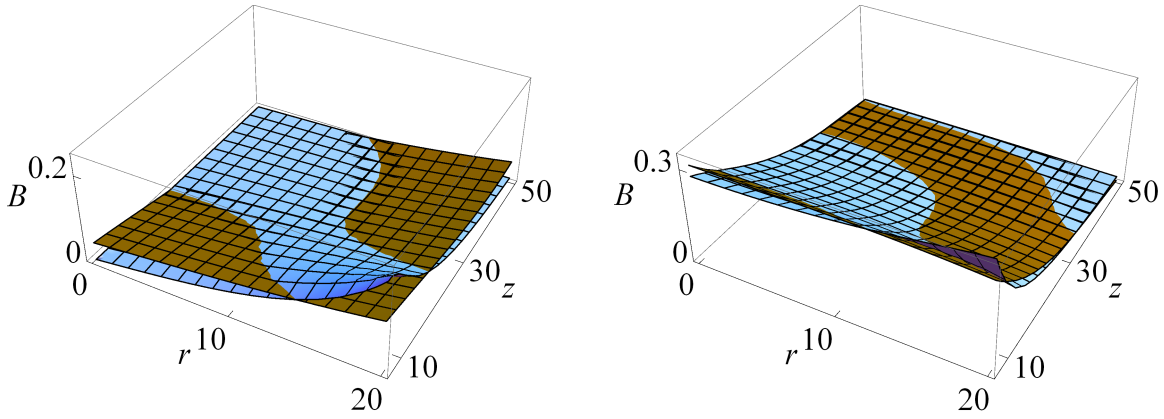

Figure 7.7: The radial (left) and axial (right) components of the magnetic field of a permanent cylindrical magnet. The blue surface represents a numerical estimation of the field and the brown surface shows a polynomial best-fit obtained in Mathematica and used in Abaqus.

The corresponding body force depends on both the magnetic field and the concentration of the carbonyl iron particles. The force is given by

$$F = \frac{(\delta\chi)VB(\nabla B)}{\mu_0} \tag{7.8}$$

taken from Veeramachaneni & Carroll (2007), where $\delta\chi$ is the volume magnetic susceptibility difference between the particle and the surrounding medium, V is the magnetizable volume of the particles, B is the magnetic flux density in Tesla (T) and μ_0 is the magnetic susceptibility of free space. For calculating the magnetic field intensity, we also need the the magnetic moment per unit volume for iron carbonyls, M. In Abaqus, we express this as the analytical field of a body force, hence the volume is directly taken from the model for each element. As explained above, the magnetic field and consequently its gradient, are obtained in an approximate, closed-form. The values of the remaining relevant parameters used in Eq. (7.8) are listed in Table 7.2.

Property	Value	Reference
PDMS specific gravity	1.03	Dow Corning (2007)
PDMS specific gravity	1.03	Dow Corning (2007)
Iron specific gravity	7.87	
Neodymium magnetization / volume	1.03×10^6 A/m	
μ_0	$4\pi \times 10^{-7}$ N/A^2	
$\delta\chi$	0.20	Gorodkin *et al.* (2009)

Table 7.2: Magnetic and material properties needed to estimate the magnetic force between a Neodymium, N42 grade permanent magnet and an iron/carbonyl-infused PDMS structure.

Loading cases

Two separate models were then tested. In one, the shell, the boundary condition and the magnetic force were all modelled as perfectly axisymmetric. In the other, an angular tilt of 5° was applied to the shell at the apex with respect x-axis. This slight modification helps explain the non-axisymmetric transition geometries. Even for slight angular eccentricity, the transition shapes differ significantly from axisymmetric geometries.

For both these cases, the strategy for the simulations was to initially place the shell at a certain distance from the virtual centre of the magnet. During a single Dynamic step the body force was continuously applied. The simulations were started with the magnet at 10 mm from the magnet and moved by 1 mm each time. The snap-through ceased to occur at 14 mm for both the axisymmetric and the eccentric case.

We mainly focus on two quantitative outcomes extracted from these simulations: In Figs. 7.8 and 7.9, the strain energy of the shell is plotted for four separate scenarios. On the top plot we show the axisymmetric case, while at the bottom plot the eccentric case. When the field is too weak for snap-through to occur, we observe an oscillation that settles at a higher energy, representing an equilibrium with the applied magnetic force. Conversely, when the snap-through does occur, a higher energy representing the second stable geometry is observed. Again, this is slightly higher than the resting energy since the magnetic field is not removed.

The other significant qualitative outcome is the transition geometry, since Abaqus allows us to take a close look at intermediate geometries during the snap-through. Some selected intermediate geometries from both cases are shown in Figs. 7.8 and 7.9. When we constrain the geometry to an idealised axisymmetric geometry, the transition is forced in an axisymmetric manner as well. Even slight deviations from a perfectly axisymmetric setup—here implemented through a slight tilt of the shell, cause a dramatically different intermediate geometry. Specifically, the characteristic S-shaped geometry—also shown in our high-speed photography footage—is observed.

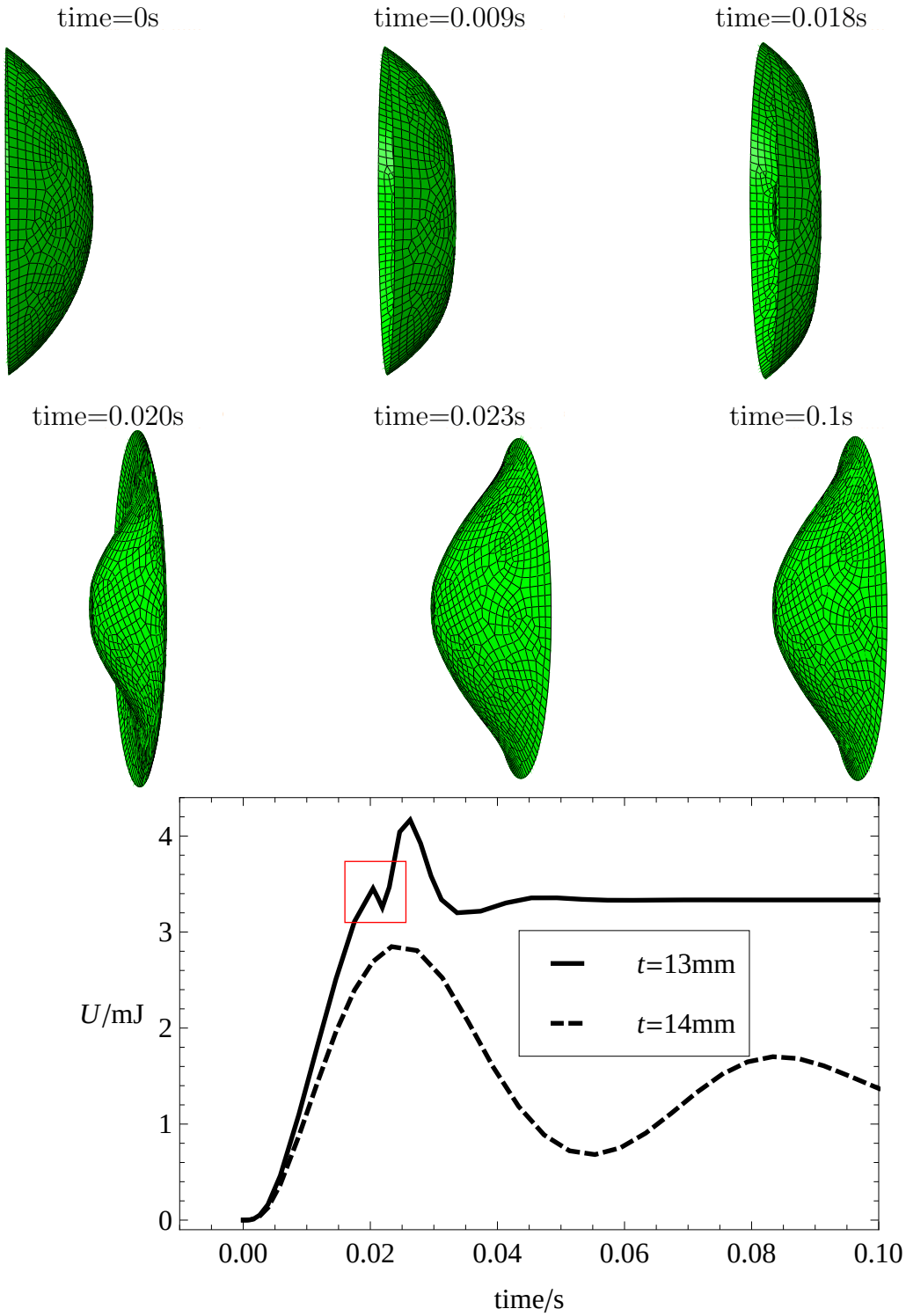

Figure 7.8: Strain energy plots for FE simulations of a symmetrically-supported shell (bottom). A series of simulations were performed at different distances to mark the location of the transition location—shown here to be between 13 and 14 mm. The successful transitions display a snap-through event and an energy minimum marked on the plots with a red square. The FE simulations afford us a closer look at the intermediate geometries (top). For the idealised symmetric case, the transition shapes are axisymmetric, an effect that we were unable to capture in a physical setup. Shown here is the spherical cap, with its centre at a distance of 13 mm from the centre of the magnet we describe in the text. The magnetic poles are along the z-direction.

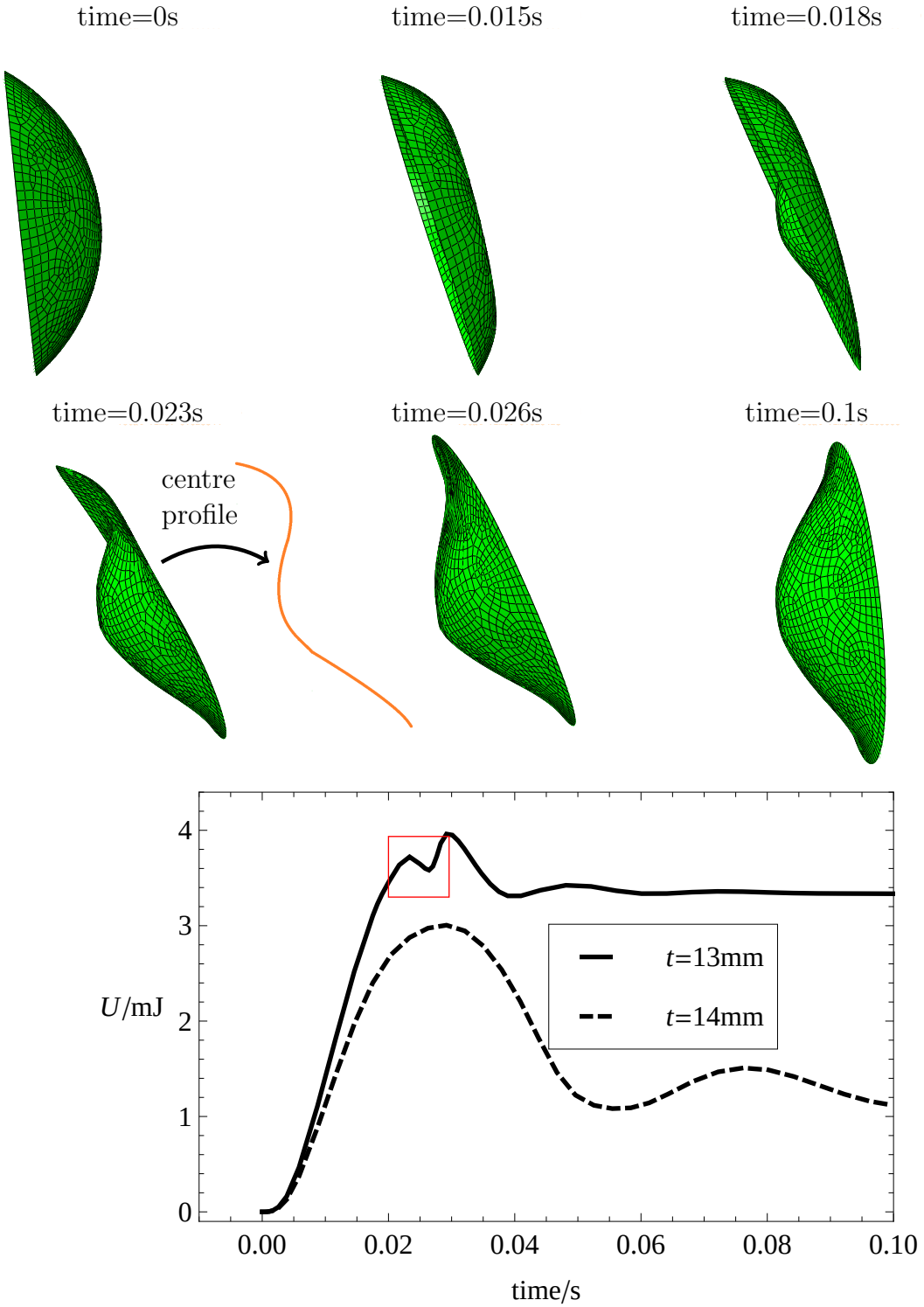

Figure 7.9: Here, the simulation in Fig. 7.8 is modified. When a slight eccentricity is introduced to the initial tilt of the shell with respect to the direction of the magnetic field, a dramatic change in intermediate geometries is observed. Specifically, the characteristic S-shaped transition shape is preferred by the structure, which agrees with our experimental observations. This shape resembles a surface with linearly varying curvature in one direction across the shell planform, and a uniform curvature in the other direction. A similar geometry is examined by Vidoli (2013) and is shown in Fig. 7.13.

7.4.4 Significance of results

This section presented a novel actuation technique for multistable shells. The most noteworthy elements of this work are summarise here:

- A material, common in other fields, was suggested for multistable shells, such that remote actuation is facilitated. Specifically, PDMS infused with iron particles is used for the construction of a bistable, spherical cap. The result is a structure susceptible to magnetic actuation.
- For the first time, the dynamic transition of the shell between the original and everted states under the influence of a magnetic field is captured on a high-speed camera. Footage of the 0.1 s transition is useful in observing intermediate geometries.
- Quantitative understanding of the inversion mechanism is made possible by exact finite element modelling of the cap throughout the deformation. This yields the system's energy during actuation as well as the corresponding stress and strain fields on the shell.

The UC framework used throughout this work is capable of accounting only for in-plane actuating stresses and consequently for embedded actuation. It is incapable of incorporating the effects of a spatially varying body force like the one described in this section. The remainder of the Chapter and Section 7.5.1 in particular, explain the limitations of the UC model further.

7.5 Quasi-static actuation and UC model limits

In section Section 7.4, we investigated some practical aspects of multistable shell actuation, in what was a display of a characteristically dynamic event. By encouraging slow, deliberate actuation, it is possible to achieve quasi-static transitions, as explained in Section 7.2 and shown in Fig. 7.2. An obvious requirement for this is fine control over the actuating forces, and real-time monitoring of the structure's stiffness—or displacement control. This suppression of the dynamic nature of the snap-through event is the only option for single-DOF systems. In higher DOF systems the same principles apply, but since the actuating path is not unique, there are sometimes paths that avoid the dynamic transition all together.

Fernandes *et al.* (2010) proposed a quasi-static route between two stable states for an asymmetric laminate shell, which is facilitated by stresses locked into the material during the curing phase. This design allows for the initial curvature to be ignored in the strain energy expression and some closed-form solutions for critical actuation values

are produced. Numerical tracking of stable solutions is an additional tool used for this investigation; for a range of values for the actuating curvature parameters, defined as H_x and H_y, the stable equilibria are solved for numerically. Figure 7.10 is taken from that work and shows the actuating curvatures used to achieve a quasi-static path, *i.e.* at each point during actuation, the actuating and built-in stresses in the shell are in equilibrium. The two plots show the real geometries that the shell goes through, while acted upon by the corresponding actuating curvatures in the second plot. By following an appropriate path, a dynamic transition is avoided, but the beginning and end geometries are different.

It is useful to expand this investigation to include initial curvatures. The motivation for this is multifaceted, but for example, initial curvature of the structure allows for a much greater range of materials to be used. Otherwise, the only materials available to us are those capable of carrying prestress or having specialised mechanical properties. In addition, we previously showed that initial curvature is a prerequisite for tristability. Hence, for examining the actuation of tristable shells, initial curvature needs to be included. At the same time, following quasi-static paths can be essential in a multitude of applications where dynamic effects are undesirable. In fact, dynamic effects are almost always undesirable and at the very least require separate study to control for their influence.

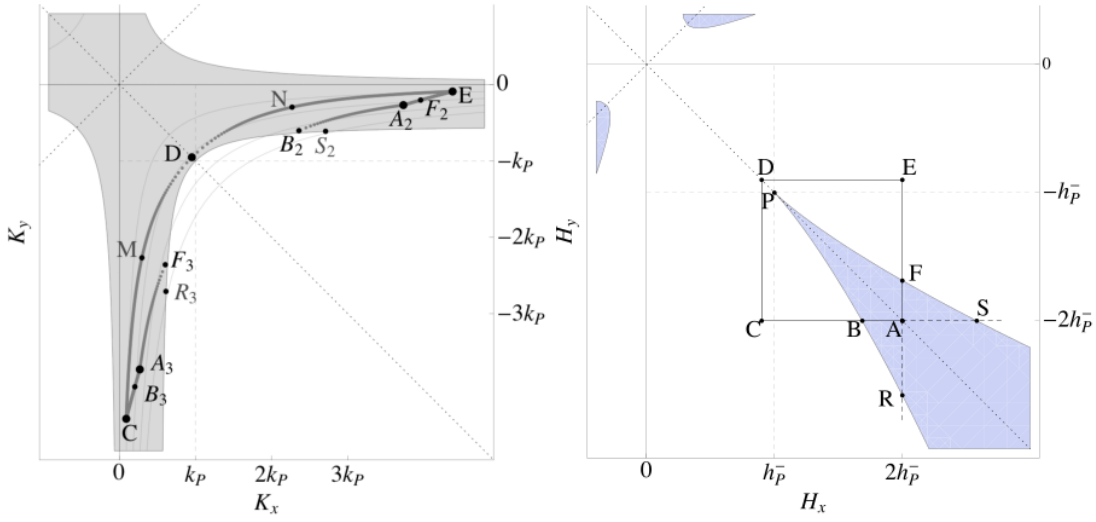

Figure 7.10: The strategy followed by Fernandes *et al.* (2010) to achieve a quasi-static transition between two (pre-stressed) stable states. On the plot on the left we see the real curvature variation from the A_3 geometry to the A_2 geometry. By adjusting the actuating curvature—shown on the right plot, the path BCDEF is followed. This avoids dynamic jumps and instead treads a quasi-static path. The point A in the right plot corresponds to both points A_2 and A_3 in the left plot, a feature made possible by allowing opposite-sense residual stresses in the material.

7.5.1 Actuation of a bistable shell

The first example we use here is a bistable, spherical cap made from an isotropic material—a structure directly comparable with the one used in Section 7.4. Using a similar visualization as Fernandes *et al.* (2010), Fig. 7.11 shows the real geometries of such a shell, in response to dual-parameter, orthotropic actuation. With respect to our formulation, these variables can be modelled directly with the h_{xF} and h_{yF} parameters, as they appear in Eq. (5.18). In practical terms, they correspond to imposed curvatures either from embedded actuators or prestressing or a heat gradient etc. The red dot and the orange squares represent the initial and secondary unstressed, stable equilibria respectively. The green triangles represent the updated stable states while actuating stresses are applied. The black diamonds represent unstable equilibria or inflection points. The background is a logarithmic contour plot of the updated strain energy of the system.

In this case, an equal negative prestress is applied in both orthogonal directions and gradually increased in magnitude. A green triangle representing the initial equilibrium departs from the original geometry (red dot), but eventually disappears from the plot when it meets an inflection point (black diamond). The infection points in turn mark locations of zero value for the determinant of the Hessian, and since we encounter such points on both the first and third quadrants, we can infer that there is no stable path between the two regions of positive Gaussian curvature.

For further information, the minimum eigenvalues of the equilibria for the region of interest are plotted in Fig. 7.12. At the value of prestress that the equilibrium meets the inflection point, the minimum eigenvalue diminishes. Hence, it is once more of interest to examine the boundaries where the determinant of the Hessian is zero—they mark the limits of possible geometries for stable equilibria. These boundaries can be found in closed-form:

$$\kappa_y = \pm\frac{(2h_{x0}^2\kappa_x - 2\kappa_x\bar{\nu}) + \sqrt{(\kappa_x^2+1)\,(h_{x0}^4 - 2h_{x0}^2\bar{\nu} + 3\kappa_x^2 + \bar{\nu}^2 - 1)}}{3\kappa_x^2 - 1}, \tag{7.9}$$

$$\kappa_y = \frac{2h_{x0}^2 + \bar{\alpha}}{2\kappa_x}, \tag{7.10}$$

and are plotted in Fig. 7.12. Recall from Section 5.3 that when the modular ratio, β, is equal to one, then $\bar{\nu} = \nu$ and $\bar{\alpha} = 4\alpha$; this assumption is made for the examples that follow. These lines define boundaries for the possible transition geometries of the shell during actuation, according to the UC model. **Not all geometries within these limits can be reached, but none outside them can**. Even though these do not give us exact, closed-form solutions for the transition path for all control parameters, they narrow down the practical shape possibilities significantly. In a recent study, Vidoli (2013) showed a similar conclusion for the transition between regions of positive Gaussian curvature, but

using a numerical argument. The same work provides some corroboration with respect to the intermediate geometries observed in Section 7.4. In particular, assuming a Linear Variation of the Curvatures (LVC), a more elaborate description of geometrical states becomes possible. One consequence of this formulation is that the transition between two geometries of positive Gaussian Curvature can be fully mapped out as shown in Fig. 7.13. A direct quantitative comparison though would be unrealistic since incorporating a spatially varying body force in the LVC model is not trivial.

7.5.2 Actuation of a tristable shell

The same technique is used to visualise the available quasi-static actuation paths through single and dual parameter actuation for a tristable shell. These efforts also establish the inability of the UC method for realistic description of complete transition geometries.

In Fig. 7.14 we track the actuated geometries of an initially doubly-curved tristable shell. The material is defined to have a high Poisson ratio and high shear stiffness ($\nu = 0.9$, $\alpha = 1.4$), while the dimensionless prestress is increased in intervals of 20, with h_{xF} and h_{yF} taking opposite signs. The intention is to actuate the initial—almost cylindrical—state to the symmetric, same-sense second stable state. The initial geometry is shown in the upper right quadrant with a red dot. The quasi-static geometries during actuation are shown with green triangles that move with the variation of prestress. At the ($h_{xF} = -h_{yF} = 40$) frame, the actuated shape originating from the primary geometry is approaching the black/diamond inflection point. Past their encounter, at frame ($h_{xF} = -h_{yF} = 60$), this actuation path is interrupted, since no continuous succession of stable solutions exists.

Similarly to the scenario in Fig. 7.11, we do not observe a continuous, quasi-static path to a secondary equilibrium state. This persists for additional uni-parameter and dual-parameter actuation paths that are omitted here for brevity. Intuitively we might expect that decreasing the high curvature—in this case in the y-direction—and increasing the low curvature—in this case in the x-direction, would plot a continuous path between the two states. This result indicates however that such a path is not available under the UC assumption and some spatial variation of curvature is necessary for quasi-static transition equilibria. In mathematical terms it shows there is a set of shell shapes for which no stable equilibria exist under the material and geometrical assumptions we are making. Since those shapes lie between the stable configurations we have established, no quasi-static path can exist between the two.

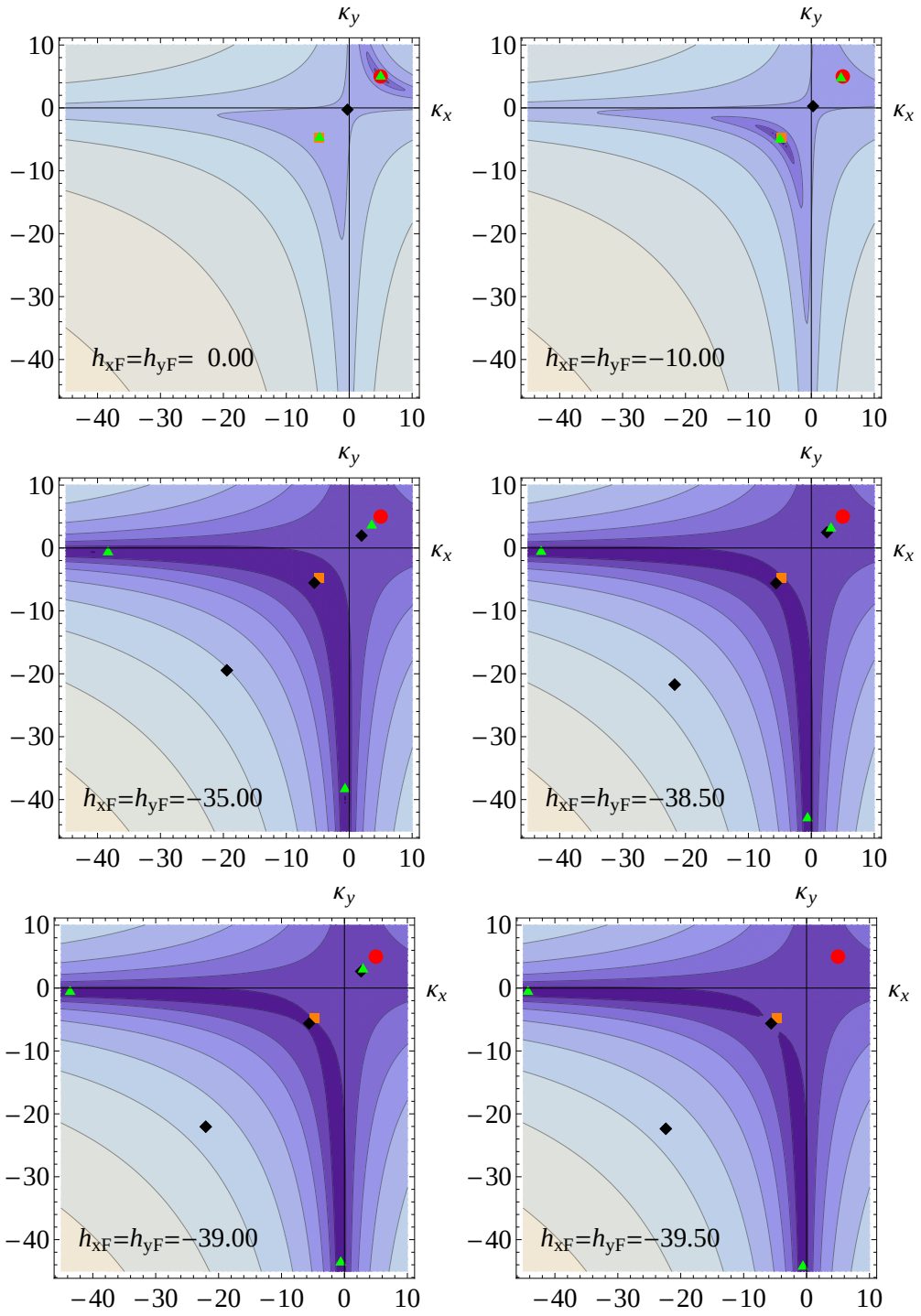

Figure 7.11: This series of graphs shows contour plots of the dimensionless strain energy for fixed material parameters and a varying prestress—one benefit of having a simple expression for the overall strain energy of the shell is that we can observe actuated behaviour with little computational expense. The red dot and orange square are the initial and secondary stable states respectively. The green triangles are actuated quasi-static geometries and the black diamonds are unstable equilibria—or inflection points. This example of a bistable spherical cap shows that a quasi-static transition is an impossibility. Even for smooth increments of the prestress, stability is lost while transitioning between the two regions of positive Gaussian curvature. This is a weakness of the Uniform Curvature model.

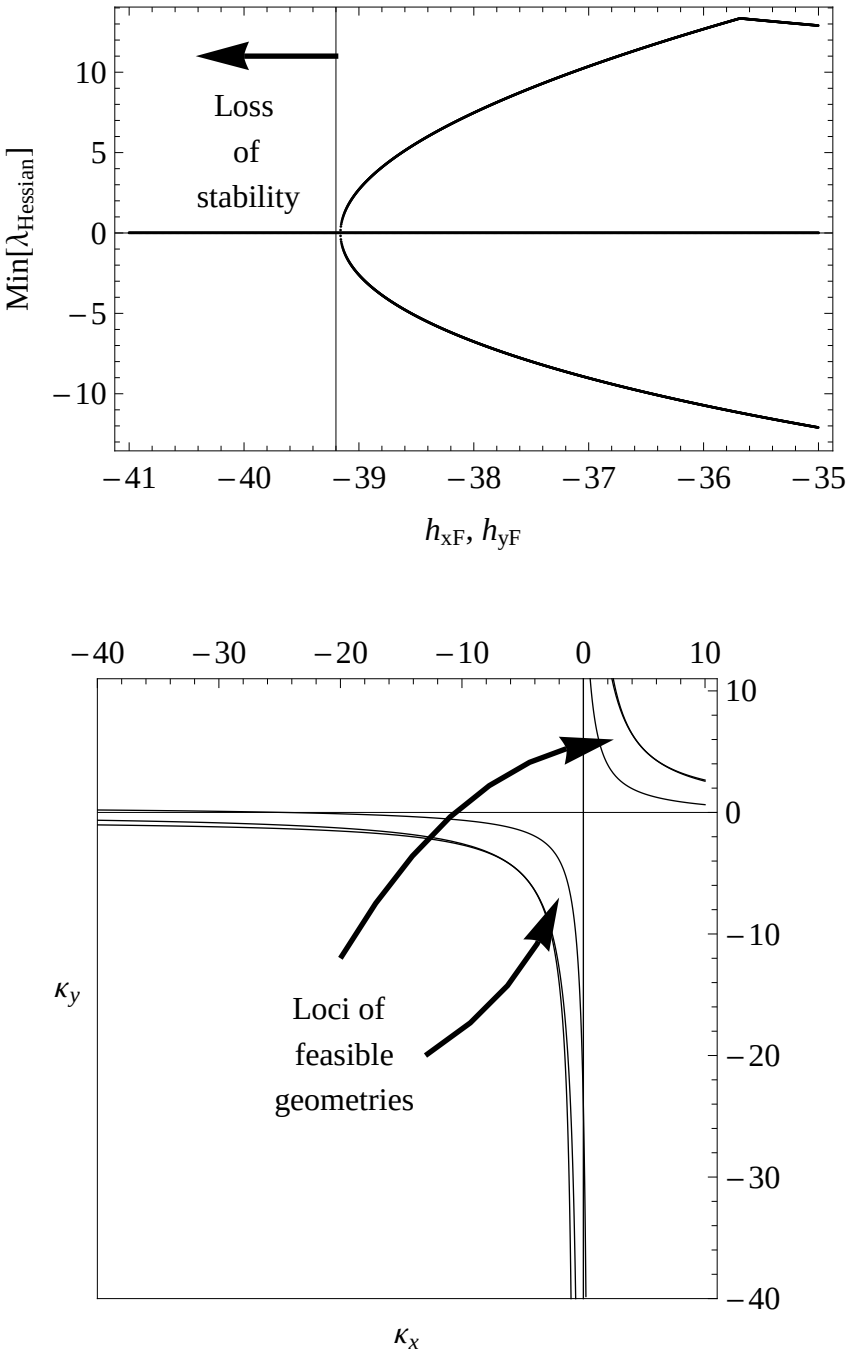

Figure 7.12: Figure 7.11 shows an effort to gauge the predictive capacity of the UC model for shell geometries during orthotropic actuation. The model is not capable of tracing quasi-static actuation between certain stable states. On the top plot here we show the minimum eigenvalues of the Hessian for the corresponding equilibria in this range of prestress. The bottom plots show closed-form boundaries—defined by Eq. (7.10)—where the determinant of the Hessian diminishes. The corresponding points on the top plot all lie on the (h_{xF}, h_{yF}) axis. They give a range of possible shapes for the shell during actuation but at the same time mark the limits of reliability for the UC model. Not all the geometries within those boundaries are feasible but those outside them are not achievable under our assumptions.

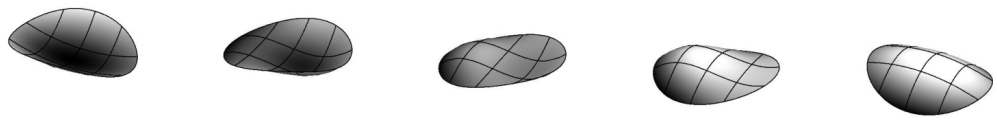

Figure 7.13: Vidoli (2013) formulated a description for multistable shells assuming a linear variation of curvatures. Consequently he was able to surpass the UC limitations established in Section 7.5.1 and described a continuous route between two geometries of positive Gaussian Curvature for an elliptical shell. Although a quantitative comparison—taking an actuating body force into account—is not possible, the intermediate geometries offer corroboration to our observations. Specifically, the characteristic S-shape of the intermediate state is favoured by the LVC model.

7.6 Energy optimization

In Section 7.5, we showed that the UC model is not always capable of providing quasi-static actuation paths. Removing the quasi-static actuation requirement, *i.e.* allowing for dynamic transitions, enables additional information to emerge. For example, in Chapters 5 and 6, the UC model proved robust in predicting the final geometries of multistable shells, or in mathematical terms the available strain energy minima. Locating the inflection points of the strain energy, and accurately describing the stress-free energy landscape can be a powerful tool in predicting energy requirements for actuation, and predicting approximate dynamic transition geometries. In this section, some relevant mathematical concepts are presented.

For a closed system, the energy landscape does not change. In the case of multistable shells, without an actuating stress field, the UC model can provide us with a closed-form energy landscape with respect to the geometry of the shell. Finding the absolute energy difference between two minima in this context is trivial. What is more significant is the energy barrier between the two. This can be measured by the value of unstable equilibria in the energy landscape. Once a shell reaches a geometrical shape matching such an inflection point, it can "fall" into a secondary state without additional energy input. The inflection points are found by requiring that:

$$\frac{\partial U}{\partial \kappa_x} = 0 \quad , \qquad \frac{\partial U}{\partial \kappa_y} = 0 \quad , \qquad \frac{\partial U}{\partial \kappa_{xy}} = 0, \tag{7.11}$$

$$\Big|\mathcal{H}\big(U\big)\Big| \leq \mathbf{0}. \tag{7.12}$$

Similarly in the absence of continuous actuation, the preferred intermediate shapes of the shell are easily identified from the energy landscape alone. For actuation-free movement between inflection points, the shell deformation follows the "valley path" on the

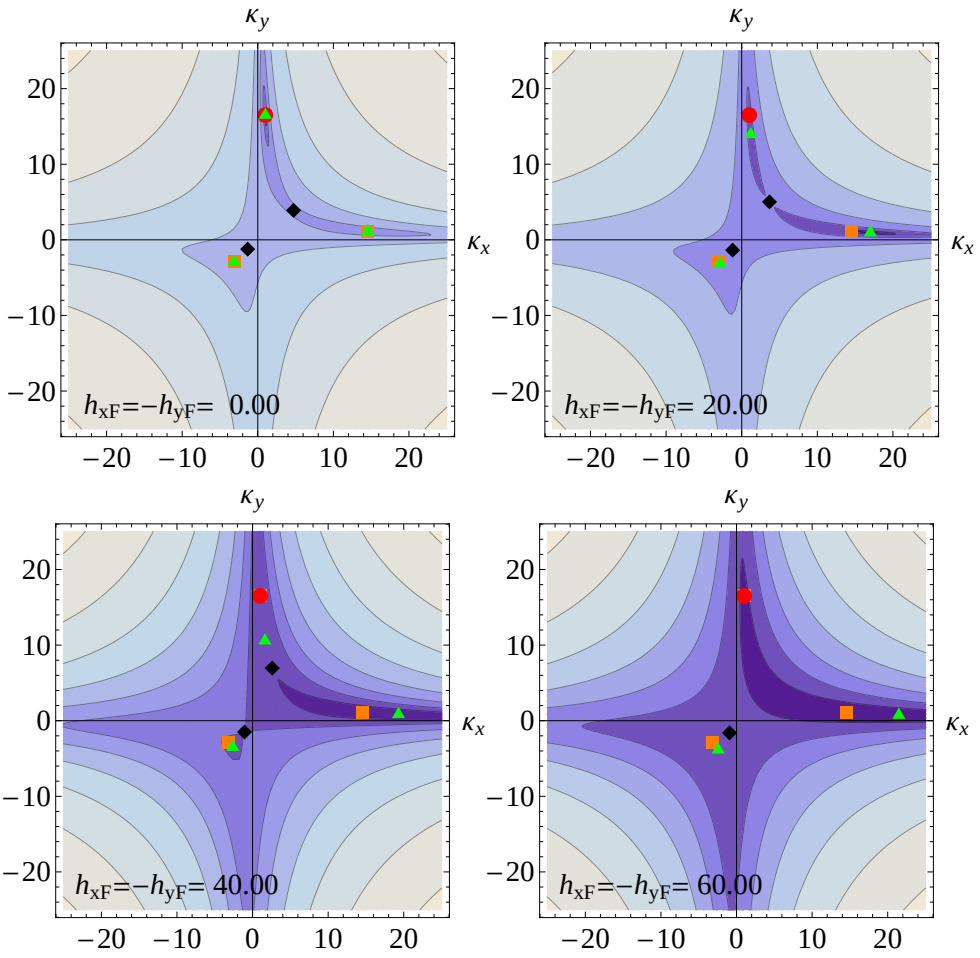

Figure 7.14: Efforts to track possible quasi-static actuation paths for a tristable shell design are not always possible under the UC model. In this scenario, dual-parameter actuation attempts to push the initial—almost cylindrical—geometry (red dot) to the second, same-sense geometry. Similarly to the spherical cap examined by Fig. 7.11, the actuated geometry becomes unstable when it encounters an inflection point. Secondary stable states are indicated by orange squares, while inflection points by black diamonds. The green triangles are the transition states during actuation.

energy landscape. Mathematically this is defined by the direction given by the eigenvector of the smallest positive eigenvalue of the Hessian (Quapp & Heidrich, 1984). The eigenvector is the solution for $\boldsymbol{v_m}$ of

$$\mathcal{H}\boldsymbol{v_m} = \lambda_m \boldsymbol{v_m} \tag{7.13}$$

where

$$\lambda_m = \min(\lambda) \quad \text{for all} \quad \lambda > 0 \quad \text{given} \quad \mathcal{H}\boldsymbol{v} = \lambda \boldsymbol{v} \tag{7.14}$$

Following the direction of this vector from a minimum will produce a continuous path to an inflection point. Each inflection point connects to at least two minima in this fashion. This route is known as the Minimum Energy Path (MEP) and is the main focus of a number of numerical methods attempting to map optimal paths in chemical reactions. Although many of the resulting algorithms are potentially of use for actuation design, they are beyond the scope of this work. We do provide a visualization of the concept though in Fig. 7.15, where we show both the set of stationary points and the MEPs connecting them in separate diagrams. Note that the MEPs in the bottom diagrams have to go through the inflection points because they define the minimum energy barrier between minima on the energy surface.

For cases where the shell is released from an unstable initial geometry, the energy landscape can again be used to predict the subsequent deformation of the shell. Similar to a ball rolling on a physical landscape under the pull of gravity, the geometry of the shell follows an MEP and rests at a minimum depending on energy dissipation. Given such an initial geometry, again a static energy landscape can be used to trace a favourable path. In this dynamic scenario though, inertial effects and energy dissipation are essential in predicting behaviour, so we do not expand on this further.

In the presence of prestress, the energy landscape is not static, hence tracking the corresponding energy values is not direct. Both inflection points and the MEPs change with respect to the geometry, while actuation stresses are applied. However, contrasting the initial energy contour plots in Figs. 7.11 and 7.14, with the subsequent actuated contour plots, note that the location of "valley paths" does not change dramatically. Hence, we can use Eqs. (7.11) to (7.14) to obtain an approximate actuation path given orthotropic actuation.

7.7 Concluding remarks

This Chapter established that the UC model can provide some useful design guidelines with respect to the actuation of different multistable shells. At the same time, it became

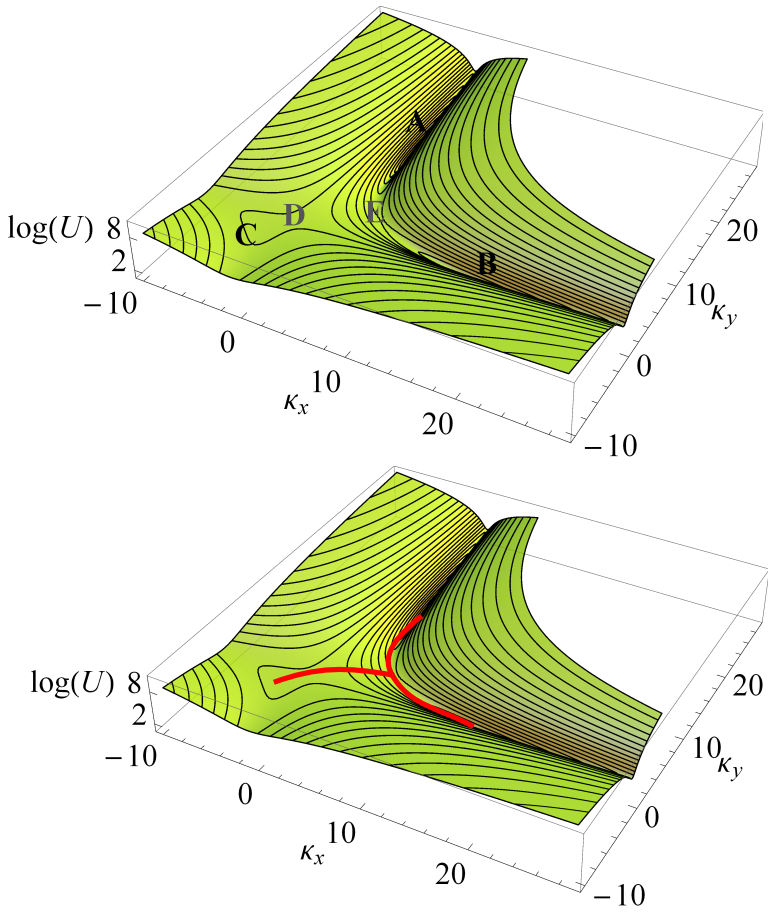

Figure 7.15: A plot of the energy surface for a tristable shell with the stable and unstable equilibria marked on the top and the Minimum Energy Paths connecting them shown at the bottom. In the top plot points A, B and C represent local minima and signify stable equilibria, while points D and E mark inflection points. The most efficient routes between stable configurations are through the inflection points as the bottom plot helps demonstrate. These are only valid when no actuating forces are applied and the energy landscape maintains this form, but they have a clear mathematical definition and can approximately guide our expectations for transition geometries.

clear that for certain cases, especially when the transition forces a change in the sign of the Gaussian curvature, the UC model fails to predict the intermediate behaviour.

In a separate section, a new material combination was used to construct a bistable spherical cap which was actuated remotely with an array of permanent magnets. The snap-through event was recorded with a high-speed camera and revealed the asymmetric intermediate geometries that the shell experiences. An FE model of the same experiment confirmed that small geometrical imperfections in the setup promote asymmetric intermediate shapes.

In the following Chapter, we propose an additional technology for the construction of multistable shells. It is shown through FE simulations and a rudimentary physical model, that multistability of thin structures can be achieved for non-composite grid shell and honeycomb structures with no prestressing.

Chapter 8

Beyond composites

8.1 Introduction

This Chapter introduces a new concept for manufacturing multistable shells. Grid shells and honeycomb shells are investigated from a homogenisation viewpoint, in order to generate appropriate material properties for multistability. A number of parametric Finite Element (FE) studies are performed and a rudimentary demonstrator is constructed.

8.2 Inspiration and motivation

Recall from Chapters 2 and 7 that manufacturing of multistable shells for the past few decades has been dominated by fibre-reinforced composites. Laminates in particular have been thoroughly studied and offer an array of beneficial characteristics. These advantages are also presented in Chapter 6, where we describe the construction of a tristable shell using exactly this category of materials. However, laminates also have a number of disadvantages: they are relatively expensive and they require skilled manual assembly and dedicated facilities. Most importantly though, they are harder to employ in continuous large-scale (in the order of tens of metres and above) and small-scale (in the order of millimetres and below) structures. For example, consider an equivalent structure for our tristable shell demonstrator at a much smaller scale. Our theoretical model does not depend on scale, so such a structure should be perfectly possible. However, scaling fibre-reinforced composites would be a very challenging—if at all possible—task; they are limited by the size of the smallest fibre and the limit at which their properties behave homogeneously. Conversely consider a design for a bistable roof structure; laminates would present a non-traditional building material and would immensely complicate construction.

Hence, there is clear motivation to find alternative ways of controlling material properties. One attractive approach is to use the local geometry of a material, as presented in Section 3.4. With such methods we can lower our dependence on more expensive

and often harder to manufacture composite materials. Some ways of manipulating the macro-mechanical properties of shells through patterning and texturing have been studied previously in this context. Recent examples of such concepts exist in the form of corrugated shells (Norman *et al.*, 2008a, 2009) and dimpled sheets (Golabchi & Guest, 2009).

Although these methods have their respective motivations and applications, here we seek as simple a technique as possible, to make manufacturing straight-forward and scalable. Taking inspiration for our composite material design, we note that the major stiffness contribution comes from the fibres. In fact the matrix mostly serves as a place-holder for those more essential structural components. Similar properties can be obtained if we removed material from a solid plate of an isotropic material, in such a way that reproduces the stiffening action of the fibres along particular directions. The creation of perforations is both a simple procedure and an easily scalable one. Recall from Chapter 3 that this concept corresponds to grid shells, honeycombs and perforated shells, whose global material properties can be manipulated by variations in the local geometry.

8.3 Grid shells

In Fig. 8.1 a diagram from Chapter 3 is reproduced to assist the reader. On the left a square beam lattice is viewed from above, while on the right, the same structure is examined from a different perspective that shows the local features of the beam cross-section. The ligaments of the grid shell are assumed to be an Euler beams, connected at fixed joints. This idealisation results in a simple homogenisation model in Chapter 3, where we show how the local geometry of simple grid shells can affect the global mechanical properties of the structure. We reproduce the related formulae from Section 3.4.1 here to assist the reader and provide some quantitative results outside the FEA that follows. The Poisson ratio and the shear stiffness parameter, as they relate to in-plane stretching, are given by:

$$\nu_{\mathrm{A}} = \frac{d^3 - 2db^2 + 2b^3(1+\nu)}{d^3 + 2db^2 + 2b^3(1+\nu)} \tag{8.1}$$

and

$$\alpha_{\mathrm{A}} = \frac{d^3 + 2b^3(1+\nu)}{d^3 + 2db^2 + 2b^3(1+\nu)}. \tag{8.2}$$

while the same parameters as they relate to bending, are given by:

$$\nu_{\mathrm{D}} = \frac{-400h^5b^2 + 252h^4b^3 - 21b^7 + 100h^7(1+\nu_s)}{400h^5b^2 - 252h^4b^3 + 21b^7 + 100h^7(1+\nu_s)}, \tag{8.3}$$

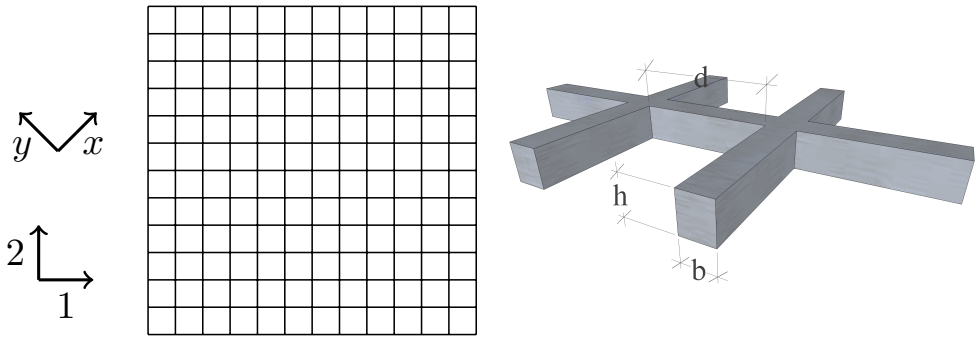

Figure 8.1: A diagram showing the square grid shell pattern and the dimensions of the beam cross-section is reproduced from Chapter 3 to assist the reader.

and

$$\alpha_{\mathrm{D}} = \frac{100h^7(1+\nu_s)}{400h^5b^2 - 252h^4b^3 + 21b^7 + 100h^7(1+\nu_s)}. \tag{8.4}$$

Substitution of dimensions under consideration can immediately produce corresponding values for these parameters, which in turn can be substituted in our dimensional expression for the energy, Eq. (6.14), from Chapter 6. This procedure is followed to produce certain plots later in this Chapter, but recall from Section 3.4.1 that typical local geometries for grid shells frequently result in values close to unity for all four of the parameters in Eqs. (8.1) to (8.4). Developable composite cylindrical shells with similar properties have been shown to exhibit multistability in the past, hence this category of structures is a likely candidate for an alternative manufacturing method. In Chapter 4 we showed that the modular ratio is a key parameter for multistability, while the absolute value of the moduli is only a scaling parameter with respect to the strain energy of the shell. Similarly, all the additional relevant design parameters can be adjusted by optimising the local geometry. Equipped with this knowledge, the idea of a grid shell or perforated shell multistable structure becomes a practical possibility.

It is to the advantage of the homogenisation method from Chapter 3 if the local dimensions are much smaller than the planform dimensions of the shell. However, in the simulations that follow, we also had to balance that theoretical requirement with practical considerations, such as the constructibility of the shell and computational cost. In the analysis that follows the global dimensions are more than 25 times the width of the unit cell. However, we also repeat our statement from Chapter 3 that we are dealing with elastic phenomena locally and hence the properties reliably scale.

8.3.1 Finite-Element Analysis

This concept for a bistable shell is tested through FE simulations on Abaqus (Abaqus, Inc., 2007). A number of parameters are required to fully define the geometry of such a structure. In this section we assume a cylindrical initial geometry for a shell with a

rectangular planform. Double curvature facilitates multistability—*i.e.* isotropic materials can be used for constructing doubly curved, bistable shells—so omitting it here ensures that the effects we observe are the product of global material properties, and not only of extensional effects. The set of required dimensions to fully define each geometry is as follows:

- Global geometry:
  - length of shell projection along x-direction (a_x)
  - length along y-direction (a_y)
  - cylinder radius of curvature—along x-direction(ρ_x)
  - global thickness: The global thickness for a grid shell is not a directly accessible quantity. We can simply assume the value given to the local beam-member height, or we can treat it with various homogenisation methods.
- Local geometry:
  - length of beam-members (d)
  - beam-member cross-section width (b)
  - beam-member cross-section height (h): We treat this as the global shell thickness as mentioned above.

These are shown in detail in Figs. 8.1 and 8.2.

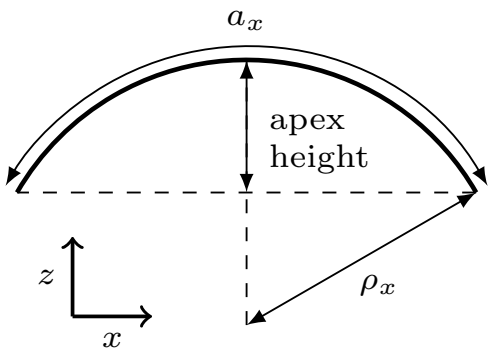

Figure 8.2: The global initial geometry of the shell is defined by the planform dimensions, a_x and a_y, and the initial curvature, ρ_x. Here we show that geometry in a side view that emphasises the relationship between apex height, planform dimension and curvature.

Abaqus has a graphical interface that facilitates defining the geometry of the structure we are examining, the loads, the boundary conditions etc. However, the resulting structures cannot be modified easily. In addition, the mesh-like, curved structure at the basis of our study, cannot be drawn with any standard tools and attempting to draw it manually (node by node) would be impractical. An alternative exists for the user in the direct

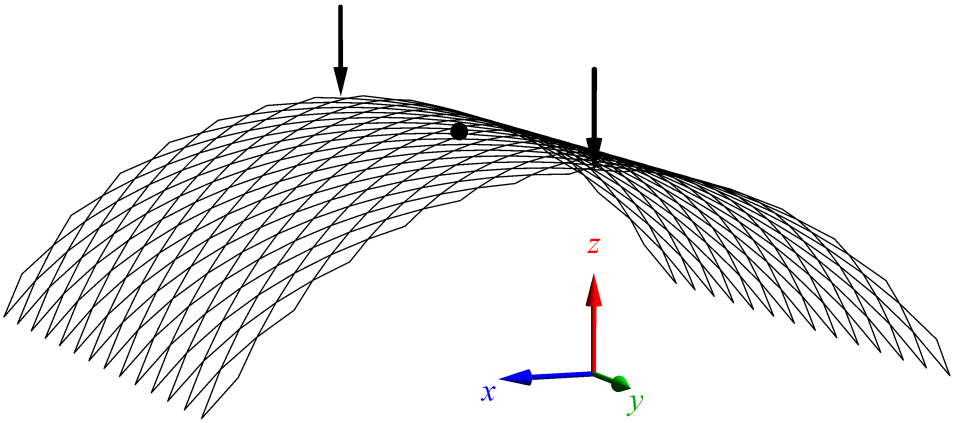

Figure 8.3: In a series of FE simulations using the Abaqus software package, a cylindrical grid shell is modelled with displacement control applied in the pattern indicated by arrows. The shell is free at the boundaries, but is constrained in all directions at the centre node (marked with a dot).

use of input (`.INP`) files that Abaqus can read in simple text and which define the entire simulation with appropriate commands. The writing of a text file can be easily automated and, in this case, the `.INP` file is created through a Python script. In this script the 3D coordinates of each node and member are defined in a parametric mathematical form, so that the local and global geometry can be changed by adjusting only the dimension(s) of interest—greatly assisting parametric studies. Similarly, all remaining options for the simulation are input as text commands—a sample script is found in Appendix A.

The simulation is composed of two Dynamic Implicit steps, with quasi-static application—a method suitable for non-linear structural problems (Dassault Systémes/Simulia, 2011). The shell node corresponding to the centre of the overall shell is held fixed for all degrees of freedom. In the first step we use displacement control on a single corner node. During the second step, displacement control is removed and the shell is allowed to return to a load-free equilibrium geometry. Elements of type B31, a three-node linear beam element, are used with four elements per ligament. That number was chosen as reasonable after a brief mesh sensitivity study, results of which are shown in Fig. 8.5, noting that results we are after are mostly qualitative.

For a set of cases that follow, the global geometry is fixed and the effects of local geometry variations are examined. The global dimensions are fixed as follows: $a_x = 520\,\mathrm{mm}$, $a_y = 520\,\mathrm{mm}$, $\rho_x = 300\,\mathrm{mm}$, thus mirroring a realistic design for a hand-held demonstrator. Later, the effect of the global curvature on multistability is also examined.

8.3.2 Proof of concept

We begin with one case, analysed in detail, to establish that indeed bistability is feasible under these specifications. Specifically, we fix the remaining spatial variables such that

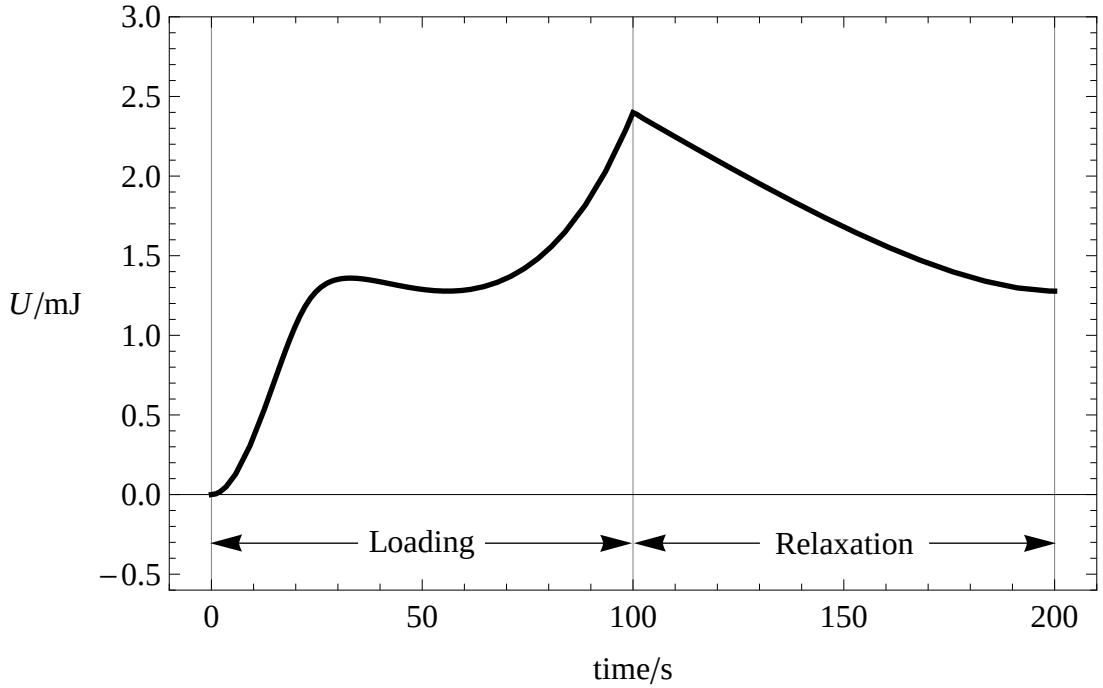

Figure 8.4: Strain energy for the shell, plotted against time. During the first 100 s the shell is gradually loaded. We can distinguish a minimum for the energy that indicates a second equilibrium geometry. After that time we remove the loading boundary condition and the shell returns to the second state. The value of the final strain energy is equal to the value at the minimum.

$d = 10\,\text{mm}$, $b = 0.2\,\text{mm}$, $h = 0.8\,\text{mm}$. For this ligament length the total number of elements is equal to 5184. The ratio of the length of the beam-member to the beam cross-sectional dimensions is more than 100 here and large enough for an Euler-beam assumption to be reasonable. The corner node is displaced by 150 mm along the z-axis over the duration of the first step. Both the loading and the relaxation steps have a duration of 100 s. The Young's Modulus for the material is set to equal those of aluminium at 69 GPa and the Poisson ratio at 0.32, to reflect a realistic material. The corresponding homogenised material properties can be found through Eqs. (8.1) to (8.4) which give ν_A and α_A approximately equal to one, $\nu_\text{D} = 0.72$ and $\alpha_\text{D} = 0.86$.

For this representative case, we present a plot of the strain energy in Fig. 8.4. The total strain energy in the whole of the shell is shown. During the loading period we see a clear minimum. When we remove the displacement boundary condition at the corner node, the strain energy settles at this value and does not return to an unstressed state. Both these observations confirm the existence of a second stable geometry for this shell. The geometry for the shell in initial, intermediate and secondary stable equilibria, as it is obtained by the FE simulation, is also presented in Fig. 8.6. The initial state, as noted above, is perfectly cylindrical. The second state, on first inspection, appears to be approximately cylindrical in the same sense as the initial state, but with the two directions of curvature reversed.

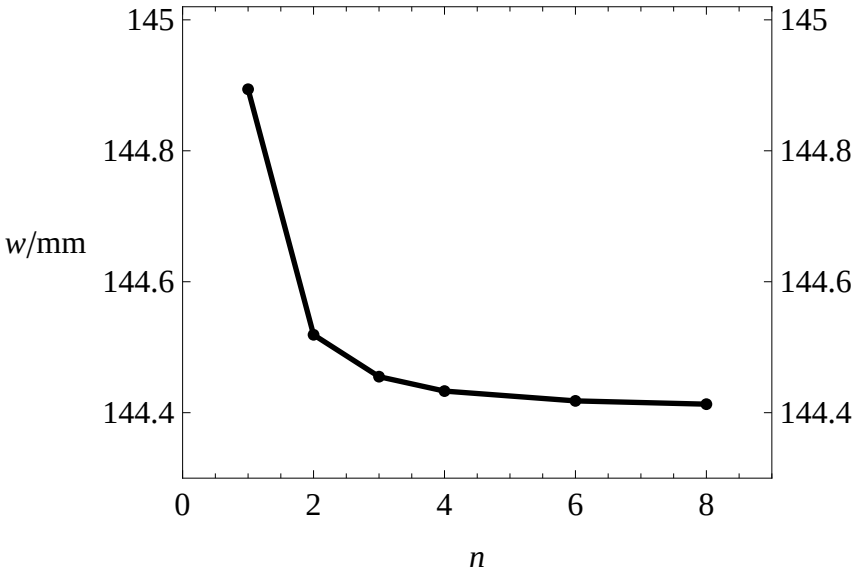

Figure 8.5: Different resolutions for the mesh were tested for the basic geometry of the shell, with n noting the number of elements per beam. The metric here was the displacement of the midpoint of one of the sides of the shell. A convergence of the results is obvious and four elements per beam were judged sufficient for the (mostly) qualitative analysis here.

A more detailed examination of the secondary stable geometry is shown in Fig. 8.7. The two half-centrelines of the shell are isolated and plotted in two separate sets of axes. The first profile, in the direction of initial zero curvature, appears almost uniformly curved, with a larger radius of curvature than the initial state. A dotted, circular arc is also plotted in the same set of axes for visual comparison, and we observe an almost perfect match. The profile in the other direction is drawn exaggerated in the z-direction. Although, the deviation from a flat profile is small, it is noticeable. Specifically, toward the centre of the shell, the geometry is slightly concave toward the positive z-axis. At an approximate radial distance of two thirds of the total shell radius, the curvature changes sign and is maintained until a boundary layer where the curvature is more pronounced. The deviation from the central node in the perpendicular direction does not exceed 13 mm at any point (less than 4.3% of the shell's half-width), while the maximum value is observed at the periphery. Given these results, it is appropriate to refer to the second stable configuration as almost cylindrical.

8.3.3 Parametric studies

To the author's knowledge, this is the first time a grid shell has been investigated in the context of multistability. Hence, almost every parameter that we have treated as a constant in the basic case is worthy of further investigation, including local and global dimensions and their relative magnitudes. In this section though, we limit our investigation to those parameters that appear the most critical or to the local geometry parameters

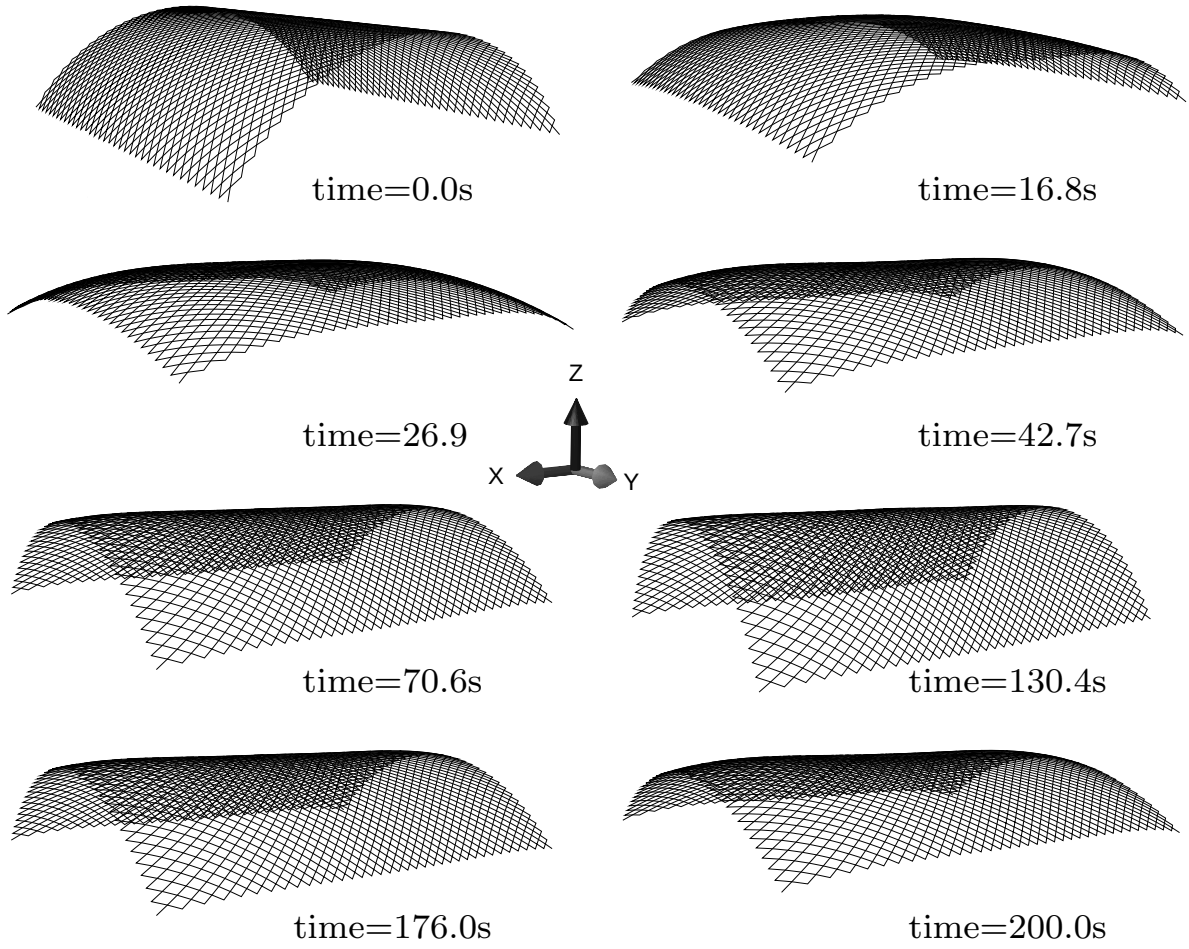

Figure 8.6: The variation of geometry during actuation of an initially cylindrical bistable grid shell viewed from the same perspective and held at the centre. The stills are taken from an Abaqus simulation, with the respective time shown in each frame. We use two steps of the Dynamic Implicit method, each lasting 100 s, with displacement control; in the first step we displace the middle nodes of the shell as shown in Fig. 8.3 and in the second step we remove all external controls. Doubly curved grid shells can also be bistable but a developable initial geometry is selected to conclusively show the contribution of the grid shell's material properties.

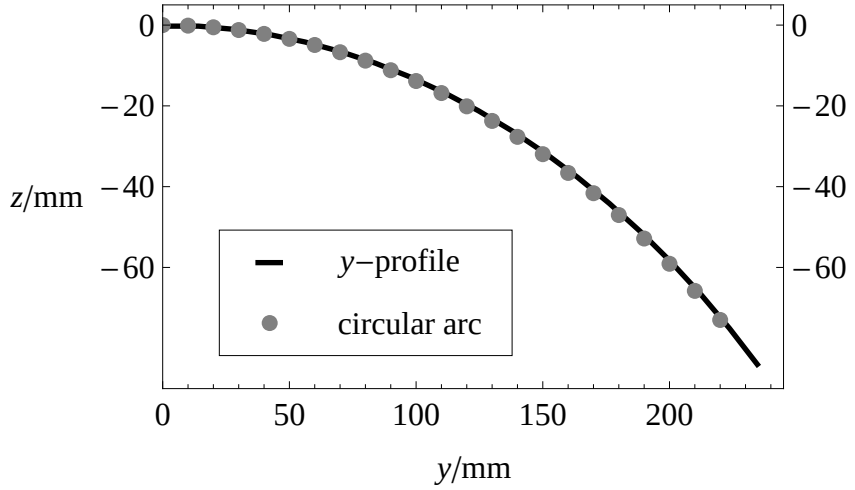

(a) Secondary state y-profile

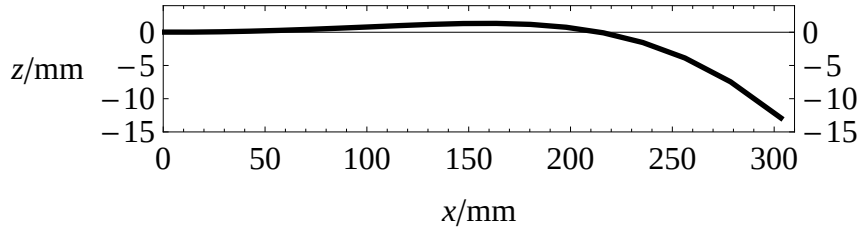

(b) Secondary state x-profile

Figure 8.7: The geometry of the second state is presented here in more detail. We plot the profile of the shell for $x = 0$ and $y = 0$ respectively. In the former case, we contrast the plot with a circular arc of 368 mm radius. The comparison shows an almost exact match. In the other perspective—shown in an exaggerated aspect ratio, curvature is more subtle. The y-profile is almost flat towards the centre, but with a more pronounced curvature towards the boundary. There is a switch in the sign of the curvature near the radial centre.

that are not directly assessed by our UC model, namely the cross-sectional dimensions of the beam-elements. Later, the initial curvature and the moment of inertia of the beam-element are also investigated with respect to multistability.

Ligament height-to-width ratio

One such parametric study focuses on the influence of the cross-sectional height of the member beams (h) on bistability. We fix all parameters except h and perform a series of simulations as described in Section 8.3.1. The cross-sectional width is set at 0.2 mm. The height is varied between that same value and increased by 0.2 mm up to a value of 1.2 mm.

Results of this study are shown in Fig. 8.8, in the form of force-displacement diagrams. In a three-dimensional structure, the force-displacement diagram for one degree of freedom is not sufficient to prove multistability. Since we have established this result though

with Strain Energy diagrams, the force-displacement diagrams can provide an alternative view of the phenomenon. The value for the force is specific to the node also used for displacement control and shown in Fig. 8.3, while displacement, w, is also referring to that same node. Both force and displacement are rendered dimensionless by multiplication with suitable parameters. Specifically, the force is multiplied by $a_x/(Eh^3)$ and the displacement is divided by the apex height, shown in Fig. 8.2.

The resulting force-displacement graphs show a characteristic snap-through effect for all cases. As h is increased, the plot crosses the displacement axis for the first time when $h = 0.8\,\text{mm}$. The case $h = 0.6\,\text{mm}$ is almost tangential to the displacement axis at its lowest point. Thus in this scenario, a ratio of h:b greater than an approximate value of three is needed for bistability, while additional simulations for $h > 0.8\,\text{mm}$ are consistent.

We add to these conclusions by returning to the material properties for the grid shell obtained in Chapter 3. We produce colourmaps of the stability regimes for specific global dimensions, matching the dimensions of the simulations, while varying the cross-sectional height and width, h and b respectively. The resulting plot, shown in Fig. 8.9 supports a constant minimum ratio of h:b for bistability to be possible, with a value close to five. Recall from earlier in this section that this is in approximate agreement with our simulations, that show an approximate value slightly above three for a similar scenario.

For larger h:b ratios our beam assumption becomes defunct. Once h and d have comparable values and while b retains a small relative value ($20b < h \approx d$), it is reasonable to begin treating each ligament as a shell. This results in a global honeycomb structure and is investigated further in Section 8.4. We should note that repetition of this study with a change in cross-sectional width shows that the ratio of the two cross-sectional dimensions is the critical parameter and not the absolute value of one or the other.

Initial curvature

Another critical parameter for bistability, as shown in Chapter 5, is the initial curvature of the shell, with respect to a planform of constant dimensions. From another perspective, we can consider the apex height of the shell as the critical parameter, since the three parameters are interconnected—the global geometry is displayed in Fig. 8.2. The relevant series of FE simulations uses the same planform dimensions as all other simulations; square $520\,\text{mm} \times 520\,\text{mm}$, *i.e.* a_x and a_y are fixed. The ligament cross-section is $0.1\,\text{mm} \times 0.4\,\text{mm}$, the length of the ligaments is 10 mm and the initial radius of curvature, ρ_x, varies between 300 mm and 550 mm at 50 mm intervals.

The results of the parametric study are shown in Fig. 8.10, where dimensionless force-displacement diagrams are plotted for all the tested values. The last case to be marginally bistable, for increasing values of the curvature, corresponds to a global radius of curvature equal to 450 mm, with a depth to planform length ratio equal to 0.16. Although this is

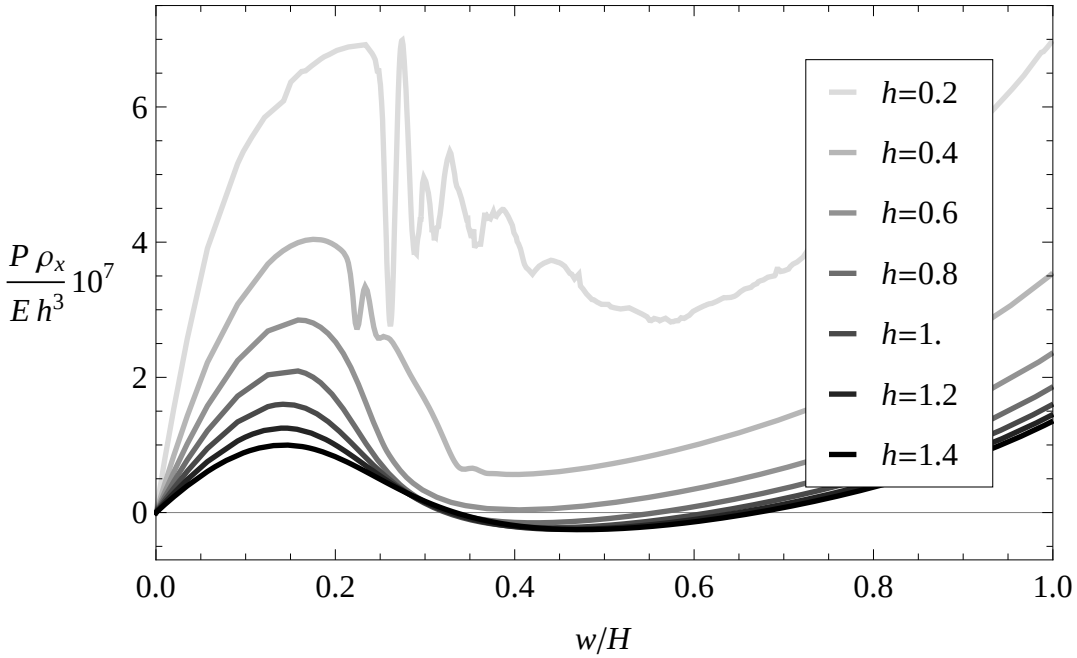

Figure 8.8: Comparison between force-displacement diagrams for different beam-member thicknesses. The vertical reaction force at the location of the displacement control is the variable P. Both the force and the displacement are made dimensionless by appropriate coefficients, while the beam-member width is fixed at 0.2 mm. For a square cross-section we observe a prominent snap-through effect, but not a second equilibrium. Increasing the thickness—and hence the ratio between beam height and width—we observe a second equilibrium for ratio approximately three and above. The irregularities in the plot for $h = 0.2, 0.4$ can be attributed to local buckling effects.

a specific case with absolute dimensions, the trend observed can greatly inform future physical designs.

Cross-sectional scaling

A notable observation regarding the strain energy of the shell is obtained by scaling the dimensions of the cross-section. For this series of simulations the ratio h:b is kept fixed (at a value of three) but the absolute values of the (h, b) pair are $(0.02\,\text{mm}, 0.06\,\text{mm})$, $(0.1\,\text{mm}, 0.3\,\text{mm})$ and $(0.2\,\text{mm}, 0.6\,\text{mm})$.

The strain energy from the simulations is pre-multiplied by a factor hb^3 and is plotted in Fig. 8.11. It is apparent that following scaling the patterns match almost exactly. The scaling used matches the moment of inertia of the cross-section, which takes the form $hb^3/12$ for a rectangular cross-section. A linear relationship between the strain energy and the local moment of inertia indicates bending-dominated behaviour throughout the geometrical transition.

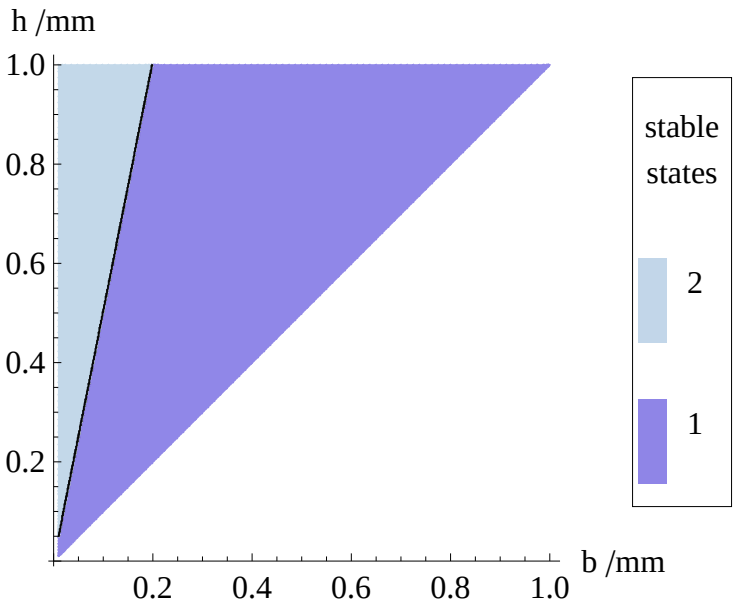

Figure 8.9: Returning to our homogenisation model for grid shell properties from Chapter 3 we produce a colourmap showing the dependence of multistability on cross-sectional dimensions. The parameter values are calculated through Eqs. (8.1) to (8.4) and then substituted in the dimensional energy expression from Chapter 6, allowing for numerical solutions for stable equilibria. We only plot values of $h > b$ in accordance with our model's assumption for Eq. (3.30), while the remaining variables match the values used in the FE simulations in this section. There is a cut-off point for bistability at a constant ratio between h:b, approximately equal to five.

8.4 Honeycombs

Honeycombs are a natural extension of grid shells. We make the distinction between the two to mainly signify a change in our assumptions about the relative ratios of the parameters h, b and d. Honeycombs are composed of a repeating pattern of thin ligaments meeting at rigidly connected nodes. We are using the same (square) pattern as for grid shells. Indeed we continue using the same symbols for the geometry as before. The subtle difference is that we are assuming a shell element for the ligaments and not a beam element. By considering this additional category of structures, any deficiencies in the beam assumption for the ligaments are resolved.

A series of FE simulations are performed under the shell assumption for the ligament geometry. A renewed array of geometries becomes accessible through this model. The model in Abaqus follows the same specifications as the earlier grid shell model in terms of global parameters. Locally, the distance between nodes, or the ligament length (d) is initially set at 10 mm, while the ligament thickness is fixed at 0.1 mm. The ratio of d:b is large enough to admit a shell geometry, as long as the h parameter is also sufficiently large. We only admit h values greater than 2 mm, or a ratio of h:b greater than 20.

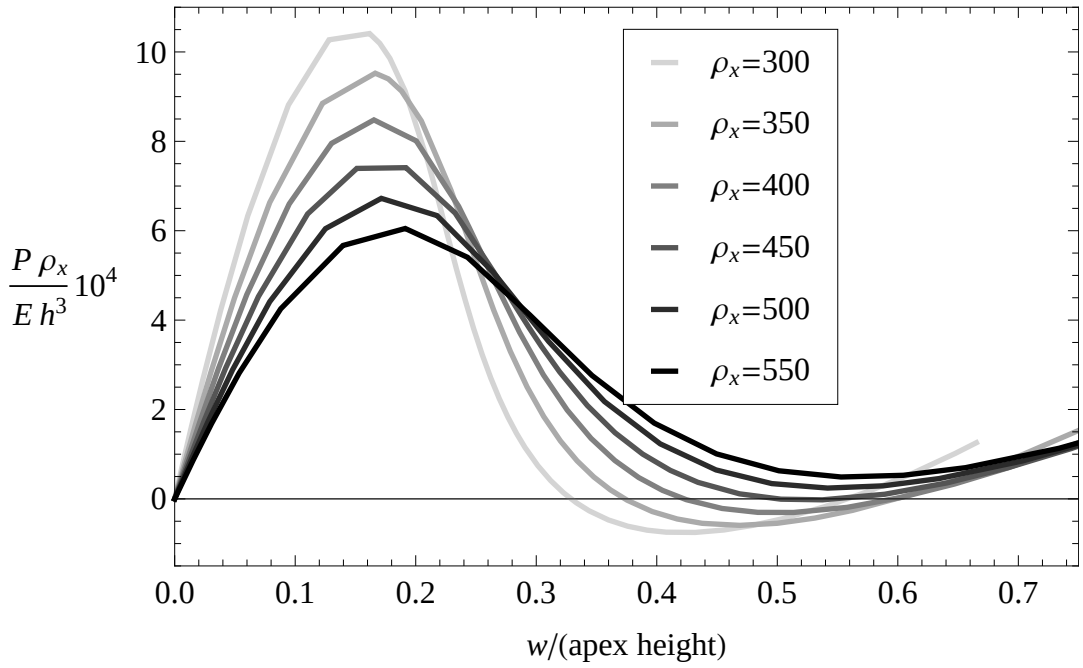

Figure 8.10: Multistability is also affected by the initial curvature of the shell. Starting with the base grid shell case, the radius of curvature is gradually increased for a series of simulations, and dimensionless force-displacement diagrams are presented here. The last marginally bistable grid shell in this progression occurs for a radius of curvature equal to 450 mm. Force-displacement diagrams with respect to one degree of freedom for a three-dimensional structure do not prove multistability, but support the evidence from the Strain Energy variation in the simulation.

In practical terms, the Abaqus model is an extension of the grid shell model, with an additional layer of nodes added at a radial offset from the original set. This updated network of nodes defines shell-elements with their mid-surface perpendicular to the global shell's mid-surface. The resulting ligaments are modelled as four-node, quadrilateral elements, defined as S4R in Abaqus. To maintain a reasonably fast simulation, the number of elements is fixed at 4×4 per rectangular plate-ligament. With $d = 10\,\text{mm}$ and planform dimensions $520\,\text{mm} \times 520\,\text{mm}$, a total of approximately 80000 elements are needed.

With this renewed geometrical capabilities, one immediate goal is to establish the limit of bistable behaviour with respect to large values of h. In Fig. 8.12 we plot the strain energy for various values of h. Only the early part of the simulation is plotted here, since we are only interested in possible strain energy minima. For low values of h, the plots are consistent with the grid shell simulations and a clear minimum for the strain energy appears during the loading phase. This minimum is eventually lost for values of $h = 30\,\text{mm}$ and higher. A value of $h = 25\,\text{mm}$ also allows bistability, but is omitted from the plot for clarity.

In Fig. 8.13 snapshots from one simulation are displayed for two reasons: they help visualise the differences in local geometry of the honeycomb model with the earlier grid

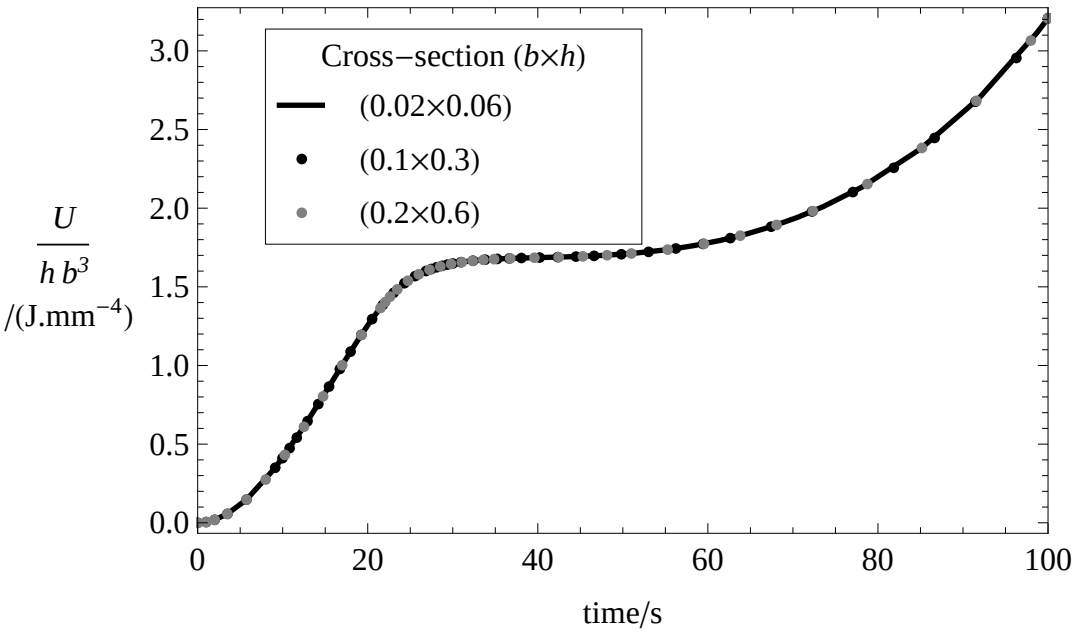

Figure 8.11: One of the notable results of our simulations is the scaling of the energy with respect to cross-sectional dimensions of the grid shell ligaments. In this plot we compare the total strain energy for three grid shells undergoing the same displacement-controlled deformation. The three cross-sections examined are 0.02 mm × 0.06 mm, 0.1 mm × 0.3 mm and 0.2 mm × 0.6 mm. The energy scales proportionally to moment of inertia of the cross-section, or hb^3, which indicates a bending dominated deformation.

shell model, shown in Fig. 8.6; they give a clear image of the intermediate and final stable equilibria of the honeycomb shell. With respect to the latter, the secondary stable configuration is extremely similar to the one obtained for grid shells, during the transition however, the honeycomb forms a saddle-shape, a behaviour that is not observed for grid shells to such an extend.

A theoretical overview of the corresponding homogeneous shell is also offered here for comparison. In Fig. 8.14 the stability regions with respect to the shear stiffness, G, and the thickness of the shell, t, are shown. The global dimensions agree with all the simulations in this Chapter. The material properties are arbitrarily chosen to roughly correspond to the analysis in Section 3.4.1; the Poisson ratio is set at 0.95—a high value that matches our analysis in Chapter 3—and orthotropic behaviour is assumed. Figure 8.14 shows that we cannot obtain bistability for a narrow band of low shear stiffness—under approximately $G/G_{\text{iso}} = 2$ in this case. When the shear stiffness is sufficiently large for bistable behaviour, bistability is lost at an approximate thickness of 22 mm. This value marginally increases with the value of the shear stiffness. The theoretical result is in rough agreement with the results of the FE simulations.

The comparison with the theory is expanded in Fig. 8.15. Figure 8.15a shows a

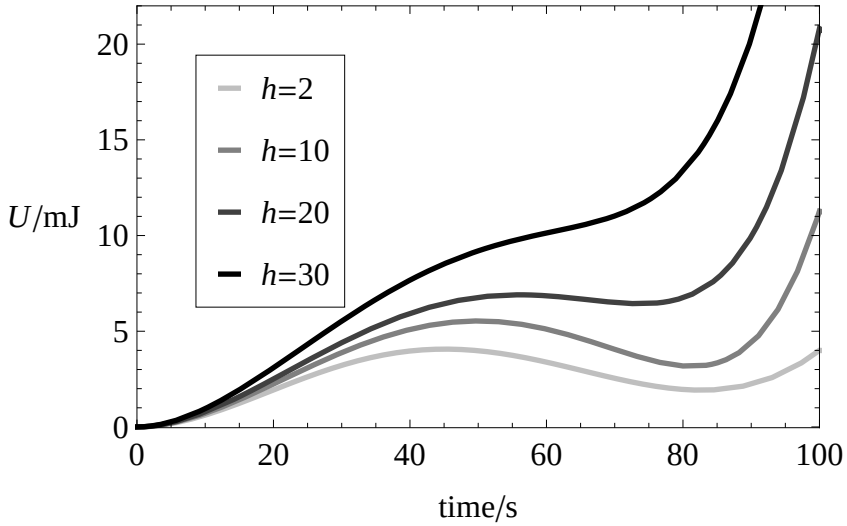

Figure 8.12: Switching to a honeycomb model on Abaqus allows for a new range of ligament geometries to be examined. An initially cylindrical shell is tested with planform dimensions (520 mm × 520 mm), ligament length $d = 10\,\text{mm}$ and ligament thickness $b = 0.1\,\text{mm}$. By varying the ligament height, h, the upper limit of the bistable behaviour is shown to be almost 30 mm.

contour of the strain energy across the (κ_x, κ_y) plane for a thickness of 10 mm. There are two distinct minima corresponding to two cylindrical geometries. The secondary state's curvature is slightly smaller. After connecting the two minima with a straight line, the strain energy is plotted along this profile. This allows for the theoretical result corresponding to Fig. 8.12 to be plotted in Fig. 8.15b. The true path during actuation is not represented by a straight line, and is discussed further in Chapter 7, but the loss of the second energy minimum is the focus here. For this purpose this profile suffices. A rough agreement with the FE simulations is again immediate.

8.5 Helical grid shell

The geometrical possibilities for a bistable grid shell are not limited to neither shallow shells nor square planforms. To establish this additional design domain, an FE simulation is performed with an initially rectangular planform, curved in a helical geometry. With respect to earlier grid shell simulations, only the global structure is changed. Locally the structural pattern is the same square grid, with each ligament modelled by a beam element.

In order to examine this concept, we arbitrarily chose dimensions similar to earlier structures, and constructed an Abaqus model. The planform is a rhomboid with sides of 300 mm and 900 mm with its largest angle equal to $\left(\frac{\pi}{2} + \arctan\frac{1}{2}\right)$. The shortest side is parallel to the x-direction. The rhomboid is then wrapped along a cylindrical mathematical surface with its axis parallel to the x-direction. The initial geometry is displayed

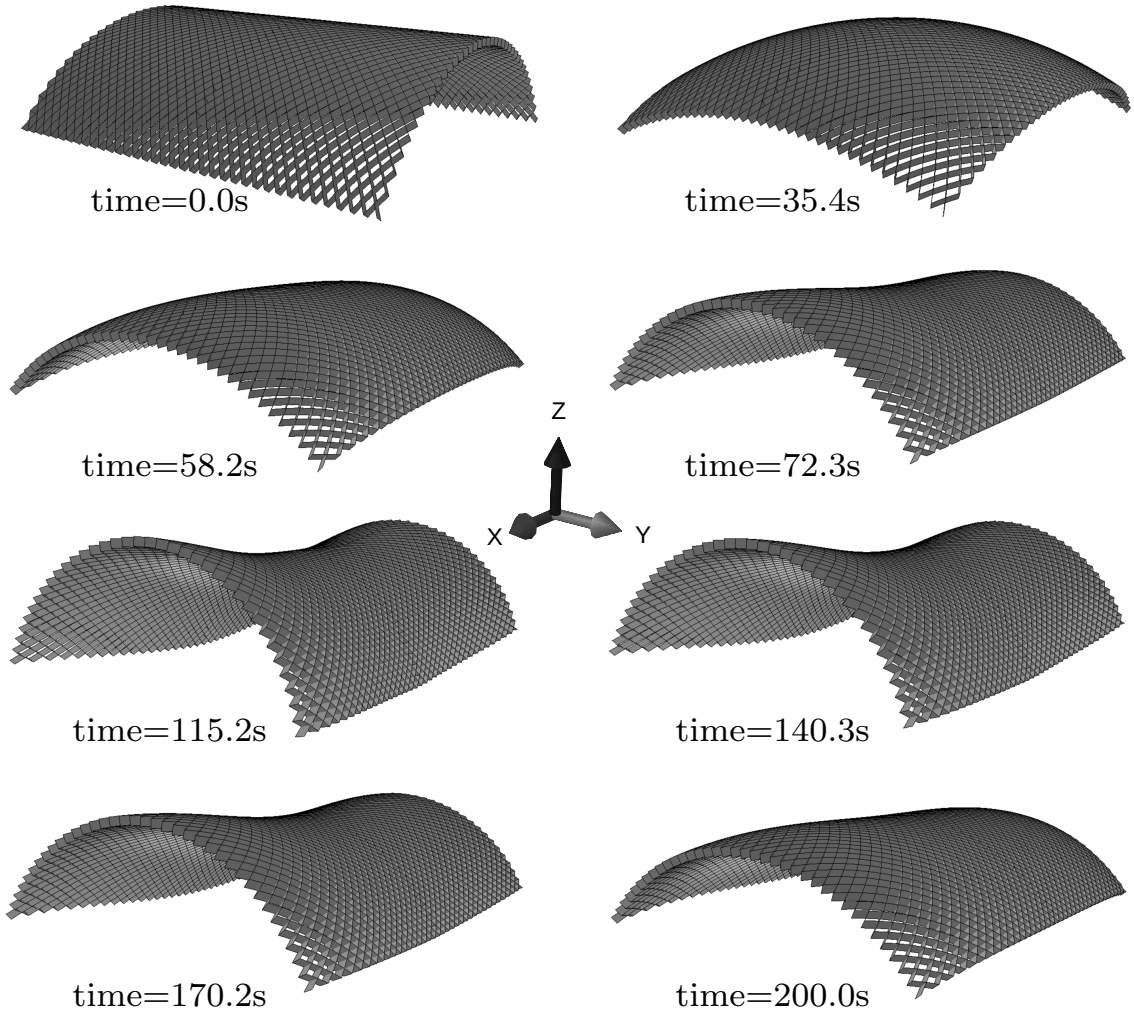

Figure 8.13: The simulated transition of a honeycomb shell from an initial cylindrical geometry to a second stable configuration. The resulting shapes are similar to those shown in Fig. 8.6 for a grid shell, where the ligaments are modelled as beams. Here, the ligaments are modelled as shells and in this particular model, each ligament has dimensions $10\,\text{mm} \times 10\,\text{mm} \times 0.1\,\text{mm}$, although thicknesses up to 25 mm achieved bistability for square shells of side 520 mm. The figure also displays the relevant thickness of the honeycomb shell compared to global dimensions.

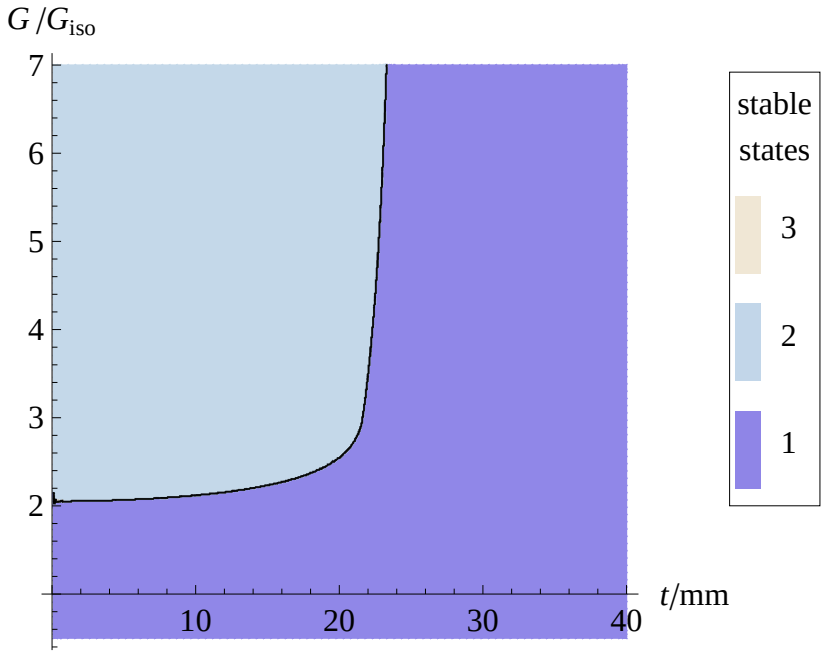

Figure 8.14: Comparison of the behaviour of the honeycomb structure for high values of ligament thickness—as shown in Fig. 8.12—with the theoretical prediction. The dimensional strain energy equation from Chapter 6 is used to obtain the equilibria and plot the stability regions for the corresponding homogeneous shell. The global dimensions have the same values as all the simulations in this Chapter, while for this plot the Poisson ratio is set to a value of 0.95. Bistability is lost for values of thickness between 20–25 mm, depending on the value of the shear stiffness.

in Fig. 8.16. The cross-section of the ligaments is once again assumed to be rectangular with dimensions 0.2 mm × 0.8 mm.

The shell is actuated by displacement control of the centre nodes on the two shorter sides. They are displaced along the y-direction, beyond the flattening of the grid shell in the y-direction, and then released. A two step, Dynamic Implicit model is setup in Abaqus, as with earlier simulations. The strain energy of the system is shown in Fig. 8.17. A clear minimum is seen after a sudden dip during the loading phase (0–100 s). After the relaxation phase, the strain energy returns to the geometry of a secondary geometry, in agreement with the earlier minimum value. The secondary stable geometry is shown in Fig. 8.16 and closely matches a cylindrical surface, with an axis along the y-direction. Such a design potentially allows for more control of the stiffness in both directions contrary to the shallower, square design.

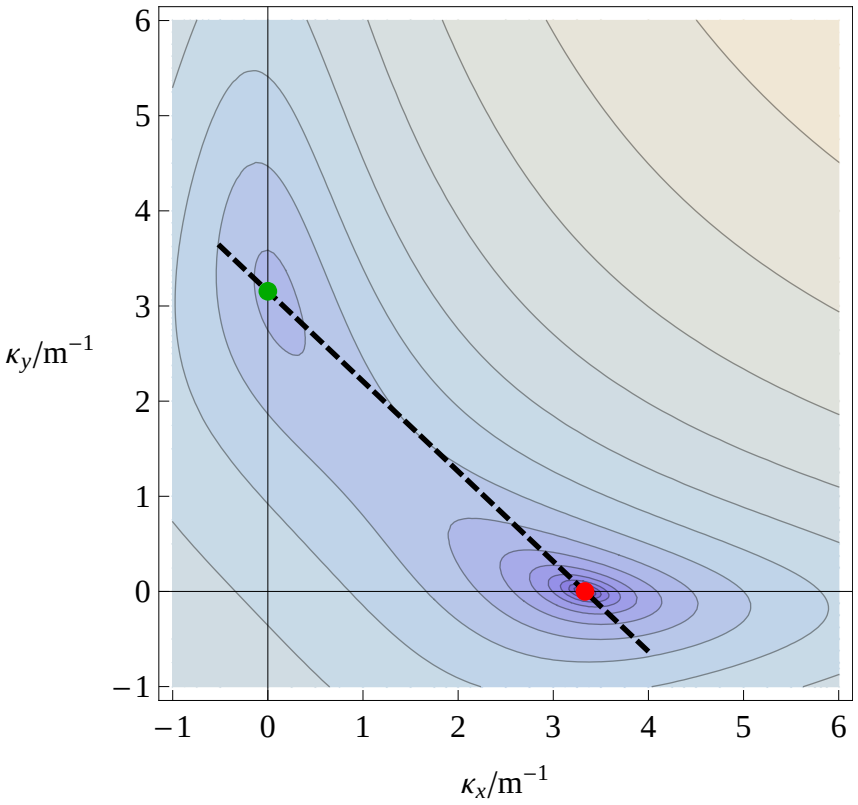

(a) Strain energy contour plot

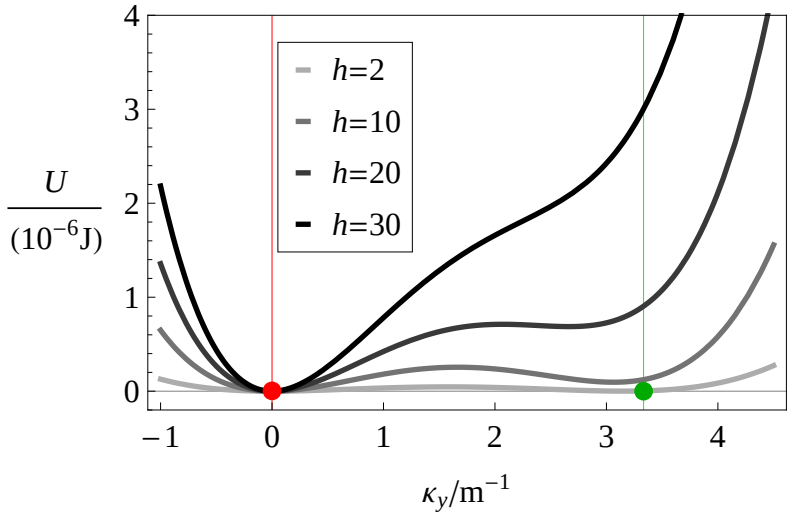

(b) Theoretical strain energy during actuation

Figure 8.15: The contour plot at the top shows the variation of the predicted dimensional strain energy according to Eq. (6.14) and our model from Chapter 4. The global geometry is the same used throughout this chapter, but we assume a homogeneous shell with a Poisson ratio of 0.95 and a shear stiffness twice the isotropic value; the thickness is set at 10 mm. The secondary equilibrium appears at $(\kappa_x, \kappa_y) = (2.45 \times 10^{-6}, 0.00316)$ or as a same-sense (almost) cylinder with a radius of 316 mm—slightly larger than the initial radius. At the bottom we plot the strain energy profile along the dashed line in the top diagram. This is done for various shell thicknesses to show the correspondence to the simulated honeycomb structure results in Fig. 8.12.

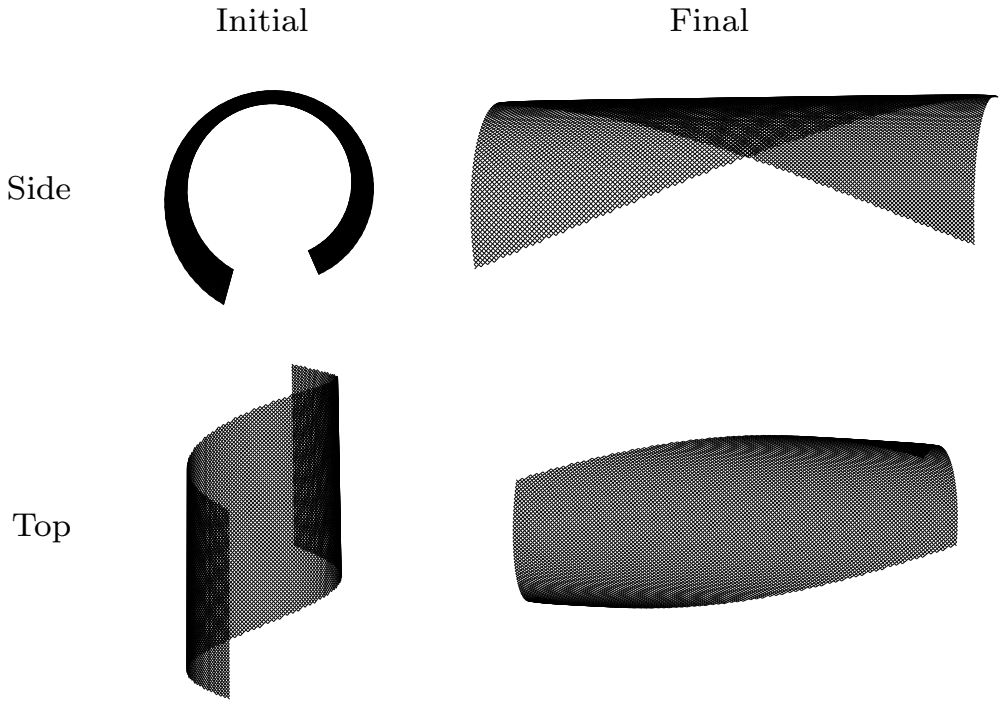

Figure 8.16: An initially helical, bistable grid shell is shown here from an Abaqus simulation. On the left column we see the initial geometry, and on the right column the final geometry after actuation and relaxation. The top row shows a side view of the shell while the bottom row shows the shell viewed from above.

8.6 Physical demonstrator

An attempt is made to confirm these results with a physical demonstrator and, as in Chapter 6, a hand-held design is pursued. This facilitates both construction with the techniques available to us and maximises the demonstrative power of the object. At such a scale, the planform dimensions are in the order of decimetres.

In terms of material, any isotropic material satisfies the mechanical properties. However, the large deformations involved in travelling from one stable state to the next need to be considered. An intermediate flat state helps establish an upper ceiling for the required strains. For example, let us consider a cylindrical shell with a square $a \times a$ planform, a thickness h and initial curvature radius of curvature ρ_i. Considering the symmetry we have noted in the transition to a secondary state, the originally curved direction of the shell ends up in an almost flat configuration. Hence an estimate for the strain of the extreme fibres is given by:

$$\epsilon = \frac{h}{2\rho_i} \tag{8.5}$$

For $h = 10\,\text{mm}$ and $\rho_i = 160\,\text{mm}$, $\epsilon \approx 3\%$. This is in the range of typical maximum strains for metals, hence alternative materials need to be considered. Thermoplastics fit

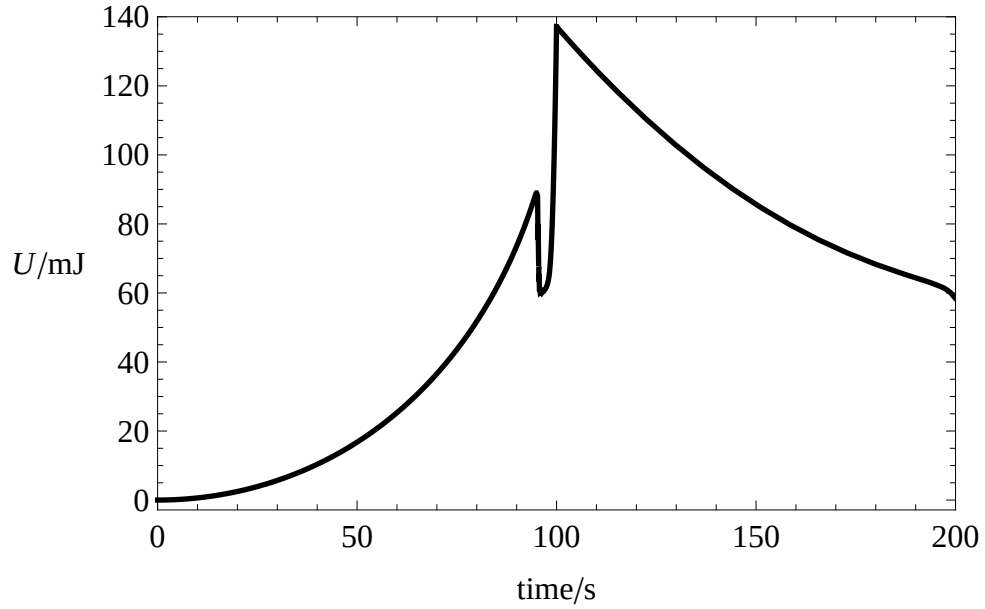

Figure 8.17: Strain energy vs time for the helical grid shell FE simulation. We can see a clear minimum during the actuation phase (0–100 s). The actuation in this case is not optimised with respect to the second stable configuration; this might explain why the dip to the minimum is more sudden than in earlier simulations. The relaxation phase concludes at the same strain energy, confirming the bistable character of this structure.

the strain requirement; they can withstand strains above 10% before yielding, depending on the type of the plastic (Biron, 2012). In addition, they can be easily cut and drilled. Finally, they can be bent and shaped at a low temperature—the so-called crystalline melting point; below 200°C in some cases (Tripathi, 2002). If the material goes beyond this temperature, deforms and then cools to below its recrystallisation temperature, it retains its deformed shape.

A demonstrator is constructed out of a 6 mm sheet of the thermoplastic polypropylene (PP), which is cheap and widely available. A water-jet cutter in CUED's workshops is used to shape the desired local geometry, starting with a 300 mm × 300 mm square. The ligament length is 10 mm and the target ligament thickness is 0.1 mm. The ligament proves too thin for the equipment used and a few imperfections are created as seen in Fig. 8.18. The sample is then constrained by a cylindrical mould with a radius of 160 mm and heated to a temperature of 160°.

After cooling the sample to room temperature and removing the mould, we observe a spring-back effect—the demonstrator does not lose all residual stress during heating. There is also some local buckling of ligaments, since the sample was forced in the mould at room temperature. Nevertheless, bistable behaviour is ascertained as documented in Fig. 8.19. The initial state has no curvature in one direction. The secondary state is almost cylindrical, with a smaller curvature in the same sense, as predicted by both the simulations and the theoretical mode. At the same time, it also carries a very mild curvature

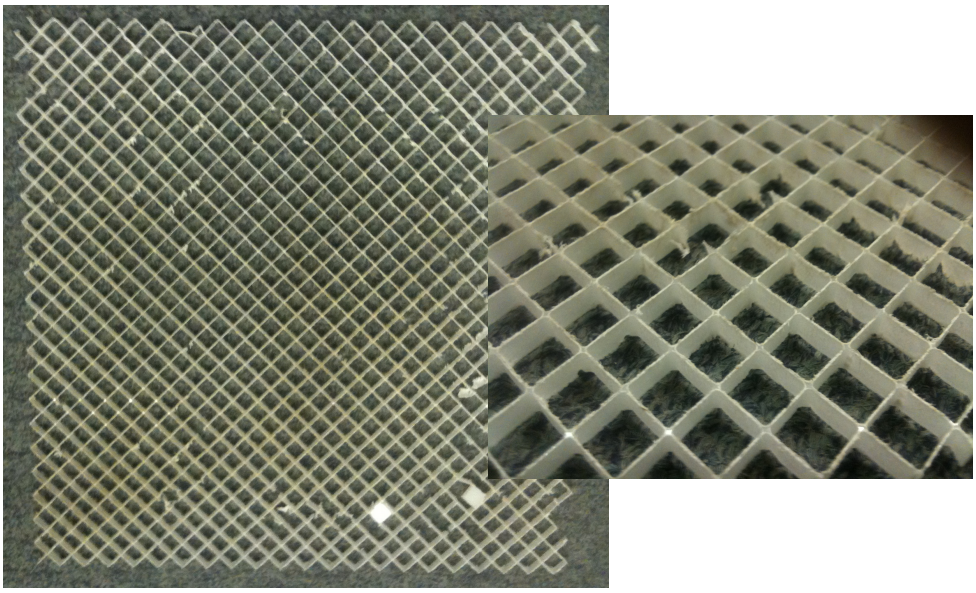

Figure 8.18: A honeycomb structure carved out of a polypropelene sheet using a water-jet cutter. The dimensions of the flat sheet are 300 mm × 300 mm. The unit cell had a length of 10 mm while the ligament cross-section was 0.1 mm × 6 mm. The required small ligament thickness proves too delicate an operation, and results in a few imperfections, seen more clearly on the right.

in the orthogonal direction. Repeated actuation produces a relaxing effect, eventually taking the curvature outside the bistable region. However, despite its lack of robustness, this novel structure proves the feasibility of developable multistable honeycombs.

8.7 Concluding remarks

This Chapter investigated a novel concept for the construction of multistable shell, normally associated with composite or prestressed materials. By taking advantage of the change in global material properties from the patterning of grid shells and honeycomb shells, suitable designs can produce multistability in relatively simple structures. In contrast to composite designs, this method is easily scalable—from the micro to the architectural scale. In addition, it facilitates light and fluid permeable structures.

A series of FE simulations helped us understand the necessary local patterning with respect to the global dimensions. Specifically, developable shells were investigated. Parametric studies focused on the limits of multistability with respect to the global thickness of the shells and to the global radius of curvature. In addition the predicted initial and secondary global geometry for bistable grid shells were explored. Finally, the FE simulations indicated that the deformation is bending dominated.

The construction of a PP demonstrator honeycomb confirmed the bistable nature of such a structure. The design could be improved by addressing creep effects and the initial

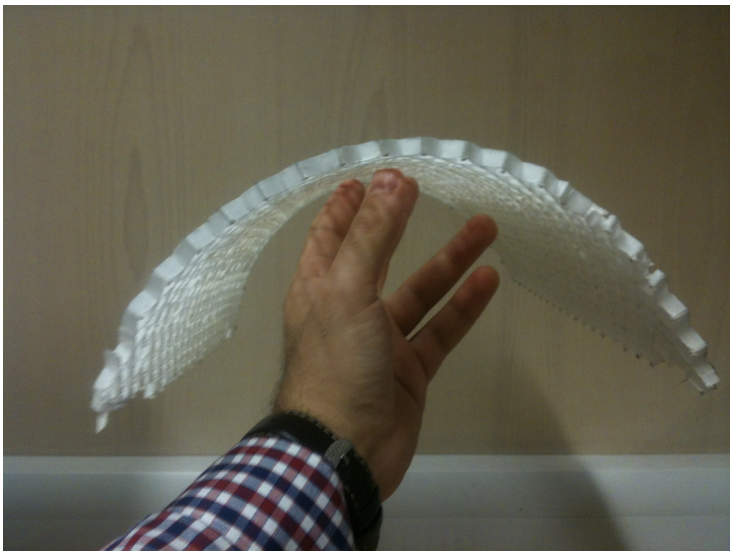

(a)

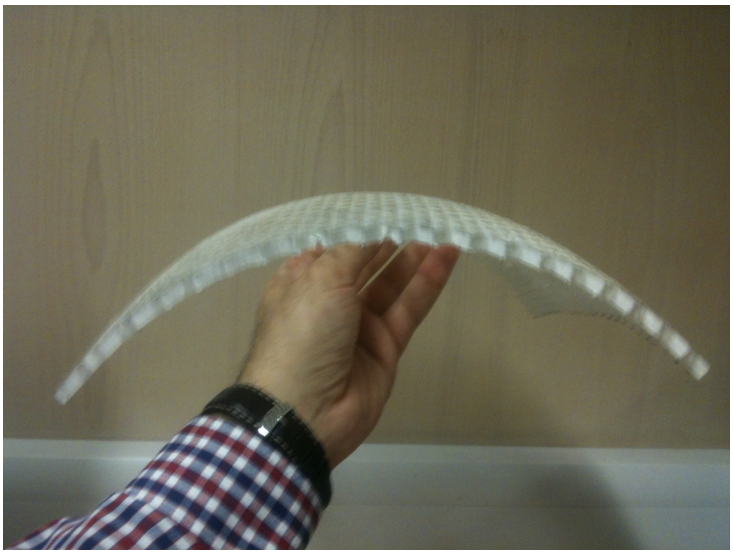

(b)

Figure 8.19: A polypropylene demonstrator showing the two stable geometries for a honeycomb shell design. The top diagram shows the initially, perfectly cylindrical geometry, while at the bottom we show the secondary geometry, rotated by 90°. Although the second geometry is also approximately cylindrical, a mild curvature is also seen in the other direction. It is also clear that the radius of curvature in the second state is larger than in the initial geometry, as predicted by both the theoretical model and the FE simulations. Due to creep effects, the success of this design—with this particular material—was short-lived.

forming process for the shell.

Chapter 9

Conclusions and future work

This work began with a specific and straightforward goal: to explore the extend of multistable behaviour for elementary morphing shells and suggest some practical design guides for engineers. In the course of this endeavour some answers were given clearly and are presented in detail in past Chapters. Other questions escape the purview of the Uniform Curvature (UC) assumption and were left open. More importantly perhaps, our investigation gave rise to new technologies that we presented in their early form. This Chapter tries to summarise these three sets of information from this dissertation, distil the most essential conclusions of this work and suggest potential avenues of research to follow these findings. The latter is presented in Section 9.1 while Section 9.2 brings together the main lessons from this dissertation.

9.1 Future work

The major question still open with respect to multistable shells is that of actuation. The particular topic is a necessary stepping stone for robust practical applications to be developed. Actuation design needs to be application specific and thus the topic is complicated further. The dynamic motion that follows bifurcation is also a major challenge for designers. This thesis scratched the surface of relevant challenges in Chapter 7 and merely established the inadequacy of the UC assumption in this regard. In the same Chapter we open the door to a new category of materials that can act as sensors, since they are actuated by environmental factors. We employ a magnetic field, but the same principle has been examined with thermal and optical actuation. Additional work is needed to study actuation through body force fields with complex directionality and to introduce additional methods, such as light-sensitive materials. Especially for applications where intermediate geometries are important, there is much to investigate.

Work is already under way to tackle the inadequacies of the UC model by employing a higher-order polynomial description (Pirrera *et al.*, 2010; Vidoli, 2013). Still, we are

very far from a complete model; admitting general initial shapes and anisotropic material properties. The efficiency and speed of modern computational methods makes it unlikely that this will be pursued on the theoretical level. However, it is the spirit of this thesis that much better designs can be achieved by simple theoretical modelling, than elaborate computational ones. This is based on the current manoeuvrability of theoretical versus computational tools and not on an anti-technological sentiment.

In Chapter 8 we introduce a novel structure for multistable shell designs. By using curved grid shells or honeycombs we were able to establish the possibility of multistability for an otherwise homogeneous material without prestressing. This category of structures was analysed to some extend, but a more thorough investigation should be carried out to ensure robustness. Specifically, the material properties homogenisation model we used was elementary and a more elaborate one would help establish more accurate design constrains. Additional experimental work is also necessary, with a range of materials and geometries.

Finally, a tristable shell based on a perforated, doubly curved shell—according to the relevant section in Chapter 3—is a possibility, but the requirements of such a design make it both computationally and practically expensive in the context of this work. A more focused study can produce both an FE and a physical confirmation.

9.2 Final conclusions

Within the context of contemporary mechanics this dissertation indicates that simple theoretical models can still greatly inform designers and promote intuition-building. The model presented in Chapter 4 allowed for major theoretical conclusions as well as the development of novel designs. We summarise the most notable findings:

- The literature review in Chapter 2 mapped out the long history associated with multistable shells as well as the vivid research currently directed in various relevant topics. Here we established the tools—theoretical, experimental and computational—traditionally associated with such work while the significant interest in such structures was confirmed.

- Chapter 4 makes some simple assumptions—most notably for Uniform initial Curvature—to form a useful but manageable strain energy-based model for multistable shells. By including both bending and stretching energies, we ensure a large range of behaviour is captured.

- In Chapter 5 we show that there is a theoretical limit for multistability of uniformly curved, untwisted shells, and that limit is at three stable geometries. The same

Chapter includes closed-form descriptions of multistability boundaries as it relates to various material and geometric parameters. Catastrophe Theory was a significant source of inspiration for this generalisation.

- In Chapter 6 we draw information from Chapters 4 and 5 to design and construct a novel tristable shell with the use of fibre-reinforced composite materials. Beyond the self-evident importance of the structure itself, the success of the design proves the practical usefulness of the model from Chapter 4.

- A magnetically actuated bistable spherical cap was constructed with a composite material in Chapter 7. The use of high-speed photography allowed us to observe intermediate geometries during transition. Our observations, combined with Finite Element modelling suggest that non-axisymmetric inversions are always preferred in non-idealised conditions.

- Chapter 8 proves that non-composite, non-prestressed materials can be used for constructing scalable multistable shells, by manipulating local geometry. Specifically, curved grid shells and honeycomb shells are considered in this context.

In conclusion, this thesis perhaps introduced more questions than it answered. At the very least, we have contributed to the notion that multistability is a rich and underdeveloped field. It is the hope of the author that the diversity of options offered to the designer through this work will quickly find a corresponding depository of everyday applications.

Appendix A

Python script for Abaqus input file creation

```
# script to write Abaqus INP file directly
# for a cylindrical grid shell
# with a square grid at 45 degrees to the curvature of the shell
import sys
import math
##############################################################
# define the geometric variables
nb= 4; # number of elements per beam
cs='.02, .02'; # cross-sectional dimensions
ax=260; d=10; ay = 260;
rx = float(300); # radius of curvature
hbc=-150.; # displacement controlled distance
##############################################################
w = math.pi/4; # for matrix rotation
fname='cylT1.inp' # name the output file
# initiate some lists
N=[] # node list
C=[] # connectivity list
##############################################################
# decimal range step function
def drange(begin, stop, step):
      r = begin
      while r < stop:
            yield r
            r += step
##############################################################
# define the surface function for a cylinder
def f3(x):
      #print x
      result=rx*math.sqrt(1 - x**2/rx**2)
```

```
        return result
############################################################
# define the rotation transformation
def rot(mat):
        res = [math.cos(w)*mat[0]+math.sin(w)*mat[1],
          -math.sin(w)*mat[0]+math.cos(w)*mat[1]]
        return res
############################################################
# initiate node and element indices
ni = 0; ei=0;
# nodes dictionary
ndict={};
# go through the 'rows' of the grid
for i in drange(-3*ax,3*ax,d):
        fi = float(i)
        ki=ni
        for j in drange(-3*ay,3*ay,d):
                fj = float(j)
                v1=[fi,fj]
                v2=[fi,fj+d]
                v1t=[round(elem,8) for elem in rot(v1)]
                v2t=[round(elem,8) for elem in rot(v2)]
                if (ax >= v1t[0] >= -ax and ay>= v1t[1] >= -ay and
                        ax >= v2t[0] >= -ax and ay>=v2t[1] >= -ay):
                        ni=ni+1
                        ei=ei+1
                        fjl = fj+d;
                        v2t1=v2t[0];v2t2=v2t[1];
                        ndict[(fi,fj)]=ni
                        N.append([ni, v1t[0],v1t[1],f3(v1t[0])])
                        C.append([ei,ni,ni+1])
        if ni>ki: # add last node from previous row
                ni=ni+1
                ndict[(fi,fjl)]=ni
                N.append([ni, v2t1,v2t2,f3(v2t1)])
# same through the columns
for j in drange(-3*ay,3*ay,d):
        fj = float(j)
        li=ni
        for i in drange(-3*ax,3*ax,d):
                fi = float(i)
                v1=[fi,fj]
                v2=[fi+d,fj]
                v1t=[round(elem,8) for elem in rot(v1)]
                v2t=[round(elem,8) for elem in rot(v2)]
                if (ax >= v1t[0] >= -ax and ay>= v1t[1] >= -ay and
                        ax >= v2t[0] >= -ax and ay>=v2t[1] >= -ay):
```

```
                    ei=ei+1
                    if ndict.get((fi,fj)) == None :
                            ni=ni+1
                            ndict[(fi,fj)]=ni
                            N.append([ni, v1t[0],v1t[1],f3(v1t[0])])
                    if ndict.get((fi+d,fj)) == None:
                            ni=ni+1
                            ndict[(fi+d,fj)]=ni
                            N.append([ni, v2t[0],v2t[1],f3(v2t[0])])
                    C.append([ei, ndict[(fi,fj)],ndict[(fi+d,fj)]])
############################################################
# make the mesh finer.
if nb > 1:
        lC= len(C)
        nC = [];
        for j in range(lC):
                el =C[j]
                newp =[];
                nA = el[1]; nB = el[2];
                pA = N[nA-1][1:4]; pB = N[nB-1][1:4];
                xpA = pA[0];ypA = pA[1];zpA = pA[2];
                xpB = pB[0];ypB = pB[1];zpB = pB[2];
                for i in range(nb-1):
                        rat=float(i+1)/(nb-i-1);
                        xpn = (rat*xpB +xpA)/(rat+1)
                        ypn = (rat*ypB +ypA)/(rat+1)
                        zpn = (rat*zpB +zpA)/(rat+1)
                        ni = ni+1
                        N.append([ni, xpn, ypn, zpn])
                        if i==0 and i!=nb-2:
                                nC.append([1,nA,ni])
                        if i==0 and i==nb-2:
                                nC.append([1,nA,ni])
                                nC.append([1,ni,nB])
                        if i==nb-2 and i!=0:
                                nC.append([1,ni,nB])
                                nC.append([1,ni-1,ni])
                        if i!=0 and i!=nb-2:
                                nC.append([1,ni-1,ni])
        C=nC;
        ei=0; # restart ei counter
        for k in C:
                ei =ei+1
                k[0] = ei
# both C and N are complete at this point
############################################################
# iniate BC sets
```

```
xzero=[];yzero=[];
# go through the nodes list and pick the boundary sets
for el in N:
	if el[1]==0 and el[2]==0:
		center=el[0]
	if el[1]==0 and el[2]!=0:
		xzero.append(el[0])
	if el[2]==0 and el[1]!=0:
		yzero.append(el[0])
#############################################################
# this function finds the normal at a point
def fn(x3,f3):
	normv=[-x3/(rx*math.sqrt(1-x3**2/rx**2)),0,-1]
	lengthn = math.sqrt(sum([el**2 for el in normv]))
	thisn = [el/lengthn for el in normv] # normalize
	return thisn

myn =[]; # list for n1 vectors
for el in C:
	node1 = el[1]; node2= el[2]
	p1=N[node1-1][1:4];p2=N[node2-1][1:4];
	x1 = p1[0]; y1=p1[1]; z1=p1[2];
	x2 = p2[0]; y2=p2[1]; z2=p2[2];
	mp = [(x2+x1)/2,(y2+y1)/2,(z2+z1)/2]; # the middle point
	# the normal vector via the gradient
	nv = fn( mp[0],f3)
	# the tangent vector is the one connecting the two nodes =>
	tv = [x2-x1,y2-y1,z2-z1]
	# n1 is merely the cross product
	myn1 = [nv[1]*tv[2]-nv[2]*tv[1],
	   nv[2]*tv[0]-nv[0]*tv[2],nv[0]*tv[1]-nv[1]*tv[0]]
	myn.append(myn1)
#############################################################
# write the INP file
#############################################################
# Heading
#############################################################
f = open(fname,'w')
f.write('*HEADING\n')
f.write('Cylindrical grid INP file\n')
f.write('Number of elem/beam: '+ str(nb)+'\n')
f.write('Cross-section: '+ cs + '\n')
f.write('Length along x: '+ str(ax)+ '\n')
f.write('Length along y: '+ str(ay)+ '\n')
f.write('Radius of curvature (x): '+ str(rx)+ '\n')
f.write('BC on high node: '+ str(hbc)+ '\n')
f.write('**\n')
```

```
############################################################
# Part
############################################################
f.write('*Part, name=GridShell\n')
f.write('** Node definition\n')
f.write('*Node\n')
f.writelines(','.join(str(j) for j in i) + '\n' for i in N)
f.write('** Element definition\n')
f.write('*Element, type=B31\n')
f.writelines(','.join(str(j) for j in i) + '\n' for i in C)
############################################################
f.write('** BC node sets\n')
f.write('*Nset, nset=xzero\n')
for i in range(len(xzero)/15 + 1):
      f.writelines(','.join(str(j) for j in xzero[i*15:(i+1)*15])
                                                + ', \n')
############################################################
f.write('*Nset, nset=yzero\n')
for i in range(len(yzero)/15 + 1):
      f.writelines(','.join(str(j) for j in yzero[i*15:(i+1)*15])
                                                + ', \n')
############################################################
f.write('*Nset, nset=center\n')
f.writelines(str(center) + '\n')
f.write('*Nset, nset=high\n')
f.writelines(str(xzero[0]) + '\n')
f.write('*Nset, nset=low\n')
f.writelines(str(yzero[-1]) + '\n')
f.write('*Nset, nset=high1\n')
f.writelines(str(xzero[-1]) + '\n')
f.write('*Nset, nset=low1\n')
f.writelines(str(yzero[0]) + '\n')
############################################################
for h in C:
      f.write('*Elset, elset=eli'+ str(h[0]) +', internal \n')
      f.write(str(h[0])+'\n')
      f.write('*Beam Section, elset=eli'+ str(h[0]) +
          ',material = Al, temperature= GRADIENTS, section= RECT \n')
      f.write(cs+' \n')
      f.write(','.join(str(i) for i in myn[h[0]-1]) + ' \n')
f.write('*End Part\n')
############################################################
# Assembly
############################################################
f.write('*Assembly, name=Assembly \n')
f.write('** \n')
f.write('*Instance, name=GridShell-1, part=GridShell \n')
```

```
f.write('*End Instance \n')
f.write('** \n')
f.write('*Nset, nset=center, internal, instance=GridShell-1 \n')
f.writelines(str(center) + '\n')
f.write('*Nset, nset=xzero, internal, instance=GridShell-1 \n')
for i in range(len(xzero)/15 + 1):
      f.writelines(','.join(str(j) for j in xzero[i*15:(i+1)*15])
                                                + ', \n')
#############################################################
f.write('*Nset, nset=yzero, internal, instance=GridShell-1 \n')
for i in range(len(yzero)/15 + 1):
      f.writelines(','.join(str(j) for j in yzero[i*15:(i+1)*15])
                                                + ', \n')
#############################################################
f.write('*Nset, nset=high, internal, instance=GridShell-1 \n')
f.writelines(str(xzero[0]) + '\n')
f.write('*Nset, nset=low, internal, instance=GridShell-1 \n')
f.writelines(str(yzero[-1]) + '\n')
f.write('*Nset, nset=high1, internal, instance=GridShell-1 \n')
f.writelines(str(xzero[-1]) + '\n')
f.write('*Nset, nset=low1, internal, instance=GridShell-1 \n')
f.writelines(str(yzero[0]) + '\n')
f.write('** \n')
f.write('*End Assembly \n')
f.write('** \n')
#############################################################
# Materials
#############################################################
f.write('*Material, name = Al \n')
f.write('*Density\n')
f.write('1e-09, \n')
f.write('*Elastic \n')
f.write('69000, 0.32\n')
f.write('** \n')
#############################################################
# Boundary Conditions
#############################################################
f.write('*Boundary \n')
f.write('center, ENCASTRE \n')
f.write('** \n')
#############################################################
# Step 1
#############################################################
f.write('*Step, name=Step-1, nlgeom=YES, inc=1000 \n')
f.write('*Dynamic,application=QUASI-STATIC,initial=NO \n')
f.write('1.,100.,1e-07 \n')
f.write('**  \n')
```

```
f.write('*Boundary \n')
f.write('high, 3, 3, '+str(hbc)+'\n')
f.write('*Boundary \n')
f.write('high1, 3, 3, '+str(hbc)+'\n')
f.write('** \n')
# uncomment below for displacement control of 'low corner'
#f.write('*Boundary \n')
#f.write('low, 3, 3, 150.\n')
##############################################################
# output requests for Step 1
##############################################################
f.write('*Restart, write, frequency=0 \n')
f.write('*Output, field, variable=PRESELECT, frequency=1 \n')
f.write('*Output, history, variable=PRESELECT, frequency=1 \n')
f.write('*End Step\n')
f.write(' \n')
##############################################################
# Step 2
##############################################################
f.write('*Step, name=Step-2, nlgeom=YES, inc=1000 \n')
f.write('*Dynamic,application=QUASI-STATIC,initial=NO \n')
f.write('1.,100.,1e-07 \n')
f.write('** \n')
f.write('*Boundary, op=NEW \n')
f.write('center, ENCASTRE\n')
f.write('*Boundary, op=NEW \n')
f.write('** \n')
##############################################################
# output requests for Step 2
##############################################################
f.write('*Restart, write, frequency=0 \n')
f.write('*Output, field, variable=PRESELECT, frequency=1 \n')
f.write('*Output, history, variable=PRESELECT, frequency=1 \n')
f.write('*End Step\n')
f.close()
# end of script
```

References

Abaqus, Inc. (2007). *Abaqus/CAE user's manual*.

Aggarwala, B.D. & Saibel, E. (1970). Thermal stability of bimetallic shallow spherical shells. *International Journal of Non-Linear Mechanics*, **5**, 49–62.

Aimmanee, S. & Hyer, M. (2004). Analysis of the manufactured shape of rectangular thunder-type actuators. *Smart Materials and Structures*, **13**, 1389.

Arrieta, A., Hagedorn, P., Erturk, A. & Inman, D. (2010). A piezoelectric bistable plate for nonlinear broadband energy harvesting. *Applied Physics Letters*, **97**, 104102–104102.

Berger, M.S. & Fife, P.C. (1966). On von karman's equations and the buckling of a thin elastic plate. *Bull. Amer. Math. Soc*, **72**.

Biron, M. (2012). *Thermoplastics and thermoplastic composites*. Elsevier.

Blinder, S. (2011). Magnetic field of a cylindrical bar magnet. Wolfram Demonstrations Project.

Brodland, G. & Cohen, H. (1987). Deflection and snapping of spherical caps. *International journal of solids and structures*, **23**, 1341–1356.

Calladine, C. (1988). The theory of thin shell structures 1888–1988. *Proceedings of the Institution of Mechanical Engineers, Part A: Journal of Power and Energy*, **202**, 141–149.

Calladine, C. (1989). *Theory of shell structures*. Cambridge University Press.

Chien, W. & Hu, H. (1956). On the snapping of a thin spherical cap. In *Proceedings of the Ninth International Congress of Applied Mechanics*, vol. 6, 309–337.

Coburn, B., Pirrera, A., Weaver, P. & Vidoli, S. (2012). Tristability of an orthotropic doubly curved shell. *Composite Structures*.

Dai, F., Li, H. & Du, S. (2012). A multi-stable lattice structure and its snap-through behavior among multiple states. *Composite Structures*.

Dano, M.L. & Hyer, M. (2002). Snap-through of unsymmetric fiber-reinforced composite laminates. *International journal of solids and structures*, **39**, 175–198.

Dano, M.L. & Hyer, M.W. (1998). Thermally-induced deformation behavior of unsymmetric laminates. *International Journal of Solids and Structures*, **35**, 2101–2120.

Dassault Systémes/Simulia (2011). *Getting starter with Abaqus v6.11*.

Daynes, S., Potter, K. & Weaver, P. (2008). Bistable prestressed buckled laminates. *Composites Science and Technology*, **68**, 3431–3437.

Daynes, S., Diaconu, C., Potter, K. & Weaver, P. (2010). Bistable prestressed symmetric laminates. *Journal of composite materials*, **44**, 1119–1137.

Daynes, S., Weaver, P. & Trevarthen, J. (2011). A morphing composite air inlet with multiple stable shapes. *Journal of Intelligent Material Systems and Structures*, **22**, 961–973.

Dow Corning (2007). *Sylgard 184 Silicone Elastomer, Product Information*. Dow Corning.

Fernandes, A., Maurini, C. & Vidoli, S. (2010). Multiparameter actuation for shape control of bistable composite plates. *International Journal of Solids and Structures*.

Forterre, Y., Skotheim, J.M., Dumais, J. & Mahadevan, L. (2005). How the venus flytrap snaps. *Nature*, **433**, 421–425.

Galletly, D. & Guest, S. (2004a). Bistable composite slit tubes. II. A shell model. *International Journal of Solids and Structures*, **41**, 4503–4516.

Galletly, D.A. & Guest, S.D. (2004b). Bistable composite slit tubes. i. a beam model. *International journal of solids and structures*, **41**, 4517–4533.

Giddings, P.F., Kim, H.A., Salo, A.I. & Bowen, C.R. (2011). Modelling of piezoelectrically actuated bistable composites. *Materials Letters*, **65**, 1261–1263.

Gigliotti, M., Wisnom, M.R. & Potter, K.D. (2004). Loss of bifurcation and multiple shapes of thin [0/90] unsymmetric composite plates subject to thermal stress. *Composites Science and Technology*, **64**, 109–128.

Gilmore, R. (1993). *Catastrophe theory for scientists and engineers*. Dover publications.

Giomi, L. & Mahadevan, L. (2012). Multi-stability of free spontaneously curved anisotropic strips. *Proceedings of the Royal Society A: Mathematical, Physical and Engineering Science*, **468**, 511–530.

Golabchi, M. & Guest, S. (2009). Morphing multiscale textured shells. In *Symposium of the International Association for Shell and Spatial Structures (50th. 2009. Valencia). Evolution and Trends in Design, Analysis and Construction of Shell and Spatial Structures: Proceedings*, Editorial de la Universitat Politécnica de Valencia.

Gorodkin, S., James, R. & Kordonski, W. (2009). Magnetic properties of carbonyl iron particles in magnetorheological fluids. In *Journal of Physics: Conference Series*, vol. 149, 012051, IOP Publishing.

Gude, M., Hufenbach, W. & Kirvel, C. (2011). Piezoelectrically driven morphing structures based on bistable unsymmetric laminates. *Composite structures*, **93**, 377–382.

Guest, S. & Pellegrino, S. (2006). Analytical models for bistable cylindrical shells. *Proceedings of the Royal Society A: Mathematical, Physical and Engineering Science*, **462**, 839.

Guest, S.D., Kebadze, E. & Pellegrino, S. (2010). A Zero-Stiffness Elastic Shell Structure. *Aerospace*, 1–12.

Huang, N.C. (1964). Unsymmetrical buckling of thin shallow spherical shells. *Journal of Applied Mechanics*, **31**, 447.

Huber, J., Fleck, N. & Ashby, M. (1997). The selection of mechanical actuators based on performance indices. *Proceedings of the Royal Society of London. Series A: Mathematical, Physical and Engineering Sciences*, **453**, 2185–2205.

Hull, D. & Clyne, T. (1996). *An introduction to composite materials*. Cambridge Univiversity Press.

Hyer, M.W. (1981a). Calculations of the room-temperature shapes of unsymmetric laminates. *Journal of Composite Materials*, **15**, 296–310.

Hyer, M.W. (1981b). Some observations on the cured shape of thin unsymmetric laminates. *Journal of Composite Materials*, **15**, 175–194.

Hyer, M.W. (1982). The room-temperature shapes of four-layer unsymmetric cross-ply laminates. *Journal of Composite Materials*, **16**, 318–340.

Iqbal, K. & Pellegrino, S. (2000). Bi-stable composite shells. In *Proc. 41st AIAA/ASME/ASCE/AHS/ASC Structures, Structural Dynamics, and Materials Conference and Exhibit*, 3–6.

Iqbal, K., Daton Lovett, A. & Pellegrino, S. (1998). Bi-stable composite slit tubes. In *Proceedings of the IUTAM-IASS 1998 Symposium on Deployable Structures: Theory and Applications*, 153–162, Kluwer Academic Publishers.

Jones, R. (1999). *Mechanics of composite materials*. CRC.

Kebadze, E., Guest, S. & Pellegrino, S. (2004). Bistable prestressed shell structures. *International Journal of Solids and Structures*, **41**, 2801–2820.

Lagrange, J. (1811). Mécanique analytique.

Lebée, A. & Sab, K. (2013). Homogenization of a space frame as a thick plate: application of the bending-gradient theory to a beam lattice. *Computers & Structures*.

Leckie, F.A. & Dal Bello, D.J. (2009). *Strength and stiffness of engineering systems*. Springer.

Lötters, J., Olthuis, W., Veltink, P. & Bergveld, P. (1997). The mechanical properties of the rubber elastic polymer polydimethylsiloxane for sensor applications. *Journal of Micromechanics and Microengineering*, **7**, 145.

Love, A.E.H. (1888). The small free vibrations and deformation of a thin elastic shell. *Philosophical Transactions of the Royal Society of London. A*, **179**, 491–546.

Lu, D. & Wong, C. (2009). *Materials for advanced packaging*. Springer.

MakerBot Industries, LLC (2012). http://www.makerbot.com/.

Malek, S.R. (2012). *The effect of geometry and topology on the mechanics of grid shells*. Ph.D. thesis, Massachusetts Institute of Technology.

Mansfield, E. (1962). Bending, buckling and curling of a heated thin plate. *Proceedings of the Royal Society of London. Series A, Mathematical and Physical Sciences*, **268**, 316–327.

Mansfield, E.H. (2005). *The bending and stretching of plates*. Cambridge University Press.

Mattioni, F., Weaver, P., Potter, K. & Friswell, M. (2008). Analysis of thermally induced multistable composites. *International Journal of Solids and Structures*, **45**, 657–675.

Mattioni, F., Weaver, P. & Friswell, M. (2009). Multistable composite plates with piecewise variation of lay-up in the planform. *International journal of solids and structures*, **46**, 151–164.

McCraig, M. & Clegg, A.G. (1987). *Permanent Magnets in Theory and Practise*. Wiley.

Miravete, A. (1999). *3-D textile reinforcements in composite materials*. CRC Press LLC.

Norman, A., Golabchi, M., Seffen, K. & Guest, S. (2008a). Multistable textured shell structures. *Advances in Science and Technology*, **54**, 168–173.

Norman, A., Seffen, K. & Guest, S. (2008b). Multistable corrugated shells. *Proceedings of the Royal Society of London-A*, **464**, 1653–1672.

Norman, A., Seffen, K. & Guest, S. (2009). Morphing of curved corrugated shells. *International Journal of Solids and Structures*, **46**, 1624–1633.

O'Donnell, W.J. (1973). Effective elastic constants for the bending of thin perforated plates with triangular and square penetration patterns. *Journal of Engineering for Industry*, **95**, 121.

Ostoja-Starzewski, M. (2002). Lattice models in micromechanics. *Applied Mechanics Reviews*, **55**, 35–60.

Panov, D. (1947). On the stability of a bimetallic membrane on heating. *Prikl. Mat. Mekh*, **11**, 603.

Pirrera, A., Avitabile, D. & Weaver, P. (2010). Bistable plates for morphing structures: A refined analytical approach with high-order polynomials. *International Journal of Solids and Structures*, **47**, 3412–3425.

Pirrera, A., Avitabile, D. & Weaver, P. (2011). On the thermally induced bistability of composite cylindrical shells for morphing structures. *International Journal of Solids and Structures*.

Pirroni, L. (2012). *On the failure mechanisms and mechanics of urethane bi-stable tubes*. Fourth-year undergraduate project, Univeristy of Cambridge.

Portela, P., Camanho, P., Weaver, P. & Bond, I. (2008). Analysis of morphing, multi stable structures actuated by piezoelectric patches. *Computers & structures*, **86**, 347–356.

Pressley, A.N. (2010). *Elementary differential geometry*. Springer.

Quapp, W. & Heidrich, D. (1984). Analysis of the concept of minimum energy path on the potential energy surface of chemically reacting systems. *Theoretica chimica acta*, **66**, 245–260.

Salamon, N. & Masters, C.B. (1995). Bifurcation in isotropic thinfilm/substrate plates. *International journal of solids and structures*, **32**, 473–481.

Schultz, M.R. (2008). A concept for airfoil-like active bistable twisting structures. *Journal of Intelligent Material Systems and Structures*, **19**, 157–169.

Seffen, K. (2006). Mechanical memory metal: a novel material for developing morphing engineering structures. *Scripta materialia*, **55**, 411–414.

Seffen, K. (2007). Morphing bistable orthotropic elliptical shallow shells. *Proceedings of the Royal Society A: Mathematical, Physical and Engineering Science*, **463**, 67.

Seffen, K. (2012). Compliant shell mechanisms. *Philosophical Transactions of the Royal Society A: Mathematical, Physical and Engineering Sciences*, **370**, 2010–2026.

Seffen, K. & Guest, S. (2011). Pre-stressed Morphing Bistable and Neutrally Stable Shells. *Journal of Applied Mechanics, Trans ASME*.

Seffen, K. & Pellegrino, S. (1999). Deployment dynamics of tape springs. *Proceedings of the Royal Society of London. Series A: Mathematical, Physical and Engineering Sciences*, **455**, 1003–1048.

Seffen, K., You, Z. & Pellegrino, S. (2000). Folding and deployment of curved tape springs. *International journal of mechanical sciences*, **42**, 2055–2073.

Seffen, K.A. & Maurini, C. (2012). Growth and shape control of disks by bending and extension. *Journal of the Mechanics and Physics of Solids*.

Slot, T. & O'Donnell, W. (1971). Effective elastic constants for thick perforated plates with square and triangular penetration patterns. *Journal of Engineering for Industry*, **93**, 935.

Stewart, I. (1983). Elementary catastrophe theory. *Circuits and Systems, IEEE Transactions on*, **30**, 578–586.

Thom, R. (1972). *Stabilité structurelle et morphogénèse*. WA Benjamin Reading, Massachusetts.

Thompson, J.M.T. (1982). *Instabilities and catastrophes in science and engineering.*. John Wiley & Sons, Inc.

Thompson, J.M.T. & Hunt, G.W. (1984). *Elastic instability phenomena*. Wiley.

Tong, L., Mouritz, A.P. & Bannister, M. (2002). *3D fibre reinforced polymer composites*. Elsevier science.

Tripathi, D. (2002). *Practical guide to polypropylene [electronic resource]*. iSmithers Rapra Publishing.

Veeramachaneni, U.K. & Carroll, R.L. (2007). Magnetic particle motion in a gradient field. In *Proceedings of the COMSOL Conference*.

Vidoli, S. (2013). Discrete approximations of the Föppl-Von Kármán shell model: from coarse to more refined models. *International Journal of Solids and Structures*.

Vidoli, S. & Maurini, C. (2008). Tristability of thin orthotropic shells with uniform initial curvature. *Proceedings of the Royal Society A: Mathematical, Physical and Engineering Science*, **464**, 2949.

Vision Research Inc. (2013). http://www.visionresearch.com/.

Wallenberger, F.T. & Bingham, P.A. (2010). *Fiberglass and glass technology: energy-friendly compositions and applications*. Springer.

Wittrick, W., Myers, D. & Blunden, W. (1953). Stability of a bimetallic disk. *The Quarterly Journal of Mechanics and Applied Mathematics*, **6**, 15–31.

Wolfram Research Inc. (2008). Mathematica edition: Version 7.0.

Young, W.C. & Budynas, R.G. (2002). *Roark's formulas for stress and strain*, vol. 6. McGraw-Hill New York.

Zeeman, E.C. (1977). Catastrophe theory: Selected papers, 1972–1977.